ABSTRACT

Title of Dissertation: MULTISCALE SENSING OF THE
PHYSICAL CELLULAR ENVIRONMENT:
PHASE-FIELD MODELING AND EXPERIMENTS

Corey Joshua Herr
Doctor of Philosophy, 2025

Dissertation Directed by: Professor Wolfgang Losert
Department of Physics

Cells constantly interact with their physical environment by sensing and responding to mechanical and topographical cues. These cues span multiple scales, from subcellular interactions with the extracellular matrix to population-scale confinement in morphogenesis. Central to this process is the actin cytoskeleton, which serves as both a local force generator and a medium for signal integration and propagation. In this dissertation, I combine multiscale computational modeling with quantitative imaging to investigate how actin dynamics drive physical sensing from the scale of single protrusions to collective cellular behavior.

The actin cytoskeleton is the primary mechanism for generating forces that cause cell protrusions and guided migration. Using 12Z cells as a model of endometriosis, we examine how exposure to the biochemical signal estradiol alters actin organization and, consequently, cell morphology. High-resolution 3D imaging reveals that estradiol treatment increases protrusion size and disorder in actin dynamics, consistent with enhanced cellular invasiveness. These findings

highlight how chemical signals modulate mechanical output through actin-based protrusions, reinforcing the role of actin as a key transducer of biochemical cues into physical motion.

At the subcellular scale, we use a 3D phase-field model to illustrate how cells exhibit unidirectional migration on asymmetric nanotopographies, with directionality controlled by actin polymerization rate and topographic scale. In this model, an asymmetric substrate alone can cause spontaneous polarization and reproduce the shape and guidance morphologies observed experimentally. These predictions align with a reanalysis of *D. discoideum* experiments, revealing that guidance on subcellular sawteeth depends on both cell velocity and feature height. This agreement indicates that membrane deformation and local curvature sensing, driven by actin forces, are sufficient to bias migration in complex microenvironments.

To study how the actin cytoskeleton responds to chemical cues found in the extracellular matrix, we analyze epithelial cell migration on collagen-coated nanoridges. On nanoridges, collagen IV enhances actin alignment and cell elongation; however, actin guidance remains decoupled from the direction of migration. Therefore, additional mechanisms, such as focal adhesion dynamics, may contribute to directional sensing.

At larger scales, we develop a scalable 2D multicellular phase-field model incorporating excitable actin dynamics. This framework enables simulations of thousands of deformable cells on consumer hardware. The model spans a range of scales, allowing cell interaction, long-distance wave propagation, and information exchange. In this model, excitable intracellular mechanics, along with local physical interactions, can lead to emergent synchronization and local sensing of the shape of large-scale confinement.

Together, these findings suggest that actin serves as a mechanochemical interface for multiscale environmental sensing by driving local protrusions, integrating physical signals, and enabling collective coordination through excitable dynamics. Actin polymerization additionally acts as an upstream regulator of other cell functions, which opens avenues for future experimental studies on the effects of actin synchronization and pulsing on biophysical behavior. By linking cytoskeletal signaling to large-scale coordination, this work lays the foundation for identifying new physical mechanisms underlying biological processes that require coordination, such as metastasis and tissue morphogenesis.

MULTISCALE SENSING OF THE PHYSICAL CELLULAR ENVIRONMENT:
PHASE-FIELD MODELING AND EXPERIMENTS

by

Corey Joshua Herr

Dissertation submitted to the Faculty of the Graduate School of the
University of Maryland, College Park in partial fulfillment
of the requirements for the degree of
Doctor of Philosophy
2025

Advisory Committee:
  Professor Wolfgang Losert, Chair/Advisor
  Professor Igor Aronson
  Professor Michelle Girvan
  Professor Maria Mukhina
  Professor Kimberly M. Stroka, Dean's Representative

Dedication

In memory of Nolan Stopfel, my best friend.

Growing up together was unforgettable.

Acknowledgments

Just like the cells in my thesis, I have been bolstered by a community at multiple scales. I have heard many of my friends and colleagues describe the isoltation of grad school. And while I agree that, at times, my work has made me feel alone. I would say that the brilliant and kind people who supported me throughout my Ph.D., some from my past, and many from my time here, have made me feel like a part of community.

First, I would like to thank my advisor, Professor Wolfgang Losert, for your support and guidance; I'm grateful for the freedom you've given me to discover a fascinating field of study. I would also like to thank my committee members, Professor Igor Aronson, Professor Michelle Girvan, Professor Maria Mukhina, and Professor Kim Stroka. Igor, for being instrumental to the phase-field work; I appreciated getting the chance to revisit Penn State while working with you. Professor Michelle Girvan and Dr. Daniel Serrano for being fantastic mentors in the COMBINE NSF program. Professor John Fourkas for the feedback in our weekly(ish) esotaxis meetings. Professor Kim Stroka for the opportunity to work on endometriosis cells. My collaborator, Shohini Banerjee, for your cell work and our boba sessions; I never expected to work with you after meeting through ballroom dance in undergrad.

I have received financial support from both the COMBINE and POLS programs, which have been fundamental for my growth as a scientist. I have valued the iPOLS network and Arpita Upadhyaya for giving me the opportunity to travel internationally and share my work.

I would like to thank all of Losert Lab, past and present, for their companionship and insight. Anna Emenheiser, for being a level-headed office mate and helping me write emails I didn't want to. Hoony Kang for the thoughtful discussions about synchronization and the less thoughtful discussions that I won't enumerate here. Jeneh, Sylvester, and Spandan, for all the fun we've had at game night. Jerry, for the help culturing dicty. Mengwen, Brianna, Benjamin, and Collin, for being truly excellent undergraduate students. Rachel and Lenny, for welcoming me to a new lab when I had I knew nothing about biology.

Most importantly, I would like to thank my friends and family, without whom I would have most likely be living in a van. Thank you to my wonderful parents, Mom and Dee, for your tireless support and willingness to answer a phone call at any time. I owe my success to your unwavering belief that I can do anything. Thank you to the Stopfels for making me feel at home whenever I visited. Thanks to my brother, Dakota, and my niece, Journee, for reminding me how much family matters. Thank you to my extended family and family friends for the repeated questions about when I would finish; all those questions motivated me to get through my degree. Thank you to my dear friend and former roommate, Rumya. Thank you to the great friends I have made throughout graduate school, Thomas, Jonquil, Tereza, Senya, Debo, Deba, Anna, Laura, and many others.

I've found a community and a home during my time in College Park, one full of caring people who stand up for their beliefs, and I've become a better person for it.

Table of Contents

List of Tables

List of Figures

List of Abbreviations

ECM	Extracellular Matrix
cAMP	Cyclic adenosine monophosphate
FHN	Fitzhugh-Nagumo
STEN	Signal transduction excitable network
1D	One dimensional
2D	Two dimensional
3D	Three dimensional
OF	Optical Flow
E2	17β-estradiol
EMT	Epithelial-Mesenchymal transition
TF	Transcription factor
CC	Collagen-coated
c.o.m.	center-of-mass

Chapter 1: Introduction

1.1 Cellular physical microenvironment

1.1.1 Cells sense physical cues

Cells *in vivo* exist in a complex microenvironment comprising both physical and chemical cues. Biology has long placed importance on the chemical signals received by cells; however, a wide range of physical cues are also present, which provide information vital for understanding living systems. Cancer metastasis provides an excellent study of the various ways cells sense the physical environment (Fig. 1.1) [1]. First, cells inside a tumor can sense the solid stress exerted on the tumor [2] by surrounding cells (Fig. 1.1A). Increasing the stress has been shown to lead to an increase in metastasis [3]. After cancer cells leave the tumor, they interact with the extracellular matrix (ECM), an extensive network of proteins and other molecules that surround the cell (Fig. 1.1A). The cancer cells then sense the orientation of the surrounding ECM and rearrange the proteins to improve physical guidance [4]. Furthermore, they respond to fluid mechanical forces, including shear flow encountered in blood vessels, which can influence adhesion, morphology, and survival during circulation [5]. Finally, cancer cells detect changes in interstitial and vascular fluid pressure during intravasation and extravasation (Fig. 1.1B) [6–8].

Cancer metastasis exemplifies the diverse range of physical cues that are crucial for cellular

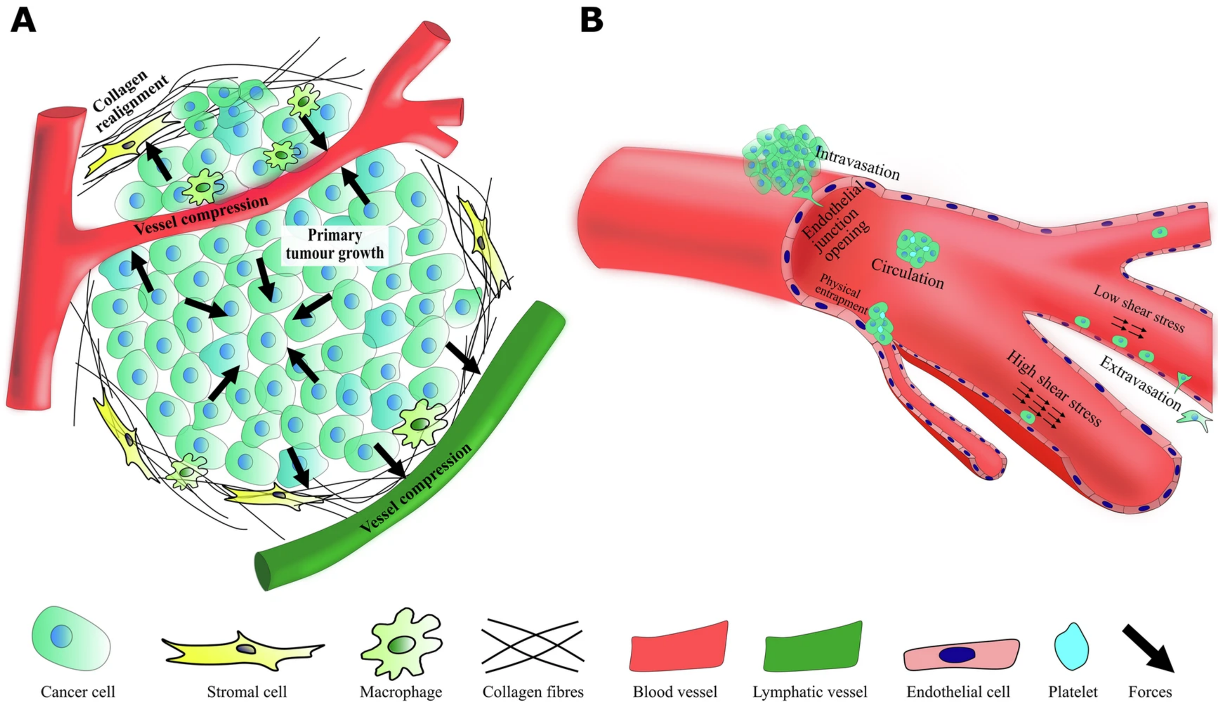

Figure 1.1: (A) Primary tumor growth. The stress in the tumor is primarily compressive in the interior and tensile at the edges, resulting in compression of the surrounding tissues. Cancer cells realign the collagen surrounding the tumor to aid in physical guidance away from the tumor. (B) Metastatic groups of cells migrate to blood vessels and must invade through the endothelium in a process known as intravasation. During intravasation, cells experience high shear stress, and during circulation, cells feel fluid drag forces. Reproduced from [9] under a Creative Commons Attribution 4.0 International License from npj Biological Physics and Mechanics.

function or dysfunction; however, these interactions are important for nearly all living cells. Unicellular organisms, such as *Dictyostelium discoideum*, sense nearby cells and form adhesive bonds after physical contact [10]. Epithelial cells sense physical defects at a wide range of scales, from subcellular elongate mineral particles such as asbestos [11] to large-scale wound sensing via the presence of a free boundary of cells near the wound [12]. Even neurons respond to physical forces; a recent study suggested that the dendritic spine increases presynaptic neurotransmitter release by applying mechanical forces during enlargement. [13].

Cells encounter a diverse range of physical forces at a variety of scales. In this dissertation, I focus on two types of physical sensing:

1. Sensing of local curvature (Section 1.1.2)
2. Sensing of the local physical environment through intracellular mechanochemical waves (Section 1.2.4)

1.1.2 Sensing curvature

Cells respond to their physical surroundings through a cycle that begins with mechanical sensing, followed by mechanotransduction, and finally results in mechanical response [14]. The cells first experience a physical cue, such as those discussed in the prior section, and then that physical cue is transduced into a chemical signal inside the cell, which leads to a change in mechanical force generated by the cell. In the example of curvature sensing, many cells use BAR protein domains to detect membrane curvature on the scale of 10 nm and can then act to maintain curvature by binding to the membrane [15].

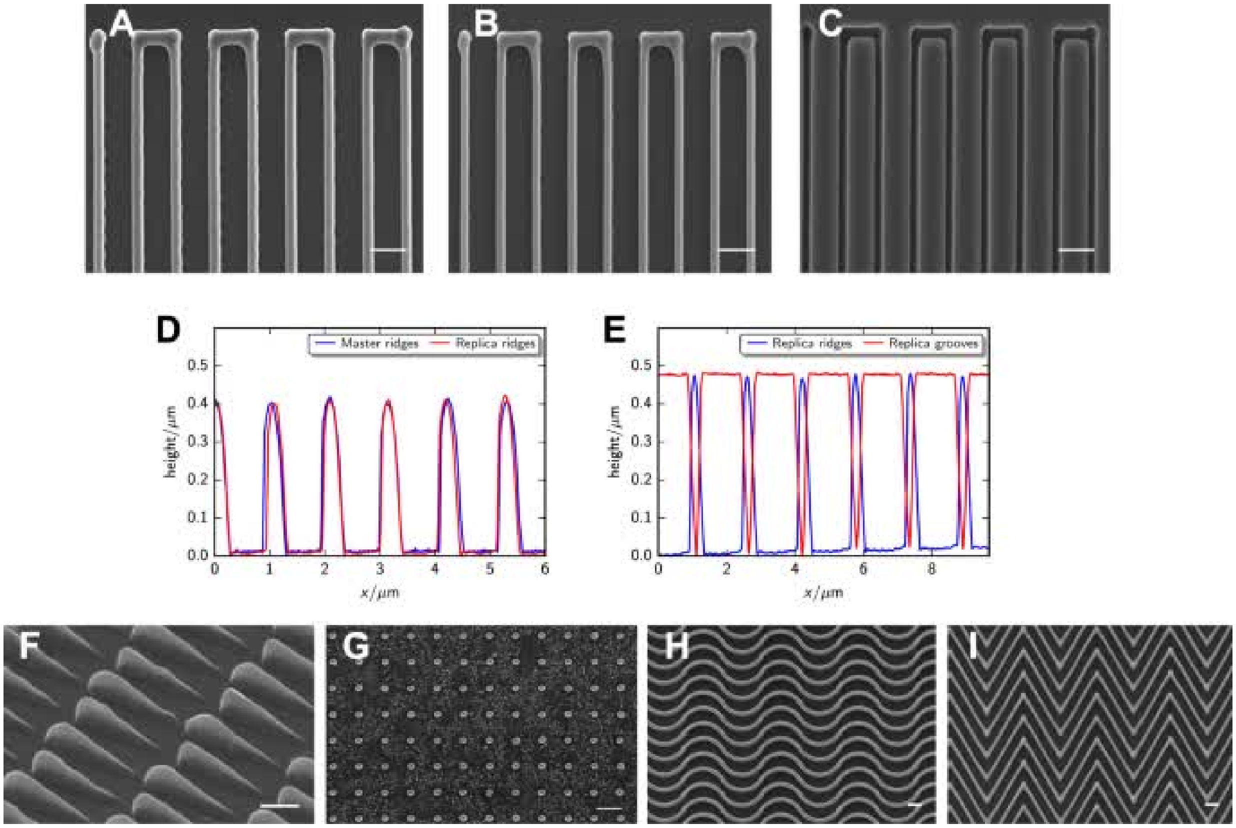

Figure 1.2: (A-C) SEM images of master molds for nanoridge surface replication, scale bar 1.5 μm. (D-E) AFM measurements of 1 μm and 1.5 μm ridges. (F-I) SEM images of topography, scale bar 2 μm (F) asymmetric sawteeth (G) nanoposts, (H) curvy ridges, (I) kinked ridges. Reproduced from [23] from Scientific Reports under a Creative Commons Attribution 4.0 International License.

In vivo, cells are subject to a non-homogeneous, 3D ECM that leads to a wide range of curvature scales [16]. [17–19] . However, traditional *in vitro* experiments are largely conducted on flat glass coverslips. Using flat surfaces neglects the inherent 3D environment of cells *in vivo* and causes cells to become artificially flattened [20–22].

In order to investigate the effect of local curvature on cell behavior, many experimentalists have pursued structured nanosurfaces with curvatures on the scale of 100 nm to 1 μm [23–25]. A variety of nanotopographic surfaces have been studied (see Figure 1.2) including ridges (Fig. 1.2A-E), sawteeth (Fig. 1.2F), pillars (Fig. 1.2G), and wavy/kinked ridges (Fig. 1.2H-I).

Studies have shown that local curvature cues from nanotopography induce migration [25–27], morphology changes [28], and differentiation [29]. Nanotopography offers a structured approach to studying curvature at ECM scales, eliminating the disorder and challenges associated with creating a biologically relevant environment. However, this picture of curvature sensing is not complete without considering the dynamic nature of the cell, which I will discuss in Section 1.2.

1.2 Excitability in the cell

1.2.1 Actin cytoskeleton

Cell motility is the process by which cells integrate local physical and chemical cues, initiating polarization and directional guidance. An essential component of cell motility is the cytoskeleton, a dynamic network of microtubules and microfilaments that maintains the cell's shape and initiates cellular motion. The cytoskeleton spans the entire cell and is composed of various components; however, I am particularly interested in the actin cytoskeleton. The actin cytoskeleton generates pushing and pulling forces vital for controlling the onset and maintenance of cell motion [30]. Actin is essential for the onset of cell polarization [31], wound healing [32], and even the activation of neutrophils [33].

The actin cytoskeleton is made up primarily of the eponymous protein actin, a globular protein that polymerizes and forms filaments that make up structures of different types and sizes [34]. Actin combines with cross-linking and branching proteins such as the Arp2/3 complex [35] to form large-scale branched organizations inside the cell (see Figure 1.3). At the front of a traveling cell, there is a dense forest of cross-linked actin [36] called the lamellipodium. The

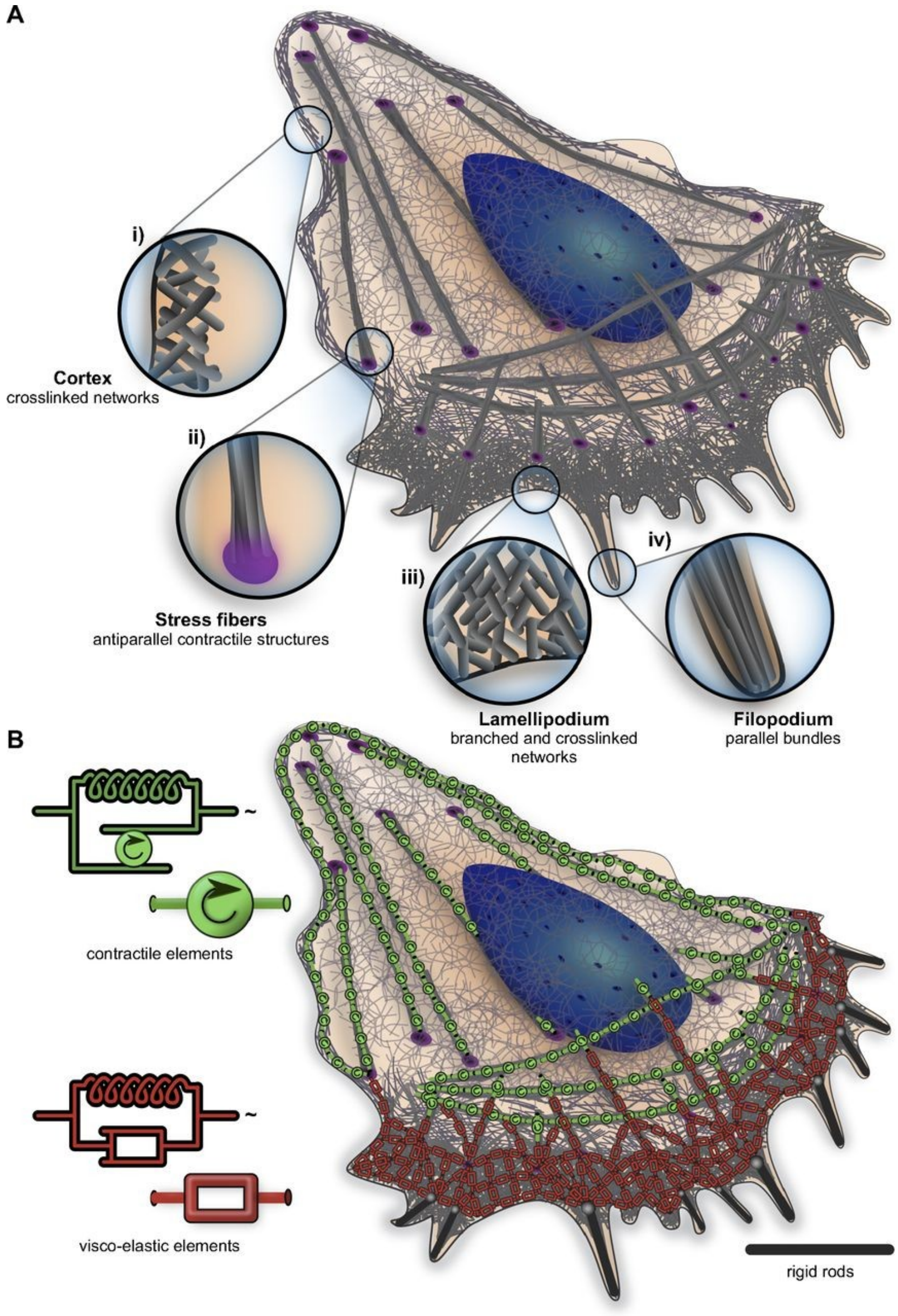

Figure 1.3: The actin cytoskeleton exhibits diverse organization. **A** A diagram illustrates the variety of structures in the actin cytoskeleton. The cortex (**i**) surrounds the entire cell and provides structure to the plasma membrane. Stress fibers (**ii**) span the cell, causing contractile forces. The lamellipodium (**iii**) is a branched, cross-linked actin structure at the front of the cell which leads to motility. Finally, the filopodia (**iv**) are small finger-like protrusions that act to sense the cell surroundings. **B** The different actin structures inside the cell have various dynamic properties, including contractile and visco-elastic forcing. Reproduced from [34] with permission from the American Physiological Society

actin cortex is a thin layer of actin that covers the interior of the plasma membrane and provides membrane tension in conjunction with myosin [37]. Finally, there are cell-spanning stress fibers [38] that provide contractility to the cell.

The way that individual actin filaments exert a force on the cell boundary is not entirely understood. The elastic Brownian ratchet theory suggests that fluctuations in the cell membrane and the actin filament itself allow actin to polymerize between a buckled filament and the membrane, thereby exerting an outward force [39]. However, current microscopy limitations mean that this process has not been directly observed. Regardless of the mechanism behind it, this force generation is the primary mechanism for cell protrusion, an essential requirement for cell motion in all environments.

These actin structures undergo dramatic changes over time. They are in constant communication with their surroundings, receiving mechanical feedback from the cell boundary. The lamellipodium dynamics are dominated by actin treadmilling, a continuous wave of polymerization at the front of the cell with depolymerization following closely behind [35]. The stress fibers pull on the edges of the cell, receiving mechanical feedback from the focal adhesions that attach the cell to the substrate [40]. The dynamic interplay of actin and its regulatory proteins can be modeled as an excitable system, which I will discuss in the remainder of the section.

1.2.2 Models of excitability

A broad range of biological phenomena can be modeled through excitable systems [41], dynamical systems that permit traveling waves with a refractory period. Excitability has been observed in neurons [42–46], heart tissues during cardiac arrest [47–49], and a broad range of cytoskeleton dynamics [50, 51]. An excitable system is highly nonlinear; under a small perturbation, a large transit in phase space will occur, effectively amplifying small inputs. Conversely, after the transit in phase space, there is a refractory period where the system at that point loses its excitability for a set amount of time. These features give excitable systems a diverse set of dynamics, including locally traveling waves, sustained global oscillations, and spiral waves1.4.

The Fitzhugh-Nagumo (FHN) model provides an illustrative example of excitable dynamics [43], which was devised to capture the dynamics of neuronal excitability. The FHN model, given by Equations 1.1-1.2, acts as a 1D activator-inhibitor model, with the activator u initially representing the membrane potential of a neuron and the inhibitor v representing the opening of the membrane channels.

$$\frac{\partial u}{\partial t} = c(v - \frac{u^3}{3} + u) \tag{1.1}$$

$$\frac{\partial v}{\partial t} = \frac{1}{\tau}(u - bv + a) \tag{1.2}$$

The nullclines of the FHN model (Figure 1.4A bottom) provide great insight into the dynamics of the system. Equilibrium rests at the intersection of the v nullcline and the u nullcline. The positioning of the equilibrium point(s) with respect to the u nullcline determines the dynamics of the system.

If the equilibrium point is between the two local extrema of the u nullcline, the behavior is oscillating (Figure 1.4A.1). The value of u, or the membrane potential in this model, will constantly oscillate. If the equilibrium point lies to the left of the local minimum of u (Fig 1.4A.2), the system is excitable; a small super-threshold input will cause a large transit in phase space, effectively one spike, before the system returns to equilibrium. The system is in the

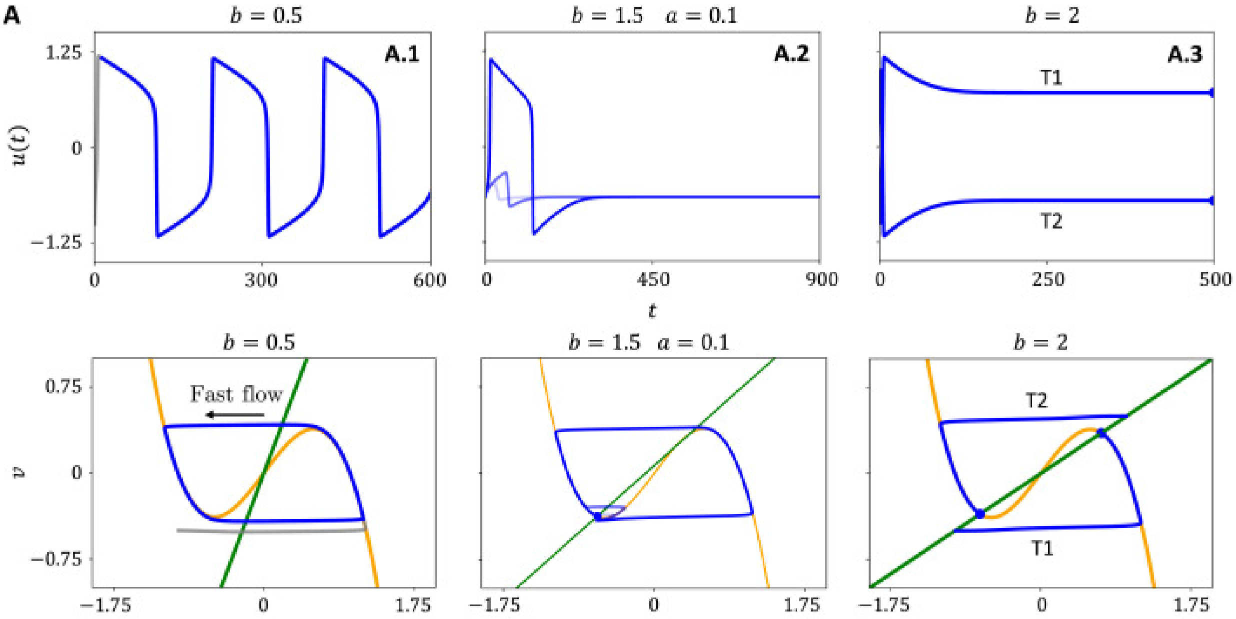

Figure 1.4: Dynamics of Fitzhugh-Nagumo model. The top row shows the dynamics of the activator u over time. The bottom row shows the u nullcline (yellow) and the v nullcline (green), along with a sample phase space trajectory (blue). Varying the system parameters creates oscillatory states (A.1), excitable states (A.2), and bistable states (A.3). Adapted from [52] with permission from Elsevier.

refractory period while the value of u is sub-equilibrium. Finally, if the parameters are chosen such that there are two equilibrium points, as in Figure 1.4A.3, the system exhibits bistability – this state is significantly less studied in biological applications.

This framework can be extended to the spatial dimension by adding a diffusion term (Equations 1.3, 1.4). When expanding to spatial dimensions, this system supports traveling waves of excitation instead of local spikes and global oscillations instead of simple oscillations [53].

$$\frac{\partial u}{\partial t} = D_u \nabla^2 u + c(v - \frac{u^3}{3} + u) \tag{1.3}$$

$$\frac{\partial v}{\partial t} = D_v \nabla^2 v + \frac{1}{\tau}(u - bv + a) \tag{1.4}$$

These traveling waves and global oscillations were the first hints that actin polymerization could be viewed as an excitable system.

1.2.3 Excitability in the actin cytoskeleton

Actin dynamics in the cell is influenced by a complex network of regulatory proteins with multiple activator-inhibitor feedback loops. For example, in *Dictyostelium discoideum* the signal transduction pathway involved in directed cell migration is made up of many distinct regulators (see Figure 1.5) that sense everything from shear flow to electric fields [54]. When viewed at the individual polymer scale, actin appears to behave like a treadmilling system, as discussed in Section 1.2.1. However, when looking at the whole-cell scale, actin exhibits excitable system patterns such as traveling waves that have been observed in a wide variety of cell types, including neutrophils [50], *D. discoideum* [54–56], *C. elegans* [57], and even frog oocytes [58].

Actin waves have been successfully modeled using excitable systems [50, 54–56, 59–63]. Actin excitability is normally modeled by coupling multiple activator-inhibitor networks at different scales. Some notable models have used a system of local excitation leading to global inhibition [63] or have focused instead on modeling the signal transduction pathway [56] and its coupling to the cytoskeleton [55].

One of the simplest models of actin excitability in *D. discoideum* is the signal transduction excitable network (STEN) model. Miao *et al.* [56] proposed a simple activator-inhibitor model (see Figure 1.6) given by Equations 1.5 and 1.6 where F is the activator and R is the inhibitor (see Figure 1.6a).

Versions of excitable models have successfully modeled the connection of actin flow to a wide range of phenomena, including polarity and directed cell migration [64], chemotaxis [65],

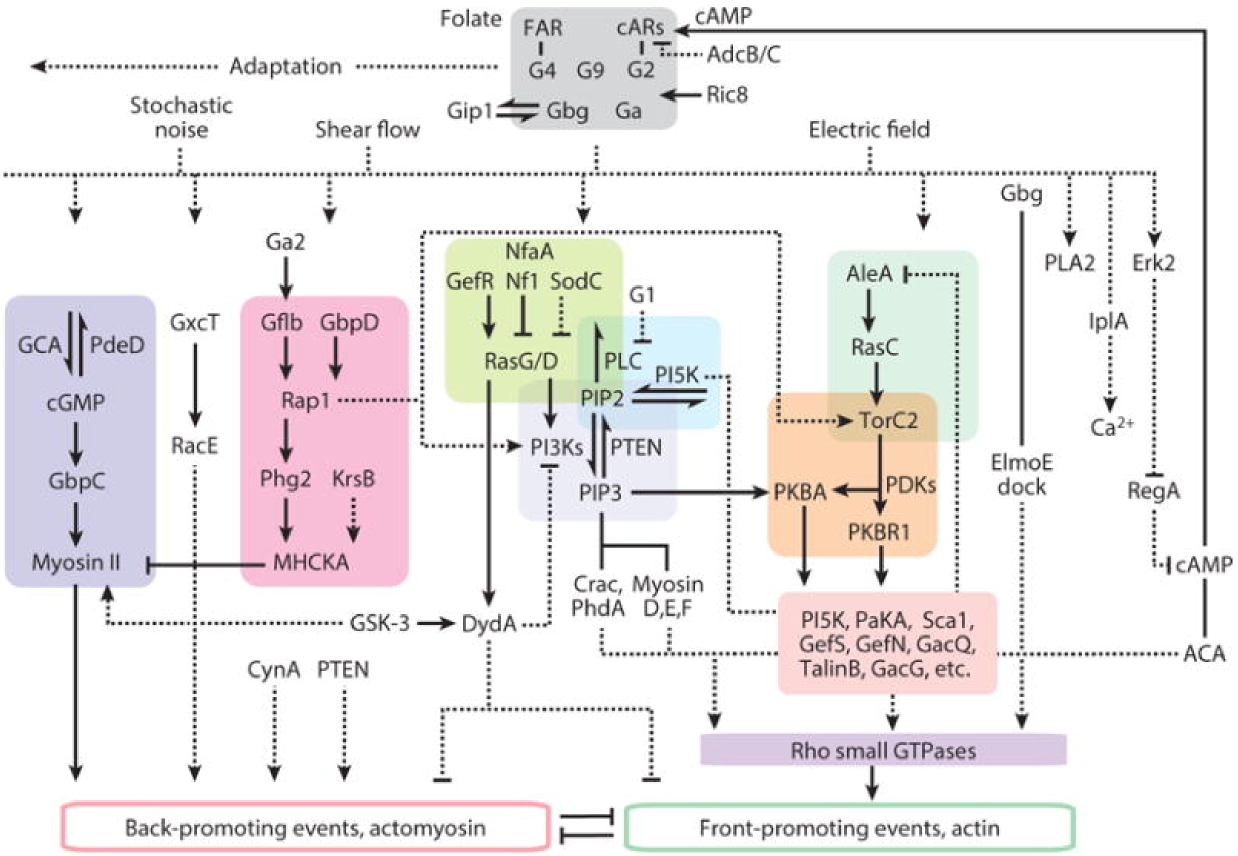

Figure 1.5: Signaling networks underlying directed cell migration in *D. discoideum*. Arrows indicate activating interactions; flat-ended lines represent inhibitory effects. Half-arrow symbols denote substrate-product interactions. Solid lines correspond to experimentally confirmed direct interactions, while dashed lines suggest inferred or possible direct connections. Reproduced from [54] with permission from Springer Nature

and guidance on nanotopography [66].

$$\frac{\partial F}{\partial t} = D_F \nabla^2 F - (a_1 + a_2 R)F + a_3 \left(\frac{F^2}{a_4^2 + F^2} + U_B \right) (a_5 - F) + a_6 U_N \tag{1.5}$$

$$\frac{\partial R}{\partial t} = D_R \nabla^2 R - c_1 R + c_2 (g - \varphi P) F \tag{1.6}$$

This minimal excitable model produces a variety of realistic actin wave and cell phenotypes. The actin system produces local traveling waves, large cell-scale waves, and global constant stimulation, as shown in Figure 1.6b. Figure 1.6c shows that these STEN activities produce amoeboid, fan-shaped, and oscillatory cells, respectively. This model is directly linked to concentrations of regulatory proteins in the cell (Figure 1.6d). Excitability gives us a powerful way to couple the internal chemical dynamics of a cell to the observed mechanical behavior of the cell.

1.2.4 Sensing with actin waves

In section 1.1.2, I discussed curvature sensing in the context of the BAR domains and small-scale curvature [67, 68]. It is known that BAR domain proteins can inhibit actin polymerization [17], which would affect actin wave dynamics, but that is on the scale of nanometers. The individual proteins may not be able to sense larger-scale curvatures, but the actin cytoskeleton changes organization in response to a variety of physical cues. Recent studies suggest that the dynamic rearrangement of the actin cytoskeleton can act as a sensor of the physical environment [69, 70].

Actin dynamics significantly change in response to curvatures smaller and larger than the

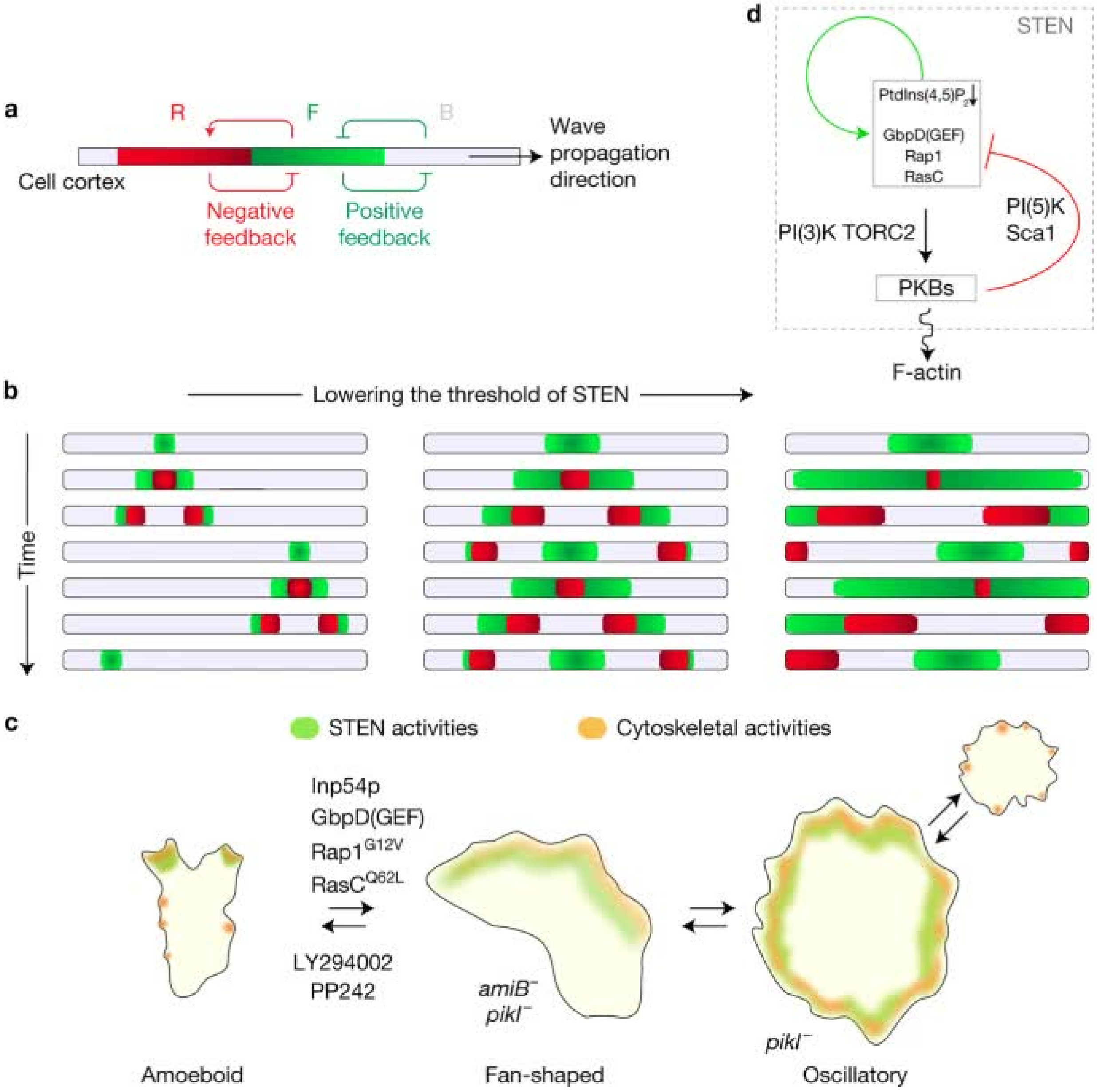

Figure 1.6: **(a)** Schematic of wave propagation in 1D. The activator is shown in green, and the inhibitor is shown in red. **(b)** Propagation of waves over time. At a high threshold (left), the waves travel for shorter distances. Increasing the threshold leads to larger waves (middle) and, finally, global oscillations (right). **(c)** Representative cell shapes produced by different STEN thresholds. **(d)** Regulatory proteins underlying the STEN dynamics. Adapted from [56] with permission from Springer Nature.

scale of a cell. At the smaller scale of nanotopography, it has been shown that nanotopographic ridges introduce a bidirectional bias in actin migration and polymerization [25, 71]. Large-scale stiffness gradients also affect the polymerization of actin waves [72]. These sensing mechanisms, along with the physical forces exerted by actin waves, suggest that the excitable dynamics themselves are necessary to sense the surroundings. Understanding the link between physical sensing, internal actin wave dynamics, and cell motion has been a challenge in the field up to this point.

1.2.5 Connecting experiment to theory with optical flow

One method to connect biological observations of actin dynamics to quantitative models such as excitable systems is through an approach called optical flow [73]. Optical flow outperforms other traditionally used methods, such as PIV, when measuring subcellular velocities [74] and has been employed in classical computer vision for decades [73]. The goal of optical flow is to capture the motion of similar intensity values within an image over time. For instance, if an image has intensity field $I(x,y)$, then optical flow is found by solving Equation 1.7, where $\mathbf{v}$ is the optical flow velocity we are solving for.

$$\nabla I \cdot \mathbf{v} = -\frac{\partial I}{\partial t} \tag{1.7}$$

The values of ∇I and $\frac{\partial I}{\partial t}$ can be found easily through classical finite-difference method approximations (See Figure 1.7 for a visualization of optical flow); however, the solution to this equation is more challenging.

A common approach for solving the optical flow equation is the Lucas-Kanade method [75], which assumes that the optical flow is constant within a small spatial window. This al-

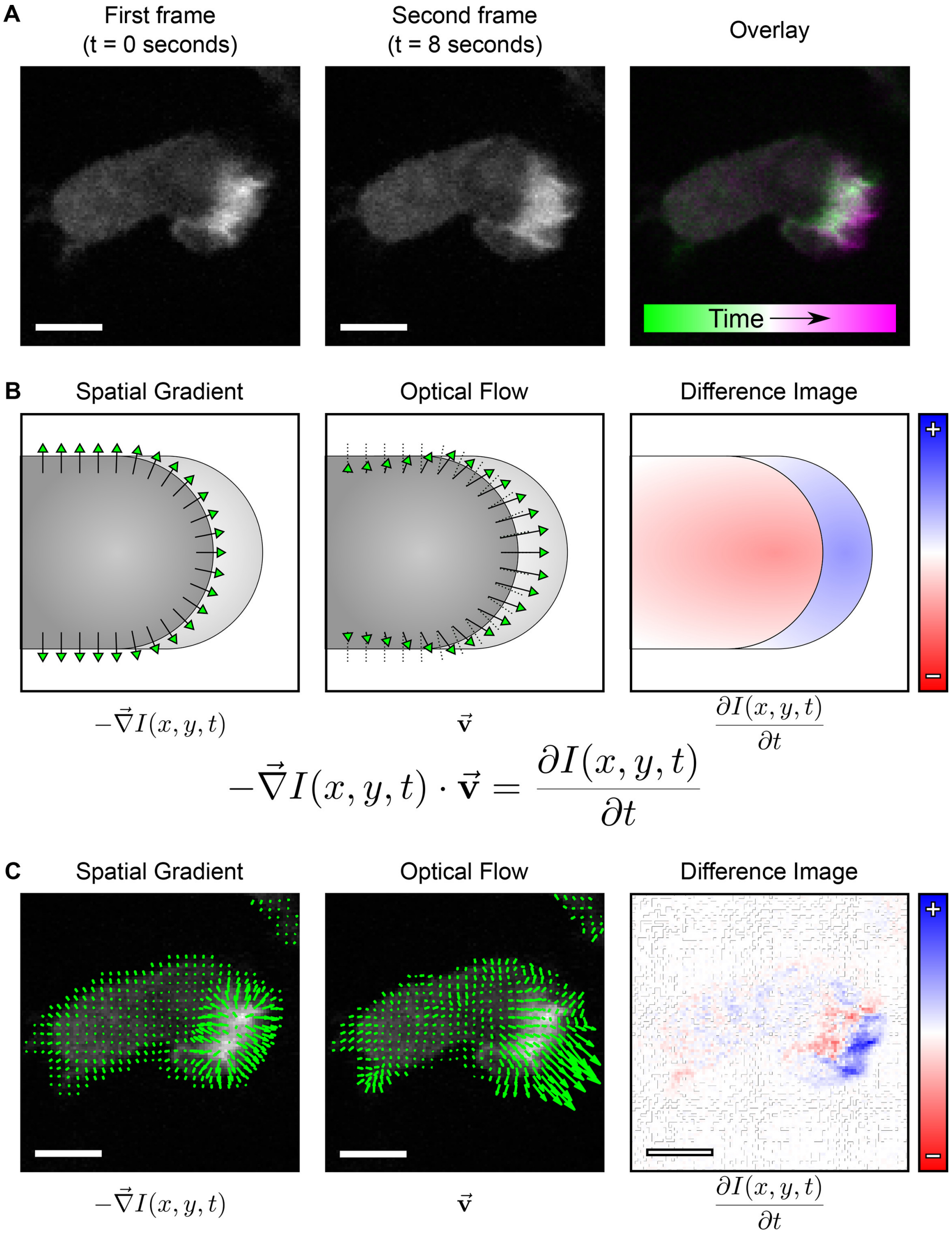

Figure 1.7: **A** Images of a cell expressing fluorescently labeled actin (grayscale). The rightmost image shows an overlay of multiple timepoints to highlight actin motion **B** Schematic illustrations of the optical flow components: spatial image gradients (∇I), estimated flow vectors, and temporal intensity differences ($\partial I/\partial t$). **C** Visualizations of the same components as in (**B**), but computed directly from the raw data shown in (**A**), illustrating how the optical flow algorithm extracts motion information from intensity changes over time. Example of how each component of the optical flow equation looks for a sample image. This figure is reproduced from [71] with permission from the American Society for Cell Biology.

lows the system to be overdetermined by incorporating additional spatial constraints: instead of solving the underdetermined problem at a single pixel, the Lucas-Kanade method fits a velocity vector that minimizes the residuals of Equation 1.7 across neighboring pixels. This local averaging enables robust estimates even in the presence of image noise, making it well-suited for the small-scale, continuous motions found in subcellular structures like actin networks.

In biological contexts, such as the study of actin dynamics, optical flow enables detailed, frame-by-frame mapping of retrograde flow and wave propagation across the cortex or leading edge of cells [50, 71]. Compared to PIV, which operates on discrete patches and often requires larger features or user-defined tracking, optical flow preserves spatial continuity and can resolve fine structures more effectively. This makes optical flow ideal for analyzing excitable actin waves, lamellipodial activity, and transitions between different dynamic regimes. By coupling optical flow–derived velocity fields with models of excitable media or mechanical feedback, researchers can more precisely quantify how local protrusive and contractile forces emerge from the underlying biochemical signaling landscape.

1.3 Cell motility

1.3.1 Guided migration is necessary for life

Many of the cues discussed in earlier sections can trigger directed cell migration. This movement is critical for life and development. However, when the mechanisms behind cell motility malfunction, they are often associated with various pathologies, including cancer metastasis and autoimmune disorders. A variety of cues can cause directed migration including nanotopography [26], stiffness gradients [76], chemical signaling [77], and direct contact with other cells via leader-follower dynamics [78]. Cell motility happens at a wide range of scales, from cell scale at 1 μm to entire organ scale on the order of centimeters. This multiscale nature makes it challenging to study the sensing and response that cells exhibit during guided migration.

Cells can migrate individually, such as neutrophils traveling to infection sites, or collectively, like epithelial cells closing a wound. Individual cell migration tends to be heavily affected by the physical structure of the ECM [79] and other surrounding physical cues. This indicates that understanding how the cells sense with the microenvironment is paramount to understanding individual cell motility. Likewise, there are a variety of mechanisms by which cells migrate collectively. In leader-follower migration, selected leader cells initiate motion and then send physical and chemical cues to the follower cells [80, 81]. There are also mechanisms of Contact Inhibition of Locomotion (CIL) that cause cells to maintain unidirectional polarization at large scales [82]. Modeling these differing mechanisms of migration is essential to understanding development, wound healing, immune response, and many pathologies.

1.3.2 Motility in pathology

Dysfunction in motility and the cytoskeleton is the underlying reason for many different pathological phenomena. Inhibition of motion through inhibition of actin polymerization causes defects in the function of NK cells, which leads to many autoimmune diseases [83]. Cancer metastasis occurs when cancerous cells from a tumor irregularly migrate throughout the body [9]. Neutrophils have been shown to be overzealous in chronic inflammation [84], continuously being recruited to sites of inflammation. Finally, there are even suggestions that microglia migration can impact the development of Alzheimer's disease [85].

As I will discuss in Chapter 2, endometriosis is a disorder where endometrial tissue grows outside of the uterus. Endometriosis affects almost 10% of women of reproductive age, causing intense pain and even infertility [86]. Investigating cell motility is necessary to understanding endometriosis because the aberrant cells migrate outside the uterus and become trapped. Existing studies suggest that there are a variety of actin-binding proteins that affect the migration of endometriotic cells, including alpha-actinin-1 [87], calponin [88], and cofilin-1 [89]. These actin-binding proteins affect endometriotic cell migration differently but tend to lead to more contractile and more migratory cells [90]. Understanding how endometriotic cells adapt their sensing and motility in response to chemical and physical cues is necessary for developing strategies to combat this common and debilitating disorder.

1.4 Models of cell motility

Modeling cell motility allows us to make both quantitative and qualitative predictions about the behavior of cells in healthy, novel, and dysfunctional environments. In this section, I will give a broad overview of the different types of cell motility models.

1.4.1 Modeling individual cells

1.4.1.1 Graded radial extension

Because the cell membrane is thin compared to the size of the cell, many prior studies have treated it as a 1D line. One of the earliest models of individual cell motion, named graded radial extension, treated the boundary as a 1D line with a fixed shape. Lee *et al.* [91] modeled the motion of a fish epithelial keratocytes, cells that are known for their consistent gliding motion, with this method. This model predicts that regions of extending or retracting membrane will move around the cell, effectively creating rotating protrusions. The model assumes that any extension or retraction of the front of the cell will occur perpendicularly to the cell boundary. The graded radial extension model has seen many updates over the years [92–94] in an attempt to make it more realistic, and it was able to obtain a force-velocity agreement for the lamellipodial actin network. However, this model only works for specific cell shapes and is not easily extensible into higher dimensions.

1.4.1.2 Level set methods

Instead of treating cell boundaries as fixed, implicit interface methods, such as the level set method, allow for changing shape and cell dynamics. The level set method defines the boundary of the cell as an equipotential line of a given potential function. This model allows for interfaces that have no inherent bending or membrane tension [95]. It has been used to successfully model the link between cytoskeleton dynamics and physical mechanisms of cell motion [96–100]. This method is comparable to the phase-field method that is the focus of this dissertation (Section 1.5), but it's extensions to multicellular systems and dimensions higher than two become computationally prohibitive. Additionally, the level set method has a distance function with poorly defined behavior that can quickly accumulate numerical error [95].

1.4.1.3 Whole cell models

Many scientists are moving to a larger-scale approach by simulating the chemical, physical, and gene regulatory methods of a single cell in its entirety. There have been incredible

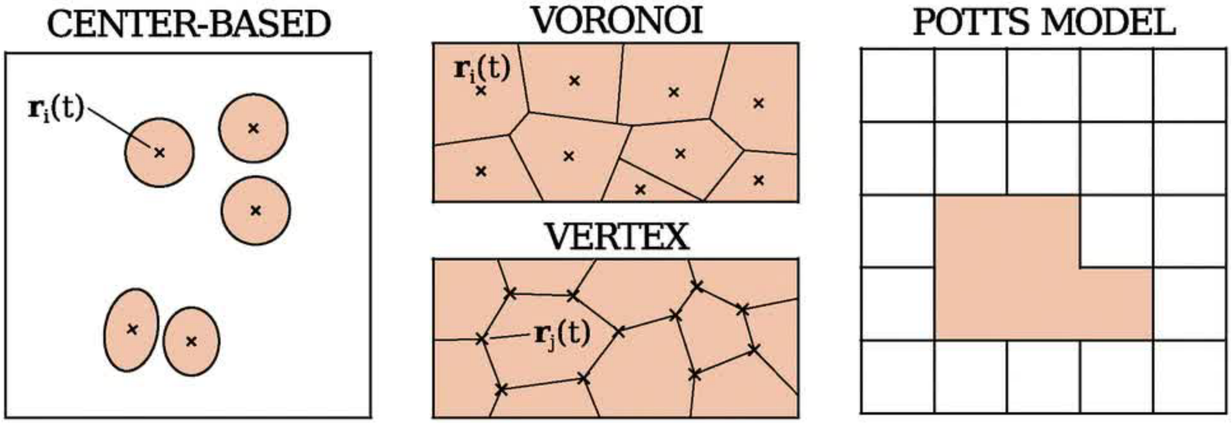

Figure 1.8: Representative schematics of collective cell motility models. Cells are indicated by the peach-colored regions. **(Left)** In center-based methods, the cells are specified by position and basic shape. **(Top middle)** Voronoi models are specified by position only. The shape is completely determined by position. **(Bottom middle)** Vertex models specify cells by the position $r_j(t)$ of every vertex of a cell that meets at a junction of three or more cells. **(Right)** Cellular Potts model represents cells as collections of "spin" states on a lattice. Adapted from [106] with permission from Nature Publishing.

efforts to capture the dynamics of every molecule inside of a cell including *Mycoplasma genitalium* [101], *Escherichia coli* [102, 103], and even a eukaryotic cell model of *Saccharomyces cerevisiae* (Brewer's yeast) [104]. These models have been remarkably successful; a spatially resolved model for the minimal cell JCVI-syn3A [105] has accurately measured the doubling time and connections between metabolism and cell growth. However, despite their success, these models lack large-scale migration, protrusions, or integration with surrounding physical cues, and they are also extremely computationally expensive. However, with time and development, they provide a promising avenue for finding quantitative links between chemical signals and physical reactions.

1.4.2 Modeling collective behavior

1.4.2.1 Agent based models

Agent-based or center-based models come in two forms: uniform particles (see Fig. 1.8a) and simple deformable particles. The key feature of these models is that the cells are not spatially resolved. Instead, the cells are stored as collections of coordinates, and interaction between cells (See Fig. 1.8 left) is based on distance, similar to scattering problems. Usually, a force balance equation is written for an overdamped system, including friction with the substrate, cell-cell interactions, and internal cellular forces [107]. The difference between uniform and deformable particles is that the force terms account for a simple cell shape. One prominent version is in Voronoi models (see Fig. 1.8 middle top)[108]. This approach has successfully modeled jamming in tissues [109–111]. When the shape is considered, it can provide an easy way to study the coupling between morphology and behavior [112]. Agent-based models provide the unparalleled power to simulate astonishingly large numbers of cells [113], but they do so at the cost of single-cell spatial resolution and fail to capture many intricate dynamics.

1.4.2.2 Vertex model

In vertex models (see Fig. 1.8 middle bottom), the cells are represented by a set of vertices that indicate the intersection of three or more neighboring cells [114]. Vertex models are one of the most widely used models of collective cell dynamics; however, they significantly limit the spatial resolution of a cell, requiring every point to be an intersection between multiple cells. They have been successful at modeling many phenomena in epithelial cell sheets [115, 116] and retrieving quantitative predictions of the tension in monolayers [117, 118]. One major downside is that these models are limited to only modeling confluent or nearly confluent sheets of cells, which does not effectively describe *in vitro* work with non-confluent cell sheets or single-cell experiments.

1.4.2.3 Cellular Potts model

The cellular Potts model [119, 120] is an extension of the large-Q Potts model for simulation of diffusive grain growth [121] intended to model cell dynamics. In the cellular Potts model, a cell is made up of a series of "sites" on a lattice representing a kind of spin that holds energy (see Fig. 1.8 right). Then, a Hamiltonian is written for the entire cell configuration that accounts for deformation, target area, and any other number of physical interactions (see [119, 120] for further details). Then, the system is updated by stochastically copying spin from one site to the next based on the energy penalty. This model is relatively computationally efficient and has been extended to solve problems in chemotaxis [122], tumor formation [123], and morphogenesis [124]. The downside of this model is that the Monte Carlo steps make it challenging to interpret the system in terms of physical forces [107]. Some studies believe that the Potts model should not be used as a kinetic model at all [125].

1.5 Phase-field model

1.5.1 Origins of the phase-field model

Moving-boundary problems occur in many physical situations throughout nature. The naive approach to solving moving-boundary problems is predefining the evolution of the bound-

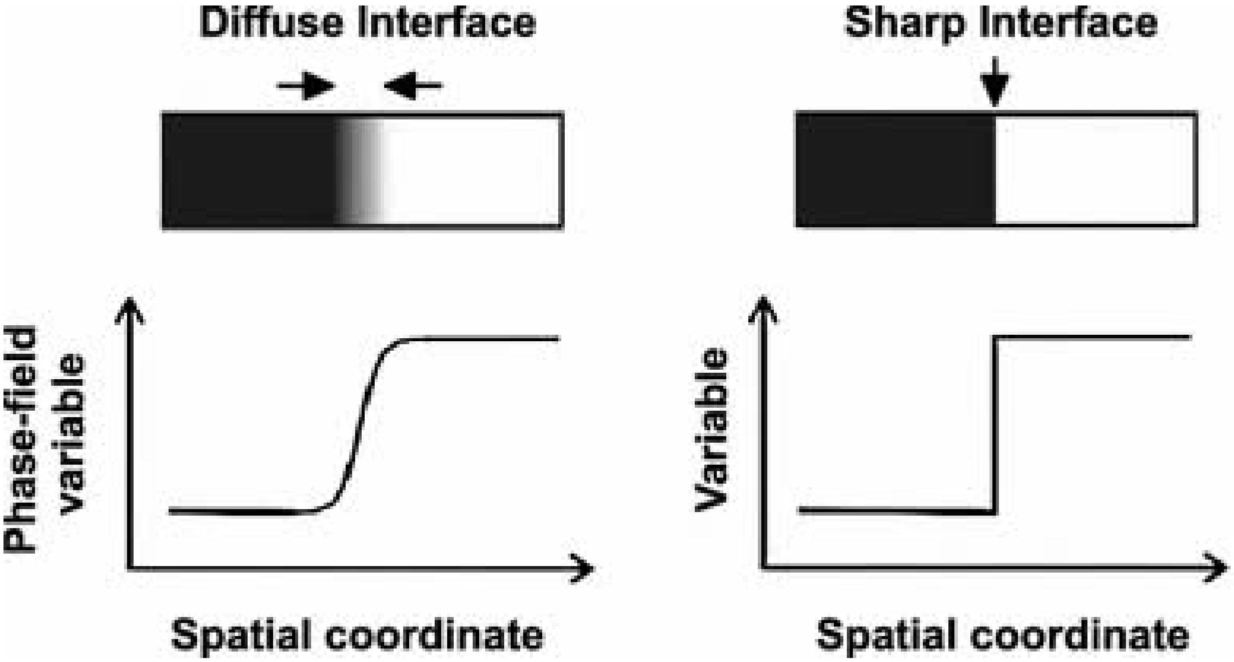

Figure 1.9: Diffuse versus sharp interface methods. **Left** Diffuse interfaces allow for a slow change from one phase to another. The diffuse interface has a size indicated by the space between the arrows. **Right** Sharp interface methods require instant transitions in space from one phase to another. Adapted from [133] with permission from Springer Publishing.

ary geometry over time. This approach is illustrated by the sharp interface methods discussed in Section 1.4.1. Phase-field modeling arose as an attempt to solve physical problems on moving boundaries; it has been applied to a variety of physical systems, including crack propagation [126, 127], solidification [128–130], and diffusion in complex scenarios [131, 132].

Modeling moving boundaries is an exceedingly complex task, requiring a simulation to track the position of a large set of points for a long period of time. For the case of cell motility, the scale of the cell membrane is on the order of 10 nanometers, whereas the whole cell is from 10-100 microns. Because the size of the cell is 5-6 orders of magnitude larger than the boundary, simulating a sharp interface would take an enormous amount of memory[133]. The increase in grid size requires a time step that is scaled by $O(\Delta x^2)$ where Δx is the separation between adjacent grid points. Sharp interface methods normally require a Δx that is 4 orders of magnitude smaller

[133] than phase field methods. This decrease in Δx leads to a simulation that is 10^8 times slower – significantly too slow to simulate the dynamics at hand with even the most advanced machines. Additionally, applying realistic forces at the scale leads to large numerical instability [134] and difficult formulations of physical laws [135]. These problems are exaggerated more in 3D, because the number of grid points necessary in a simulation is $O(N^3)$, meaning that the simulation size scales with the cube of the number of grid points instead of the square.

Additionally, to solve for physical constraints in sharp interfaces, many simplifications need to be made. In classic phase separation theory, they simplify the shape of the boundary to be ellipsoids, paraboloids, or hyperboloids [135]. This drastically reduces the applicability of sharp interface methods to real-world problems. To simulate realistic conditions, we must move past the natural inclination to track the boundary as a sharp interface.

Implicit interface methods, also known as diffuse boundary methods, were developed to get past these limitations. By defining the boundary to be the isosurface of a continuous variable, we gain the ability to implicitly model a boundary without explicitly tracking it (see Figure 1.9). This method comes with some limitations, such as slower simulation, because all points in space must be updated. However, we gain the ability to use Hamiltonian dynamics to assign an energy to the boundary. The key method for choosing this Hamiltonian came from the study of phase separation in chemical systems, which we will discuss next.

1.5.2 Preserving the laws of physics with diffuse boundary modeling

The fundamental advance of the phase-field model is decoupling the sharp geometrical constraint of a boundary from the shape dynamics. An auxiliary field $\phi(\mathbf{r}) \in [0,1]$, known as the phase-field, is introduced. We define $\phi = 0.5$ as the transition point between phases. In practice, we choose the dynamics for ϕ such that a characteristic length scale exists for the transition from 0 to 1. In this, we have an approximation for the location of the boundary and a way to retrieve the sharp interface limit by taking the characteristic length scale of the transition to 0.

The first step to constructing a moving boundary model is to describe the energy associated with that boundary. This problem was initially studied by Cahn and Hilliard [136], who looked at the interfacial energy of a nonuniform system. They proposed that for any nonuniform property ϕ, the free energy of the interface $\mathscr{F}_{\mathrm{CH}}$ is given to second order by Equation 1.8.

$$\mathscr{F}_{\mathrm{CH}} = \int_V \left(f_0(\phi) + \frac{\gamma}{2}(\nabla\phi)^2 + \ldots \right) dV \tag{1.8}$$

This free energy is dependent on the local value of the nonuniform parameter ϕ and its gradient and leads to useful properties for moving boundary problems. The interface is diffuse, and the thickness of the interface is controllable by choice of $f_0(\phi)$ and γ.

The chemical potential μ (Equation 1.9) is found by taking the functional derivative of the free energy.

$$\mu = \frac{\delta \mathscr{F}_{\mathrm{CH}}}{\delta \phi} = \frac{\partial f_0(\phi)}{\partial \phi} + \gamma \nabla^2 \phi \tag{1.9}$$

Cahn and Hilliard used this chemical potential along with mass conservation to derive Equation 1.10, known as the Cahn-Hilliard equation, that gives the earliest and one of the simplest phase-field models.

$$\frac{\partial \phi}{\partial t} = \nabla \cdot [m(\phi) \nabla \mu] \tag{1.10}$$

The Cahn-Hilliard equation was used with great effect to model spinodal decomposition [137] and has become a cornerstone method for discovering properties of complex materials [138, 139]. However, it also provides an easily extensible model for problems outside of material science simply by including the free energy associated with the interaction that needs to be modeled.

1.5.3 Single cell phase-field models

From here on, I will focus on the application of phase-field methods to cell motility. In order to construct a functioning phase-field model of cell motility, we must find the energetic contributions of each physical part of cell motility. We use the Cahn-Hilliard free energy (Equation 1.8) along with a double well potential, $G(\phi) = \phi^2(1-\phi)^2$, to get the energy contribution of a membrane (Equation 1.11).

$$H_{\text{membrane}} = \int_V \left[\frac{1}{\varepsilon^2} \phi^2 (1-\phi)^2 + D(\nabla \phi)^2 \right] dV \tag{1.11}$$

This gives us Equation 1.12, a phase-field model for a resting cell with characteristic membrane width ε. $G'(\phi)$ is given by the derivative of the double well potential with respect to ϕ.

$$\frac{\partial \phi}{\partial t} = \gamma(\nabla^2 \phi + \frac{1}{\varepsilon^2} G'(\phi)) \tag{1.12}$$

With this equation alone, if we initialize the field ϕ with random values, we will see phase separation into one region of $\phi = 0$ and one region of $\phi = 1$. After long times, the boundary will become circular in order to minimize the wall-tension. In relation to cell motility simulations, a $\phi = 1$ circle initialized with a radius of r_0 will maintain the same radius, but develop diffuse boundaries. This gives a model of a resting cell.

There are two successful approaches to extending the basic phase-field model of a resting cell to address questions about cell motility. The first type of model accounts for the polarization of actin filaments, such as the model of self-polarizing keratocyte fragments from Ziebert et al [140]. This type of model couples the dynamics of a phase-field variable to a vector field $\mathbf{p}$ that describes the orientation of actin filaments, giving spatial resolution to the actin orientation. From Ziebert *et al.* [140], the dynamics of the phase-field ϕ are given by Equation 1.13 and the dynamics of the actin filament orientation, $\mathbf{p}$ are given by Equation 1.14.

$$\frac{\partial \phi}{\partial t} = D_\phi \nabla^2 \phi - (1-\phi)(\delta-\phi)\phi - \alpha \nabla\phi \cdot \mathbf{p} \tag{1.13}$$

$$\frac{\partial \mathbf{p}}{\partial t} = D_p \nabla^2 \mathbf{p} - \tau_{\mathbf{1}}^{-\mathbf{1}} \mathbf{p} - \tau_{\mathbf{2}}^{-\mathbf{1}} (\mathbf{1} - \phi^{\mathbf{2}}) \mathbf{p} - \beta \nabla\phi - \gamma(\nabla\phi \cdot \mathbf{p})\mathbf{p} \tag{1.14}$$

Where $\delta = \frac{1}{2} + \mu(\int_V \phi \mathrm{d}V - A_0) - \sigma|\mathbf{p}|^2$. D_ϕ determines the width of the interface. The term $(1-\phi)(\delta-\phi)\phi$ is an altered version of the double well potential that accounts for area conservation and contraction given by $\sigma|\mathbf{p}|^2$. The final term of the Equation 1.13 accounts for advection between the actin polarization and the order parameter. Equation 1.14 accounts for diffusion of actin polymerization with diffusion $D_{\mathbf{p}}$, actin depolymerization inside the cell with rate τ_1^{-1}, suppression of polarization outside the cell with rate τ_2^{-1}, generation of actin polarization

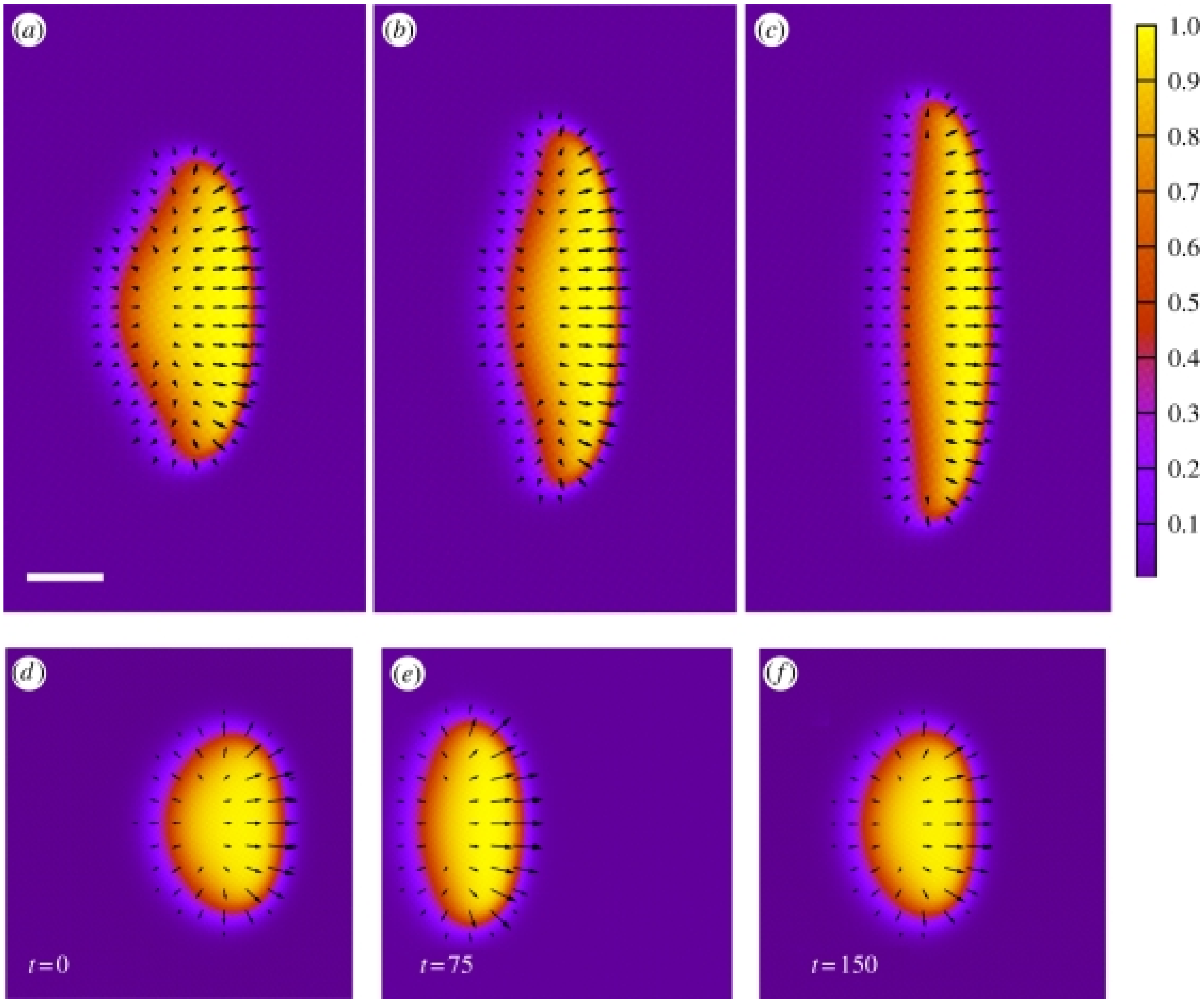

Figure 1.10: **Shape dynamics reproduced by Equations 1.13, 1.14** The color shows the value of the phase-field $\phi(x,y)$ and the arrows show the orientation vector field $\mathbf{p}$. By increasing contractility from (a) $\sigma = 0.3$ (b) $\sigma = 0.5$ and (c) $\sigma = 0.7$, the cell shape becomes more elongated. In a different parameter regime, cells display oscillatory behavior instead (d-f), going from a wedge shape to a more elongated shape. This figure was reproduced from [140] with permission from RSIF.

with rate β, and finally course grained modeling of actomyosin contraction. Details of the 3D extension of this model are further discussed in Chapter 3.

The basic version of this model successfully modeled the motion of keratocyte fragments, exhibiting discontinuous onset of motion, lamellipodia dynamics, and a variety of cell shape dynamics. Figure 1.10 shows some example dynamics of this model. The original approach by Ziebert *et al.* was extended to include many more physical elements of cell motility [141–145] including interactions with the substrate [146], implementing spiral wave dynamics [141], and arbitrary 3D topography [147].

The other approach to phase-field modeling of cell motility involves coupling a velocity field to the cell membrane. This is typically achieved by assuming an overdamped system, such that the force balance equation given by Equation 1.15 is satisfied.

$$F_{\text{membrane}} + F_{\text{protrusion}} + F_{\text{intercellular}} = F_{\text{friction}} = -\xi v \tag{1.15}$$

The velocity is related to the phase-field through the advection equation $\frac{\partial \phi}{\partial t} = \nabla \phi \cdot \mathbf{v}$ giving us a general form of the phase-field Equation 1.16 where the first term is the active components of the system and the second term is the internal energy of the phase-field.

$$\frac{\partial \phi}{\partial t} = -\nabla \phi \cdot \mathbf{v} + \frac{\delta \mathscr{F}_{\text{int}}}{\delta \phi} \tag{1.16}$$

This was originally done by Shao *et al.* [148], and the full version of their model was able to qualitatively reproduce the dynamics of cell motion. This version of the phase-field model can also be computationally coupled to other fields and has been extended in many ways [149, 150].

1.5.4 Multicellular phase-field methods

One of the key strengths of phase-field modeling is the easy extension to multiple cells. This is done by assigning each cell its own phase-field variable ϕ_i and adding interaction terms between cells. The two most important interactions to consider are steric repulsion and adhesion. Many multiphase models use steric repulsion, $\mathscr{F}_{\text{rep}}$, proportional to power law relations between the phase-field variable (Equation 1.17). The choice of power does not matter much, but most models choose n=2 for simplicity because even powers are more stable [151, 152].

$$\mathscr{F}_{\text{rep}} = \sum_{i \neq j} \int_V \phi_i^n \phi_j^n \mathrm{d}V \tag{1.17}$$

Adhesion is typically chosen to be proportional to $\nabla\phi$ and is an active force on the cell body. Usually, this is accounted for outside the free energy, such as in Equation 1.18.

$$\frac{\partial \phi}{\partial t} = \sum_{i \neq j} c \nabla \phi_i \cdot \nabla \phi_j \tag{1.18}$$

Other methods have been proposed, including more realistic adhesion and repulsion dynamics [152, 153] that can produce more biologically feasible results, albeit requiring significantly more complicated models.

The phase-field model is a natural choice for simulating multiple cells due to its ease of theoretical extension. However, introducing a separate phase field for each cell comes at a steep computational cost. There have been methods that reduce this burden, such as introducing an auxiliary field that stores multiple spaced-out cells [154, 155] or by simulating cells only in a small region surrounding the cell [156]. Moving from two to three dimensions only increases the computational expense. The phase-field method is a promising tool for modeling complex cell dynamics; however, its computational limitations must be carefully addressed.

1.6 Dissertation overview

Cells constantly interact with their physical environment by sensing and responding to mechanical and topographical cues. These interactions occur across various scales, ranging from subcellular engagements with the extracellular matrix to the broader population-scale confinement observed during morphogenesis. At the heart of these processes lies the actin cytoskeleton, a dynamic structure that not only generates local forces but also serves as a medium for signal integration and propagation. The actin cytoskeleton is versatile, acting as a driver of protrusions while also functioning as an excitable system within the cell. This dual function enables cells to adapt and respond effectively to their complex environments.

A key contribution of this work is the development of the first multicellular mechanics simulation that incorporates spatially resolved internal chemical signaling. This approach enables predictive modeling of how intracellular concentrations of signaling proteins influence collective dynamics, offering a new avenue for hypothesis generation and mechanistic insight into excitable cellular systems. Phase-field modeling traditionally requires high computational resources, and here I have implemented substantial GPU speedup in order to simulate both single cells in 3D and many cells in 2D. Importantly, the structure and dynamics of the model were informed by experimental observations of actin behavior in both single- and multi-cell contexts, ensuring biologically grounded simulations. This capability opens the door to testing how specific molecular perturbations affect outcomes in multicellular systems.

In this dissertation, I employ a combination of multiscale computational modeling and quantitative imaging techniques to study the nature of actin dynamics. By exploring how actin dynamics influence physical sensing, I aim to bridge the gap between the mechanisms that drive cellular behavior at the small scale of single protrusions to tissue-scale collective cellular behavior. This work presents a framework for understanding the interplay between actin dynamics and environmental sensing, highlighting the actin cytoskeleton's role as a mechanochemical interface across various scales.

Actin drives protrusions and motility in both healthy and diseased cells. In Chapter 2, I discuss how chemical cues affect cell dynamics in pathological cells. Many pathologies result from changes in motility and cell guidance, yet the dynamics of the cytoskeleton are not often observed. Using a model cell line for endometriosis, I study the effect of estradiol 17-β on cell morphology and actin dynamics. Endometriosis is characterized by the invasion of cells outside their usual environment, particularly in response to estrogen. Using 3D lattice light sheet microscopy, I gather cell shape and actin dynamics of 12Z cells. After 24 hour treatment with estradiol, cells show a significant increase in protrusion size and more disordered actin polymerization. These results suggest that exposure to estrogen causes endometriotic cells to become more protrusive and possibly more invasive. Importantly, the findings suggest that underlying actin polymerization could be a predictor of pathological response.

Chapter 3 extends the investigation of actin-driven protrusions by introducing a modified 3D phase-field method to study substrate curvature effects on cell dynamics. I use a model with phenomenological lamellipodium dynamics that accurately reproduces cell shapes on flat surfaces. In most cell motility models, polarization needs to be artificially introduced or randomly selected. However, I show that cells spontaneously polarize with the introduction of asymmetric nanotopography. I also conduct a reanalysis of experimental data where *D. discoideum* move on the same asymmetric substrate. In agreement with the phase-field model, the experiment shows that higher velocity cells are selectively guided up the substrate. Through morphological changes alone, the 3D phase field model is able to make quantitative predictions about guidance direction.

For cell studies *in vitro*, surfaces are often functionalized in order to create a more realistic biological microenvironment, effectively attempting to simulate the ECM. In Chapter 4, I analyzed the effect of different surface treatments for epithelial cells placed on nanoridges to study the relationship between ECM sensing and physical topography. I analyze the shape, orientation, and trajectory of cells moving on ridges coated with various levels of collagen IV, an ECM ligand. Surprisingly, I found that the actin polymerization dynamics and the cell orientation/guidance direction may be less coupled on these surfaces than previously suggested. By creating a more realistic environment, we observed a higher number of motile cells; however, actin dynamics remained unchanged regardless of the direction of cell guidance. Prior studies have not addressed the

I return to the phase-field model in Chapter 5 with a model of collective dynamics in two dimensions. The 3D model studied in Chapter 3 used a phenomenological model of actin polymerization, but the two experiments in Chapters 2&4 studied the dynamics of actin polymerization waves. To unify the two approaches, I introduce an excitable model of actin dynamics into a multicellular phase-field model. With only intracellular chemical dynamics and intercellular physical interactions, this model shows emergent multiscale behavior, including synchronization, traveling waves, pulsing, geometry sensing, and texture sensing. To my knowledge, this is the first multicellular model with spatially resolved excitable dynamics. The model suggests that mechanical waves provide a mechanism for synchronization of multicellular systems. Additionally, we show that intracellular excitable systems provide a sufficient condition for mechanical waves observed experimentally in multicellular tissues. These results support a unifying view in which excitable actin dynamics not only shape subcellular behavior but also mediate large-scale coordination and information flow across tissues. The integration of spatially refined biochemistry into mechanically coupled simulations represents a significant step toward understanding emergent behavior in multicellular tissues.

Finally, in Chapter 6, I summarize how the models and experiments presented across chapters converge on a central narrative: that actin serves as a mechanochemical interface for multiscale sensing of the physical environment. From local protrusions shaped by chemical and physical inputs to long-range collective behaviors driven by mechanical wave propagation, this work provides a framework for linking single-cell responses to tissue-scale coordination in both healthy and pathological contexts.

Chapter 2: Estradiol alters actin and protrusion dynamics in endometriotic epithelial cells

This chapter is adapted from Banerjee*, Herr*, Losert, and Stroka [157]. Shohini Banerjee cultured the cells, Corey Herr and Shohini Banerjee collected the data, and Corey Herr conducted the optical flow analysis and assisted with the shape analysis. Corey Herr and Shohini Banerjee jointly drafted the initial manuscript. See Section 2.7 for full author contributions.

2.1 Overview

Estradiol (E2), a sex steroid hormone molecule, plays a key role in regulating the actin and shape dynamics of cells in a multitude of normal and pathophysiological conditions. While cytoskeletal rearrangements, membrane dynamics, and cellular protrusions are intimately involved in cell motility and invasiveness, little is known about the impact of E2 on these processes in estrogen-dependent epithelial cells. In this study, we quantified the impact of E2 on cell shape and actin dynamics in 12Z human endometriotic epithelial cells transfected with LifeAct-GFP and observed with lattice lightsheet microscopy, a new imaging technique fast enough to capture 3D dynamics on second timescales. E2, when applied for 24 hours, significantly decreased cell circularity, solidity, and rate of change of circularity, indicating a transition to a more elongated and less variable morphology. 24-hour E2 treatment also induced the formation of large membrane protrusions reminiscent of invadopodia and led to a more disordered flow of actin within those protrusions. However, these effects were not seen after 15 minutes of E2 treatment, suggesting that longer-term signaling is required to drive these structural changes. Together, these results suggest that E2 modulates actin polymerization and membrane protrusion dynamics in endometriotic epithelial cells and may prime them for cell invasion. This work highlights a role for hormonal signaling in mediating cytoskeletal plasticity and migratory cell phenotypes.

2.2 Introduction

The ability of cells to dynamically alter their structure and shape plays a critical role in numerous healthy and disease processes, such as cell proliferation, migration, invasion, and tissue remodeling. Estrogens can play a key role in regulating these cellular activities. For example, estrogens are known to mediate cell invasiveness in estrogen-dependent conditions, such as endometriosis [158–161], estrogen receptor-positive breast cancers [162–165], and gynecological cancers [166–169]. Moreover, estrogens have been linked to cytoskeletal remodeling [158, 170–172], which likely influences cell motility and morphodynamic flexibility—a trait which helps cells to migrate through diverse environments such as tissue microtracks and peritoneal, vascular, and lymphatic barriers.

Actin dynamics play a key role in directed cell migration [173–175] and the formation of cellular protrusions such as filopodia [176], lamellipodia [177], and invadopodia [178, 179]. Upregulating actin polymerization by itself does not create protrusions, however changing actin cytoskeleton dynamics can drive formation and suppression of protrusions [180]. The impact of estrogen on protrusion dynamics and cytoskeletal arrangement over time remains unclear. Moreover, most previous cytoskeleton studies fix cells prior to immunofluorescence, which does not allow for the observation of real-time, live-cell dynamics. To overcome this, actin dynamics have been studied in mammalian cells transfected with GFP-tagged actin and imaged using methods such as 2D fluorescence microscopy [181] and the nanoscale precise imaging by rapid beam oscillation (nSPIRO) method [182] for 3D, but these techniques are still limited in terms of resolution and photobleaching.

In the present study, we sought to clarify the effect of 17β-estradiol (E2), a dominant and potent estrogen molecule, on cytoskeletal and shape dynamics in the 12Z human endometriotic epithelial cell line. This cell line has been designed to model estrogen-dependent epithelial behavior, as seen in endometriosis [183]. We used 3D lattice light sheet microscopy to capture unprecedented volumetric time-lapses of LifeAct-GFP-labeled actin in live 12Z cells. Live-cell imaging revealed dynamic cytoskeletal reorganization, 3D membrane protrusions, and membrane ruffling. We quantified the effects of E2 on cell shape, membrane protrusion dynamics, and actin polymerization using custom image analysis pipelines, including optical flow analysis. Our study reveals that 24-hour E2 exposure significantly alters cell morphodynamic behavior, increases protrusiveness, and disrupts actin polymerization coordination in 12Z cells. These findings provide new insight into the role of estrogen in modulating epithelial structural plasticity and promoting invasive phenotypes in estrogen-dependent diseases.

2.3 Results

2.3.1 3D profiling of cell shape dynamics with lattice lightsheet microscopy

We captured cell shape changes, membrane dynamics, and cytoskeleton organization over time using lattice lightsheet microscopy. 12Z cells were cultured, trypsinized, nucleofected with the LifeAct-GFP plasmid for F-actin, and imaged with lattice lightsheet microscopy (Figure 2.1a). Nucleofection is an electroporation-based method in which an electrical field applied to the cells allows nucleic acids to enter the cytoplasm and nucleus. Cellular dynamics were then visualized with a lattice lightsheet time-lapse microscopy, which illuminates planes of the sample with long thin beams to produce a 3D image with high spatial resolution and minimal photobleaching. To clarify whether the boundary actin dynamics visualized with the LifeAct-GFP probe coincided with the cell membrane, a plasma membrane stain was also added to the cells. Maximum intensity projections of these two channels demonstrate that the boundary of the LifeAct-GFP-expressing cell has a strong overlap with the plasma membrane (Figure 2.1b), indicating that the actin cortex covers the whole membrane. We caution that the LifeAct-GFP label would not detect actin cortex-free protrusions, such as initial stages of blebs [184]. An example time series of maximum intensity projections from lattice lightsheet imaging of a LifeAct-GFP-expressing 12Z cell with many active protrusions is shown (Figure 2.1c).

We captured several notable features of the LifeAct-GFP-expressing 12Z cells, indicated with white arrows, at high spatial resolution in 3D from lattice lightsheet microscopy that are visible from isosurfaces (Figure 2.2). For example, some cells exhibited actin waves pushing against the membrane at the leading edge of the cell, with hair-like protrusions at the trailing edge of the

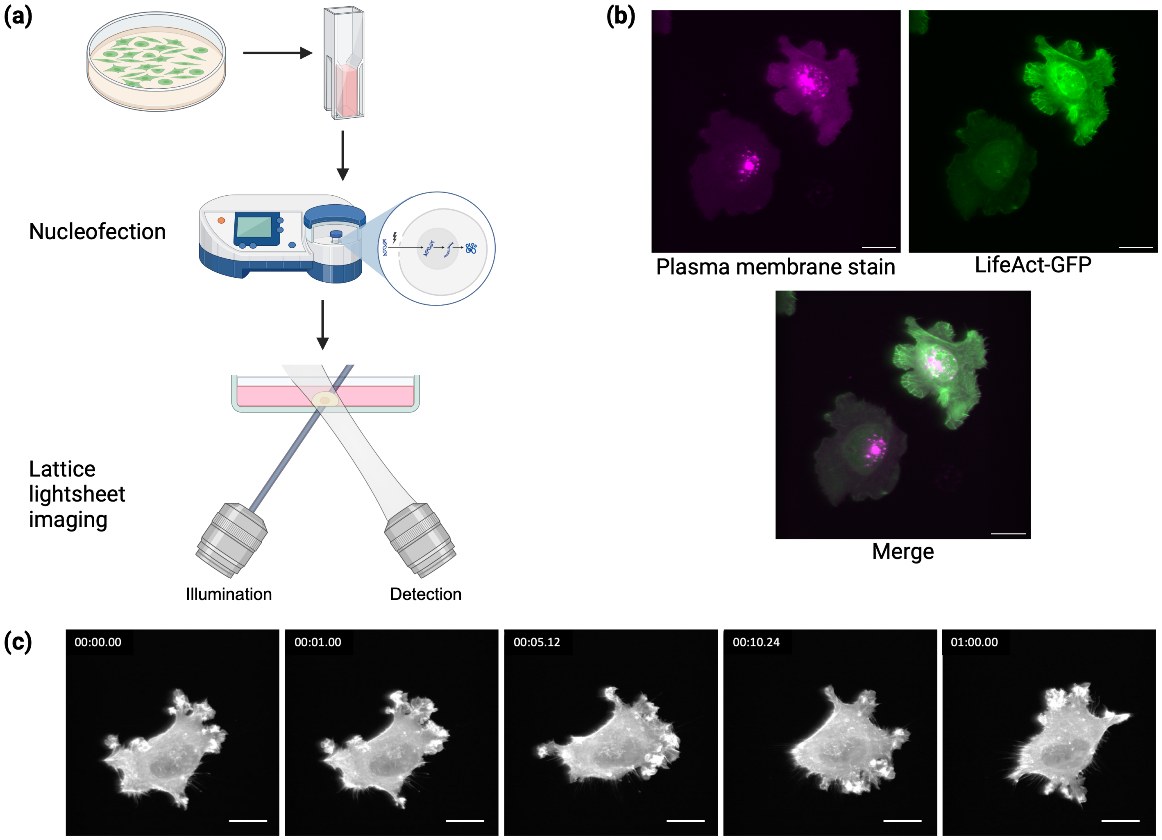

Figure 2.1: Experimental setup. **a** 12Z cells were transfected with a LifeAct-GFP plasmid via nucleofection (an electroporation-based method) and imaged over time using volumetric lattice lightsheet microscopy, which employs long thin beams to illuminate the sample with subcellular resolution. **b** A maximum intensity projection showing that the boundary of the actin cytoskeleton (LifeAct-GFP) coincides with the plasma membrane. **c** An example output maximum intensity projection from a lattice lightsheet microscopy time-lapse of a cell transfected with LifeAct-GFP with frames from t = 0, 1 min, 5 min, 10 min, and 60 min. Scalebars = 20 μm.

cell (Figure 2.2a). Several cells exhibited 3D membrane ruffles (Figure 2.2b and e), filopodia (Figure 2.2c and d, Figure 2.2f and g), lamellipodia (Figure 2.2e and f), and invadopodia-like protrusions (Figure 2.2d and g). Time series isosurfaces of 12Z cells show membrane ruffle dynamics (Figure 2.2e), lamellipodia growth and retraction (Figure 2.2e and f), and protrusion growth and retraction (Figure 2.2f and g).

2.3.2 E2 treatment alters 12Z cell shape and morphodynamics

To study 12Z morphology and shape dynamics in response to E2 treatment, we analyzed maximum intensity projections of cells transfected with LifeAct-GFP as acquired from lattice lightsheet time-lapse imaging. Cells were treated with vehicle and E2 treatments for 15 minutes or 24 hours and morphological parameters and morphodynamic speeds were averaged over the duration of each experiment (Figure 2.3). Cells treated for 15 minutes did not exhibit any significant E2-induced changes in circularity or solidity (Figure 2.3a and 2.3c, respectively) but did experience more rapid changes in circularity and solidity upon E2 treatment (Figure 2.3b and 2.3d, respectively). Of the cells treated for 24 hours, E2 treatment resulted in significantly decreased cell circularity (Figure 2.3a), solidity (Figure 2.3c), and rate of change of circularity (Figure 2.3b) compared to the vehicle control. 24-hr E2 treatment did not significantly alter the rate of change in solidity but a slight downward trend persisted (Figure 2.3d). In summary, over a short-term period, E2 treatment did not alter cell morphology but did induce more rapid shape fluctuations; over a long-term period, E2 induced clear morphological changes and reduced fluctuations in shape over time (Figure 2.3).

A more in-depth shape-over-time analysis of 12Z cells shows differential behaviors be-

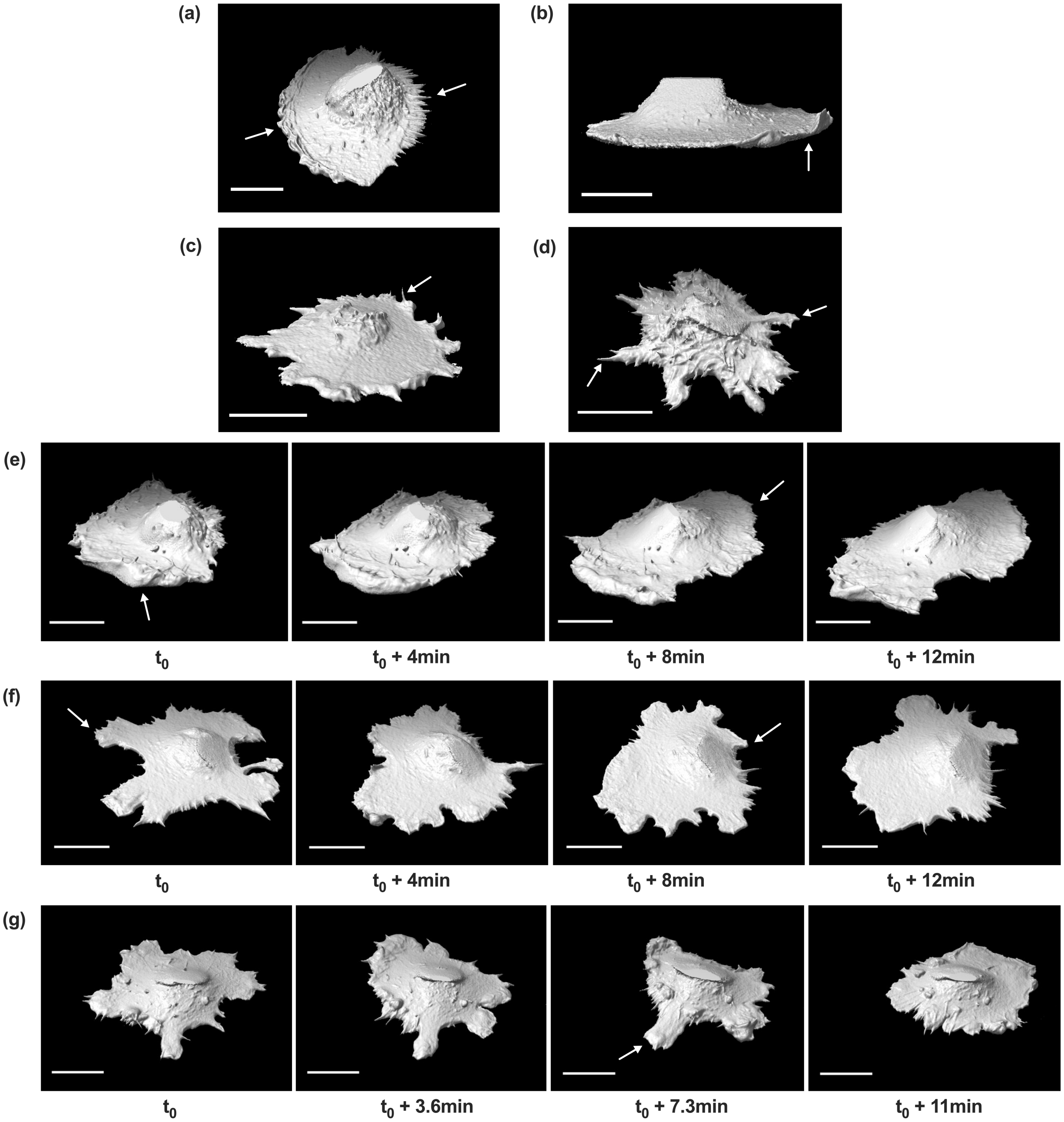

Figure 2.2: 3D isosurfaces of 12Z cells obtained from lattice lightsheet imaging, with some notable cellular features (a-d) and representative time series (e-g). **a** Some cells exhibited actin waves at the leading edge of the cell and hair-like protrusions at the lagging edge of the cell (indicated by white arrows). Several cells also exhibited membrane ruffling **b**, 3D filopodial extensions **c, d**, and active protrusions **d**. The dynamics of the membrane ruffling and lamellipodia growth were captured **e**. Protrusion retraction **f, g** and formation **f** were also visualized. All scalebars = 20 μm.

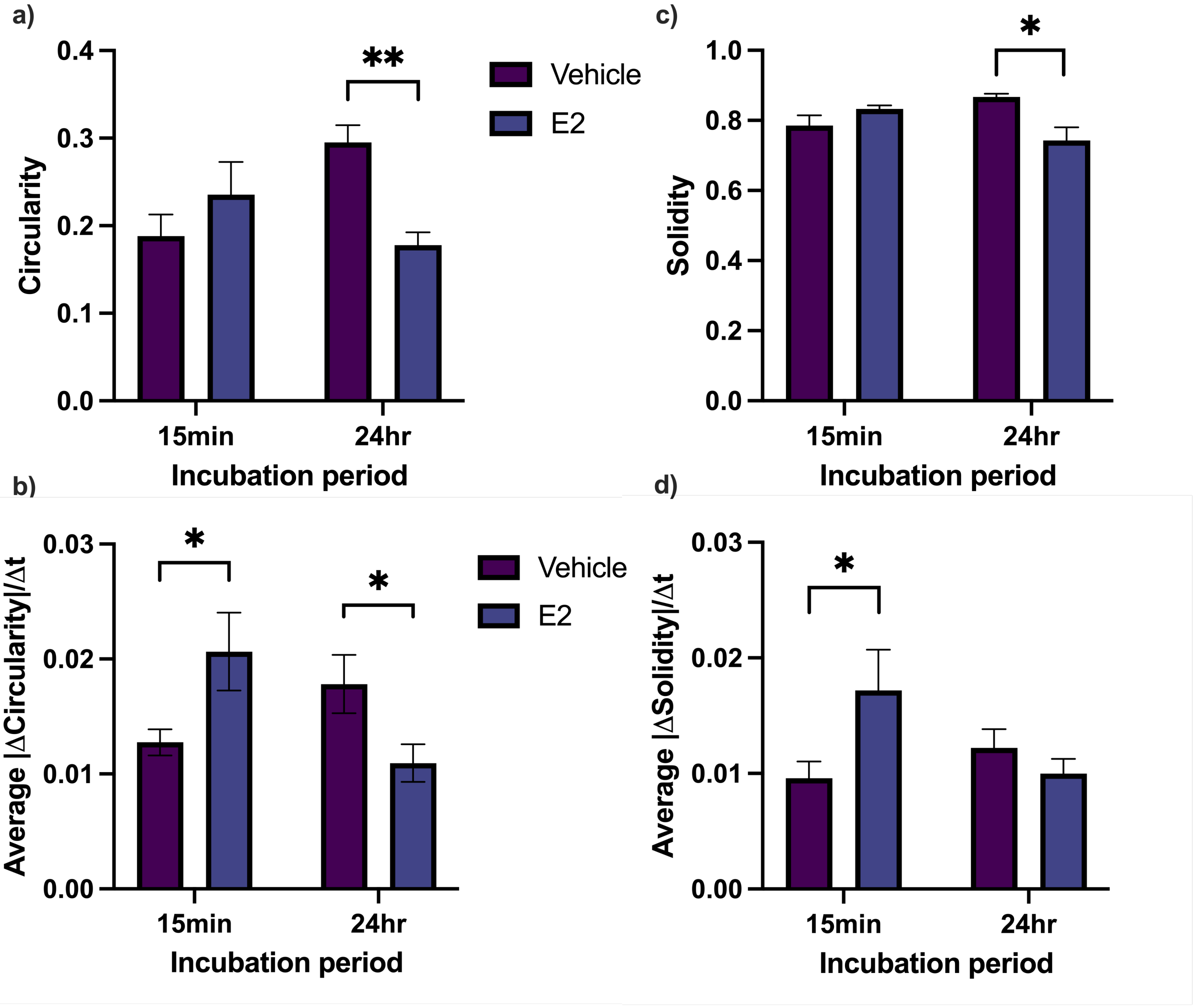

Figure 2.3: Effect of E2 on 12Z shape and morphodynamics after 15 minutes or 24 hours of treatment incubation. Circularity **a**, rate of change in circularity **b**, solidity **c**, and rate of change in solidity **d** over the duration of each time-lapse were extracted from binarized maximum intensity projections, and the means ± SEM are plotted. * $P \leq 0.05$, ** $P \leq 0.01$.

tween the vehicle control and E2 groups (Figure 2.4). Plots of circularity and solidity over time for 15-minute treatment appear relatively disordered (Figure 2.4a) compared to the noticeable separation between vehicle control and E2 groups for 24 hours of treatment (Figure 2.4c). Morphological changes normalized to initial values were plotted across different time spans, reported as multiples of 10-second Δt intervals (Figure 2.4b and 2.4d). For both 15 minutes (Figure 2.4b) and 24 hours (Figure 2.4d) of treatment, short time spans generally resulted in very small morphological changes while longer time spans resulted in larger changes of up to $\sim 15\%$. Most cells exhibited peak morphological percent changes at 300-fold Δt (equivalent to 50 min), with vehicle-treated cells experiencing larger percent changes than E2-treated cells. Of the cells treated for 15 minutes, vehicle-treated cells tended to increase in circularity and solidity over broad time spans while E2-treated cells tended to decrease in circularity over time (Figure 2.4b). On the other hand, among cells treated for 24 hours, both the vehicle and E2-treated groups ultimately increased in circularity and solidity over time (Figure 2.4d).

2.3.3 E2 treatment increases membrane protrusions in 12Z cells after 24 hours

To study the effect of E2 on 12Z membrane protrusions, protrusion area and cell area were quantified from fluorescence maximum intensity projections. We automatically segmented the protrusions using morphological operations (see Materials and methods) and two broad categories of cell protrusion dynamics were seen. The first category observed was invadopodia-like dynamics (Figure 2.5a) which are characterized by large, non-uniform protrusions with no front of the cell clearly demarcated. Invadopodia are commonly observed in cancer cells as a means for metastasis and migration [179], however here we use the term due to visual similarities between

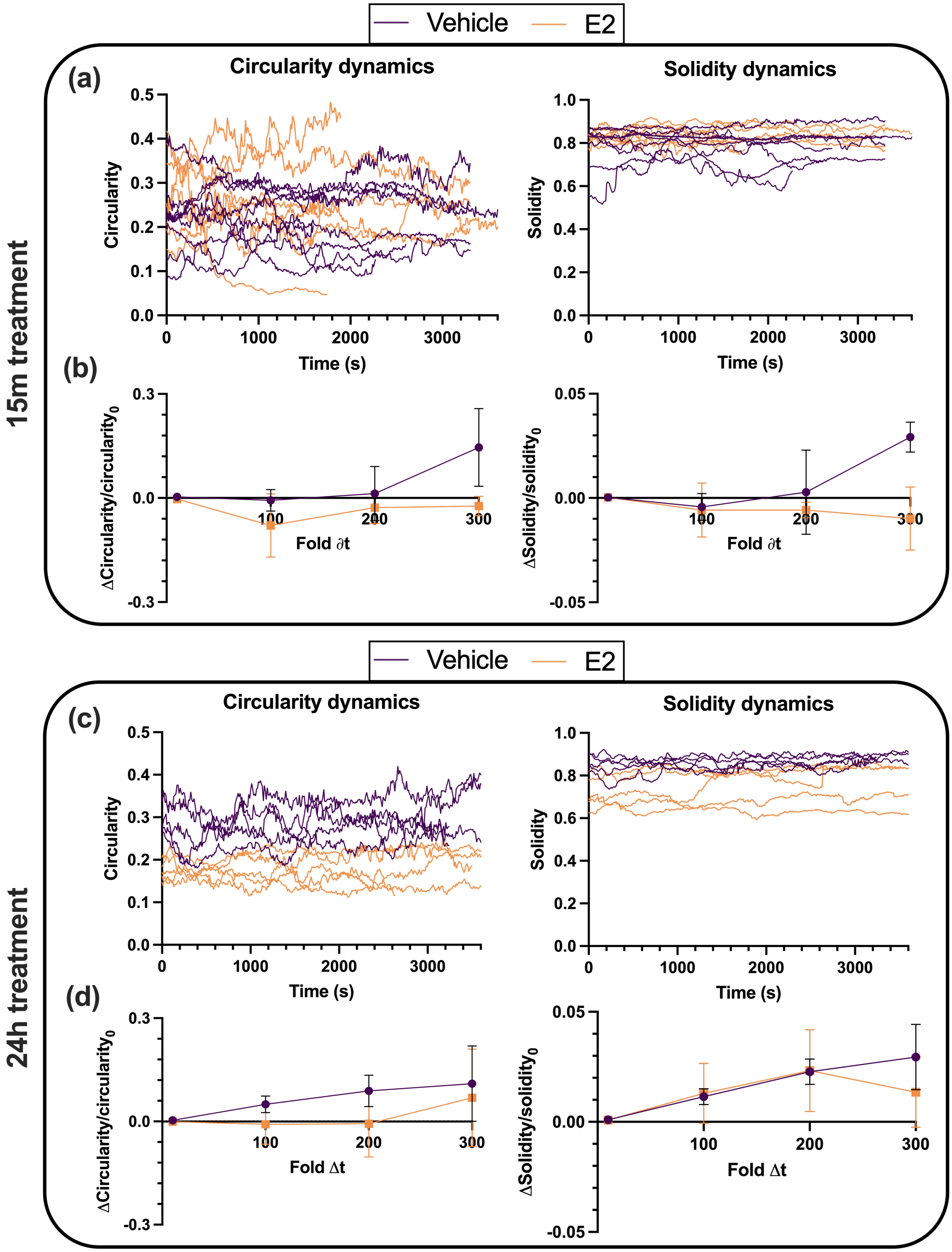

Figure 2.4: Effect of E2 on 12Z morphodynamics after 15 min (top) or 24 hr (bottom) of treatment incubation. Circularity and solidity were tracked over the duration of each experiment and plotted **a, c**, along with the average change in each parameter normalized to initial value over time intervals of varying lengths **b, d**. The base time step Δt = 10 seconds.

the protrusions in our cells and true invadopodia. The other category observed was lamellipodia-like protrusions (Figure 2.5b), which we classify as cells having broad, flat protrusions focused mainly at the front of the cell. These protrusions tend to be much smaller than the size of the cell and are largely present in unidirectional guidance [185].

To determine how E2 treatment affected protrusion dynamics we found the protrusion area for all cells. E2 treated cells have no change in protrusion area compared to vehicle control cells after 15 minutes (Figure 2.5c, left panel), but significantly larger protrusions than vehicle control cells after 24 hours of treatment (Figure 2.5c, right panel). We accounted for variability in cell size by looking at the ratio of protrusion area to cell body area. Figure 2.5d shows that after 15 minutes of E2 treatment (left panel) the ratio of protrusion area:cell area does not change compared to the vehicle control cells. Again, this difference is significant for the cells treated for 24 hours (Figure 2.5d, left panel), indicating that result holds across cell sizes.

2.3.4 E2 treatment decreases actin optical flow alignment in 12Z cells after 24 hours

To this point, we have focused mainly on cell morphodynamics; however, we have fluorescently tagged actin in the cell to investigate the impact of E2 treatment on the dynamic shift in the location of the F-actin scaffolding. Dynamics may be driven by a combination of polymerization, depolymerization, myosin contraction, or cytosolic flow. To quantify actin dynamics, we use optical flow [71] to find the speed at which the actin is moving within the cells. The optical flow is a 2D vector field (Figure 2.6a) that gives the shift in location of the actin scaffolding as well as an approximation of the speed with which it moves. Areas of the cell with higher actin optical flow

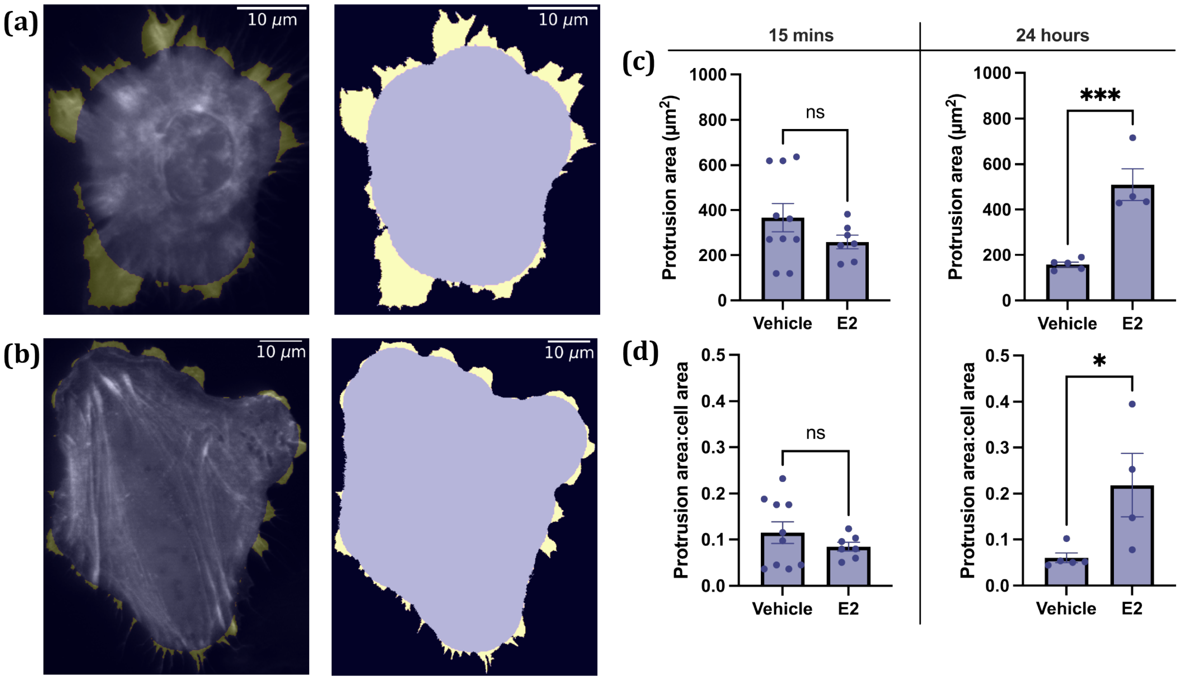

Figure 2.5: Effect of E2 on cellular protrusions. **a** A cell with invadopodia-like dynamics, which are characterized by large protrusions on all sides of the cell. The first image of the series shows cell protrusions in yellow overlaid onto the actin fluorescence image. The second image shows the binarized mask of the cell body (purple) and protrusions (yellow). **b** A cell with lamellipodia-like dynamics, which are characterized by broad, short protrusions. **c** Protrusion area in μm^2 and **d** protrusion area:cell area ratio were extracted from binarized images, and the means ± SEM are plotted. * $P \leq 0.05$, *** $P \leq 0.001$.

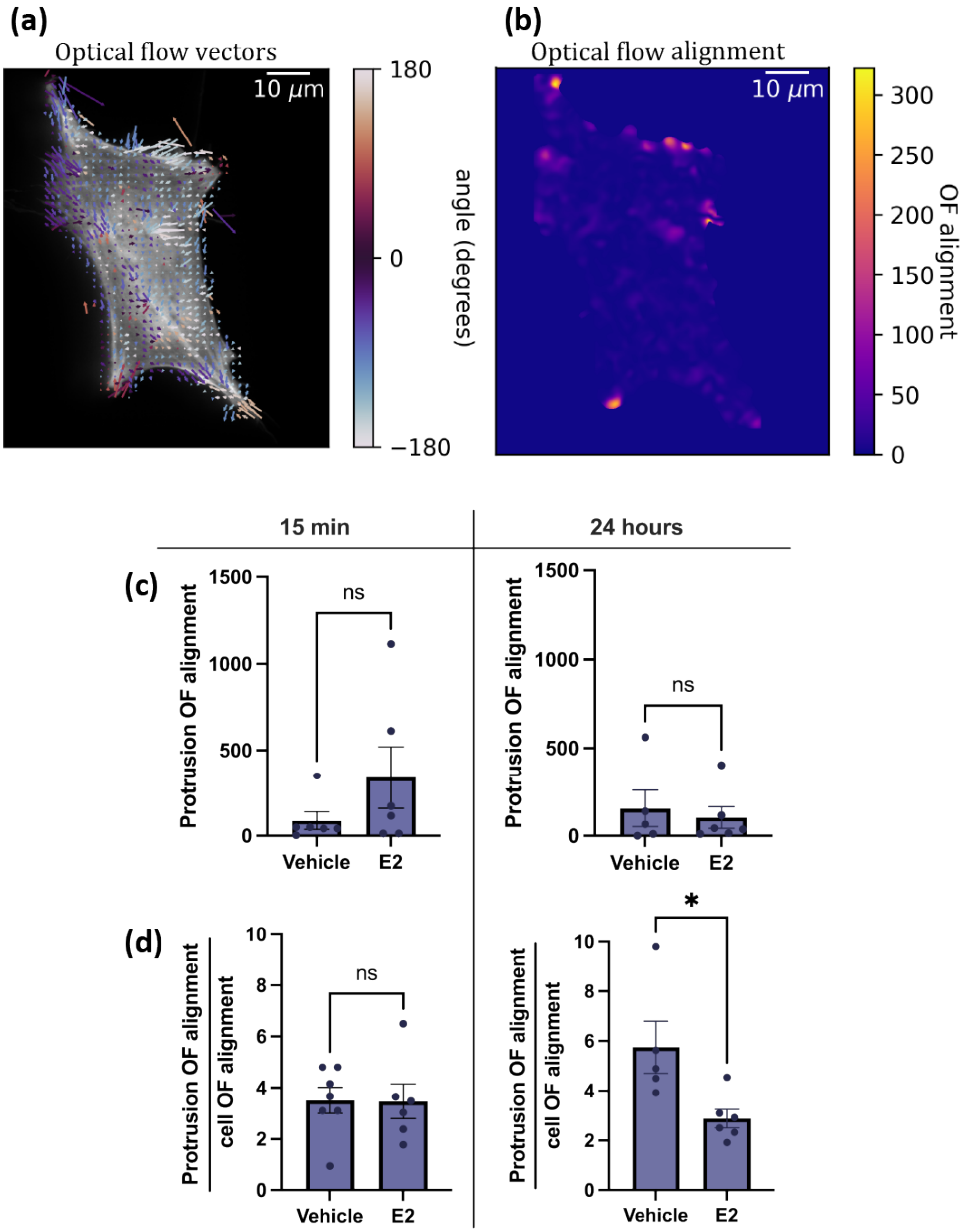

Figure 2.6: Impact of E2 on actin optical flow alignment in 12Z cells. **a** Optical flow (OF) was calculated from actin fluorescence for all timepoints to determine how the actin is moving within the video. The optical flow vectors are displayed on top of one of the corresponding actin fluorescence images. **b** The actin optical flow alignment (OF alignment) is displayed for the cell in **a**. Higher values of optical flow alignment mean that the optical flow in that region is pointing in the same direction (see Materials and methods). Using the binarized masks from Figure 2.5 the average optical flow alignment was found inside the protrusions and the cell body. The mean protrusion optical flow alignment **c** and mean ratio of protrusion optical flow alignment to cell body optical flow alignment **d** are plotted ± SEM. * $P \leq 0.05$, ** $P \leq 0.01$.

have faster changes in their scaffolding at that point. However, there was no significant difference in the actin optical flow distributions between the E2-treated cells and the vehicle control cells.

In order to quantify how the actin was moving collectively within the cell, we calculated the alignment of the optical flow vectors (Figure 2.6b). Regions of high alignment indicate regions where coordinated shifts in the cellular scaffolding occur, for instance, an actin polymerization wave that travels in one direction. The optical flow alignment was calculated by taking the spatial average of the dot product of each optical flow vector with its neighbors (see Material and methods). At any given point, higher alignment means the optical flow vectors around that point have similar directions. Lower values of alignment either mean that the optical flow was very small in that region or that the vectors are unaligned. Since coordinated shifts in the scaffolding are needed to generate protrusions, we expected the alignment to be higher in protrusions than in the cell body. Therefore, we calculated the average alignment in both the cell body and the protrusions separately.

Figure 2.6c shows no significant difference in the average protrusion optical flow alignment; the protrusions have similar levels of actin alignment in both treatments and incubation times. However, if we consider the ratio of protrusion optical flow alignment:cell body optical flow alignment we see that the ratio is significantly lower for the E2-treated cells compared to the vehicle control in the 24-hour group, but not the 15-minute group (Figure 2.6d). This means that the E2 treatment, after 24 hours, makes the cell's actin significantly less aligned in the protrusions compared to the bulk of the cell. With the E2 treatment, the actin in the protrusions becomes more disordered compared to the actin in the bulk.

2.4 Discussion

We used lattice light-sheet microscopy to capture high-resolution cell dynamics, enabling an unprecedented visualization of protrusive activity and actin polymerization dynamics in live endometriotic cells. We showed that this technique can be used to visualize a variety of 3D cytoskeletal structures, including those associated with ruffles, filopodia, lamellipodia, and invadopodia-like protrusions over time. This study aimed to elucidate the effect of E2 on actin and shape dynamics using the 12Z human endometriotic epithelial cell line. We demonstrated that 24-hour E2 treatment significantly reduced average cell circularity and solidity compared to the vehicle control—changes indicative of a transition to a more invasive phenotype as cells adopt a more elongated, protrusive shape. In the short term (15 minutes), E2 did not alter cell morphology but did induce more rapid morphodynamic changes. This contrasts with 24-hour E2 treatment, which resulted in slower morphodynamic changes. These results suggest that E2 may stimulate rapid, transient fluctuations in the short-term—potentially due to rapid, non-classical estrogen signaling pathways—and cause a more stable but invasive morphological state in the long-term—a time scale more on par with classical estrogen signaling that directly regulates transcription [186]. In line with the results in Figure 2.3, detailed shape analysis over time revealed that although E2-treated cells are highly morphodynamic after 15 minutes, clear, stable morphological shifts are only seen after 24 hours. Both the vehicle and E2 groups experienced shape changes that accumulated over time. Peak morphological changes (up to ∼15%) occurred over a window of 15-50 minutes, which may reflect the time scale of 12Z membrane protrusion turnover. After 24 hours, vehicle-treated cells generally exhibited larger fluctuations in circularity compared to E2-treated cells, which settled into a more stable but invasive morphology. Given that E2 is generally known to promote cell invasiveness in several diseases [158, 164, 168, 169], this result matches our expectation. Future studies could clarify the mechanisms underlying E2-mediated morphodynamic states in the 12Zs; for example, investigating the distinct, time-dependent contributions of classical and non-classical estrogen signaling pathways to cytoskeletal remodeling would elucidate the impact of E2 on cell shape over time.

We discovered that 24-hour E2 treatment leads to different protrusion dynamics as well as modified actin dynamics within those protrusions compared to vehicle control cells. E2-treated cells generally displayed invadopodia-like dynamics, with high protrusion areas and high ratio of protrusion area:cell body area. These higher area protrusions tended to jut out of the cell in every direction. Large protrusions in non-polarized cells tend to be a marker of invasive cells [187, 188]. This suggests that the E2-treated cells are primed to be more invasive than the vehicle control cells, because they are forming larger, non-uniform protrusions that are reminiscent of invadopodia. This effect appears only after 24 hours of treatment, not after 15 minutes, suggesting that E2-induced invadopodia-like protrusions are not formed as a result of rapid signaling. Future work could investigate the expression of invadopodial proteins, such as cortactin or MT1-MMP, in 12Z protrusions and determine whether E2 treatment enhances their proteolytic activity. This would clarify mechanisms driving E2-mediated invasion in benign and malignant estrogen-dependent conditions.

Within the membrane protrusions, the actin behaved differently in E2-treated cells. After 24 hours, the ratio of protrusion actin alignment:cell body actin alignment was significantly higher in vehicle-treated cells than E2-treated cells, indicating that the actin was more well-aligned in the vehicle control. When E2 was added to the cells, it appeared to make the actin in the protrusions more disordered. This suggests that actin polymerization is less coordinated in the E2-treated cells, which would be beneficial in sensing non-uniform local topography. This exploratory, protrusive state could support cell invasion in complex 3D environments where an adaptable cell shape is advantageous. Prior studies show that estradiol activates both RhoA and p21-activated kinase (PAK) [172], which are essential regulators for the formation of lamellipodia and pseudopodia [189, 190]. Our results suggest that this change in RhoA and PAK may result in more disordered actin polymerization over a 24-hour time scale.

Some limitations of this study should be noted. LifeAct-GFP, a widely used F-actin probe, has been previously shown to influence actin dynamics in other cell types [191–193] and has been unable to stain actin-based filopodia within chick embryo mesenchymal cells [194]. LifeAct-GFP also has a relatively high affinity to G-actin [195] which generates background fluorescence. Although our imaging validates LifeAct-GFP localization with plasma membrane staining, other methods of fluorescently labeling F-actin should be tested and compared with our results. Additionally, many cells that were imaged experienced a reduction in cell area over time, especially after about one hour of imaging, which could be due to some degree of photosensitivity. Future studies that image other cell types using lattice lightsheet microscopy will provide more context on the relative photosensitivity of the 12Z cells. Finally, we were limited in our ability to quantify the 3D dynamics of actin due to computational constraints. However, we demonstrated that the maximum intensity projection of the 3D data can be effectively analyzed for morphodynamics and actin dynamics. Future advances in computational analysis pipelines and hardware will allow us to gain further insight on cytoskeletal remodeling in 3D.

Together, our findings suggest that estradiol alters cytoskeletal plasticity and shape dynamics in endometriotic epithelial cells, potentially priming them for increased invasiveness. These insights lay the groundwork for future studies exploring the molecular signaling pathways and mechanical feedback loops that underlie hormone-driven motility in estrogen-responsive processes.

2.5 Methods

2.5.1 Cell culture

The 12Z cell line was purchased from Applied Biological Materials (Cat. #T0764). Cells were cultured in DMEM/F12 (Gibco) supplemented with 10% FBS (Gibco) and 1% penicillin-streptomycin (Gibco). For estradiol studies, about 48 hours prior to imaging, the culture media was replaced with phenol-free DMEM/F12 (Gibco) supplemented with 10% charcoal-stripped FBS (Gibco) and 1% penicillin-streptomycin (Gibco). 17β-estradiol (E2) was purchased from Sigma Aldrich (Cat. #E8875-1G) in powder form and dissolved in 100% ethanol to create a stock solution. Cells were treated with a vehicle control (0.001% ethanol) or 10 nM E2 for 15 minutes or 24 hours prior to imaging. This E2 concentration and incubation time was chosen according to prior literature [158, 160, 165, 196]. The cell line was authenticated by the company prior to shipping and our experiments were conducted at passages 58-68.

2.5.2 Cell transfection and staining

The LifeAct-GFP plasmid, a probe for globular and filamentous actin, was a generous gift from Dr. Denis Wirtz's lab (Johns Hopkins University, MD, US). 12Z cells were transfected with a LifeAct-GFP probe for globular and filamentous actin using electroporation technology. Briefly, cells were suspended in 100 μL of a supplemented nucleofector solution (Lonza, Cell Line Nucleofector Kit L, cat. #VCA-1005, Germany) with 5 μ g of LifeAct-GFP plasmid, transferred to a cuvette, and subjected to electroporation via the Nucleofector device (Amaxa, Germany). The Nucleofector program X-001 was selected based on viability optimization experiments. Transfected cells were immediately seeded on a chambered coverslip (Ibidi, Germany) coated with 10 μg/mL collagen I from rat tail (Corning, cat. #354249, NY, US) and incubated overnight prior to imaging. For validation studies, to ensure that the borders of the actin cytoskeleton were coincident with the plasma membrane, cells were exposed to a plasma membrane stain (CellMask, ThermoFisher, cat. #C56129, MA, US).

2.5.3 Lattice lightsheet microscopy

Fluorescent actin time-lapses were captured using the Zeiss Lattice Light Sheet 7 (LLS7) microscope equipped with the Hamamatsu ORCA-Fusion camera system and the ZEN Microscopy software (Zeiss, Germany). The 30 μm x 1000 nm light sheet was utilized for all imaging. LifeAct-GFP was visualized using the 488 nm laser and for cells with the additional plasma membrane stain, the 560 nm laser was also used. Image slices were 0.2 μm in thickness. Cells were maintained at 37°C in 90% humidity and 5% CO2 for the duration of imaging.

2.5.4 Shape dynamics analysis

Cell morphodynamics were analyzed from fluorescence maximum intensity projections obtained from lattice lightsheet microscopy. Time-lapse image stacks were loaded into ImageJ and individually thresholded for optimal object segmentation. Morphology parameters, including circularity, aspect ratio, and solidity, were then obtained from binarized image stacks. Circularity is defined by the formula:

$$\text{circularity} = \frac{4\pi(\text{Area})}{(\text{Perimeter})^2}$$

where a value of 1.0 indicates a perfect circle and a value closer to 0 indicates an elongated polygon. Aspect ratio is defined as:

$$\text{aspect ratio} = \frac{\text{Major axis}}{\text{Minor axis}}$$

Solidity is defined by:

$$\text{solidity} = \frac{\text{Area}}{\text{Convex hull area}}$$

where a cell that is perfectly circular would have a value of 1.0 and a cell that has protrusions and/or indentations would have a value closer to 0. We refer to the absolute value of the rate of change of morphology – such as the rate of change in circularity – as “morphodynamic speed”.

Protrusions were derived from the binarized image stacks via morphological operations. Each image was first downsized by a factor of 2 in each dimension for the future morphological operations to be computationally feasible. Next, the image was morphologically eroded and dilated with a structuring disk of size 30 pixels in order to remove the protrusions from the cell body. Finally, the binarized protrusion image was found by upsizing the morphologically altered image and subtracting it from the original image.

2.5.5 Optical flow and optical flow alignment

First the actin fluorescence images were jitter corrected using phase cross-correlation [197, 198]. Actin optical flow was found by applying iterative Lucas-Kanade [199] successively to each

2-frame combination of images in every fluorescence video. Optical flow confidence is calculated using the spatial Hessian matrix [200] in order to only account for the optical flow vectors that accurately track actin. The alignment metric was calculated by finding the dot product of each optical flow vector with its surrounding neighbors [71]. To compute this effectively, the optical flow matrix was convolved with a 2D N×N gaussian kernel A with elements:

$$A_{ij} = \frac{1}{2\pi\sigma^2} e^{-\frac{(j-N/2)^2}{2\sigma^2}} e^{-\frac{(i-N/2)^2}{2\sigma^2}}$$

with the center $(i, j = N/2)$ set manually to 0. Then, the optical flow alignment was calculated by taking the element-wise inner product of the convolution with the original optical flow matrix. In this study we use $\sigma = 1, N = 13$ in order to capture longer range alignment effects, however the results do not change drastically for values of N between 5 and 31. The protrusion optical flow alignment (protrusion OF alignment) was found by calculating the average value of the optical flow alignment inside of the protrusion binary image. Previous studies have used different metrics for finding areas of high actin activity that account only for actin fluorescence strength [201], however that does not account for the movement of actin within the cell.

2.5.6 Statistics

Statistical calculations were performed in GraphPad Prism version 10.2 (GraphPad software, CA, US). For comparisons between vehicle control and E2 groups, unpaired Student's t-tests were performed. For all tests, P values < 0.05 were considered statistically significant. Data are represented as mean ± standard error of the mean. Experiments were performed in at least triplicate.

2.6 Acknowledgments

The authors acknowledge funding from an NIGMS MIRA #R35GM142838 (to KMS), from an NSF grant PHY- 2014151 (to WL and CH), and from the Clark Doctoral Fellowship (to SB). We thank the Biosciences Core Imaging Incubator at the University of Maryland for providing access to the Zeiss LLS7 microscope. Schematics in Figure 2.1 were created with Biorender.com.

2.7 Author Contributions

SB performed sample preparation, data collection, and data analysis. CH performed data collection, code development, and data analysis. SB and CH drafted the manuscript together. KMS and WL provided guidance on the experiments and analysis, manuscript structure, and figures. All authors reviewed the final manuscript.

Chapter 3: Spontaneous polarization and cell guidance on asymmetric nanotopography

This chapter is adapted from Herr, Winkler, Ziebert, Aranson, Fourkas, and Losert [202]. The text and figure are used under a Creative Commons Attribution 4.0 International License. Corey Herr wrote the manuscript, conducted the simulations, and reanalyzed the experimental data. Winkler and Ziebert developed the original model. All authors contributed to the writing and editing of the manuscript. See Section 3.6 for full contributions.

3.1 Overview

Asymmetric nanotopography with sub-cellular dimensions has recently demonstrated the ability to provide a unidirectional bias in cell migration. The details of this guidance depend on the type of cell studied and the design of the nanotopography. This behavior is not yet well understood, so there is a need for a predictive description of cell migration on such nanotopography that captures both the initiation of migration, and the way cell migration evolves. Here, we employ a three-dimensional, physics-based model to study cell guidance on asymmetric nanosawteeth. In agreement with experimental data, our model predicts that asymmetric sawteeth lead to spontaneous motion. Our model demonstrates that nanosawteeth induce a unidirectional bias in guidance direction that is dependent upon actin polymerization rate and sawtooth dimensions. Motivated by this model, an analysis of previously reported experimental data indicates that the degree of guidance by nanosawteeth increases with the cell velocity.

3.2 Background

Most cells produce motion through the coupling of the actin cytoskeleton and the cell membrane to the surrounding substrate. *In vivo*, cell guidance is affected by a variety of external and internal stimuli, including the extracellular matrix (ECM) [203], surface rigidity[204], chemical gradients [205], and nanotopography. Local nanotopography has a substantial effect on cell behavior. For instance, it has been reported that nanotopographic substrates can lead to cell guidance and can influence cell morphology [206–209]. Nanoridges can lead to the bidirectional contact guidance of cells, causing cells to speed up and elongate parallel to ridges [25]. *In vivo* environments are often asymmetric [210, 211], in the form of the porous ECM. Such asymmetries are not often considered in modeling cell migration. Asymmetric nanotopographic substrates have recently been shown to lead to a unidirectional bias in cell migration, with a preferred guidance direction that depends on both the details of the nanotopgraphy [24] and cell line [26].

Physical modelling has been highly successful in describing cell migration, allowing for the creation of conceptually simple, whole-cell models with wide-reaching implications [140, 142, 146, 149, 151, 212–218]. Much of the previous modelling of cell migration has focused on cells on flat surfaces. However, the contact-guidance experiments discussed above suggest that the topography encountered in 3D, *in vivo* environments can have a profound effect on cell migration. We have previously developed a model that successfully captures some aspects of migration on nanotopographic substrates [219]. Here we extend this model to rows of asymmetric nanosawteeth. The cell is modeled as a deformable boundary in which actin polymerizes at the front, forming lamellipodia and pushing the cell boundary outward. This extended model reproduces the key qualitative aspects of cell motility on asymmetric nanotopography.

Our work reveals that on asymmetric, nanoscale sawteeth, cells exhibit spontaneous onset of motion and directed guidance. For a cell in a deterministic model to move on a flat substrate, the cell must initially be polarized [140, 146, 151, 219]. However, when the same cell model is implemented on asymmetric nanotopography, spontaneous cell polarization is readily observed. In agreement with previous experimental results [24, 26], our model exhibits biased unidirectional motion on asymmetric nanosawteeth, and exhibits a guidance direction that is dependent upon both the details of the nanotopography and actomyosin dynamics. Our model reproduces qualitative cell-shape phenotypes observed experimentally, including cell elongation parallel and perpendicular to the guidance direction, depending upon the parameters of the nanotopography and the cells. The model also predicts that the degree of guidance by asymmetric sawteeth depends on cell velocity. This prediction is supported by a re-analysis of previous experimental data.

3.3 Results

3.3.1 Phase-field Model

To explore cell migration on nanotopography, we extended a 3D phase-field model that was originally developed to model cells in confined environments [219]. This model uses two dynamical variables to describe the state of the cell. The first, $\rho(\mathbf{r},t)$, is a scalar phase-field that describes the cell boundary and assumes values between 0 and 1. The cell boundary lies at $\rho = 1/2$, with $\rho > 1/2$ inside the cell and $\rho < 1/2$ outside of the cell. The second is a 3D vector field $\mathbf{p}(\mathbf{r},t)$. The direction of $\mathbf{p}$ gives the orientation of the actin filaments and the magnitude of $\mathbf{p}$ gives the ordering of the filaments. As in the previous 3D phase-field model [219], we describe the substrate using two auxiliary fields: $\Phi(\mathbf{r})$ is a steric field that models the volume exclusion of the cell and the substrate and $\Psi(\mathbf{r})$ restricts actin generation to occur close to the surface. The modeling framework is described by two coupled equations for ρ and $\mathbf{p}$, as detailed in the Methods section. In the equations the unit of length is 1 μm and the unit of time is 10 s.

Here we study the effect of three model parameters on guided cell migration and cell shape. The first, β, is the actin polymerization rate, which determines how fast actin polymerizes at the surface of the cell. The second, θ, determines the preferred angle of actin polymerization with respect to the local substrate geometry. When far away from the substrate, actin polymerizes normal to and away from the local cell membrane. Near the substrate, θ determines the component of actin polymerization normal to the substrate. For $\theta = 0$, actin polymerizes tangentially to the local substrate, whereas for $\theta = 1$ the actin polymerizes normal to the cell boundary. The third parameter, σ, determines the rate of acto-myosin contraction. A larger value of σ represents more acto-myosin contraction in the cell. Collectively, these parameters can describe a wide variety of cell migration and shape phenotypes [219].

3.3.2 Asymmetric nanotopography causes spontaneous polarization

We studied cell dynamics on an array of in-registry rows of asymmetric sawteeth, in which

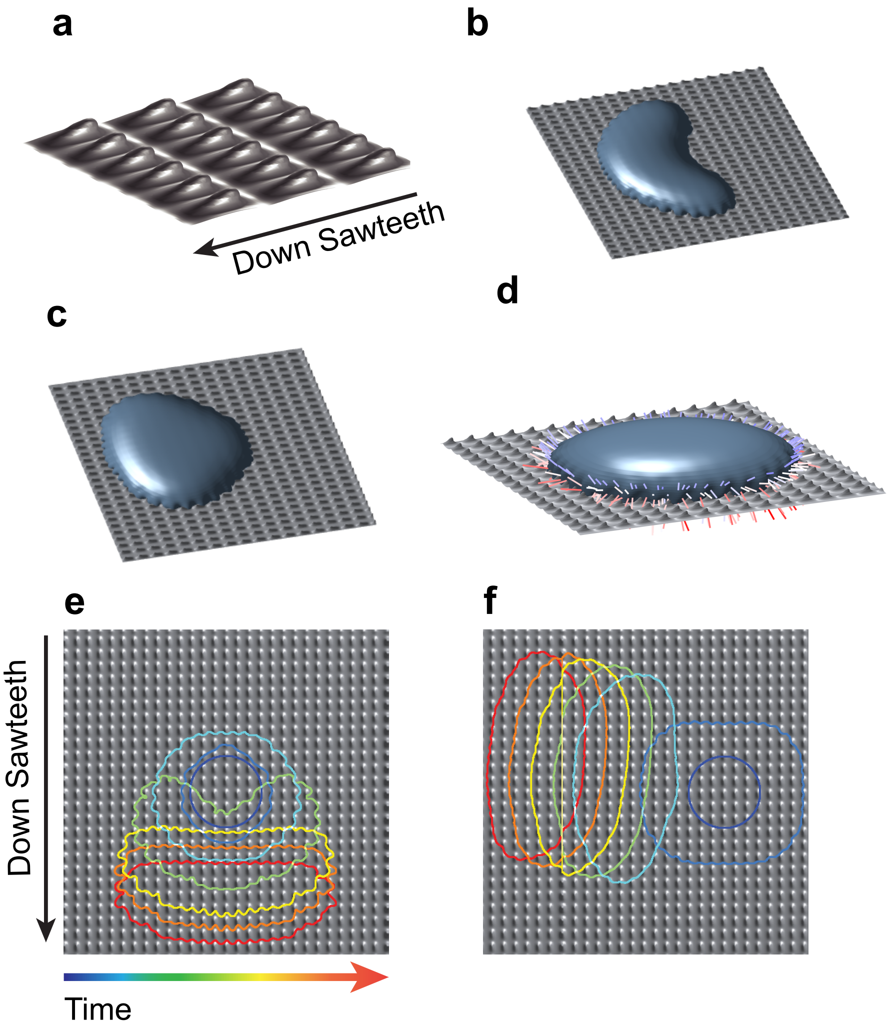

Figure 3.1: **Asymmetric sawteeth and dominant phenotypes.** **a** Zoomed-in schematic of the array of asymmetric sawteeth used in the phase-field model. Multiple cell-shape phenotypes are observed, including **b** crescents and **c** wedges. **d** Polarization vector field of a cell moving down the sawteeth. The polarization vector field indicates the directions of the actin polymerization and the membrane pushing force. The color denotes the strength of the polarization **p**, with blue being the weakest and red being the strongest. All polarization vectors point out of the cell. The asymmetric sawtooth nanotopography can cause the cell to polarize spontaneously **e** either down the sawteeth or **f** perpendicular to the sawteeth.

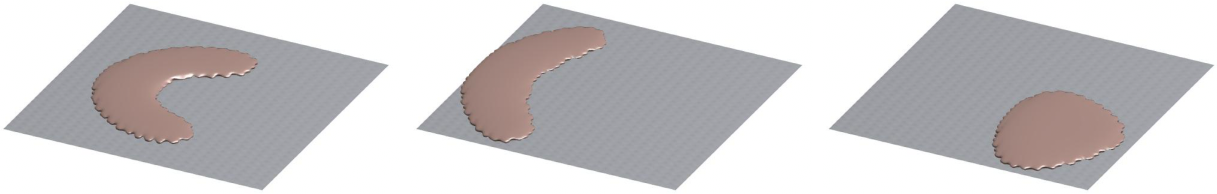

Figure 3.2: Snapshots of cell transitioning from the crescent to the wedge phenotype. Time increases from left to right.

both the sawteeth and the spacings between rows were of subcellular dimensions (Fig. 3.1a). Such sawteeth have been shown experimentally to be able to bias cell guidance unidirectionally. Sun et al. [24] reported that different nanosawtooth heights lead to opposite guidance directions of *Dictyostelium discoideum*. Furthermore, Chen et al. [26] reported that the different cell lines were guided in opposite directions on nanosawteeth with the same height.

For this study, the sawtooth height was varied between 0.75 μm and 2 μm and the sawtooth length was varied between 2.5 μm and 6 μm. We investigated how this nanotopography affects the onset of cell migration and the corresponding migration and shape phenotype evolution by placing a single cell on the substrate without initial polarization and observing the subsequent dynamics. The model produces two major cell-shape phenotypes. The crescent phenotype (Fig. 3.1b) is representative of more contractile cells, such as the M4 cell line that has been studied on asymmetric sawteeth [26]. The wedge phenotype (Fig. 3.1c) is representative of cells on the lower end of the contractility spectrum, such as *D. discoideum*, which has also been studied on asymmetric sawteeth [24]. Figure 3.2 shows a model cell transitioning from the crescent to the wedge phenotype.

Spontaneous polarization is not observed in phase-field models of cells on flat substrates because the resting state is stable. Thus, the cells in this situation cannot migrate without inducing polarization externally [220] or via initial conditions [92, 140]. However, the asymmetry of the substrates studied here allows cells to generate propulsion even in the absence of an initial polarization. The polarization occurs because the cell adheres to the asymmetric surface, which causes a break in the directional symmetry of actin polarization. Fig. 3.1d shows the polarization vector field for a cell that is polarized spontaneously by sawteeth. There are points of strong polarization underneath the cell that have a tangential component up the sawteeth (against the net direction of cell motion). However, there is strong enough polarization at the leading edge of the cell to propel the cell forward. This cell moves spontaneously with $\theta = 0$. Therefore, the impetus for spontaneous motion on sawteeth is actin polymerization tangential to the substrate. In this model, a cell can only move spontaneously down the sawteeth (Fig. 3.1e) or at an angle to the sawteeth (Fig. 3.1f).

3.3.3 The direction of cell guidance is influenced by actin polymerization

In experiments with cells on asymmetric nanosawteeth, the guidance direction has been observed to depend on the sawtooth height and length [24], as well as on the cell type [26]. We next explore why different types of cells can be guided in different directions on the same sawtooth pattern. When inducing an initial polarization up the sawteeth, we observed three possible outcomes in our model: the cell moves up the sawteeth persistently (Fig. 3.3a), the cell initially moves up the sawteeth and then turns around to move down the sawteeth (Fig. 3.3b), or the cell stops. We induce the polarization up the sawteeth to counter the preferred spontaneous polarization down the sawteeth. Trajectories for these three representative behaviors are shown in Fig. 3.3c.

To probe the selective guidance direction systematically, we created a phase diagram (Fig. 3.3d) in which we varied β and θ while keeping the sawtooth parameters the same. In all cases

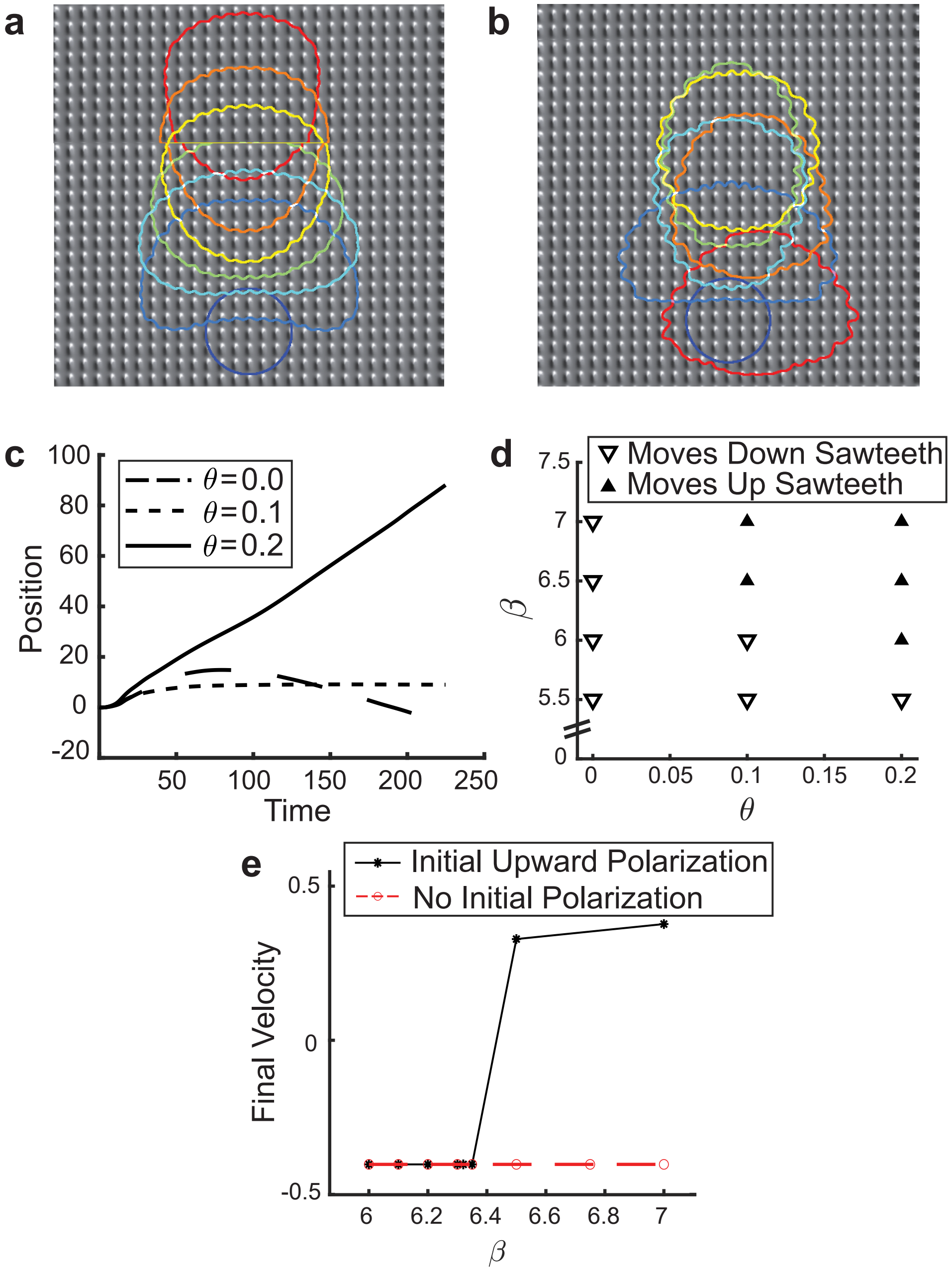

Figure 3.3: **Reversal of direction and evolution of shape phenotype.** **a** A cell guided unidirectionally up the sawteeth following initial polarization up the sawteeth. **b** Decreasing the actin polymerization rate leads to a trajectory in which the cell initially moves up the sawteeth but then turns around. **c** Trajectories representing the three most common outcomes when a cell on the sawteeth is polarized up the sawteeth. **d** A phase diagram showing how the guidance direction depends on the actin polymerization rate β and the angle θ of actin polymerization relative to the substrate. The cell moves up the sawteeth when both β and θ are in the larger range of the values examined here. **e** The asymptotic guidance velocity exhibits hysteresis for $\theta = 0.1$. For cells with an initial polarization, the transition from moving up the sawteeth to moving down the sawteeth is sudden. For unpolarized cells, guidance is only observed down the sawteeth.

the cell had an initial upward bias. After 250 seconds, we measured the center-of-mass velocity. This velocity was used to determine the guidance direction shown in Fig. 3.3d. The data in this figure indicates that as the actin-polymerization rate increases, the cell is able to overcome the nanotopography guidance direction and move down the sawteeth.

We studied the transition in guidance direction by changing β at a fixed θ of 0.1. Fig. 3.3e shows that for a cell with an initial polarization, there is a sharp transition of guidance direction at $\beta = 6.5$. Similar transitions occur at other values of θ; As shown in Fig. 3.3d, increasing the value of θ makes the cells more active, shifting the directional guidance transition towards lower values of β. The phase transition is not significantly altered if the phase field simulation mesh size is doubled (See Fig. 3.4). Below $\beta = 6.5$, the cell always has the same final (asymptotic) velocity. This guidance velocity is determined by the sawtooth properties, rather than by the model parameters. Additionally, we observe hysteresis in the guidance direction. If the cell is not polarized initially, the cell can only be guided down the sawteeth. This observation indicates that the preferred guidance direction is down the sawteeth. Finally, a cell that reverses direction does not move solely parallel to the sawteeth. We find instead that a cell can turn to move at an oblique angle to the sawtooth orientation.

3.3.4 The substrate parameters can be used to control the cell shape and the guidance direction independently

Our model exhibits a range of stable shape phenotypes that were studied in relation to the guidance direction. To control shape, we modified the contractility of the cell, σ. Contractile forces control the shape of the cell [221], and are linked closely to cell motility [222]. Here, we investigate the effect that contractility has on the direction of guidance. Fig. 3.5a depicts a phase

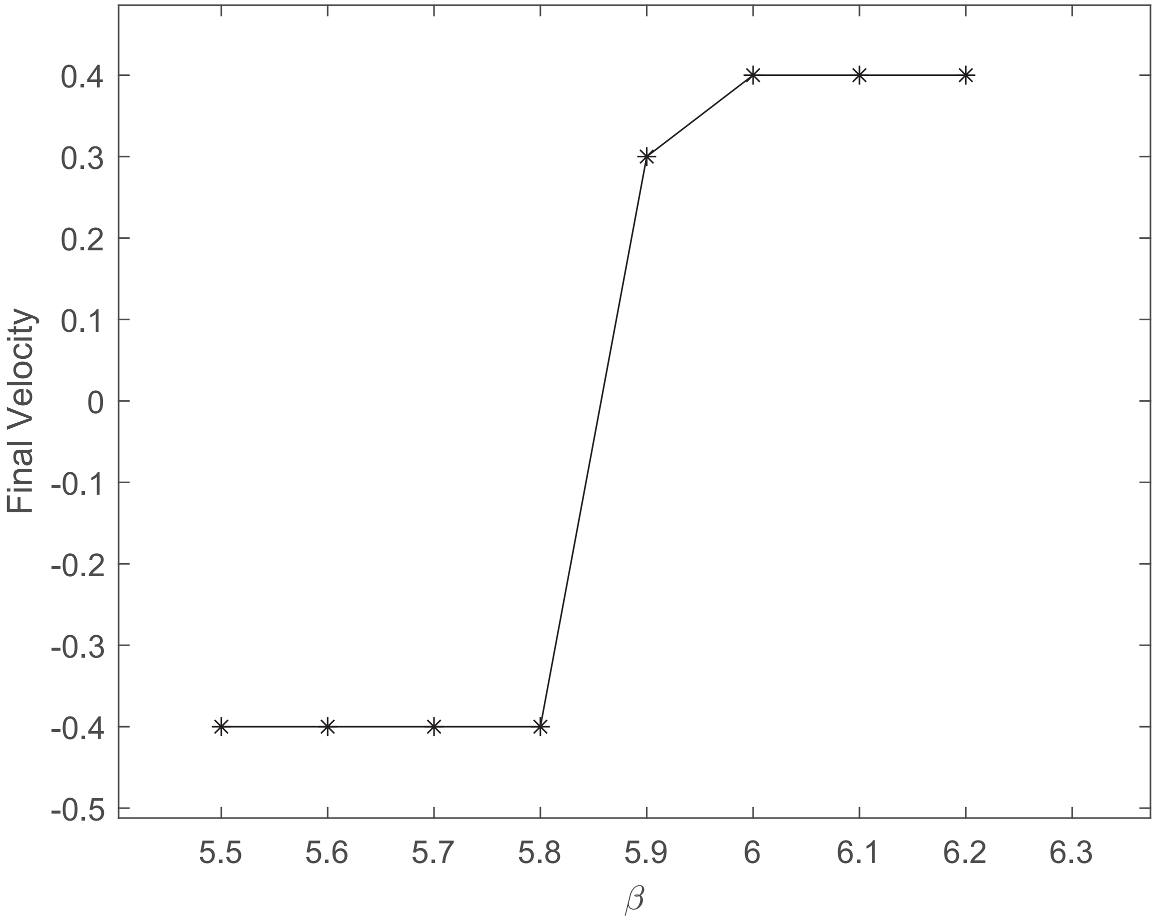

Figure 3.4: Phase transition for N=256 mesh points. We investigate the phase boundary between up and down sawtooth motion dependent on actin polymerization strength for a simulation window of half the size (N = 256 mesh points). For periodic boundary conditions to hold we had to reduce the length of the sawteeth to N=16, so the transition occurs at a different value of beta. With sawteeth heights of only 2 mesh points, we were able to retrieve a phase transition from motion down the sawtooth the motion up the sawtooth that is shifted by less than 10% and of comparable sharpness to that shown in Fig 3.3e.

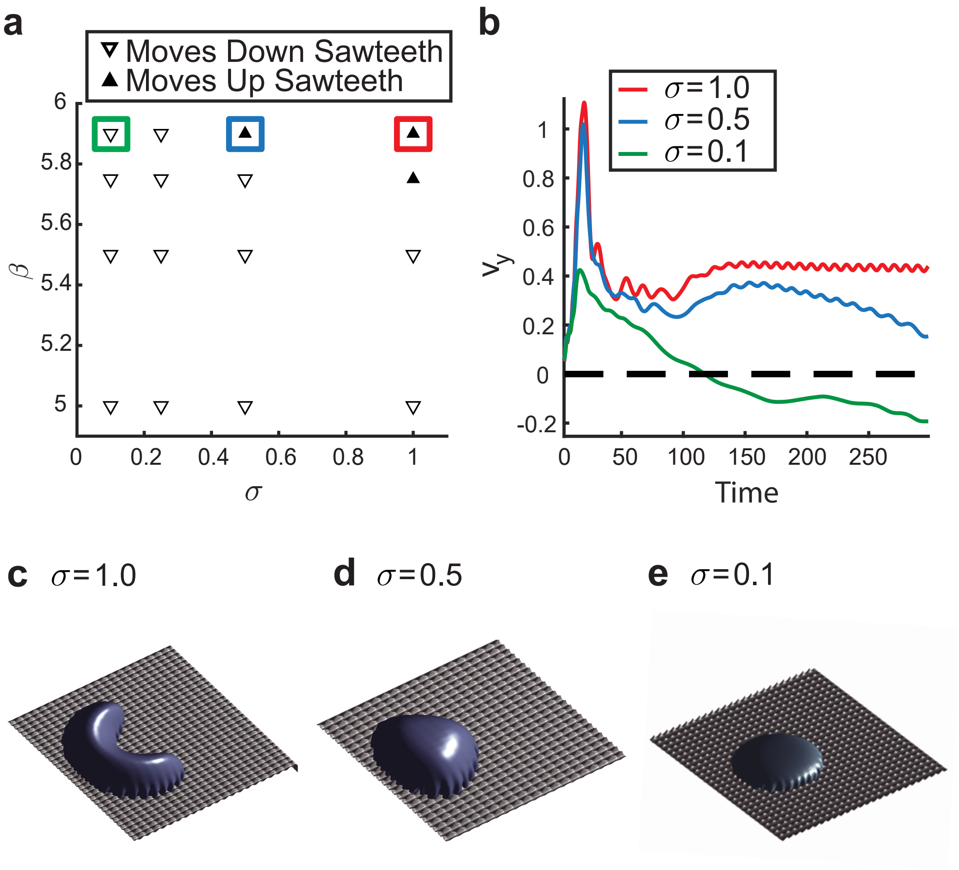

Figure 3.5: **The model parameters can be used to control shape and guidance independently.** **a** A phase diagram showing the guidance direction as a function of the contractility σ and the actin polymerization rate β ($\theta = 0.1$) with initial polarization up the sawteeth. Increasing the contractility leads to a reversal in the guidance direction. **b** Cell migration behavior for different values of β and σ. For $\sigma = 1$, the cell's initial velocity decays rapidly to a more stable final velocity. For $\sigma = 0.5$, the cell's initial velocity decay mirrors that for $\sigma = 1$, before decaying further at longer times. For $\sigma = 0.1$, the cell reverses direction at $t \approx 100$ to move down the sawteeth. 3D visualizations of the stable cell-shape phenotype for **c** $\sigma = 1$, **d** $\sigma = 0.5$, and **e** $\sigma = 0.1$. As the contractility σ decreases, the cell becomes more oval shaped.

diagram of guidance direction as a function of σ and β ($\theta = 0.1$). Cells with higher contractility σ and higher actin polymerization rate β can persistently move up the sawteeth, given an initial polarization in that direction, counter to the preferred direction of spontaneous motion.

By examining the dynamics at individual points in the phase diagram (Fig. 3.5b), we can separate the velocity trajectories into two distinct regions: the first peak and dip in velocity due to the initial polarization and change in shape of the cell, and the ensuing long-term behavior. The initial peak and dip occurs for all values of σ, followed by a positive rebound in velocity that occurs at $t \approx 150$. The major differences among the trajectories are in the long-time behavior. For $\sigma = 1$ there is a small negative acceleration, but the velocity up the sawteeth is persistent. The long-term velocity oscillations can be attributed to two factors: the cell slows down as it crawls up the sawteeth at its leading edge and small cell shape changes cause fluctuations in the center-of-mass velocity. The persistent velocity and the strong contractility of the cell results in elongation perpendicular to the direction of motion and leads to a persistent crescent shape (Fig. 3.5c). For $\sigma = 0.5$, the long-time positive velocity is not persistent. During the period of the simulation the cell moves up the sawteeth, but with a steadily decreasing velocity at long times. The contractility is high, so the cell is again elongated perpendicular to the direction of motion (Fig. 3.5d). Finally, for $\sigma = 0.1$, the long-time velocity is negative. A short period of positive acceleration at $t \approx 175$ is observed but does not lead to a second change of direction. The cell in this case has an oval shape that is elongated parallel to the direction of motion (Fig. 3.5e).

3.3.5 Comparison to experimental cell shapes and motion

Next we conduct a re-analysis on previous experimental data of *D. discoideum* migration on asymmetric sawteeth to capture additional details of cell motion. We find that the deterministic

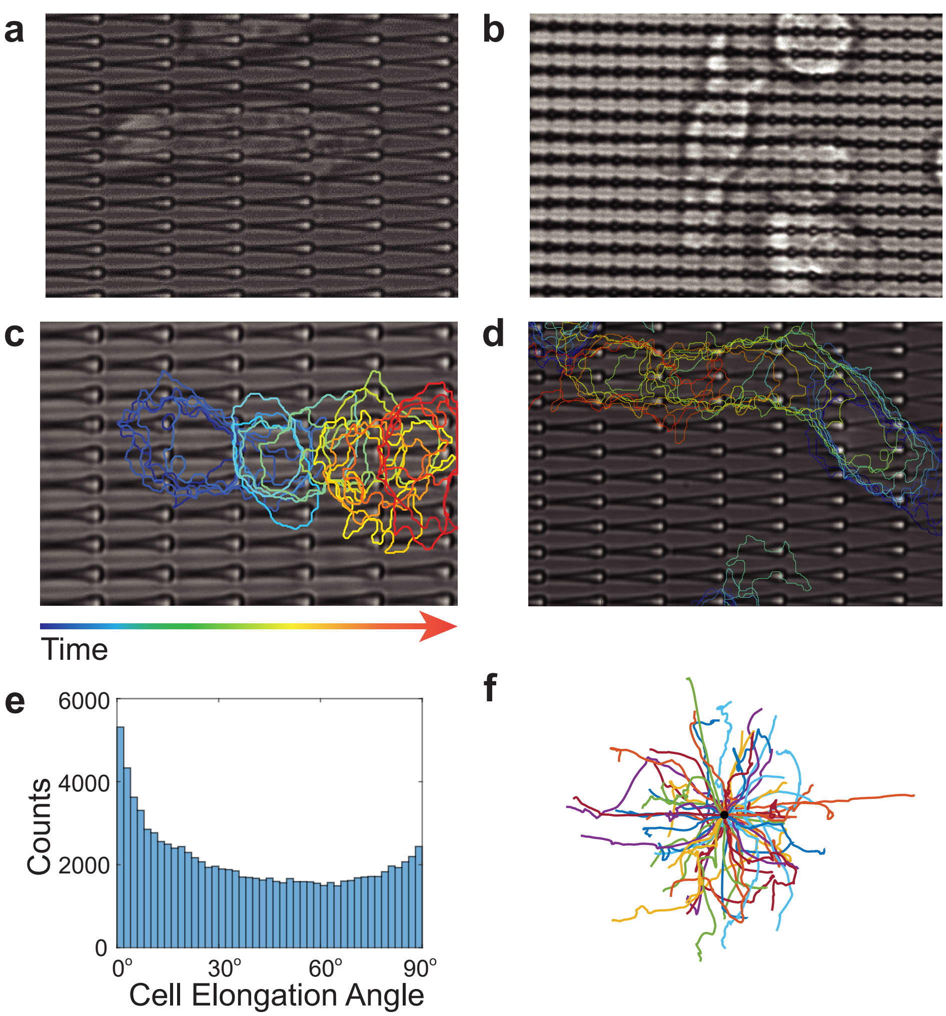

Figure 3.6: **Experimental data support the predictions of the model.** *D. discoideum* cells on asymmetric sawteeth are observed to elongate both **a** parallel and **b** perpendicular to the sawtooth direction during cell migration. Motion of *D. discoideum* **c** down and **d** up the sawteeth. **e** The full distribution of elongation angles of *D. discoideum* on asymmetric sawteeth. The distribution is peaked around the parallel and perpendicular directions, as seen in the model. However, cells can exhibit other orientations as well. **f** The full distribution of directions of motion of *D. discoideum* on asymmetric sawteeth of heights 1 μm to 2.4 μm. The model can also produce the full range of directions of motion (see Fig. 3.3).

phase-field model can reproduce both the observed cell shapes and the preferred guidance direction. Figures 3.6a-b show that *D. discoideum* can be elongated both parallel and perpendicular to the sawteeth, in analogy to the shape phenotypes seen in the model. *D. discoideum* cells moving along sawteeth tend to elongate in the direction of motion, in accordance with the less contractile cells shown in Fig. 3.5. Additionally, in a study of different cell lines migrating on sawteeth by Chen et al. [26], it was observed that M4 cells, a cancerous mutant of MCF10A epithelial cells, exhibit elongation perpendicular to the direction of motion. This behavior agrees with the observation that cancerous cells are generally more contractile than their progenitor cells [222]. Although asymmetric sawteeth create a unidirectional bias of motion, *D. discoideum* is capable of moving down the sawteeth (Fig. 3.6c), up the sawteeth (Fig. 3.6d), as well as at arbitrary angles relative to the sawteeth.

A variety of cell elongation angles with respect to the sawtooth orientation are observed experimentally, as seen in Figure 3.6e. The distribution of elongation angles has two local maxima at 0° (parallel to sawteeth) and 90° (perpendicular to sawteeth). Fig. 3.6f shows a combined spider plot of cell trajectories on sawteeth of height 1 μm to 2.4 μm. By changing the direction of initial cell polarization, a model trajectory can be produced that travels in any direction, and therefore the model can reproduce the arbitrary elongation angles (Fig. 3.7) that are present experimentally.

The simulated cell trajectories in the continuum model are deterministic, and so cannot reproduce the stochasticity of experimental trajectories. Nevertheless, we observe that the direction of stable simulation trajectories corresponds to the preferential guidance direction of cells on asymmetric sawteeth. To determine the effect of sawtooth dimensions on cell guidance direction

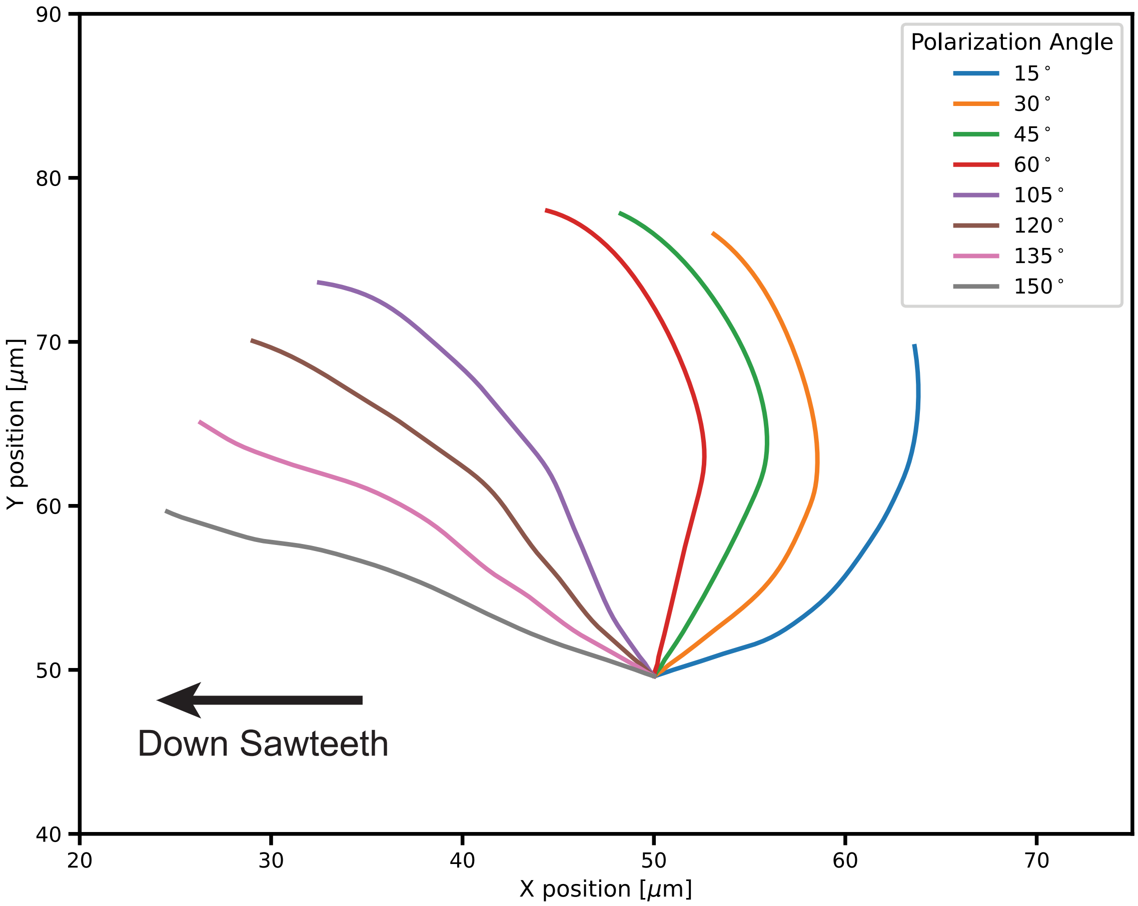

Figure 3.7: Cell trajectory when polarized at an angle relative to the sawteeth. Cells can maintain a steady trajectory in an arbitrary direction for a short period of time.

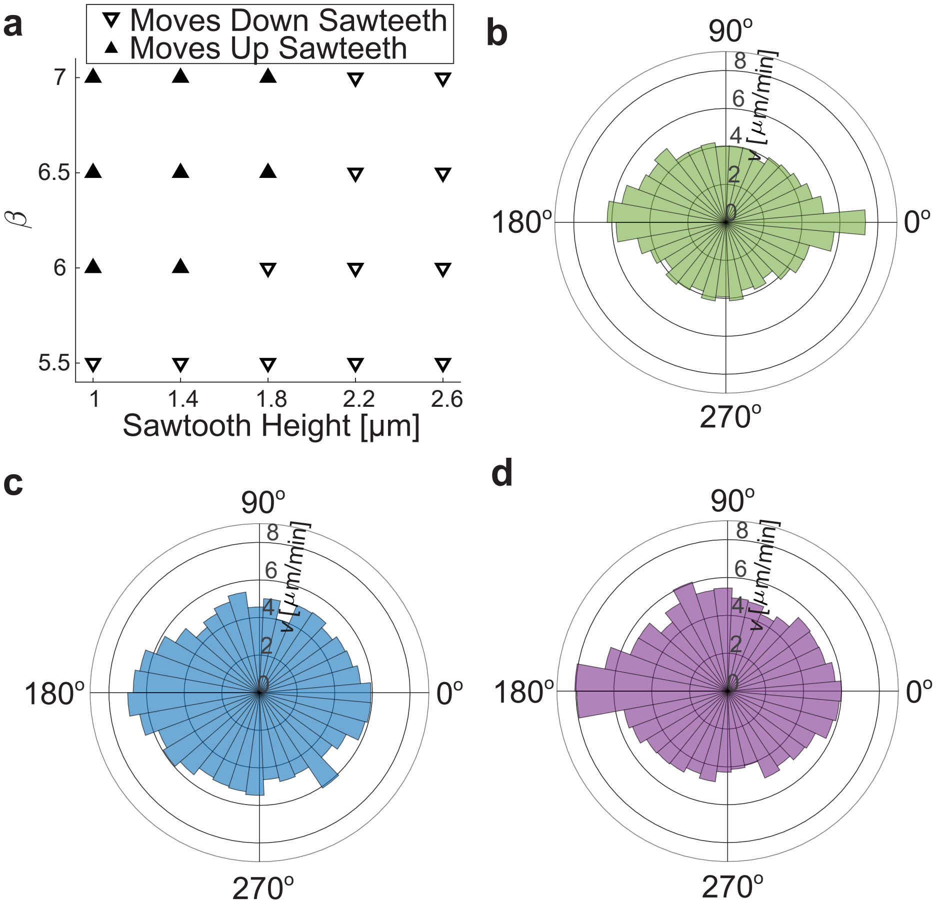

Figure 3.8: **Asymmetric sawteeth preferentially guide cells with high velocities. a** A phase diagram demonstrating dependence of guidance direction on β and sawtooth height (fixed $\theta = 0.1$) on a cell initially polarized up the sawteeth in the phase-field simulations. The average velocity distributions derived from experimental data for *D. discoideum* on asymmetric sawteeth of three different heights: **b** 1 μm, **c** 1.8 μm, and **d** 2.4 μm. For the 1μm sawteeth, the distribution is peaked at 0°, indicating that the faster cells are guided preferentially up the sawteeth. This observation is consistent with the phase diagram in **a**, in which cells with higher actin polymerization rates are guided up the sawteeth. For sawtooth heights of 1.8 μm and 2.4 μm, the velocity distribution is peaked at 180°, indicating that the faster cells move preferentially down the sawteeth.

we compared the model to experiments of cells on sawteeth of three different heights: 1 μm, 1.8 μm, and 2.4 μm. The model predicts that cells with higher actin polymerization rates will move up the higher sawteeth (Fig. 3.8a). Because cells with higher actin polymerization rate tend to have higher velocities [64, 223], one implication of our model is that faster-moving cells will move up sawteeth with smaller heights and down sawteeth with greater heights. Therefore, the model indirectly predicts that cells with higher velocity will move up the sawteeth for lower sawteeth heights and down the sawteeth for higher sawteeth heights.

To determine the guidance direction of cells in experiments, we measured the average velocity of the *D. discoideum* cells as a function of direction relative to the sawteeth, with the angle 0° defined as moving up the sawteeth (Fig. 3.8b-d). For the 1 μm-high sawteeth, the average velocity peaks at 0° (Fig. 3.8b). This observation is consistent with the phase diagram (Fig. 3.8a), in which cells with a higher actin polymerization rate move up the sawteeth. For the 1.8 μm-high and 2.4 μm-high sawteeth the average velocity is peaked at 180°. This result indicates that the *D. discoideum* cells do not reach the threshold velocity necessary to move up these sawteeth. Our observations suggest that asymmetric sawteeth can be used to guide cells with high velocities selectively, and that the velocity cutoff can be modified by changing the sawtooth height.

3.3.6 A toy model for cell migration on nanotopography

To strengthen the predictive power of the full phase field simulations it is useful to capture the main observations in a toy model amenable to analytical extrapolation. The extrapolated positions can be validated in both the phase field simulations and experimental observations. The toy model incorporates two key observations from the full phase-field model: the sub-critical onset of cell motion on flat surfaces and the unidirectional bias of motion by the sawtooth substrate.

This toy model allows us to investigate stability of cell guidance. If there is no topography on the substrate, the equations of motion can be cast in the dimensionless form:

$$\varepsilon \partial_t \mathbf{v} = \mathbf{v}(-1 + \beta|\mathbf{v}|^2 - |\mathbf{v}|^4) \tag{3.1}$$

Here $\varepsilon \ll 1$ is the relaxation parameter, β is the driving parameter related to actin polymerization, and v is the center-of-mass velocity of the cell. For $\beta > 2$, equation (3.1) possesses 3 stable fixed points: $V_0 = 0$, and $V_s^2 = \beta/2 + \sqrt{\beta^2/4 - 1}$. Correspondingly, there are two unstable fixed points $V_u^2 = \beta/2 - \sqrt{\beta^2/4 - 1}$.

In the presence of asymmetric nanotopography, the equation of motion assumes the form

$$\varepsilon \partial_t \mathbf{v} = \mathbf{v}(-1 + \beta|\mathbf{v}|^2 - |\mathbf{v}|^4) + f(x)\mathbf{x}_0 \tag{3.2}$$

Here $\mathbf{x}_0$ is the unit vector in x-direction. In the case of asymmetric sawteeth, $f(x)$ can be written in the form

$$f(x) = c(ax - \text{floor}(ax)) \tag{3.3}$$

Here a is the spatial frequency (spatial period $L = 1/a$) and c is the magnitude of the sawtooth modulation. Note that the sawteeth provide a positive bias, because $\langle f(x) \rangle > 0$.

Despite their simplicity, Eqs. (3.2) and (3.3) capture many salient features exhibited by the fully 3D, continuum phase-field model as a function of the driving parameter β (Fig. 3.9). In particular, for pure one-dimensional motion (i.e., in the x-direction), for a large enough value of β the model exhibits two stable solutions, with motion up or down the sawteeth (Fig. 3.9a). For smaller values of β, the model only shows spontaneous motion down the sawteeth. For even

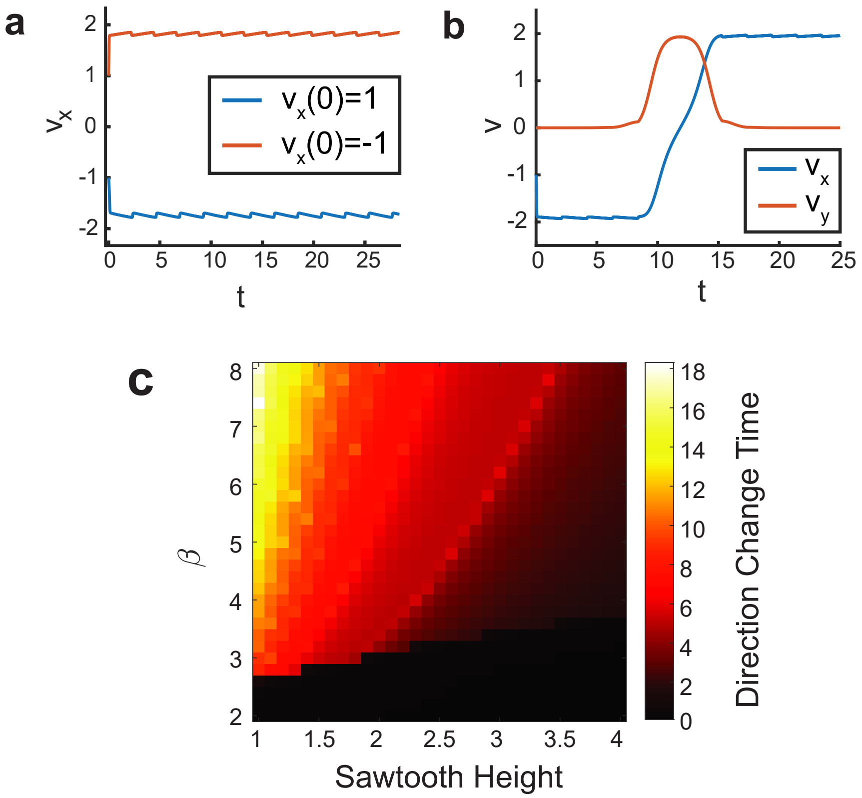

Figure 3.9: **Toy model capturing the main features of the full 3D phase-field model. a** Trajectories up and down the sawteeth in the simplified model, Eq. (3.2), in the 1D case. **b** A cell that initially moves up sawteeth in the 2D model, Eq. (3.2) performs a U-turn at $t \approx 10$. The initial trajectory is unstable. **c** Heat map of the time for cells with initial negative velocity to change direction in the 2D model. For higher values of β in this model, the velocity up the sawteeth persists for a longer time. For higher values of c (height of sawtooth pattern) in this model, the velocity up the sawteeth persists for a shorter time.

smaller values of β, no motion is possible, all in agreement with the phase-field model.

The two-dimensional version of Eqs. (3.2) and (3.3) yields an intriguing prediction that motion up sawteeth is always unstable (Fig. 3.9b). However, as β increases, the reversal time diverges (Fig. 3.9c). Thus, the model indicates that the complex migration behavior observed both in the phase-field simulations and in the experiments is a synergistic effect of the sawtooth substrate and the cell's intrinsic threshold for motion. By incorporating only three properties, the toy model leads to three nontrivial predictions: hysteresis between motion up and down the sawteeth, the existence of a critical sawtooth height above which motion up sawteeth is impossible, and the instability of motion up the sawteeth. These predictions identify the that the minimal model ingredients needed to capture velocity-based selective guidance are: sub-critical onset of motion on flat substrates and unidirectional bias by the sawtooth substrate.

3.4 Discussion

We have demonstrated that a 3D phase-field model enables a rigorous investigation of cell motility on asymmetric nanotopography. Previous work has focused on cell scale or system scale gradients. Here we demonstrate that the model can also capture how cells integrate subcellular asymmetry into cell scale guidance. The phase-field model captures the spontaneous onset of motion and the experimentally observed range of shapes and motions of cells that sense asymmetric guidance cues that are an order of magnitude smaller than the scale of the cell.

Cell-migration experiments on asymmetric sawteeth have demonstrated that the guidance direction is affected by the sawtooth dimensions [24] and the specific cell line used [26]. The phase-field model reproduces the key phenomena observed in these experiments, including spontaneous polarization, unidirectional guidance, and elongation phenotypes. By tuning model parameters, we can change the guidance direction and cell shape in accordance with the behavior observed for different cell lines. The correspondence between the model and experiments yields insights into the relative importance of actin polymerization, contractility, or other cell properties in promoting cell-type-dependent guidance behavior.

On flat surfaces, the phase-field models require an initial polarization [140, 219] or a strongly randomized internal actin density [141] to observe directed cell motion. In contrast, asymmetric sawteeth provide guidance cues that cause the cell to move spontaneously. Consequently, surface asymmetries may be one factor that initiates directional migration *in vivo* and in natural environments.

Our model shows that the actin polymerization rate is a primary driver of the cell guidance direction on asymmetric sawteeth. There is a transition in guidance direction from down the sawteeth to up the sawteeth at a critical value of the actin polymerization rate. This critical value is dependent on other model parameters as well, such as the sawtooth height.A toy model based on findings from phase-field simulations verifies this relationship and gives analytical evidence that motion up-sawtooth is unstable. The actin polymerization rate is directly related to the cell velocity, so faster cells should tend to move up the sawteeth. In agreement with the predictions of our model, experimental data for cell guidance on asymmetric sawteeth show velocity-dependent selective guidance. Additionally, the model predicts that increasing the sawtooth height should increase the velocity threshold for cells to move up the sawteeth. We verified this prediction by showing that faster *D. discoideum* cells are preferentially guided up asymmetric sawteeth that are 1 μm high. However, on asymmetric sawteeth with heights of 1.8 μm and 2.4 μm, faster cells are still guided down the sawteeth.

In our model, contractility affects both the shape and the guidance direction of a cell. Larger values of contractility are associated with the cell moving up the sawteeth. Thus, more contractile cells are not guided in the more typical direction on asymmetric sawteeth. Studies have linked higher contractility to invasiveness in cancer cells [222], and this connection may be related to the change in guidance direction that we observe.

The simple physical model presented here can explain many features of cell motility on asymmetric nanotopography. Because the phase-field model is highly modular, it can be extended further to obtain a fuller picture of cellular dynamics on asymmetric nanotopography. An even more realistic model could include the modulation of specific or non-specific adhesive effects (e.g., focal adhesions). Additionally, the actin dynamics can be modified to include the effect of regulatory proteins via an excitable network model such as local excitation global inhibition biased excitable network [63] or linked excitable networks [55].

Although our approach captures many important aspects of subcellular environmental asymmetries on cell migration, *in vivo* the dynamics can be affected by many other factors. It is known that the cells can remodel, and even degrade, the local topography, especially in the context of some invasive cancers [224, 225]. Many cancer cells form invadopodia, i.e., actin-rich protrusions of the plasma membrane that are associated with degradation of the extracellular matrix. Incorporation of such phenomena into a phase-field model can shed light on cancer invasiveness and metastasis and is highly desirable. However, a 3D phase-field model on deformable and degradable substrates is a formidable computational task that we leave to future study.

3.5 Methods

3.5.1 Phase-field equations

The following model was used to describe the cell migration in 3D:

$$\begin{aligned}
\partial_t \rho &= D_\rho \Delta\rho - \rho(1-\rho)(\delta[\rho] - \sigma|\mathbf{p}|^2 - \rho) \\
&\quad -\alpha \mathbf{p}\cdot\nabla\rho - \kappa\nabla\Phi\cdot\nabla\rho - \lambda\rho\Phi^2, \qquad (3.4) \\
\partial_t \mathbf{p} &= D_{\mathrm{p}}\Delta\mathbf{p} - \beta e^{-Tc\Delta S}[(1-\theta)\hat{P}(\nabla\rho) + \theta\nabla\rho]\Psi - \tau^{-1}\mathbf{p} \\
&\quad -\gamma(\nabla\rho\cdot\mathbf{p})\,\mathbf{p} - \Phi^2\mathbf{p}. \qquad (3.5)
\end{aligned}$$

Here, the phase-field ρ describes the cell shape, $\mathbf{p}$ characterizes the actin orientation, $\Phi(\mathbf{r})$ models a steric field moderating the cell's interaction with the surface, and $\Psi(\mathbf{r})$ restricts actin generation close to the surface. The entire motility mechanism is captured by Eqs. (3.4), (3.5). Actin polymerizes near the cell boundary and produces a protrusion force via the polymerization ratchet mechanism[226]. As the cell moves forward, the actin polarization at the back of the cell degrades based on a model of acto-myosin contraction [140]. The cell volume is conserved as a fixed point through the term $\delta[\rho]$. Additionally, contractility is modeled through the term $\sigma|\mathbf{p}|^2$. As per Ref. [140], the contractility of acto-myosin bundles can be described as a nematic tensor S_{ij}. According to the active gel theory, the stress tensor is proportional to the nematic tensor. Therefore, we say that the tensor invariant is proportional to the deformations of the cell boundary.

This model of cell motility has been shown to reproduce the lamellipodium-based motion of keratocytes on flat surfaces [140]. We use a modified version of the model that accounts for cell surface tension [147]. Surface tension is introduced using the exponential term $e^{-Tc\Delta S}$, where T is the surface tension strength, c is the curvature, and ΔS is the difference between the surface area at a given time step and a reference surface area. This term makes the actin polymerization rate lower at points of high curvature, thereby preventing the cell from tearing apart. We introduced this term by necessity based on the high curvature of the nanotopography studied here.

Table 3.1: Default model parameters

Parameter	Value	Description
D_ρ	1	Diffusion constant for ρ
$D_{\mathbf{p}}$	0.2	Diffusion constant for $\mathbf{p}$
α	1.5	Actin pushing strength
T	25	Surface tension strength
γ	1	Front-back asymmetry
τ^{-1}	.1	Actin degradation rate
κ	2	Surface adhesion strength
θ	0.1	Actin polymerization angle

3.5.2 Numerical Method

The model used here is an extension of a previously published method [219]. Equations (3.4) and (3.5) were solved on a 100 μm × 100 μm × 25 μm rectangular grid (corresponding to $576 \times 576 \times 128$ mesh points) in the domain using a split operator method on a periodic domain. The algorithm was implemented on graphical processing units (GPUs) using the NVIDIA CUDA programming language. The diffusion terms were calculated in Fourier space, and other operators were calculated using finite-difference methods. The curvature c in Eq. (3.4) was calculated using

$c = \nabla \cdot \frac{\nabla \rho}{|\nabla \rho|}$. Unless otherwise mentioned, the model parameters used were those given in Table 3.1.

The substrate with asymmetric sawteeth was implemented via prescribing the static fields Φ and Ψ. The substrate studied for this paper was a sawtooth of length 4.2 μm and a default height 1.4 μm; other heights were used as discussed above.

3.5.3 Cell Tracking

Cell tracking was performed on bright-field movies of *D. discoideum* moving on asymmetric sawteeth reported in a previous paper [24]. First, the threshold of the fast Fourier transform (FFT) of the images was used to remove the bright spikes associated with the periodic sawteeth. A low-pass Hamming filter was applied to the FFT. An inverse FFT was then applied to recover an image with sawteeth removed. Next, the image contrast was changed so that 1% of the brightest and darkest parts of the image were saturated. A morphological top-hat filter was applied to remove high frequency noise. Finally, the image was binarized using the Otsu thresholding method [227]. The cells were tracked using the MATLAB *regionprops* function to find elongation and centroid location. The cell trajectories were found using a particle tracking algorithm fed the centroids of the cell locations.

3.6 Contributions

C.H., I.S.A., and W.L. designed research; C.H. performed research; B.W., F.Z., and I.S.A. designed model; C.H. analyzed data; and C.H., B.W., F.Z., I.S.A., J.F.T., and W.L. wrote the paper.

Chapter 4: Guided actin dynamics regulate directed cell motion along nanoridges regardless of the availability of collagen IV

This chapter is adapted from work in preparation by Hourwitz, Herr, Bull, Losert, and Fourkas with substantial editing to fit within the context of this dissertation. Matt Hourwitz designed the experiments, collected the data, and prepared Fig. 4.4. Abby Bull conducted the optical flow analysis. Corey Herr conducted shape and trajectory analysis, reanalyzed optical flow data, and prepared Figs. 4.1–4.3,4.5. All authors contributed to the writing and editing of the original manuscript.

4.1 Background

The ability to control cell migration with cell-type specificity is a focus of research and development for disease treatments [228]. Still, such control requires profound knowledge of the target cell, as well as its environment. Cell motion may be controlled by any of its governing internal components and processes, such as the cytoskeletal network [229, 230], molecular signaling pathways [231–237], gene expression [231, 238, 239], protein synthesis [240, 241], and post-translational modifications [242–245], all of which coordinate to regulate cell migration [246].

Many of these internal components can be impacted by external factors, including chemical and physical stimuli [247]. In natural environments, these cues are generated by neighboring cells and the ECM. For example, in neural crest cells that undergo the epithelial-to-mesenchymal transition (EMT) [248], these environmental processes control changes in cell-cell adhesion. At the same time, an EMT can also facilitate the progression of cancer and endometriosis by similarly altering the adhesion and motility characteristics of cells [90, 248] and increasing ECM detachment [249]. Controlled changes in migration state also often involve additional feedback: for example, the transcription factors (TFs) produced during the EMT program promote DNA repair [250] and inhibit apoptosis [250, 251].

Cells perpetually sense their physical environment to determine whether to maintain or adapt their behavior and to execute necessary functions. Differentiation, for example, can be induced through sensing of topography [252–256]. Changes in the physical interactions with the environment can have dramatic implications for cell health. For instance, detachment from the ECM induces cell apoptosis, also called anoikis, in endothelial and epithelial cells. Cells can sense a variety of facets of their physical environment, including substrate stiffness [257–259], and topography [28, 260–266], primarily through the detection of gradients [247, 267]. Physical stimuli are often sensed by inducing changes in the conformation and distribution of biomolecules near the plasma membrane, which then initiate signaling [268, 269]. Protrusions, such as filopodia, can provide information about the physical surroundings, including the presence of neighboring cells and nearby changes in topography [270, 271]. Sensing of the physical environment can also enable the detection and creation of chemical signals. For instance, cancer cells have demonstrated the ability to exploit physical stimuli to create chemical gradients [268]. Similarly, nanoscale topographical organization of membrane protrusions on the cell surface enables efficient antigen recognition and immune response [272–274].

The ability to sense a given physical cue depends on molecules at or near the surface of the cell, as well as on the properties of the cue. A cell must be able to orient itself such that sensitive molecules can detect changes in the physical landscape. Integrins often serve as sensors on the membrane surface. Depending on the biomolecular nature of the ECM, specific integrins can sense stretching of the substrate or shear stress from blood flow [275], allowing the activation of transcription factors and molecular pathways that result in changes in cell function and behavior [275, 276]. Other proteins, such as those with BAR domains, can sense curvature [277–279]. Curvature can also influence myosin contractility [280] and stress-fiber organization [206].

Recent work has demonstrated that the dynamic architecture of the cell, specifically the actin cytoskeleton, also serves as a primary sensor of the physical environment, including electric fields and nanotopography. Although the involvement of the actin cytoskeleton in sensing has often been considered part of the transduction network attached to transmembrane sensors, such as integrins [281], it has recently been suggested to play a more active role in force detection [282]. Actin dynamics is sensitive to both electrical and nanotopographic cues that generate distinct actin wave behavior[283, 284]. We previously found that the dynamic response of F-actin to nanotopographic cues can vary by cell line [26], and many studies have shown that changes in the dimensions of nanotopography prompt distinct cytoskeletal organization [23–25, 66, 285–288]. Cytoskeletal dynamics drive shape changes involved in processes such as migration [173] and cell division [289–291]. The cytoskeletal reorganization can also impact DNA repair and replication [292, 293] as well as protein transport [294]. The organization of the dynamic actin network is achieved by a multitude of other proteins that are responsible for further polymerization/filament formation, branching, anchoring/tethering, contraction, and depolymerization [295]. Luo *et al.* found that different forces applied to cells can prompt specific actin-associated proteins to respond, thereby influencing the cytoskeletal change resulting from the applied force [296]. It remains unclear which proteins near the membranes must be guided to accomplish directed migration.

Many of the transmembrane proteins involved in extracellular sensing are responsible for adhesion. For instance, the spatial density and organization of integrins control the strength and duration of adhesion to the ECM [295]. Additionally, integrins that cluster into focal adhesions form sites of strong adhesion [297]. The organization of integrins and the formation of adhesions are modulated by actin and actin-binding proteins, myosin, microtubules, GTPases, and kinases [246, 298, 299]. Similar relationships have been observed between GTPases and actin-binding proteins and other sensory and adhesion proteins [300].

The nature of the cellular environment can determine how strongly a cell adheres to the ECM. Most cells respond to changes in substrate stiffness, with the organization, size, and strength of adhesions generally increasing on stiffer substrates [301]. The ECM can also promote distinct adhesion characteristics depending on its molecular composition [302], due to the organization of protein components and the presence of ligands to which specific integrins preferentially bind [80, 303]. Adjusting the concentration of ECM protein can change the stiffness of the substrate without modifying the biomolecular composition, and this selective tuning of environmental properties has been shown to alter the behaviors of epithelial cells, such as the degree of proliferation, migration, adhesion, and activation of the signaling pathway [304]. The structural characteristics of the components of ECM can vary depending on anatomical location [305], and topographical properties have been shown to influence the localization of adhesion complexes [23, 26, 306]. However, the state of the cell can also dictate its adhesion, as well as alter the properties of the surroundings, such as by producing matrix metalloproteinases to degrade the ECM. Cancer cells with lower collagen production exhibit less adhesion to the ECM and more tumorigenicity [307]. Even cells without integrin-modulated focal adhesions, such as the amoeboid Dictyostelium discoideum, can sense and respond to nanotopography [25]. The local characteristics of the ECM and the unique properties of the various cells encountering the environment determine the nature of adhesion to the substrate, which, in turn, affects cell function and behavior [308].

To simplify the study of this system, we instead ask if there are other ways to reproduce the local microenvironment *in vitro*. Topographical cues can generate an actin-sensing-based morphological response that is uncharacteristic of directed motion on flat substrates *in vitro*, while still achieving guided migration due to texture sensing from integrins. For example, small-amplitude wavy ridges influence lamellipodial actin to organize at the wave peaks away from the leading edge of the cell, yet focal adhesions form in the direction of the nanoridges [306]. Although adhesions are often necessary for accurately directed migration [309], some of the actin-binding proteins are also required for guidance [310]. Previous studies of T cells indicated that actin polymerization and adhesion are necessary for cells to follow the guidance cues of nanoridges [311, 312]. The conditions and limitations of actin sensing must continue to be probed.

In this study, we investigate how F-actin is influenced by the interaction of physical cues with the local chemical environment. Specifically, we explore how the cellular response to nanoridges is affected by the concentration of the extracellular matrix (ECM) ligand collagen IV. We found that cells on collagen-coated (CC) ridges were more likely to spread and migrate. The amount of collagen did not significantly affect these tendencies, although any difference decreased over time during the experiments. Cells that spread and migrated on uncoated ridges were also relatively well guided, and, again, this guidance improved over the course of the experiment. In general, the nanoridges provided strong guidance for migrating cells, with many cells maintaining alignment with the ridge axis as they traveled over tens or even hundreds of microns. The preferred orientation of actin polymerization was also along the ridge. More densely coated ridges and the passage of time both increased the likelihood of aligned actin. However, the ability of polymerizing actin to sense the topography and orient accordingly was not affected by the migratory behavior of cells. Persistent, turning, and random motion all exhibit similar actin optical flow distributions.

4.2 Results

4.2.1 Collagen IV facilitates cell elongation

We examined cell shape and motion to develop a better understanding of how the availability of ECM ligands for integrins and adhesion affects guidance by topography. We first quantified the morphological response of the MCF10A cells. Based on a description of the mechanism by which fibroblast cells spread on fibronectin, the organization of adhesion proteins initiates spreading [313]. Therefore, we varied the surface coating density of collagen IV to observe the effect on the rate and extent of cell spreading. The cell shape was monitored, and the eccentricity was calculated to determine the degree of spreading and provide a measure of the cells' ability to sense and respond to the topographic cues of the nanoridges. Specifically, we measured the eccentricity of the cells on the ridges and how it changed when different amounts of collagen were coated onto the surface (Fig. 4.1A–D). We found that the expected cell eccentricity was higher on CC surfaces than on uncoated surfaces at each experimental time point (Fig. 4.1E). The majority of cells on uncoated ridges remained circular throughout the observation period. Despite this preponderance of round cells, the proportion of cells that elongated or spread (eccentricity $>$ 0.5) on uncoated ridges increased after approximately 24 hours. A greater increase in the fraction of elongated cells over time was observed on ridges coated with collagen. MCF10A cells are known to deposit their own ECM proteins [314], which likely explains why the average cell eccentricity on uncoated nanoridges increased over time. The population of eccentric cells did not differ greatly on nanoridges coated with distinct densities of collagen IV. Cell spreading on the nanoridges was dependent on the presence of the ECM protein coating, but could be achieved across a range of coating densities.

4.2.2 Availability of collagen IV does not strongly impact cell-ridge alignment

We next examined how cell shape responds to nanoridges when different amounts of adhesive cues are available for the cell to sense by analyzing the distribution of cell alignment with respect to the ridge direction (Fig. 4.1F–H). Our goal was to determine whether ridges orient spreading, and whether collagen influences the extent of any such alignment. We denote the first time window, with an approximate midpoint of 2.75 hours after plating, as the "early" timeframe in our experiments. Cells on uncoated nanoridges did not respond to the topographic cues within this time window (Fig. 4.1F). However, the discrepancy in alignment with the ridge axis between cells on uncoated and CC surfaces is smaller than might be expected. Indeed, in the early timeframe, the density of collagen does not seem to influence the distribution of cell alignment. After approximately 24 hours after plating (the “middle” timeframe), the cells exhibit a significant degree of alignment with the ridges, but there is little distinction in the degree of alignment

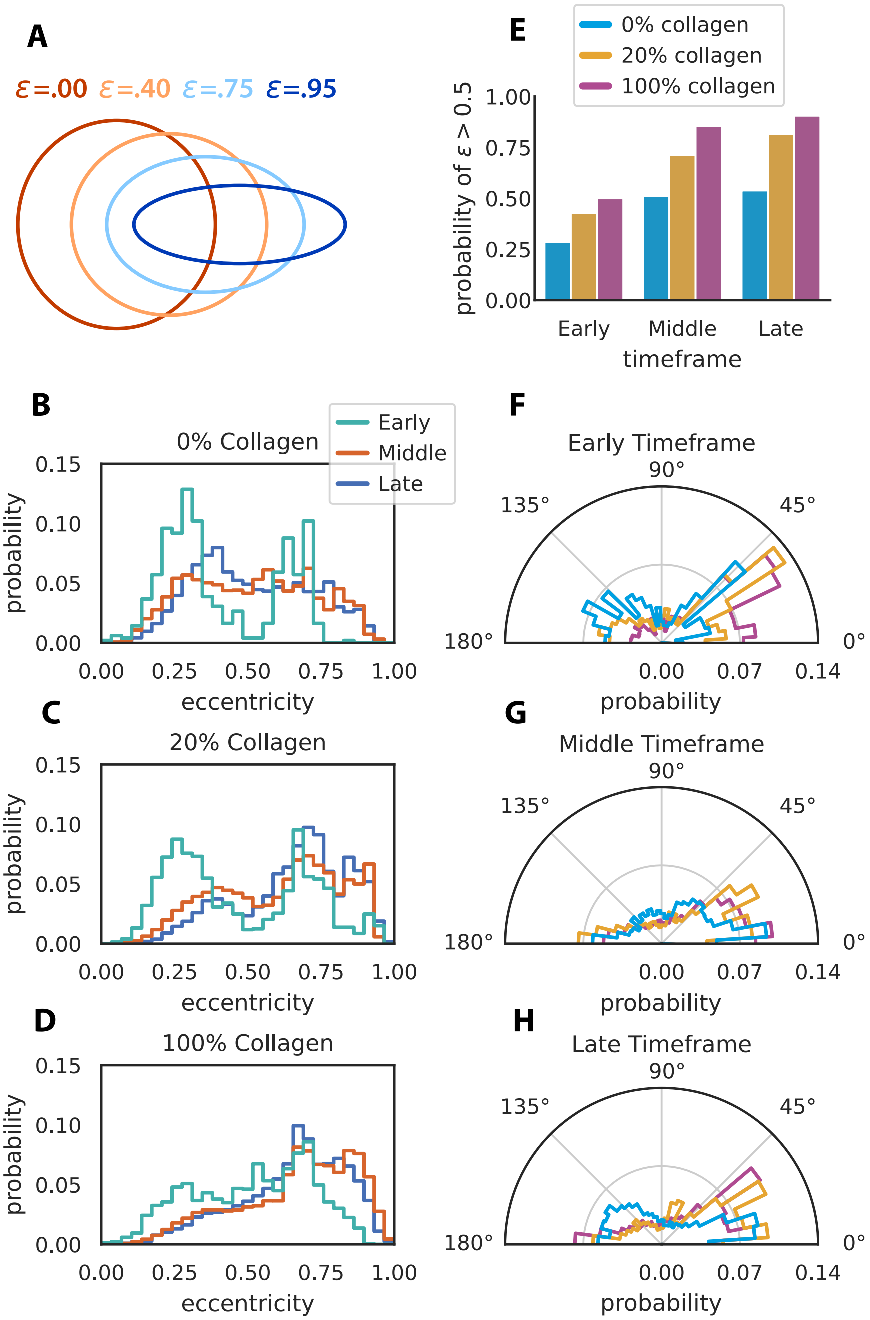

Figure 4.1: Collagen promotes cell elongation and nanoridges cause cells to align with the ridge axis. **A** Schematic showing eccentricities for different ellipses. **B–D** Histograms of the eccentricities of cells on nanoridges with approximate collagen IV coating densities of 0 (0%), 0.65 (20%), and 3.25 μg/cm^2 (100%) at different experimental time points. The early time has an approximate midpoint of 2.75 hours after plating, the middle time occurs approximately 21.5 hours after plating, and the late time occurs at approximately 40.5 hours after plating. **E** The proportion of cells exhibiting an eccentricity greater than 0.5 on ridge surfaces for different collagen coating densities as a function of experimental time. $P \leq 0.01$ for comparison between all conditions across all times. F–H. Rose plots of the proportion of cells oriented at angles with respect to the ridge axis at different times after plating. The ridges are aligned with 0°/180° line. The color coding is the same as in panel **E**

among the different coating conditions (Fig. 4.1G). Similar results were observed in the "late" timeframe, nearly 2 days after plating (Fig. 4.1H).

4.2.3 Cell migration is well guided by ridge direction regardless of collagen concentration

Although most of the cells that we observed spread on CC substrates, few of the cells migrated. The limited number of migrating cells might be a result of the stiffness or adhesive nature of the combination of collagen IV and the acrylic ridge material. On ridges coated with collagen, cells can adopt an exaggerated, spindly mesenchymal shape, indicative of stable and well-organized adhesions induced by both surface chemistry and nanotopography. Indeed, on surfaces with a sufficiently high coating of collagen, some cells can stretch to lengths of hundreds of microns and tear themselves apart.

Migration was observed more frequently on coated substrates than on uncoated substrates (Fig. 4.2A). For cells whose displacement reached a minimum threshold during the observation period, we used a tracking algorithm to trace their trajectory. As shown in Fig. 4.2B, the motion of most of the cells follows the ridges, which are oriented along the horizontal axis. Migrating cells were guided by the ridges over tens of microns. Although there are a few exceptions, most cells that migrate along the nanoridges travel in the direction of the ridge. Previous studies have demonstrated the role of focal adhesion organization in enabling cells to sense and follow nanotopographic cues during migration [26, 306]. In analogy to our results for cell spreading on the ridges, in which the surface density of ECM ligands for adhesion influenced cell eccentricity (Fig. 4.1A–E), but had a limited impact on alignment with the nanotopography over the course of the experiments (Fig. 4.1F–H), we found that adhesive cues affect the likelihood of migration (Fig. 4.2A), but do not appear to be predominantly responsible for directed migration, as shown in the histograms of the direction of motion with respect to the ridges (Fig. 4.2D–F). However, across all coating densities, there were more occurrences of instantaneous motion away from the ridge axis (more aligned with the normal) during the early time period (Fig. 4.2D–F, green curves). However, the frequency of these unaligned movements was higher on the uncoated substrates, with several peaks oriented perpendicular to the ridges on the polar histogram (Fig. 4.2D, green curve). Cells that are motile on the uncoated ridges exhibit instantaneous motion at all angles relative to the ridge direction. However, in the middle timeframe, it became difficult to distinguish the prevalence of aligned motion for cells on surfaces that were uncoated and surfaces with 20% collagen coating (Fig. 4.2D,E, orange curves). The guidance on the nanoridges with 100% collagen coating was slightly stronger, based on the greater prominence and narrower width in the polar histogram (Fig. 4.2F, orange curve). The strength of directed migration became even less distinct during the late timeframe (Fig. 4.2D–F, blue curves).

Overall, the nanoridges were capable of guiding cell motion, regardless of whether adhesive cues were present or absent. There were, nevertheless, many moments at which cells on CC nanoridges appeared to be oriented away from the ridge direction, although this phenomenon became somewhat rarer with increasing time following plating. The relatively large occurrence of instantaneous motions at angles deviating from the ridge axis on all nanoridge surfaces makes the overall fidelity of the cell tracks to the ridge axis even more remarkable.

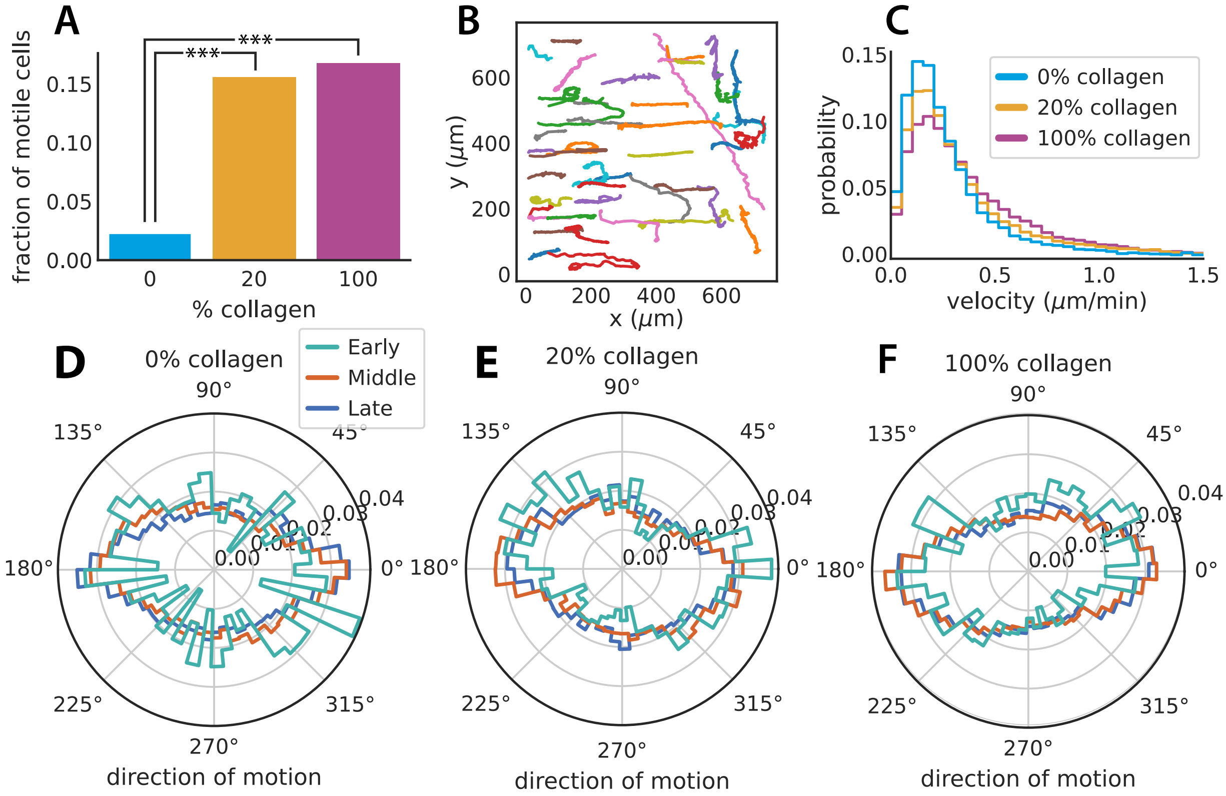

Figure 4.2: Cell migration on nanoridges is modulated by the surface density of collagen IV. **A** Fraction of cells that are motile on the nanoridges as a function of collagen coating density. **B** Tracks of cells migrating on or adjacent to the nanoridges. **C** Distributions of populations of cells as a function of migration velocity on nanoridges with different coatings. **D–F** Instantaneous orientation of cells migrating on nanoridges at different experimental times with no collagen, 20% collagen, and 100% collagen, respectively. ***P≤0.001

4.2.4 Collagen promotes faster migration on nanoridges

We next examined how adhesion to collagen affected the velocity at which cells migrated on the ridges. An early study by DiMilla et al. surmised that the maximum speed of smooth muscle cells occurred within an optimal range of ECM-ligand surface density, and thus is related to the adhesion strength between the cell and ECM [315]. If adhesion to the substrate is too strong, there will be fewer motile cells, and those cells that do migrate will move more slowly. A more recent study by Keely and coworkers investigated how fiber alignment, ligand density, and stiffness combine to impact the rate at which breast-cancer cells travel in collagen gels and CC polyacrylamide gels [316]. This group found that cells moved more slowly if the ligand density surpassed a threshold, yet fiber alignment did not influence cell speed [316]. Interestingly, a report by Wang et al. determined that aligned haptotactic cues of fibronectin induced fibroblasts to migrate faster than on non-aligned patterns of fibronectin, regardless of ECM ligand density [317]. We found that on surfaces both with and without collagen, most of the motile cells migrating on the ridges travelled at speeds below 0.5 μm/min (Fig. 4.2C). We note that this relatively low average velocity is, in all likelihood, influenced by the material composition of the nanoridges. The velocity distributions broaden with increasing coating density, such that a larger proportion of the population has a speed between 0.5 and 1 μm/min.

4.2.5 High surface density of collagen IV increases actin guidance

Considering the essential role of actin in cell motion, we studied how actin dynamics varied on ridges with different surface coating densities of collagen IV. Nanoridges have been shown to lead to enhanced nucleation of actin polymerization [25, 285, 288] and to guide the waves of polymerization [25, 71, 288], a process known as esotaxis [23, 24]. To quantify esotaxis, fluorescence movies of MCF10A LifeAct-GFP cells were analyzed using optical flow (OF) (Fig. 4.3A–B). Images were generally collected at a z plane near the basal membrane of the cells, where the cytoskeleton has its strongest interaction with the nanotopography. In the representative image in Fig. 4.3A, actin streaks are seen to have a spacing approximately equal to that of the ridges, and they align with and propagate along the ridge axis. The flow vectors determined for the representative image in Fig. 4.3A are shown in Fig. 4.3B. The orientations of the flow vectors relative to the ridge axis were collected for cells on the different coatings at the different experimental timeframes (Fig. 4.3C–E). Cells on ridges with 100% collagen coating exhibited the best guidance of actin polymerization throughout the experiments, as well as the lowest occurrence of polymerization perpendicular to the ridges. However, a majority of the actin polymerization flux was nearly parallel to the nanoridges regardless of coating. Even cells that were recently plated on substrates without collagen exhibited esotaxis. Additionally, the fraction of flow vectors aligned with the ridges for cells on the uncoated nanoridges and the nanoridges with 20% collagen were consistently similar throughout the experiment. In Fig. 4.3F, we plot the fraction of actin flux that propagated along the ridge axis (i.e., the mean prominence) for the different coatings and experimental timeframes. In Fig. 4.3G, we plot the amount of actin polymerization that significantly deviated from the ridges (i.e., the mean width) for the different coatings and timeframes. These results show a substantial increase in esotaxis for the 100% CC surface. There is a significant increase in mean prominence when collagen is increased to 100% regardless of the time period. Additionally, we see that on 100% CC ridges, the mean prominence increases significantly from the middle to the late time period. Finally, at the late time period, the mean width decreases significantly for 100% collagen concentration. These results suggest that collagen concentration is linked to the cell's sensitivity to nanotopography.

Although the majority of OF vectors are aligned within 30° of the ridge axis on all coatings and in all experimental timeframes (Fig. 4.3C–E), there is a quantifiable difference in the distribution of OF orientations between cells on the nanoridges with 100% collagen coating and the nanoridges under other coating conditions. These histograms provide only a limited visualization of how the orientational dynamics of actin polymerization and organization might differ in cells on topography with the various coating densities. We therefore examined how the angle of actin flux throughout a representative cell varied with time on nanoridges with a given collagen coating density. From kymographs of the direction of actin flux with respect to the ridge axis and the actin fluorescence intensity as a function of time (Fig. 4.3Hi–iv), the influence that collagen coating has on actin guidance is evident. Based on a comparison of actin dynamics in a cell on uncoated nanoridges in the early timeframe (Fig. 4.3Hi) with a cell on nanoridges with 100% collagen coating in the same timeframe (Fig. 4.3Hiii), collagen IV appears to promote a consistent sense of, and response to, nanotopographic cues. The cell on uncoated ridges experienced intense, unidirectional actin flux (appearing as horizontal bands in the kymograph in Fig. 4.3Hi) along the ridges that was interrupted periodically by probing motion at other angles, followed by reversal of direction. The cell on the nanoridges with 100% collagen maintained intense actin dynamics in both directions along the ridge axis with few fluctuations in intensity and limited probing of other orientations. During the late timeframe, less actin propagated perpendicularly to the ridge axis for each coating condition (Figure 4.3Hii,iv) than was observed in the early timeframe. In both timeframes, actin polymerization is more confined along the nanoridges with 100% collagen coating than on the uncoated nanoridges. These results suggest that esotaxis can occur in these cells even without a large supply of ECM ligands available for adhesion, but that the adhesive cues help to sustain esotaxis.

Images of the fluorescently labeled F-actin provide information regarding how the dynamic organization of the actin cytoskeleton near the basal surface (the plane of interest in our study) responds to the nanoridges (Fig. 4.4A–E). There is a slight decrease in the fluorescence intensity at the rear of each cell in this figure. It is evident from these images that the majority of actin polymerization occurs at or near the ridges. Comparing individual frames of actin movies enables visualization of changes in the cytoskeleton that occur during motion, including the formation of protrusions. Fig. 4.4E shows a cell sensing an approximately 1-μm gap between adjacent nanoridges. We also observed one cell that rapidly altered its morphology and took on less common shapes (Fig. 4.4D). These results suggest that esotaxis is linked to microthigmotaxis, the preferential migration of cells parallel to the nanoridges, as has been previously observed for MCF10A cells [24–26, 286, 288, 306].

4.2.6 The cell trajectory phenotype is not linked to actin flow

The trajectories in Fig. 4.2B fall into three distinct categories: trajectories in which the cells move tens or even hundreds of microns in a straight path; trajectories in which the cells exhibit no directional bias; and trajectories in which the cells move straight for a period of time and then reverse to move the opposite direction. To quantify these trajectories, we use the autocorrelation function $R(t')$

$$R(t') = \frac{1}{T-t'} \sum_{t=0}^{T-t'} \frac{v(t) \cdot v(t+t')}{|v(t)||v(t+t')|} \tag{4.1}$$

where v(t) is the instantaneous velocity of the cell at time t and T is the total time spanned by the trajectory. $R(t')$ ranges from -1 to 1, and quantifies how similar a trajectory is to itself when

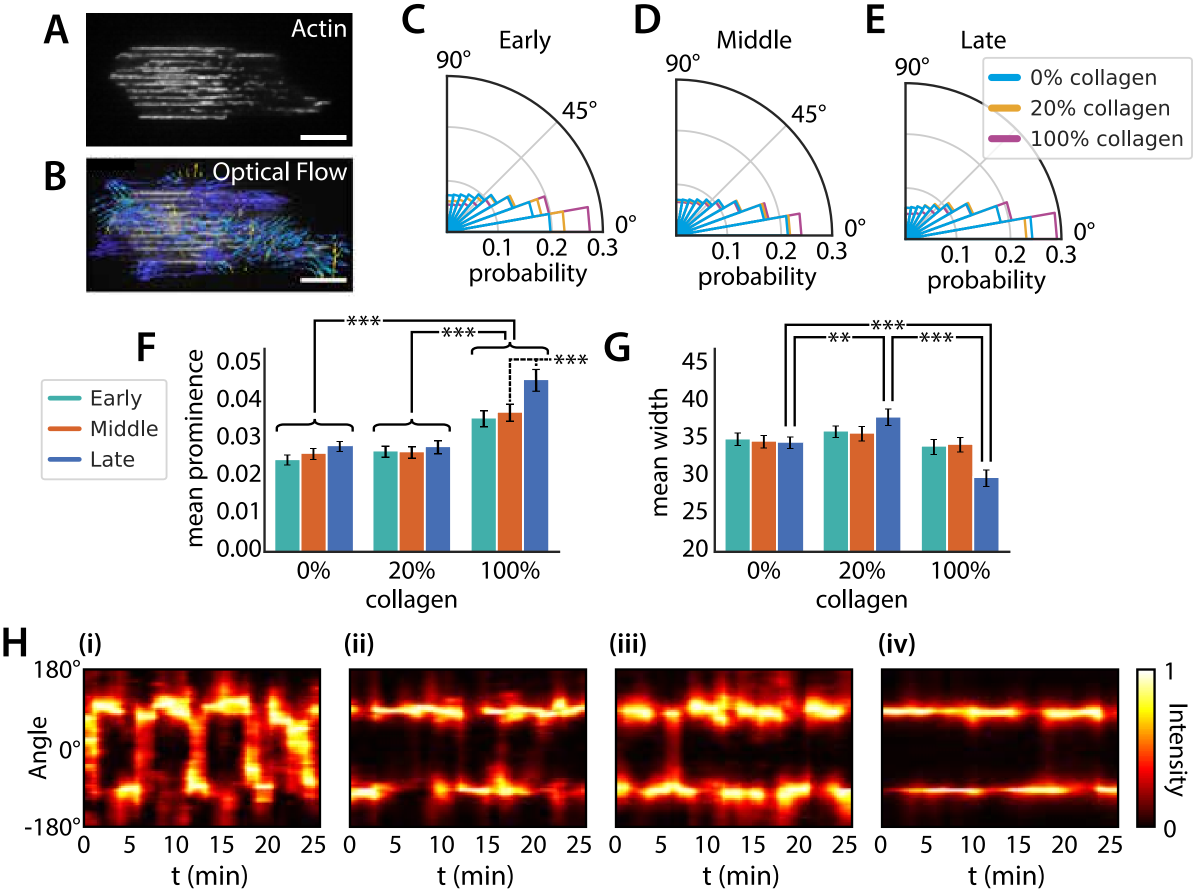

Figure 4.3: Nanotopography can guide actin polymerization even in the absence of added ECM coating, although collagen IV coating can limit actin-polymerization oscillations perpendicular to the ridge axis. **A** Representative image of fluorescently labeled F-actin plated on nanoridges with 100% collagen coating and imaged in the late timeframe. **B** Corresponding image of OF vectors depicting the actin flux between adjacent image frames. Scale bars: 10 μm. **C–E** Polar histograms showing fractions of actin polymerization propagating at different orientations relative to the ridge axis (0°) in the early, middle, and late experimental timeframes, respectively. **F** Histogram of the mean prominence of the polar histograms (i.e., the value along the polar axis), as a function of experimental timeframe and the coating condition. Braces indicate p-value between respective timeframes (e.g. 0% early compared to 0% middle) **G** Histogram of the mean width of the polar histograms (i.e., the width normal to the polar axis), as a function of experimental timeframe and the coating condition. **F** and **G** share the same color coding. **H** Kymographs showing the actin polymerization flux throughout representative cells as a function of the angle relative to the nanoridge axis and of time. i–ii. Heat maps of a cell on uncoated nanoridges in the early and late experimental timeframes, respectively. iii–iv. Heat maps of a cell on nanoridges with 100% collagen coating in the early and late experimental timeframes, respectively. $^{**}P \leq 0.01$, $^{***}P \leq 0.001$

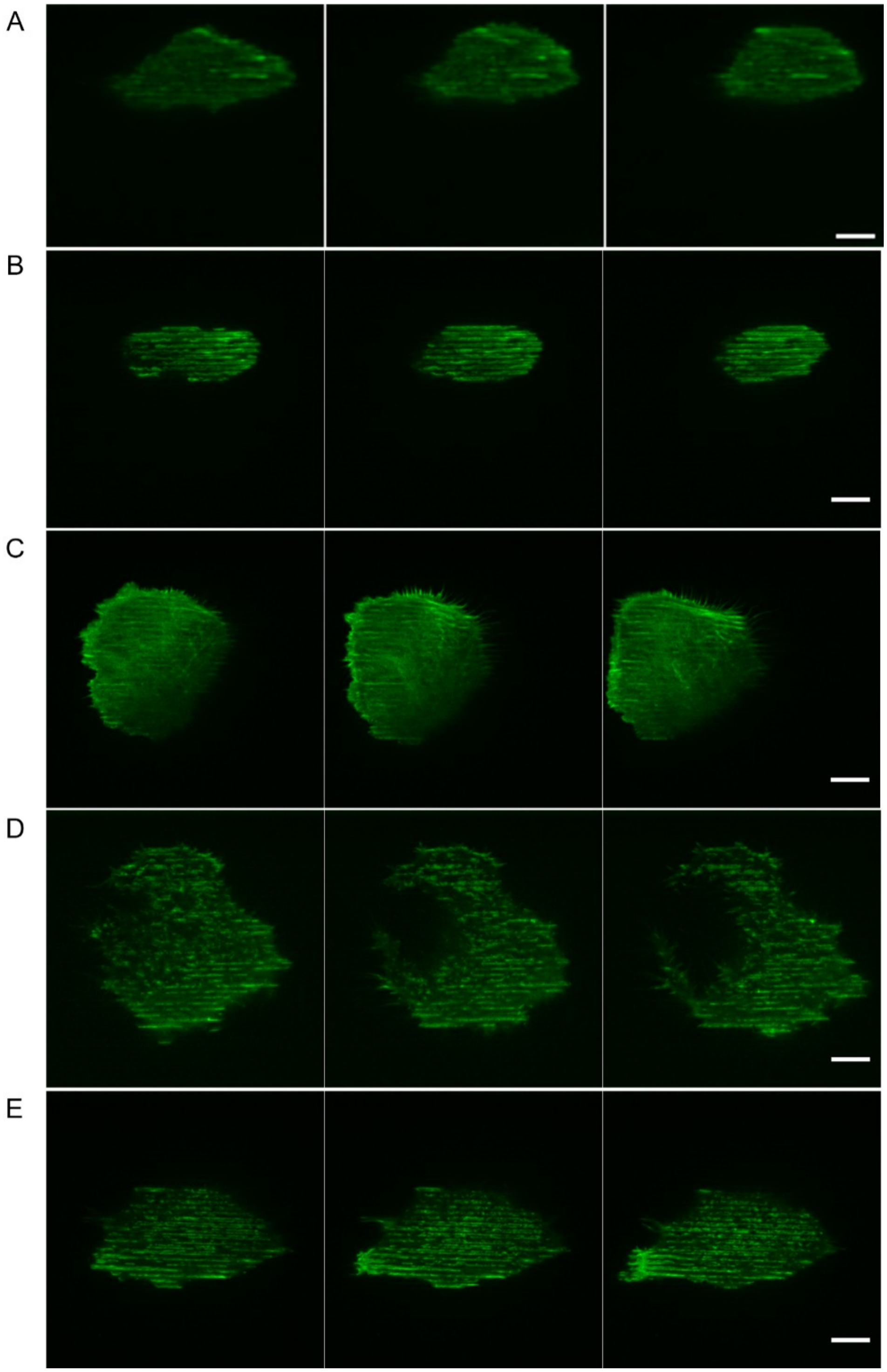

Figure 4.4: Actin distribution at the ventral surface of MCF10A cells migrating on nanoridges. Fluorescently labeled F-actin enables visualization of the dynamic cytoskeletal response to the nanoridges. The time between successive images is 15 min. **A** Cell on uncoated nanoridges. **B–D** Cells on nanoridges with 20% collagen coating. **E** Cell on nanoridges with 100% collagen coating. Scale bars: 10 μm.

separated by a timestep of t'. A completely straight trajectory has $R(t') = 1$ for all values of t', as seen in Fig. 4.5A. A completely random trajectory has $R(t') \rightarrow 0$ as $t' \rightarrow \infty$, as seen in Fig. 4.5B. Finally, a reversing trajectory will exhibit a sign change in $R(t')$ from positive to negative at the time of the turn, as seen in Fig. 4.5C. We classified the trajectories into these three phenotypes based on $\bar{R}$, the average value of $R(t')$. Straight trajectories were defined as having $\bar{R} \geq 0.9$, random trajectories were defined as having $0.25 < \bar{R} \leq 0.9$, and reversing trajectories were defined as having $\bar{R} < 0.25$. These classifications were chosen based on the set of trajectories, and the ranges of $\bar{R}$ for each category could change if T were different. The value of $\bar{R}$ is greater for a random trajectory than for a reversing trajectory because even in the case of random motion, there is a persistence time for directional changes, such that $R(t')$ remains close to unity for small enough values of t'. The same holds true for a reversing trajectory, but the fact that the dot product changes its sign but maintains its magnitude following a reversal tends to lead to a smaller value of $\bar{R}$, as long as the reversal does not occur too early or too late in the trajectory. Most reversing trajectories had $\bar{R} < 0$.

Once the trajectories were classified by phenotype, we compared the actin OF for those phenotypes. In representative individual cases, we found that the actin-flow kymographs look similar for straight (Fig. 4.5E) and random (Fig. 4.5F) trajectories. Both of these kymographs have peaks at 0° and 180°, i.e. along the nanoridges. In fact, Fig. 4.5G shows that the angular distribution of actin-flow vectors is essentially indistinguishable among the different trajectory phenotypes.

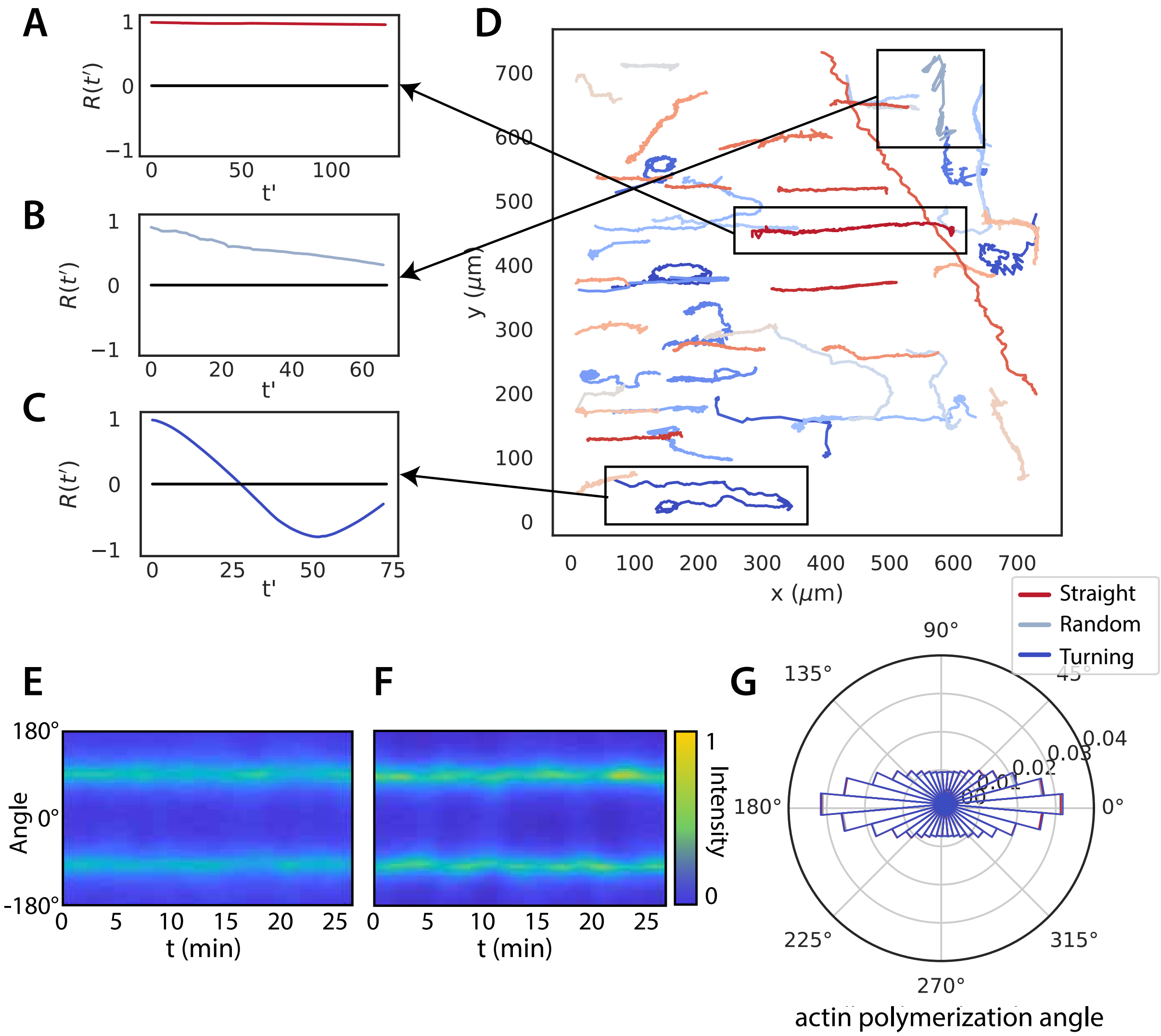

Figure 4.5: **Cells with different trajectory phenotypes have similar actin OF distributions.** The autocorrelation function $R(t')$ is distinctly different for each type of trajectory: **A** straight, **B** random, and **C** turning. **D** Representative cell trajectories. The trajectories are classified into the three categories based on the value of $\bar{R}$. The kymographs of actin optical flow for: **E** a straight trajectory; and **F** a random trajectory are very similar. **G** The overall OF distribution for all trajectories classified by trajectory type. The color coding of migratory phenotypes in D is the same in **A–C** and **G**. There are no significant differences among the distributions.

4.3 Discussion

This study examined the effect of collagen IV, an ECM ligand, on the cellular response to nanoridges. We studied the spreading and migration of MCF10A cells, as well as the guidance of these processes, as quantified by shape and motion orientation relative to the nanoridges. We investigated how esotaxis was affected during spreading and migration, as well as by the density of collagen IV.

Previous studies reported that when D. discoideum cells are plated on nanoridges, cells that are more elongated are most likely to be oriented along the ridge axis [25]. For epithelial cells, on the other hand, we found that elongation and orientation were not strongly linked. The distributions for the early timeframe show that cells on the uncoated nanoridges are more round and exhibit a greater likelihood of orienting perpendicular to the ridge axis, whereas cells on the CC nanoridges frequently deviated from the ridge axis at large angles (but usually less than 45°). As time progressed, the correlation between eccentricity and orientation became weaker. After 24 hours, and continuing through the end of our observations, the proportion of elongated cells remained lower on uncoated nanoridges, even though the proportion of cells aligned with the nanoridges was similar for all coating conditions. These results suggest that cell elongation and orientation on nanoridges can be decoupled to a certain extent. The extent to which adhesion and nanotopography contribute to the ability of MCF10A cells to be guided with limited cell spreading remains an open question.

The protein surface density is expected to be lower on uncoated nanoridges than on CC nanoridges throughout the course of our observations, despite the ability of human epithelial cells to produce ECM proteins. Although the lower density of adhesive cues on the uncoated nanoridges resulted in a lower average eccentricity, the uncoated nanoridges did not lead to a greater population of misaligned cells. The slight misalignment of recently plated cells on uncoated nanoridges supports the idea that adhesion facilitates a small degree of enhancement for contact guidance. However, spreading and migrating cells exhibited alignment with the uncoated nanoridges that was similar to 20% or 100% CC nanoridges, especially 10-15 hours after plating. The extent of alignment shortly after plating, both of the cells themselves and of the polymerizing actin, suggests that strong, stable adhesive interactions are not the main determinant of guidance. The similarity in cell orientation distributions between uncoated and CC nanoridges indicates that the initial guidance is not influenced by the presence of ECM ligands. In the case of the *D. discoideum* cells, which lack integrins, and are often studied on untreated surfaces, even cells with low eccentricity are apt to orient along the nanoridge axis, although the difference in preference for elongated cells was evident [25]. Taken together, these studies support the notion that nanotopography can cause a directional bias in cells that employ distinct molecules and mechanisms for interacting with the underlying substrate.

The cell tracks we measured illustrate the strong guidance of cell migration by nanoridges, often over distances of greater than 100 μm. The majority of cells in this study traveled at speeds below 0.5 μm/min (Fig. 4.2C). The cell speeds depend on the properties of the substrate; therefore, changes to the topographical cue, the substrate material, or the protein coating density (as shown in the figure) will alter the velocity distribution of the cells. Cells that traveled at higher velocities in this study frequently exhibited a round cell shape. The low prevalence of cells moving at these speeds may be due to the limited ability of MCF10A cells to exhibit amoeboid migratory characteristics, such as reduced adhesion complexes and contractility, under the experimental conditions.

Our OF data reveals that the predominant motion of actin polymerization is along the ridges, regardless of the coating condition. The OF data further show that, after less than 12 hours, in cells plated on uncoated nanoridges, the actin motion was largely guided by the nanotopographic cues, even though many of the cells had not yet spread on the surface. The actin is not as well organized in cells recently plated on uncoated nanoridges as in cells recently plated on CC ridges, which often feature streak-like filaments on both sides of a single nanoridge. However, F-actin polymerization in cells on the uncoated ridges remains biased along the nanoridges. As collagen concentration was increased to 100%, the OF became significantly more guided by the ridges.

Both cell migration and actin dynamics were guided along nanoridges, yet our results reveal a disconnect between these two phenomena. Despite the bidirectional guidance of actin in both motile and nonmotile cells, migratory behavior—-whether persistent, reversing, or random—-did not correspond to distinct patterns of actin organization or orientation. Analysis of actin dynamics using kymographs and rose plots failed to differentiate between these behavioral categories. Although a temporal offset in data collection resulted in some actin videos being acquired hours after migration tracking, the overall lack of correlation suggests that actin polymerization at the ventral surface alone does not determine the migratory phenotype. This raises the possibility that other factors, such as the spatial regulation of focal adhesions, may be responsible for breaking symmetry and facilitating directional migration. The lack of motile cells on uncoated ridges supports this idea, suggesting that strong adhesive interactions might cause distinct directional guidance even when actin guidance appears similar. Future work could address how focal adhesion dynamics integrate with actin-based sensing to produce coordinated migration in response to topographic cues.

In addition to integrin-mediated adhesion, the plasma membrane likely plays a complementary role in sensing nanotopographic features. Contact with nanoridges can deform the membrane, generating localized curvature and increased tension [318]. These deformations can recruit curvature-sensitive proteins and influence actin polymerization at those sites. Indeed, actin-binding proteins that respond to membrane curvature may help initiate or reinforce cytoskeletal organization along topographic cues [319]. Such membrane-based sensing mechanisms are thought to function independently of specific lipid compositions like PIP2 and may help explain how actin guidance occurs even in low-adhesion environments. While membrane deformation contributes to topography sensing, our results emphasize that actin itself acts as a primary sensor of nanotopographic cues, with adhesive cues such as collagen IV enhancing—but not initiating—this guidance.

In summary, our findings demonstrate that actin polymerization is intrinsically sensitive to nanotopographic cues, independent of strong adhesive interactions caused by ECM ligands such as collagen IV. This actin-based guidance occurs even in the absence of robust cell spreading, underscoring a fundamental capacity of the cytoskeleton to detect and respond to physical features of the substrate. However, this topographic sensing is enhanced in the presence of higher collagen concentrations, where adhesive cues most likely further confine actin dynamics. Thus, while actin sensing of nanotopography is largely adhesion-independent, collagen-mediated adhesion refines and strengthens the fidelity of this guidance.

4.4 Methods

4.4.1 MAP

The nanoridges were created using MAP, as described elsewhere [320]. A drop of a resin mixture containing acrylate monomers, ethoxylated(6)trimethylolpropane triacrylate (CAS: 28961-43-5, Sartomer) and tris(2-hydroxyethyl)isocyanurate triacrylate (CAS: 40220-08-4, Sartomer) (1/1 w/w), and a small amount of the photoinitiator Irgacure TPO-L (CAS: 84434-11-7, BASF) (3% w/w total solution) was placed on the surface of a microscope slide that had previously been treated with an oxygen plasma and functionalized with acrylate groups. An ultrafast, near-infrared laser (Coherent Mira 900-F Ti:sapphire; 200 fs pulses; 76 MHz repetition rate; wavelength set to 800 nm) was focused through a microscope objective with high numerical aperture (Zeiss α Plan-Fluar 100×, NA: 1.45), enabling multiphoton absorption in the focal region. Patterning was achieved using a LabVIEW (National Instruments) program that controlled the stage position. Once patterning was complete, the material was developed in ethanol twice (3 min. each). The patterned substrate was then baked at 110 °C overnight to harden. Functionalization and Molding of the MAP-Fabricated Pattern The ridges fabricated with MAP were functionalized with ethylenediamine (CAS: 107-15-3, Sigma-Aldrich) and, subsequently, perfluorooctadecanoic acid (CAS: 16517-11-6, Alfa Aesar), as detailed more extensively in Chapter two. The substrate was rinsed in ethanol after each functionalization step, and then was baked at 110 °C for over 1 hour. As has been described previously [23], a hard polydimethyl siloxane (h-PDMS) mixture was prepared from a mixture of vinylmethylsiloxane (CAS: 67762-94-1, Gelest) and methylhydrosiloxane (CAS: 68037-59-2, Gelest), each copolymerized with dimethylsiloxane. A platinum catalyst (CAS: 68478-92-2, Gelest) and modulator (CAS: 2554-06-5, Sigma-Aldrich) were also added. Hexane was added to decrease viscosity and improve the resolution of the molding process. This mixture was spin-coated onto the patterned substrate and allowed to sit at room temperature for 2 hours prior to baking at 60 °C for 1 hour. A mixture (10:1) of the elastomer base and curing agent of Sylgard 184 (Dow Corning) was then poured atop the h-PDMS film, and the pre-mold mixture was baked at 60°C for 70 min. The relief mold was then peeled from the acrylate pattern.

4.4.2 Replication via nanoimprint lithography

Replicas were produced by placing a drop of the same acrylate resin on the relief pattern in the PDMS mold and pressing down on the drop with a coverslip functionalized with acrylate groups. After the sandwiched drop was secured, the resin was exposed to ultraviolet light (Blak-Ray, B-100AP, 100 W, 365 nm). The total exposure time was 5 min and the replica pattern was peeled away from the mold. The acrylic replicas were soaked in ethanol for at least 12 hours, and subsequently dried in an oven at 110 °C for 1 hour. The nanotopographic surfaces were then soaked in 1 mL of distilled water (Invitrogen, Catalog: 10977015) for at least 12 hours.

4.4.3 Coating nanoridge substrates with collagen IV

Nanoridged substrates that were to be left uncoated received no further treatment. For all other samples, mouse collagen IV (Engelbreth-Holm-Swarm lathrytic mouse tumor; 0.05 M HCl; Corning; Prod.: 354233) was used to coat the surfaces. The density/concentration of the collagen stock solution, the area to be coated, and the coating density were the factors used to determine the volume of the original collagen solution that should be used. The calculated volume of collagen stock was diluted in 0.05 M HCl to a volume that covered the entire area of the cover slip that would be in contact with cells during the experiments. A coating density of 3.25 μg/cm^2 was determined by identifying when cell morphology and behavior on flat acrylic films coated with collagen resembled those properties on CC glass. A lower coating density of 0.65 μg/cm^2 was selected to test how cell shape and migration change on the nanoridges. The diluted collagen IV solution was allowed to sit on the substrates, which were placed on ice, for approximately 1 hour. The solution was then aspirated. The substrates were then rinsed with distilled water and aspirated twice. The substrates subsequently sat on ice or were stored at 4 °C prior to experiments.

4.4.4 Cell culture

The MCF10A LifeAct-GFP cells were cultured in a cell medium composed of DMEM/F12 (Gibco, Catalog: 11330057), 5% horse serum (v/v) (Gibco, Catalog: 26050088), 10 μg/mL insulin (Gibco, Catalog: 12585014), 20 ng/mL epidermal growth factor (EGF; PeproTech, Catalog: AF-100-15), 0.5 μg/mL hydrocortisone (Sigma-Aldrich, Product: H4001), and 0.1 μg/mL cholera toxin (Sigma, C8052). Puromycin dihydrochloride (A. G. Scientific; Product: P-1033-SOL) was subsequently added to the medium (0.5 μg/mL). The cells were stored in a humidified incubator set at 37 °C and sustained with 5% CO2.

4.4.5 Imaging

Prior to plating the cells on the substrates, the cell medium was aspirated and the cells were rinsed with Dulbecco's phosphate buffered saline (Quality Biological, Product: 114-057-101). The cells were trypsinized (Gibco, Catalog: 25200056) and centrifuged in the cell medium. The cell density was adjusted to 104 cells/mL, and 2 mL of cell solution added to the dish or plate to which the substrate was attached. Cells were imaged within 1.5 hours of plating using a PerkinElmer UltraView VoX confocal spinning disk system attached to a Nikon Ti inverted microscope. Culture conditions were maintained in a Tokai Hit stage-top incubator (37 °C, 5% CO2, humidity). The cells were imaged for at least 3 hours with a 10× phase-contrast objective (Nikon CFI Plan Fluor, NA 0.3) to monitor migration. Images were collected with a rate of 1 frame every 3 min. Next, individual cells were selected for imaging at 100× (1.49 NA, oil-immersion objective) in bright-field and fluorescence modes (488-nm laser power: 9%) at a rate of 1 frame every 10 s. After imaging individual cells, migration data were again collected at 10× in phase-contrast for at least 12 hours. Then, actin fluorescence data from individual cells were again recorded. The imaging switched between migration and actin-dynamics data collection one more time.

4.4.6 Analysis

Cell tracking and shape detection were performed on the bright-field movies of MCF10A cells on CC nanoridges, in a manner employed previously [287]. To remove the ridges from the image, we thresholded the image in Fourier space and applied a low-pass box filter. An inverse Fourier transform was then applied to render an image without any ridges. Next, the image was binarized using the Otsu thresholding method [227]. Using these binarized images, the cell shapes and centroids were captured using regionprops from the Python library scikit-image. To obtain cell tracks, the centroid data were processed using a tracking algorithm from the Python library, trackpy. An OF algorithm, previously described in detail [71, 284], was used to quantify the flux of actin polymerization within cells. This adapted algorithm is based on the Lucas-Kanade method [75]. The algorithm identifies the spatial fluorescence intensity gradient within a given image frame as well as the intensity gradient between consecutive image frames, the difference image. Combining these two gradients determines the optical flow. Optical flow reveals the velocities of regions of intensity in images, allowing us to account for both changes in intensity of actin and changes in location

4.4.7 Statistics

For comparisons between all groups, each measurement was averaged over the experimental time period for each cell, and the Whitney-Mann U test was performed. For all tests, P values < 0.01 were considered statistically significant. Data are represented as mean ± standard error of the mean, ** represents $P = 0.01$, *** represents $P = 0.001$.

Chapter 5: Multiscale sensing and synchronization with excitable mechanochemical waves

This chapter is adapted from work in preparation by Herr, Fourkas, Aranson, and Losert. Corey Herr designed the model, conducted the research, and drafted the initial manuscript. All authors contributed to the writing and editing of the manuscript.

5.1 Overview

Cell migration is pivotal for understanding essential biological processes, from morphogenesis and wound healing to tumor growth and metastasis. To perform these functions, migratory cells exhibit multiple dynamic phenotypes and behavioral switches, such as the epithelial-mesenchymal transition and embryogenesis. Despite intensive research, cell motility models struggle to capture the rich biological phenotypes crucial for unlocking fundamental mechanisms of cell behavior. Contemporary computational approaches often overlook the underlying cytoskeletal dynamics that drive the forces generated by cells, instead focusing solely on physical interactions. It is not yet well understood how intracellular cytoskeletal dynamics affect the emergent tissue-scale properties. Here, we apply a stochastic activator-inhibitor system, known as a cell excitable network, which has been validated as a model for the dynamics of the actin cytoskeleton. The excitable network is coupled to a multicellular phase-field model as a driver of motility. This model spans a range of scales, allowing cell interaction, long-distance wave propagation, and information exchange. We demonstrate that excitable intracellular mechanics, along with local physical interactions, can lead to emergent synchronization and sensing of the shape of the large-scale confinement. Our results provide insight into cell information processing and long-range sensing, which is pivotal for understanding biological functions and life-threatening pathologies.

5.2 Background

Cell and tissue motility is a broad research topic that encompasses multiple concepts, from biomechanics and organ engineering, to non-equilibrium physics and active matter [107, 321–324]. From a physics perspective, individual and collective cell migration is a self-organized, out-of-equilibrium biomechanical phenomenon powered by a sophisticated network of metabolic reactions [95, 107]. At the single-cell scale, the excitable dynamics of actin polymerization and depolymerization have been successfully modeled to capture the emergent behavior of mechanochemical waves and oscillations [63, 296, 325]. However, at the tissue scale, recent studies have demonstrated that a few well-characterized physical mechanisms are sufficient to create simple models that capture complex emergent behavior [326].

Oscillations and wave propagation are widely observed in biology at multiple scales [327]. Local actin oscillations occur within a cell on the order of minutes [328] and during embryogenesis. Tissues undergo coordinated contraction and expansion within similar periods[329–331]. At larger scales, mechanical waves propagate through tissues during wound-healing and tissue expansion [332–335]. Despite the prevalence of mechanical waves, the physical mechanisms governing their propagation and their role in biological processes are not well understood.

A variety of computational models have been devised to understand these complex tissue and cell population dynamics, including vertex, agent-based, and phase-field models [114, 336–340]. These deterministic physics-based models have been successful at capturing a variety of individual and population-level behaviors, including the unjamming transition and cell population expansion over time. Phase-field approaches realistically capture extracellular forces – such as friction, adhesion, and repulsion – but often use deterministic active polar gel models or coarse-grained polarization machinery [151, 152, 154, 341]. As a result, these models usually exclude the intracellular signaling processes that generate the forces driving motility.

In living cells, the migratory motion is tightly coupled to internal cytoskeletal dynamics, particularly the actin network. *In vivo*, actin dynamics depends on a complex network of regulatory proteins that are well-described by excitable systems formulation [54]. *In silico*, actin dynamics has been modeled in a wide range of cells with coupled activator-inhibitor networks called cell excitable systems [50, 54–56, 59–63] characterized by traveling waves and oscillations. These intracellular chemical waves control protrusive and contractile forces. In turn, in confluent tissues, each cell can mechanically interact with its neighbors. These contact interactions enable the propagation of mechanical signals throughout a tissue. As a result, local cell behavior can control the emergence of the population-scale oscillations and propagation of mechanical waves. Prior phase-field models have integrated variations of excitable networks into single-cell systems and shown that it produces behavior consistent with actin polymerization driving cell motion [141, 150]. However, to our knowledge, there is no model of collective behavior driven by two-dimensional, excitable dynamics.

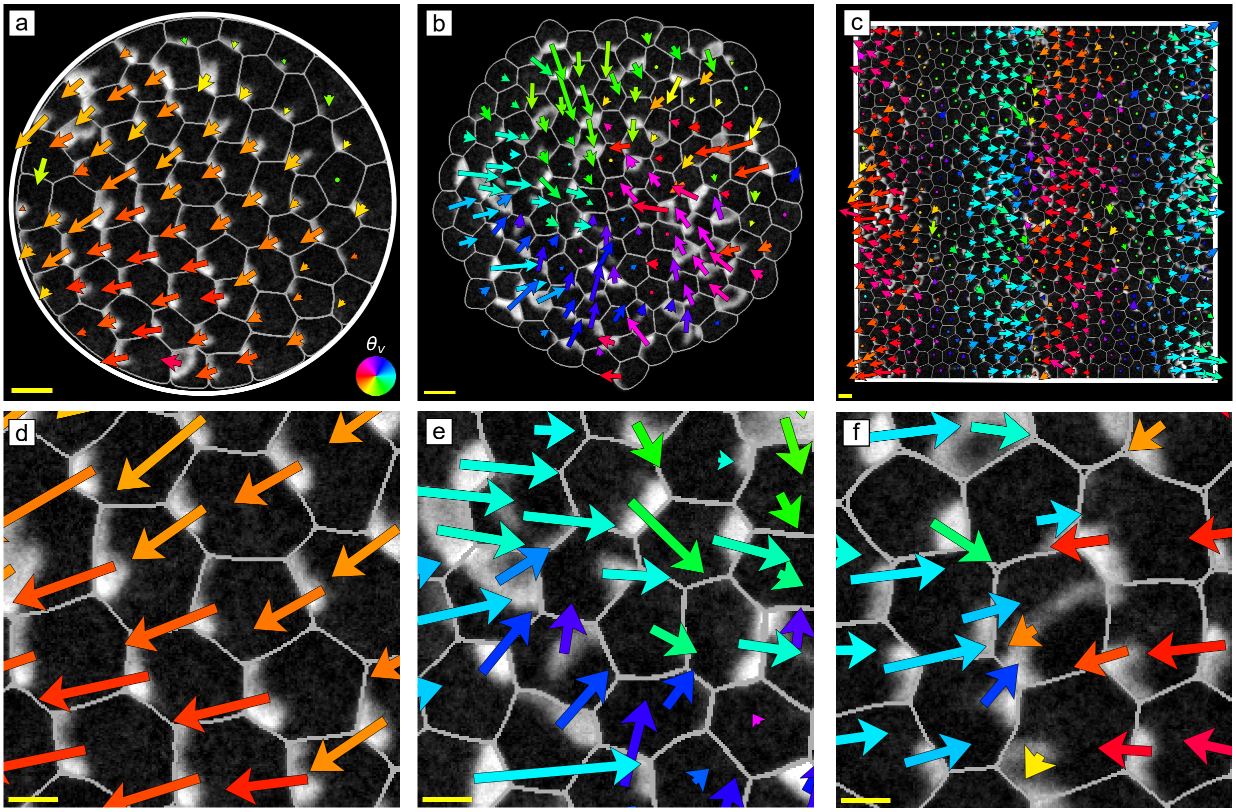

Figure 5.1: **Multicellular phase-field model with excitable waves**. **a-f** Individual cells are represented through phase-field order parameter ϕ_i. For visualization purposes, we show the membrane, denoted by $\phi_i = 0.5$ as a gray line, and the activator A as a grayscale overlay. The arrows are the velocity of the center-of-mass ($v_{\text{c.o.m}}$ where the color of the arrows denotes θ_v, the angle of $v_{\text{c.o.m}}$. If confinement is present, it is indicated by a bold white line. The upper row shows the full simulation domain, and the lower row depicts zoomed-in regions. **a,d** In circular confinement, cells synchronize their motion. **b,e** In free space with high adhesion, cells spontaneously pulsate. Displayed is a time instant where all the cells are contracting towards the center of the tissue. **c,f** In square confinement, the cells exhibit standing linear mechanical waves. This observation is supported by the bands of velocity $v_{\text{c.o.m}}$ that point in opposing directions. Scale bars are 10 μm in **a-c** and 5 μm in **d-f**

Here, we incorporate internal cytoskeletal dynamics into a multicellular phase-field model. We show that collective behavior emerges from physical contact interactions between excitable cells and does not require the exchange of chemical signals. This collective behavior manifests as traveling mechanical waves and global tissue synchronization, and is robust to noise and fluctuations of individual cell properties. The time and length scales of the dynamics are consistent with a wide range of experiments, from global actomyosin contraction in embryogenesis to collective rotations in epithelial cells.

Our results reveal that intracellular signaling and mechanical feedback provide a mechanism for the information propagation and multiscale emergent sensing in tissues. Local actin dynamics encodes information about immediate cellular environments, while emergent mechanical waves propagate this information and mediate local synchronization. This mechanochemical framework provides insight into how cells collectively interpret and respond to local and global environmental cues.

Results

We employ a two-dimensional, multicellular phase-field model coupled with an excitable system to simulate cellular dynamics as described by Eqs. (5.1)-(5.3). Each cell i is assigned a two-dimensional scalar field $\phi_i \in [0,1]$ such that $\phi_i = 0.5$ denotes the boundary of the cell with values above 0.5 being within the cell. We introduce an excitable system with two components: an activator with value A and an inhibitor with value R, which are restricted to move within the membrane. In our formulation, the activator A represents a generic upstream regulator of F-actin, such as Ras and Rap proteins. In contrast, the inhibitor R represents a generic inhibitory protein, such as coronin, which downregulates actin polymerization. These excitable dynamics create traveling activator waves that are arrested after a characteristic length scale when the inhibitor catches up. Finally, we introduce cell-cell interactions in the form of adhesion and steric repulsion.

In the framework of our computational model, Eqs. (5.1)-(5.3), a single cell can exhibit three motion phenotypes: stationary, locally exploratory, and ballistic. The stationary state supports short-time oscillations and small local protrusions but has zero average center-of-mass velocity. The locally exploratory state has larger-scale protrusions and a small average center-of-mass (c.o.m) velocity. In contrast, the ballistic regime shows persistent cell polarization and a sustained, large c.o.m. velocity. These three dynamical states represent the majority of cell behavior on flat surfaces in the absence of external stimuli.

5.2.1 Emergent synchronization and collective pulsations

A distinct collective dynamics emerges if multiple cells are simultaneously seeded in the integration domain. At high packing fractions (close to the confluency) and small cell-cell adhesion, we observe the onset of synchronization of subcellular excitable systems (Fig. 5.1a,d). Here, the activator center-of-mass (c.o.m.) synchronizes, and all the cells move in the same direction. This regime is manifested as a global wave propagating in the angular direction. At higher adhesion values, global contraction and expansion arise (Fig. 5.1b,e). Finally, we see mechanical waves that sense global geometry. If we introduce square confinement, square mechanical waves occur (Fig. 5.1c,f). This study explores the physical conditions that give rise to these distinct collective dynamics and their relationship to experimentally observed behaviors in multicellular systems. See Appendix Figures A.1-A.3 for snapshots over time of synchronized systems, pulsating waves, and square confinement respectively.

We studied multiple interacting cells with excitable dynamics. To enable continuous steric cell interaction, we implemented a confinement protocol. For circular confinement, this was done by introducing a phase-field for the confining wall with the form $\phi_{wall} = \frac{1}{2}(1+\tanh((r-R_{\text{wall}})/\varepsilon))$, which interacts with the cells through steric repulsion. There is evidence that cell-wall adhesion can affect escape dynamics [342]; however, we neglect this term for simplicity.

Notably, when cells with excitable dynamics are confined, they exhibit spontaneous emergent phase synchronization (Fig. 5.1a,d). Synchronization has recently been suggested to be necessary for the onset of collective motion in cell tissues and other forms of active matter [326, 343–346]. Individual cells exhibit oscillating spiral waves, consistent with actin oscillations in many cell types [50, 58, 59, 328], similar to that in Ref. [141]. As we simulate the system with variable cell sizes, we observe that phase synchronization remains robust to cell size variations. The robustness of the observed phenomenon suggests that phase synchronization is not merely a rotation at the natural frequency of the excitable system. Moreover, the synchronization occurs in the parameter range for locally exploratory, motile cells rather than stationary cells. The confinement stabilizes the rotating spiral wave state that would only be transient in isolation.

By creating a free adhesive cluster – through increasing adhesive forces and decreasing packing fraction – we observe self-localized collective pulsing states (Fig. 5.1b,e). The pulsations occur on the timescale of two minutes, in faithful agreement with collective actomyosin oscillations during embryogenesis [329–331]. Thus, using biologically relevant excitable dynamics parameters, our simulation displays pulsing periods consistent with *in vivo* observations.

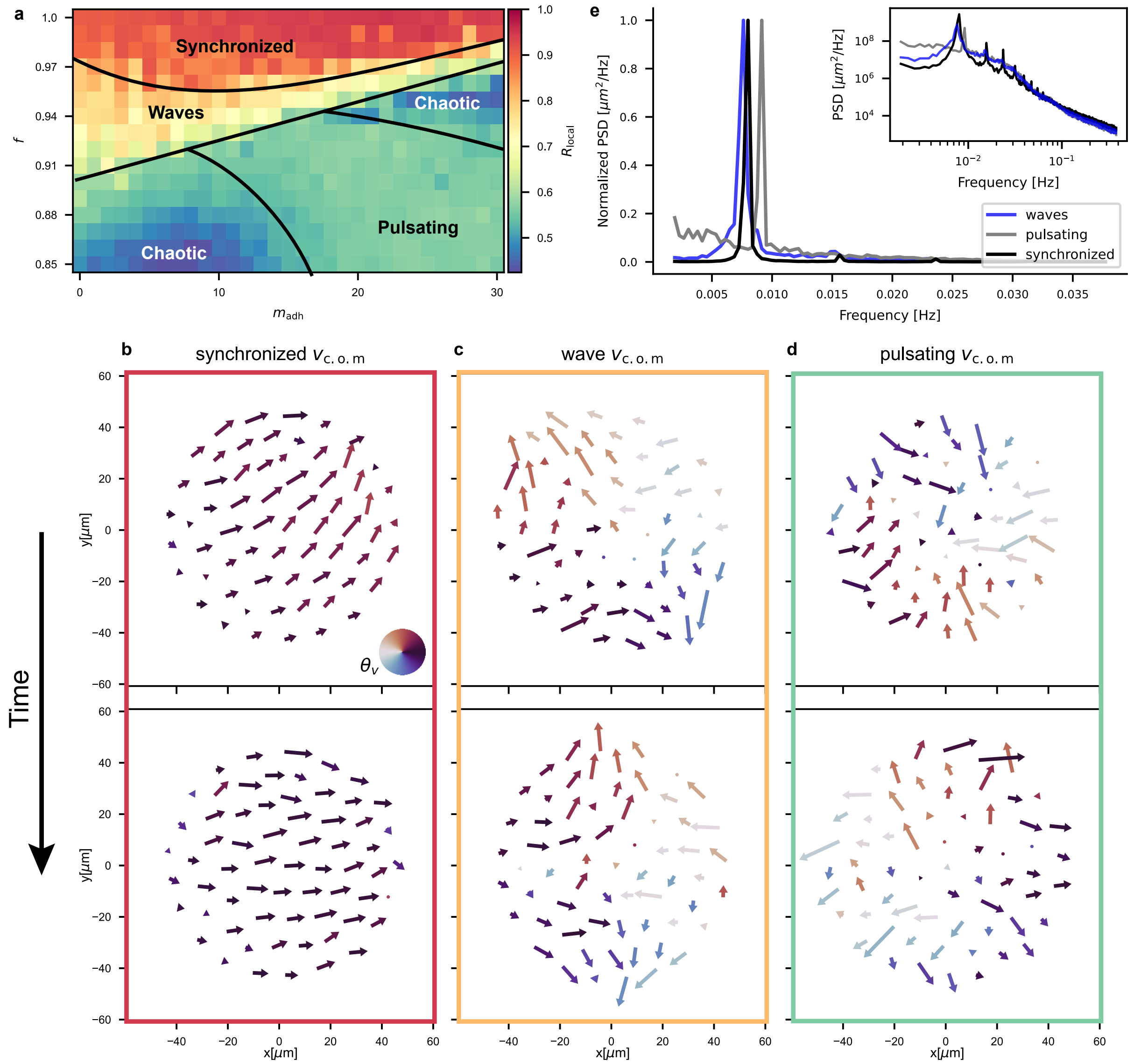

Figure 5.2: **Collective synchronized behavior in circular confinement depends on intercellular forces**. **a** A phase diagram showing the local Kuramoto order parameter (R_{local}), as a function of adhesive strength, m_{adh}, and packing fraction, f. Black lines are present as visual indicators for the transition between states. **b-d** Select vector plots of the center of mass velocity, $v_{\mathrm{c.o.m}}$, for the different behaviors. **b** Globally synchronized state rotates over time. **c** Waves of expansion and contraction rotate around the system. **d** Cells alternate between total contraction and expansion. **e** Power spectral density (PSD) of the polarization x component, p_x, for the wave, pulsating, and synchronized state, normalization was performed such that the peak is 1 (inset: log-log scale of the raw PSD). The pulsating state has a higher fundamental frequency than the synchronized state and a relatively high broadband noise level. The synchronized state displays higher harmonics with a much lower noise level.

To investigate the synchronization phenomenon quantitatively, we created a phase diagram by varying the intercellular forces: changing the packing fraction, f, and the adhesive strength, m_{adh} (Fig. 5.2a). For convenience, we define the polarization of the cell $\mathbf{p}$ as the vector that points from the phase field ϕ center of mass to the activator A center of mass for a given cell. We characterize the cell synchronization by the local Kuramoto order parameter R_{local} (see methods), which gives the alignment of a cell's polarization vector with the surrounding cells. Four distinct states arise with different levels of synchronization: complete synchronization (Fig. 5.2b), traveling waves of expansion (Fig. 5.2c), pulsating clusters (Fig. 5.2d), and chaotic motion. When varying the packing fraction f at a fixed value of the adhesion force m_{adh} of 10 pN/μm, we observe that the system transitions from chaotic motion to traveling contraction waves and finally becomes globally synchronized. This mechanism of local synchronization is seen in many physical systems [347] and is consistent with the expectation that a higher intercellular force leads to more local synchronization. Global synchronization occurs regardless of cell size (Fig. 5.3), and the natural frequency of the cell oscillations does not strongly depend on cell size, indicating that the oscillation is limited by the excitable parameters, not the mechanical ones.

To distinguish between pulsing and other states, we introduced the average power spectral density $\bar{P} = \sum_{i=0}^{N} |\hat{A}_{\text{c.o.m.},x}|^2$, where $\hat{A}$ denotes the fourier transform (Fig. 5.2e). For the phase-synchronized state, there is a high relative prominence at the natural frequency, the presence of higher harmonics, and a relatively low noise level. The pulsing state has one lower relative dominant peak at the natural frequency and a higher noise level. Finally, the chaotic state has no sharp peak present in the average power spectral density.

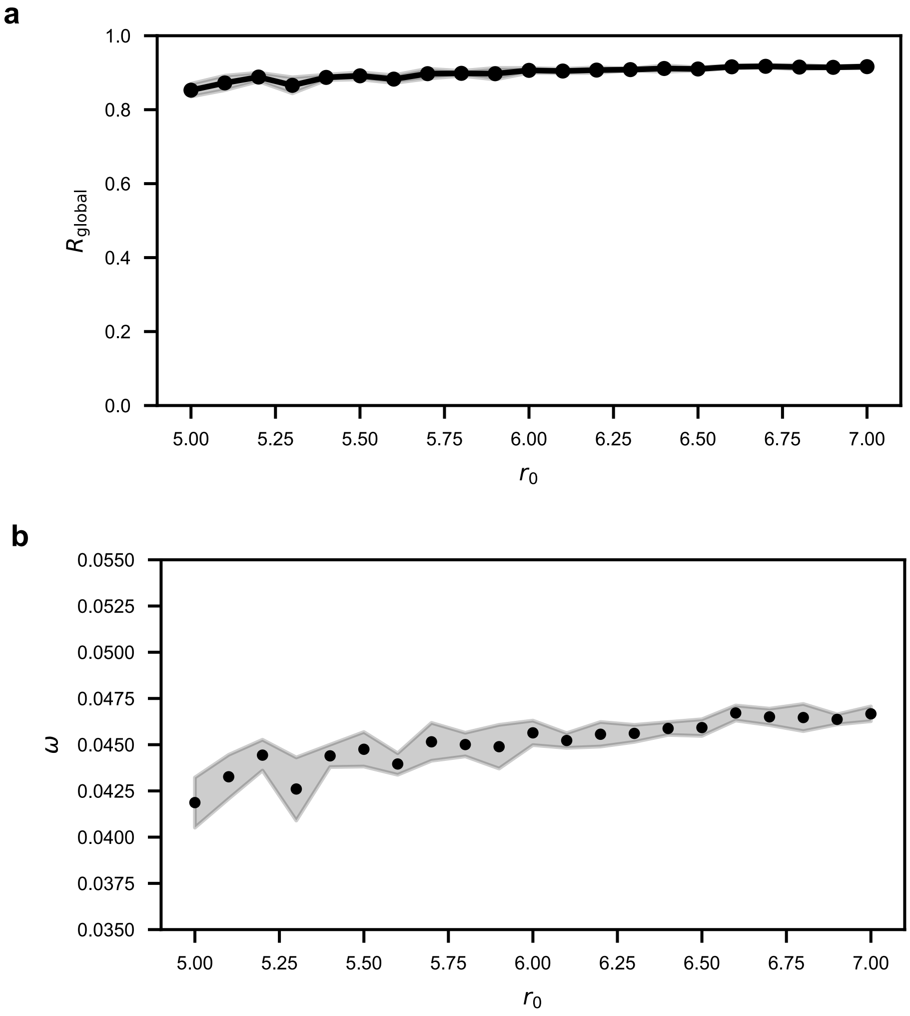

Figure 5.3: **Global synchronization doesn't depend on cell size**. **a** The global Kuramoto order parameter versus cell size. The system stays globally synchronized for the entire range of cell radii we are interested in. **b** The average frequency of the polarization vector versus cell size. The period only decreases by 7 seconds over a cell size change of 40%, indicating no strong size dependence on internal oscillation frequency.

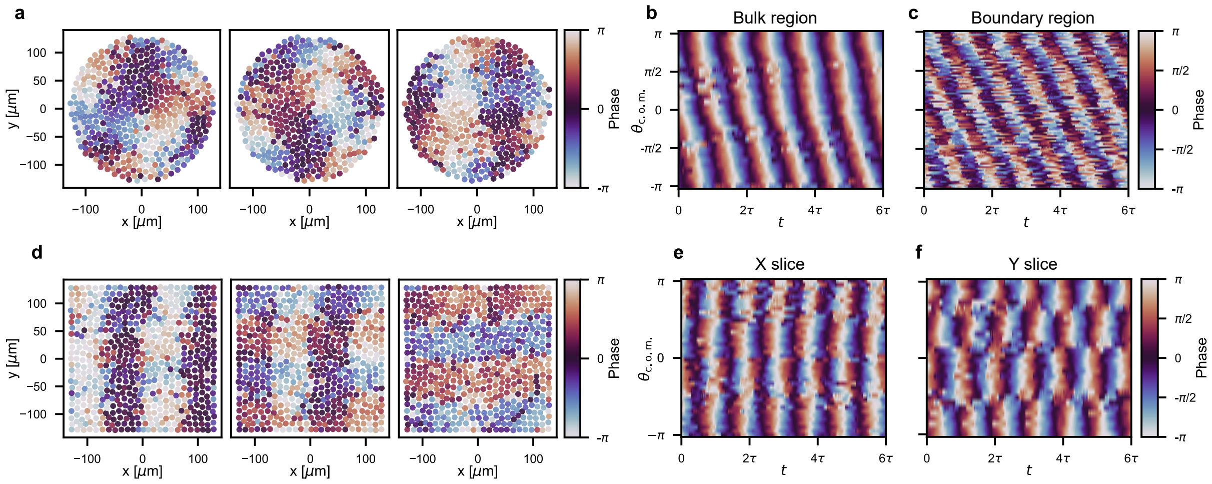

Figure 5.4: **Mechanical waves sense global geometry**. **a** Snapshots of the phase of each cell show two different traveling waves, one in the center and one at the boundary. **b,c** Kymographs of the activator phase vs c.o.m. position for the center region (**b**) and boundary region (**c**) of the system. This observation indicates that both sections have CCW mechanical phase waves with different periods. **d** Snapshots of the cell phase in square confinement show traveling phase waves. **e,f** Kymographs of the activator phase vs c.o.m. position in square confinement for an x-slice (**e**) and y-slice (**f**).

5.2.2 Mechanical waves sense global geometry

Mechanical waves have been observed in a variety of cell tissues [332, 333, 344, 348, 349]. Yet, their underlying mechanism remains unclear. As we increase the number of cells in our simulation, we begin observing mechanical waves propagating throughout the cell population (Fig. 5.4a). There is no chemical interaction between cells, so the only mechanism that can sustain waves are mechanical cell-cell interactions (adhesion and steric repulsion). We notice that these waves are dependent on the size and shape of the system.

In free space with high adhesion, two distinct types of traveling mechanical waves occur. These waves are easily seen through traveling shifts in the polarization phase. In the center of the tissue, we observe a counterclockwise rotating (CCW) wave. The system can also exhibit clockwise rotating waves in the same parameter regime. The center of mass of the activator,

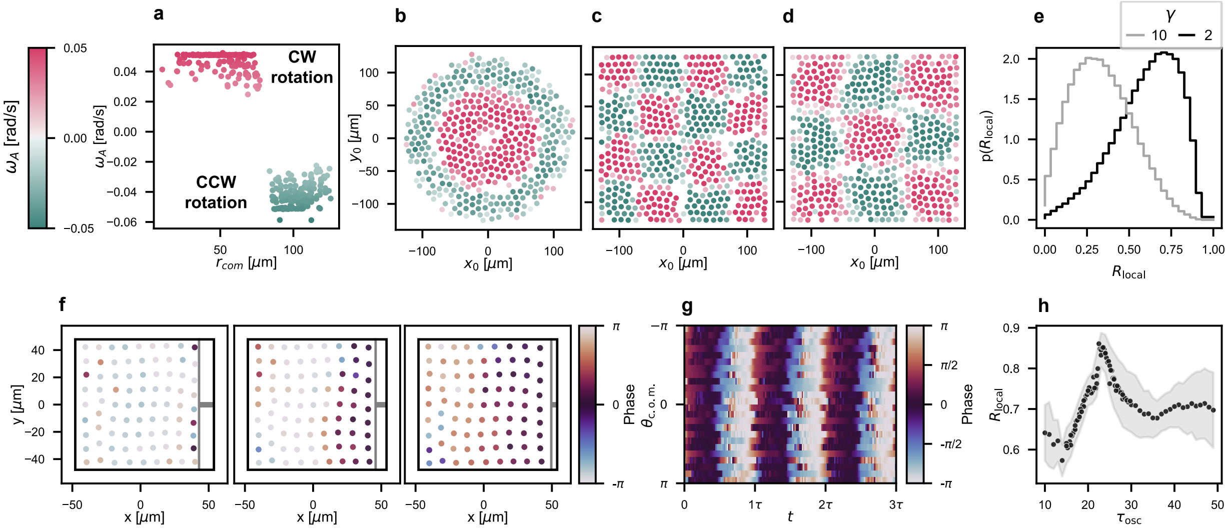

Figure 5.5: **Oscillation modes reflect boundary conditions**. **a** Cell oscillation frequency, ω_A, versus the c.o.m. position for Figure 5.4a. The oscillation frequency of individual cells depends on their position. The side axis shows the number of cells $N(\omega_A)$ with a given frequency. **b** The separation between boundary and bulk exhibits rotational symmetry. **c,d** Square oscillation patterns. By changing the membrane tension γ, we can adjust the size of the geometry sensing patterns. **c** For the tension $\gamma = 2.0$ (corresponding to the snapshots in Fig. 5.4d) we observe four nodes. **d** For the tension $\gamma = 2.5$ we observe three nodes. **e** Probability distributions of R_{local} for different membrane tensions. For low membrane tension ($\gamma = 2$), we observe that the majority of cells exhibit high synchronization, whereas for high membrane tension ($\gamma = 10$), most cells display lower synchronization. **f** Snapshots of cell phase when mechanical waves are externally imposed with period $\tau_{\text{osc}} = 25$ s. The black border indicates global confinement, and the gray line represents the periodic compression. **g** Observing an x-slice of the simulation in **f** over time shows that the cells synchronize to the frequency of the imposed mechanical wave. τ_{osc} is the oscillation period of the driving mechanical force. **h** Average local Kuramoto order parameter vs external driving frequency. The average value is plotted as points, and the standard deviation is denoted by the gray area. By varying the oscillation period of the driving mechanical force, we observe a peak in synchronization at a resonance frequency close to the natural oscillation frequency of a single cell.

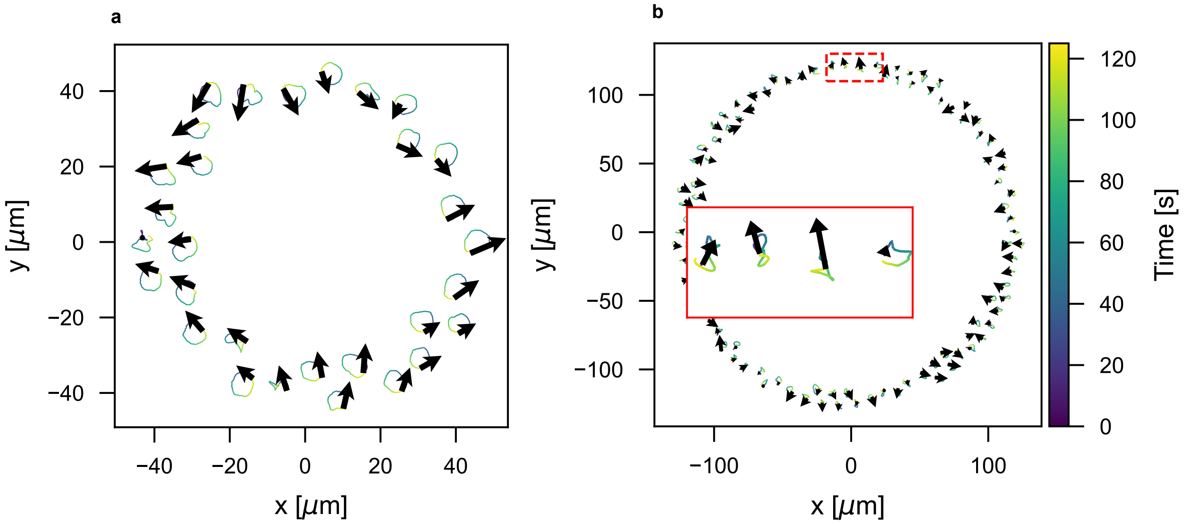

Figure 5.6: **Individual cell dynamics in free adhesive cluster**. **a,b** $A_{\mathrm{c.o.m}}$ dynamics over the course of one period for bulk (**a**) and boundary (**b**) cells. The color denotes the time of the observation, and the arrows represent the time derivative of the polarization at the beginning of the period. The cells in the bulk exhibit smooth orbits, while the cells in the boundary have periodic but more chaotic trajectories.

$A_{\text{c.o.m.}}$, of each cell follows a smooth CCW trajectory (see Fig 5.6), forming a traveling mechanical phase wave. This phase wave propagates at a period approximately equal to the natural period of individual cell oscillation (see Fig. 5.6).

At the tissue boundary, we observe very different dynamics. Instead of a smooth orbit, the activator A is strongly affected by noise. However, the activator at the c.o.m., $A_{\text{c.o.m.}}$ still traces out an orbit (Fig. 5.4b). Contrary to the bulk, the activator in the boundary cells $A_{\text{c.o.m.}}$ oscillates in the clockwise (CW) direction. Despite the local reversal, the global phase wave still travels CCW (Fig. 5.4c), but at a slower rate – roughly twice the period of a single cell's oscillation.

As shown in Fig. 5.4d, these mechanical waves are not restricted to circular geometries. In square confinement, the mechanical waves exhibit a standing-wave pattern. By investigating the kymographs of phase along X and Y slices of the system (Fig. 5.4e-f), we observe that the system exhibits traveling plane wave patterns.

The spatial pattern of oscillation frequencies is determined by the type of global geometry. In a circular cluster, the transition boundary between opposite-frequency oscillators is also circular (Fig. 5.5a-b); in square confinement, the transition boundary is square (Fig. 5.5c-d). This suggests that mechanical waves inform individual cells about their location within the tissue. The space between the bulk and the boundary features pulsing cells instead of rotating cells, resulting in distinct intercellular forces and, consequently, different dynamics near the boundary.

We can further justify that these waves are mechanical by examining how their properties respond to changes in the model's mechanical parameters. For a membrane tension of $\gamma = 2.0$, we observe a standing wave with five nodes (Fig. 5.5c). If we increase the membrane tension to $\gamma = 2.5$, we notice the wave shifts to a standing wave with only four nodes (Fig. 5.5d). Thus, we can tune the sensing of the geometry by altering the physical properties of the cell.

The mechanical wave propagation can be controlled by changing the mechanical coupling between cells. To study the effect of the waves, we chose to remove them by increasing the membrane tension γ. The cells are still able to exert physical forces and move as the tension γ increases. Figure 5.5e illustrates how the system supports high synchronization states at low tension γ and low synchronization states at high values of γ.

To complete the study of mechanical waves in this system, we applied a periodic driving force in the form of an oscillating wall with period τ_{osc} and amplitude of half the average cell radius. We choose the values of tension $\gamma = 4.0$ and the adhesion $m_{\text{adh}} = 30$ such that there is no synchronization for these conditions. Then, when we add an external driving force, the cells exhibit mechanical waves and synchronization (Fig. 5.5f,g). The multicellular system exhibits resonance (Fig. 5.5h). Below the resonance period, the cells are not able to synchronize. Above the resonance period, we observe that the cells synchronize whenever the wall is moving inward. The cells are somewhat sensitive to longer-term oscillations and insensitive to fast oscillations. These results show that mechanical waves are a crucial factor in mechanochemical synchronization.

5.2.3 Global scale rotations

It is well-known that epithelial cells in confinement exhibit global rotation [350, 351]. However, up to this point, we have considered only non-motile, confluent tissues. Our model can reproduce epithelial rotations in the fluid-like tissue state [352]. As we reduce substrate friction ξ, the system allows for both motile and flowing states, depending on the cellular forcing.

We observe the transition from jammed to motile state by varying the actin pushing strength,

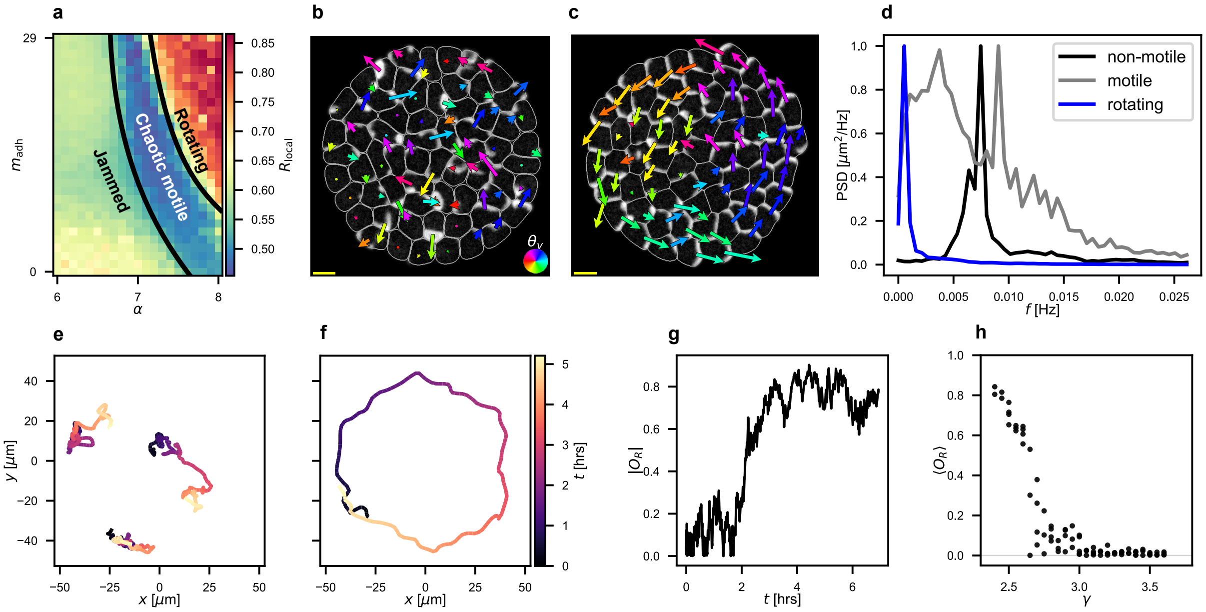

Figure 5.7: **Global rotations in circular confinement**. Confined cells with packing fraction $f = 0.85$ and friction $\xi = 4.0$ pN·s/μm^2 exhibit global rotations. **a** A phase diagram of the local Kuramoto order parameter R_{local} created by varying actin pushing strength (α) and adhesive strength (m_{adh}) shows the transition from jammed to collectively rotating states. A sudden dip in synchronization appears for the motile chaotic states, and then an increase in synchronization for collectively rotating states. **b,c** Snapshots illustrating the chaotic motile state (**b**) and global rotation (**c**). The gray outlines denote the phase field level $\phi = 0.5$, the grayscale shows the activator strength, and the arrows show the c.o.m velocity $v_{\mathrm{c.o.m}}$ with the color denoting the angle. Scale bars are 10 μm. **d** Normalized power spectral density (PSD) for non-motile, chaotic motile, and rotating states. The rotating states display a sharp peak at the low frequency of global oscillations. **e** Trajectories of selected cells from a chaotic motile system. **f** The trajectory of a selected cell from **c** shows that the period of the global rotation is $T \approx 5$ hours. **g** The order parameter over time demonstrates that collective motion emerges after two hours when $O_r \to -1$. **h** The time-averaged order parameter, $\langle O_{\mathrm{R}} \rangle$, versus membrane tension, γ, shows that the removal of mechanical interactions suppresses the global rotations. Scale bars are 10 μm in

α, and the adhesive strength, m_{rep}. There are two motile states shown in the phase diagram in Figure 5.7a: the chaotic-like state characterized by low local Kuramoto order parameter R_{local} and the collectively rotating state characterized by high order parameter R_{local}. These states arise from generic initial conditions. Systems in the chaotic motile regime exhibit non-zero displacement, but random polarization (Fig. 5.7b). Whereas in global rotation, cells display circular polarization (Fig. 5.7c). The power spectra (Fig. 5.7d) show that rotating states have low-frequency rotations, whereas the chaotic states have random spectra. Observing selected trajectories of the chaotic motile state (Fig. 5.7e) shows that cells remain relatively localized while displaying random walk behavior. See Appendix Figures A.4 & A.5 for snapshots over time of the chaotic motile and globally rotating states respectively.

The timescale of this global rotation has a period of $T \approx 5$ hours (Fig. 5.7f). This timescale is in agreement with experimental results showing that the period of global epithelial rotations in confinement varies between 5-8 hours [341, 349]. To characterize the collective rotations, we calculate the rotational order parameter O_R (see Methods). When $O_R = \pm 1$, the cells are moving collectively in the same direction around the circle. We find that the collective motion emerges at 2 hours when the order parameter approaches 1 (Fig. 5.7g).

We suppress mechanical waves from the system by increasing the tension of the membrane γ to test the impact of mechanical wave detection on an experimentally observed phenotype. Figure 5.7h shows the order parameter $O_{\text{R}} \to 0$ as the membrane tension γ increases. Thus, we hypothesize that mechanical waves facilitate the synchronization necessary for the onset of global rotation.

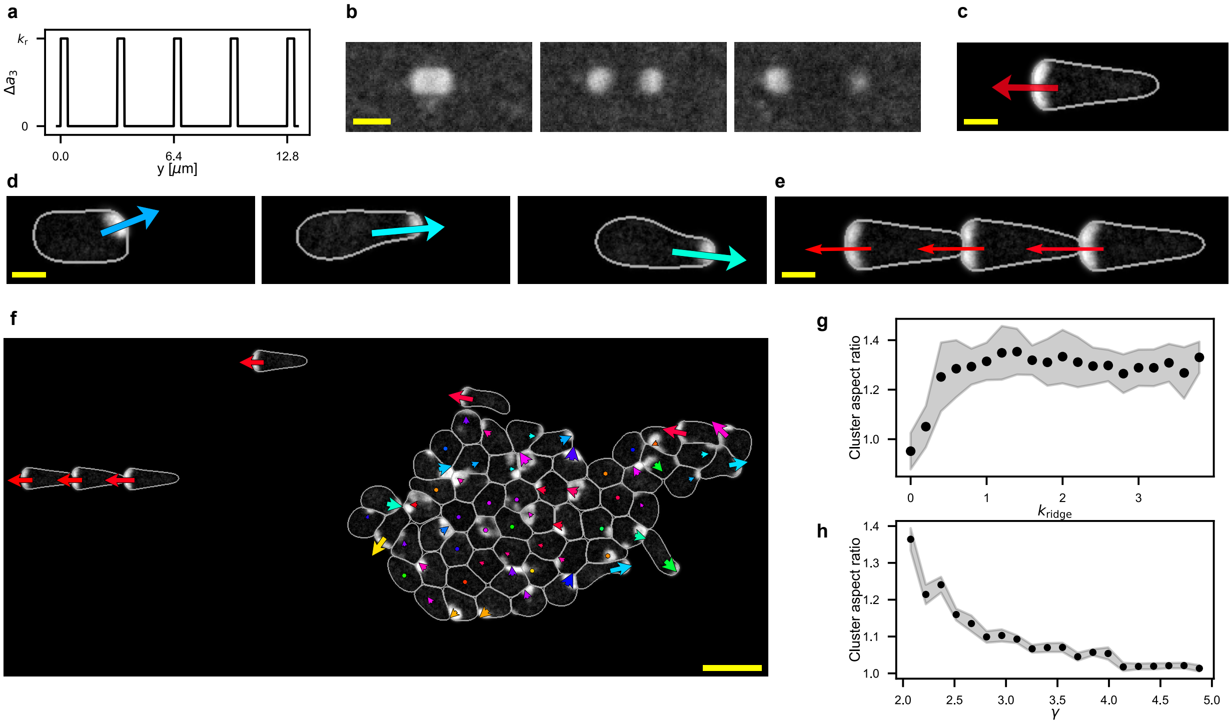

Figure 5.8: **Ridges cause cluster elongation and guided migration**. **a** The ridges are modeled by periodically changing the value of $a_3 = a_{3,0} + \Delta a_3$. **b** Activator waves on ridges prefer to move within the boundaries of one ridge. **c,d** Snapshots of single-cell motion on ridges. Cells on ridges exhibit two forms of guided motion, a stable locomoting cell (**c**) and oscillating protrusions (**d**). **e** When groups of cells are simulated on ridges, they form long adhesive chains. **f** For larger multicellular systems, we see elongation of a cluster of cells along the direction of the ridges. **g** The mean cluster aspect ratio (width of cluster divided by height of cluster) as a function of ridge strength. The cluster elongates more with stronger ridge strength. **h** As we remove mechanical interactions by increasing γ, the cluster stops sensing the ridges. For plots with error bars, the mean across ten trials is plotted as points, and the standard deviation is plotted as the shaded region.

5.2.4 Mechanical interactions promote cluster elongation on ridges

By using an experimentally verified model for actin dynamics, we can probe collective dynamics in controlled physical environments. Local topography has been shown to affect actin dynamics on a variety of scales [24, 25, 58]. Our 3D phase-field model [202] captured cell dynamics on subcellular topography by modeling the physical shape change of the boundary. Here, we instead study the impact of nanotopography on actin waves within the cell in a 2D setting.

Previous research has discovered that subcellular ridges modify the excitable system by lowering the activation threshold in the valley of the ridges [66]. We integrate this into our model by increasing the value of the excitability parameter a_3 in a periodic fashion. We used a square-wave profile, Eq. (5.4, as shown in Fig. 5.8a, in order to replicate the sharp edges of ridges in experiments [25]. This ridge pattern causes activator waves to nucleate preferentially in the valleys and travel along the direction of the ridges (Fig. 5.8b).

There are two different modes for single cells to travel on the ridges: (i) simple polarization with a flat cell front as seen in Fig. 5.8c; (ii) oscillating protrusions that travel along the ridges (Fig. 5.8d). Oscillating protrusions have been studied in previous phase field models [146, 353]. However, we reproduce them here with periodic ridges alone. When we simulate a cluster of cells on the ridges, we observe two significant qualitative effects. First, we observe that bidirectional guidance cues from the ridges promote the long-distance guidance of cell clusters (Fig. 5.8e). Second, the cells and the cluster elongate along the direction of the ridges (Fig. 5.8f), which is consistent with epithelial cells and amoeba *D. discoideum* experiments [354, 355]. This insight is relevant because it demonstrates that subcellular sensing of topography enables emergent global-scale mechanical responses. Increasing the strength of the ridge guidance causes marginally more cluster elongation. However, there appears to be a maximum possible cluster length (Fig. 5.8g). Figure 5.8h shows that the mechanical interactions are necessary for collective ridge sensing. As the membrane tension γ increases, the cluster loses its ability to elongate along the direction of the ridges.

These findings suggest that the strength of collective guidance is not only determined through subcellular sensing but also dependent upon mechanical interactions between cells. Compliant cells with lower membrane tension are able to coordinate their sensing of texture, causing the cluster as a whole to elongate. However, stiffer cells (which still exhibit guided direction on the ridges) are unable to collectively organize and elongate along the ridges. The same physical mechanism that permits synchronization and mechanical waves also leads to collective texture sensing within our model.

5.3 Discussion

We have demonstrated that the intracellular excitable dynamics, representing actin polymerization, generate emergent collective behavior and long-scale mechanosensing. Through intracellular chemical waves and intercellular physical interactions, the system demonstrates synchronization, pulsations, global rotations, and geometry sensing via mechanical waves.

Mechanical waves have been the subject of many recent experimental studies [332, 333, 344, 348, 349]. Our results suggest that single-cell excitable dynamics, when coupled mechanically through cell-cell interactions, are sufficient to produce coherent, global-scale mechanical waves. This finding provides a minimal physical mechanism for tissue-wide coordination, even in the absence of organism-scale chemical communication. Although long-range signaling (e.g., ERK waves in wound healing or cAMP signaling in *Dictyostelium discoideum*) plays a vital role *in vivo*, our results show that mechanical coupling can account for wave propagation over large distances.

These emergent mechanical waves provide a remarkable capacity for multiscale spatial sensing. At the system level, the mechanical waves in the system reflect a global geometry of the tissue, e.g., circular waves in circular tissues and linear waves in square confinement. At the local level, individual oscillations identify the position of the cell within the culture. For instance, boundary cells oscillate in the opposite direction to the bulk cells in circular cultures. When mechanical waves are inhibited by increasing membrane tension, local synchronization decreases, and when mechanical waves are imposed by a mechanical driving force, synchronization occurs. These observations suggest that mechanical waves play a crucial role in enforcing local synchronization. This hypothesis could be tested by treating cells with cyclodextrins, which are known to increase cell membrane tension [356], and observing if synchronization lapses.

Our model of mechanical waves is particularly significant in systems where synchronization is essential for proper function. A recent study on primary rat cardiomyocytes revealed that heart cells, which are both chemically and electrically excitable, can synchronize solely through mechanical forcing[357]. Coupled with the evidence of traveling mechanical waves in the heart [358, 359], our model offers insight into synchronization across various biological systems driven by excitability. It is noteworthy that the mechanical resonance frequency is on the order of minutes, which is significantly slower than naturally occurring mechanical rhythms, such as the heartbeat and natural breathing rate. By having natural mechanical oscillations occur off-resonance, the body may have evolved to prevent catastrophic mechanical interference.

We show that mechanical interactions are necessary for the observation of relevant motion phenotypes in our model. As the membrane tension increases, it inhibits synchronization, and the system is no longer able to initiate global rotations. The local excitable network can also sense subcellular features through local topography that induces changes in excitability. However, as membrane tension is increased, the cluster does not elongate on the ridges, indicating the importance of mechanical interactions in collective behavior.

Our results point to a fundamental role for coupled excitable dynamics in facilitating collective sensing and coordination. Cells can infer both their position within the tissue and the shape of their local microenvironment, as well as the broader geometric context, purely through mechanochemical feedback. This framework not only reproduces experimentally observed behaviors but also provides a physical explanation for how individual cells, with limited sensing range, can contribute to coherent multicellular dynamics on the scale of entire tissues.

Our findings suggest that synchronization and mechanical waves are essential factors for organizing collective behavior and guidance. Emerging studies have found that some cancer metastasis occurs with clusters of cells undergoing collective migration [360]. The current consensus often assumes that this collective behavior is dominated by leader-follower dynamics. However, we demonstrate that collective motion relies upon mechanical interaction and synchronization between cells. Therefore, one way to disrupt pathological collective behavior may be to target cell mechanical properties.

The multicellular excitable phase-field framework informs an emerging class of communicating active matter models [326, 345]. It enables long-range communication via mechanical waves and local signal processing through excitable dynamics. We speculate that long-range communication and decision-making processes underlie the robust self-organization present in biological systems.

5.4 Methods

Table 5.1: Model Parameters

Parameter	**Description**	**Value**
γ	Surface tension	2.5 pN μm
ε	Interface width	1.5 μm
B	Soft area constraint	15 pN/μm^2
ξ	Friction coefficient	5 pN s/μm^2
α	Actin pushing strength	5.5 pN/μM
a_1	Activator degradation rate	1 s^{-1}
a_2	Degradation rate from inhibitor	1 μM^{-1}s^{-1}
a_3	Activation rate	10 s^{-1}
a_4	Activation threshold	1 μM
a_5	Basal activation rate	0.1 s^{-1}
c_1	Inhibitor degradation rate	0.1 s^{-1}
c_2	Inhibitor activation rate	3 s^{-1}
D_A	Activator diffusion coefficient	0.5 μm^2/s
D_R	Inhibitor diffusion coefficient	0.5 μm^2/s
σ	Noise intensity	0.1 μM^2/μm^2/s
Δt	Time step	0.001 s
m_{adh}	Adhesion strength	0-30 pNμm
m_{rep}	Repulsive strength	0-30 pN/μm
L	Contraction normalization	37.5

5.4.1 Phase-field model with excitable network

The multicellular interactions are cast as follows:

$$\begin{aligned} \xi \frac{\partial \phi_i}{\partial t} = \quad & \gamma(\nabla^2 \phi - G'(\phi)/\varepsilon^2) - (B(\textstyle\int \phi \mathrm{d}^2\mathbf{r} - S_{i,0}) + \alpha A \phi)|\nabla \phi| \\ & + \sum_{j \neq i} m_{\mathrm{rep}} \phi_i \phi_j^2 + \sum_{j \neq i} m_{\mathrm{adh}} \frac{\nabla \phi_i \cdot \nabla \phi_j}{\sqrt{1 + L|\nabla \phi_i||\nabla \phi_j|}} \end{aligned} \tag{5.1}$$

$$\frac{\partial(A\phi)}{\partial t} = D_A\nabla\cdot(\phi\nabla A) + \phi\left[-(a_1 + a_2R)A + \frac{a_3A^2}{a_4^2 + A^2}(a_5 - A) + \eta(t)\right] \tag{5.2}$$

$$\frac{\partial(R\phi)}{\partial t} = D_R\nabla\cdot(\phi\nabla R) + \phi(\beta A - R)/\tau \tag{5.3}$$

This is a non-equilibrium system, driven through excitable dynamics shown in Eqs. (5.2), and (5.3). This model of excitability is widely used to model actin polymerization via signaling networks [54, 56], and a similar model has previously been integrated into a single-cell phase-field model by Cao *et al.* [150]. The membrane of the cell is represented by a phase-field order parameter ϕ_i. The motility dynamics are implemented through a coupled activator-inhibitor network, with activator A and inhibitor R.

The dynamics of the boundary for a given cell ϕ_i is given by Eqn. 5.1. The first term gives the membrane tension γ of a cell and is derived from the Cahn-Hilliard free energy. $G(\phi)$ is the double well potential given by $G(\phi) = 18\phi^2(1-\phi)^2$ that prevents the cell from splitting apart. There is a soft area constraint given by $B(\int \phi \mathrm{dV} - S_0)$ where $S_{i,0}$ is the initial area of cell i.

The key interaction between intracellular dynamics and cell mechanics occurs through the coupling of the activator to the cell boundary through the term $\alpha A\phi$. Regions of high activator concentration locally promote protrusion by modifying the cell's active force term in the phase-field equation (Eq. (5.1)). In effect, this coupling allows localized actin activity to generate deformations and motility, creating a feedback loop where internal signaling controls cell shape, and changes in shape influence local actin dynamics.

We introduce multicellular interactions through established interaction terms. The repulsion force term is the standard square term used in many eirlier studies [151, 152, 154, 361]. The adhesion term is also of the standard form, but we use a regularization term that was initially introduced by Löber *et al.* [151] to add stability to high gradient regions. More physically realistic forms of these interactions have been studied in previous studies [152]. However, there are many different possible choices for other cell types. We chose to keep a generic model that could be extended in future studies.

The dynamics for the coupled activator-inhibitor system are given by Eqs. (5.2) and (5.3) respectively. In order to effectively restrict the chemical signal to the cell's interior, we solve the dynamical system for $A\phi$ and $R\phi$. The first terms on the right-hand side of the equation allow diffusion with no flux across the cell boundary. The remainder of the terms are chosen in agreement with prior models of actin regulatory proteins [56].

For the ridge simulations, we introduced a square perturbation to the activation rate a_3 via Eq. (5.4)

$$a_3 = a_{3,0} + k_{\text{ridge}}[1 + \text{sgn}(\sin(x/x0))] \tag{5.4}$$

The model parameters can be found in Table 5.1.

5.4.2 Kuramoto order parameter

We use the local Kuramoto order parameter given by Eqn. 5.5 where $\theta_{\mathbf{p}}$ is the angle of the polarization vector that points from the cell center of mass to the activator center of mass, and d_t is the cutoff distance above which two cells will not be compared. $R_{\text{local}} = 1$ when local cells have completely aligned polarization vectors and $R_{\text{local}} = 0$ when there are uniformly distributed polarization vectors.

$$R_{\text{local}} = \left\langle \left| \frac{1}{n} \sum_{|\mathbf{r}_j - \mathbf{r}_k| \leq d_{\text{t}}} e^{i\theta_{\mathbf{p}}} \right| \right\rangle_j \tag{5.5}$$

For confluent cell sheets, we chose d_t as twice the radius of the cell in order to only account for the nearest neighbors; however, changing this parameter to include more surrounding cells did not dramatically change the result. The most extreme case is increasing d_t to infinity, which retrieves the classic Kuramoto order parameter. In this case, we only achieve high values for globally synchronized cases.

5.4.3 Rotational order parameter

To quantify collective rotations, we use the rotational order parameter given by Eqn. 5.6 where $\hat{\mathbf{r}}_i$ is the unit vector pointing from the center of the confinement to the cell's center of mass and $\hat{\mathbf{v}}_i$ is the unit vector pointing in the direction of the cell's center of mass velocity.

$$O_R = \frac{1}{N} \sum_{i=0}^{N} \hat{\mathbf{r}}_i \times \hat{\mathbf{v}}_i \tag{5.6}$$

$O_R \in [-1, 1]$ gives the degree of collective rotation. $O_R = \pm 1$ corresponds to states where all cells are traveling counterclockwise/clockwise around the confinement. $O_R = 0$ corresponds to random motion.

Chapter 6: Summary and future directions

6.1 Summary

Cells interact with their surroundings through a combination of sensing, transduction, and response. Traditionally, biologists have focused on how cells sense chemical signals and how the transduction mechanisms change cell dynamics. Now, growing evidence suggests that cells are sensing their physical surroundings in addition to chemical cues. Additionally, due to historical limitations in microscopy and experiments, much of cell biology has focused on the 2D analysis of cells on flat surfaces. This differs dramatically from the complex, 3D ECM that cells experience *in vivo*. To address this, I employed phase-field modeling to gain insight into the physical forces generated during cell motion, and conducted experiments to examine cellular responses to environmental cues. This research reveals the interplay between cells and their physical environment, highlighting the importance of mechanical forces across multiple scales – from subcellular nanotopography to global geometric confinement.

Actin dynamics plays a central part in this dissertation, linking cellular sensing, response, and collective behavior. Whether responding to hormonal cues, navigating nanotopographic features, or coordinating within multicellular assemblies, the cytoskeletal machinery functions as a core integrator of physical and chemical information. In single-cell systems, I observed how changes in actin polymerization relate to the formation of protrusions, guidance, and motility. In multicellular systems, the excitable nature of actin dynamics gives rise to emergent phenomena such as synchronization and mechanical wave propagation. Across both experimental and modeling studies, actin emerges not only as a passive indicator of cell state but as an active mediator of physical sensing and decision-making. This underscores its critical role as a biophysical and biochemical nexus that connects subcellular activity to larger-scale coordination and environmental response.

I first investigated the impact of disease-related chemical signals on actin-driven protrusion dynamics. In Chapter 2, I studied the effect of disease or dysfunction on actin dynamics and morphology. By examining endometriosis, characterized by the abnormal migration of cells in response to estrogen, I probed how pathology and chemical cues alter cellular behavior within their physical environment. Using 12Z cells as a model for endometriosis, I focused on the influence of E2 on cell morphology and actin dynamics. It has been established that endometriotic cells become more invasive in the presence of estrogens [158, 159, 161]. Endometriotic lesions even emit estrogens, resulting in a feedback loop of disorder [160]. Employing 3D lattice light sheet microscopy, I captured detailed observations of cell shape and actin behavior, revealing how these cells navigate their surroundings at scales of 1-10 μm. After a 24-hour estradiol treatment, the cells demonstrated a significant increase in protrusion size and a more disordered pattern of actin polymerization, suggesting that exposure to estrogen enhances the protrusiveness and potential invasiveness of endometriotic cells. Although centered on a chemical signal, this study highlights the impact such signals have on the physical interactions between cells and their environment. Because protrusions are tied to cellular sensing, the increase in protrusions observed in 12Z would likely lead to more mechanosensing of the ECM *in vivo*. Additionally, because estrogens normally increase the invasiveness of cells, this work supports the common understanding that local changes in cell morphology can lead to dramatic large-scale migration. This work not only advances our understanding of cellular dynamics in pathological contexts but also underscores the relationship between chemical signals and the physical forces that shape cellular behavior.

At the subcellular level, curvature is sensed at a small scale via the BAR protein domains, which in turn lead to larger signaling cascades that affect actin dynamics. However, the effects of larger-scale curvature can not be explained through protein dynamics alone [69]. Engineered nanotopography has been a key player in studying the changes in actin cytoskeleton dynamics that result from local curvature changes[23–25]. Despite this, many models of motion on nanotopography do not account for physical deformations of the membrane. In Chapter 3, I explored how local curvature changes, introduced through asymmetric nanotopography, bias cell migration. I showed that asymmetric membrane deformations on the scale of 1 μm are enough to reproduce the full range of cell motions observed experimentally. This suggests that the physical deformation of the membrane may play a greater role in actin dynamics than previously thought. Instead of simply recruiting BAR protein domains, it is possible that altered diffusion on a curved membrane results in different migration phenotypes.

I then linked the 3D phase-field model to experimental results of *D. discoideum* traveling on the same asymmetric sawteeth. My model predicts that there is a threshold sawtooth height above which high velocity cells will be preferentially guided down the sawteeth. After a reanalysis of the *D. discoideum* data, I found that indeed there is a threshold sawtooth height where high velocity cells move preferentially down the sawteeth. Cells are able to move in any direction, likely due to internal polarization, but high-velocity cells tend to move down the taller sawteeth. This result suggests that the phase-field model could be used to help discover surfaces that selectively control cell motion.

Cell motility *in vivo* involves extensive interaction with the ECM, which provides both physical and chemical cues. In Chapter 4, I studied how the chemical cues of the ECM interact with the physical cues. To achieve this, I analyzed the motion of epithelial cells on nanoridges coated with collagen IV, a fundamental protein of the basement membrane ECM. Through the use of cell shape analysis, I found that cells on collagen-coated surfaces tend to elongate earlier, whereas, after an extended period, most cells become elongated and aligned with the nanoridges. Trajectory analysis shows that increasing collagen IV concentration results in higher speeds. Additionally, higher collagen concentration leads to more alignment of actin optical flow with the nanoridge direction. This indicates an interplay between chemical signaling and physical cues in guiding actin dynamics. We observed three main motile cell trajectories: straight, turning, and random motion. Within these three motile phenotypes, the actin guidance was unchanged. Regardless of the direction the cell was moving, the actin polymerized along the direction of the ridges. This decoupling of guidance direction and actin flow implies that another mechanism, in addition to actin polymerization, is responsible for directional guidance in the presence of collagen IV. One potential mechanism for this guided migration is integrin-induced focal adhesions, which are caused by transmembrane ECM binding of integrins. However, actin sensing of the topography was only affected by the

Finally, I moved to tissue-scale physical sensing in Chapter 5 with the introduction of a multicellular phase-field model. Single-cell experiments, like the ones conducted in Chapters 4&2, are fantastic for deeply understanding intracellular signaling dynamics and individual cell forces. However, most complex life exists as multicellular organisms, composed of ECM and confluent tissues of various cell types. To determine if individual cellular dynamics are sufficient to drive realistic collective behavior, I integrated an excitable system model of the cytoskeleton into a multicellular phase field. This model simulates actin dynamics on the submicron scale, local physical interactions on the micron scale, and global geometry on the millimeter scale. The model exhibits emergent dynamics across multiple time and length scales, including synchronization, pulsation, global rotation, and traveling mechanical waves.

Mechanical waves exhibit the capability to sense global geometry and position. These mechanical waves have been observed in many other multicellular systems [332–335], though their causes remain unclear. Simulating these systems in different geometries revealed mechanical waves that adapt to boundary conditions; circular confinement leads to circular waves, and square confinement leads to square waves. Furthermore, in free adhesive clusters, cells within a wave change oscillation direction based on their proximity to the boundary, indicating that waves aid in positional sensing. My research showed that these waves serve as a mechanism for local synchronization. Notably, when an external driving force is applied, oscillations of the actin cytoskeleton become more synchronized and exhibit resonance.

Although I consider chemical excitability, this model provides insight into cells with other forms of excitability, such as cardiac cells. A recent study by Ido *et al.* showed that primary myocardial cells were able to synchronize to the motion of a probe through mechanical coupling only. Additional support for this hypothesis is shown by traveling mechanical waves seen in heart tissues[362, 363], albeit on a faster timescale because the underlying excitability is electrical. My model shows that the excitable systems underlying many cellular behaviors, especially actin dynamics, lead to the emergence of traveling waves. These results suggest that coupled excitable systems play a fundamental role in enabling collective physical sensing and coordination.

Taken together, the results from this dissertation show that the physical environment has a profound impact on cellular dynamics at multiple scales. Experimentally, cells interact with their physical environment through rearrangements of the actin cytoskeleton, which is in turn influenced by the surrounding physical environment. Phase-field modeling offers a method for simulating mechanochemical interactions, demonstrating that excitable chemical dynamics couple with the cell's mechanical boundary to sense and respond to physical cues. The insights gained from this research underscore the importance of considering physical aspects of cellular environments, paving the way for advancements in understanding cell behavior in complex biological systems. By demonstrating how cells interpret and respond to the physical structure of their environment, this work deepens our understanding of mechanobiology. It opens new avenues for investigating processes such as tissue morphogenesis, wound healing, and cancer metastasis, where cell guidance and invasion are governed by tightly coupled chemical and physical cues.

6.2 Future directions

6.2.1 Phase-field model extensions

One goal of modeling biological systems is to find the minimal set of requirements necessary to reproduce cellular function. Cells exhibit highly nonlinear, multidimensional dynamics that depend on many system inputs and outputs; however, choosing a proper model can help us determine and drive those dynamics. The phase-field models presented in Chapters 3&5 choose to model separate important systems inside the cell. In Chapter 3, I used a 3D model to study the effect of local curvature changes on cell function. In Chapter 5, I used a 2D multicellular model with more realistic chemical dynamics to study emergent sensing in cell populations. The models were limited because the 3D model used a coarse-grained model of actomyosin dynamics, while the 2D model doesn't account for the true 3D environment.

First, I propose the straightforward extension of combining my two models, creating a 3D multicellular model with realistic chemical dynamics. In my current 2D model, chemical signaling is bound to the entire phase field. In moving to 3D, we must now account for the fact that the chemical signals that regulate actin dynamics are membrane-bound [54, 56]. Prior phase-field modeling work has restricted chemical dynamics to the 1D boundary of a cell [361] by coupling the chemical dynamics to $\nabla\phi$ rather than simply to ϕ. This extends easily into 3D; the only additional consideration required is restricting actin polymerization far from the substrate. For cells on flat surfaces, which are typically quite flat, this model should produce similar results to the current 2D model. However, this extension could allow us to model novel 3D dynamics such as embryogenesis and cancer metastasis, which are inherently three-dimensional.

Cells *in vivo* are constantly remodeling the surrounding ECM. As I showed in Chapter 4, both the chemical and physical surroundings affect cell behavior. In fact, interactions between focal adhesions and the ECM are responsible for many intracellular signaling cascades [364]. To my knowledge, no currently existing phase-field models attempt to tackle either physical or chemical interactions with the ECM. The simplest approach to ECM modeling is through continuum dynamics. Specifically, the ECM can be modeled as a vector field, where the orientation is defined by the direction of the field and the concentration is represented by the magnitude of the field. When coupled with ϕ, this could efficiently model interactions with small-scale ECM alignment and larger-scale porosity. Another possible approach would be modeling the ECM as a deformable phase field itself, which would account for the discrete nature of ECM fibers. This would be significantly more computationally expensive, but it would potentially give better mechanistic insight into cell-ECM interactions.

The excitable phase-field model from Chapter 5 was not able to produce the longer timescale radial waves in fibroblasts during tissue expansion observed by Serra-Picamel *et al.* [332]. I believe that this is due to the lack of cell division in my model. Cell division is an essential part of tissue expansion [365], and a 1D model of mechanical waves in tissues was only able to produce waves through the inclusion of cell division [366]. Prior models have implemented cell division through simulating spindle position [367] or using experimental knowledge of the division plane [368], but none take into account the chemical signaling within the cell. The significant shift in actin dynamics observed during cell division [369] presents a promising avenue for further investigation into the role of mechanical forces in tissues.

When studying division, another question that may arise is how the nucleus affects cell dynamics. Of course, during division in most cells, the nuclear membrane dissolves. But, during cell migration, the nucleus is one of the most significant contributing factors to cell drag and resistance [142, 370]. Two major forms of cell migration, lobopodial and mesenchymal, are dominated by interactions between the nucleus and the physical environment [82]. The centrosome, which handles the structure of microtubules throughout the cell, is also usually co-located with the nucleus. The phase-field model can be trivially extended to include nuclear dynamics by introducing another phase-field for the nucleus. The nucleus phase field would be coupled to the cytosol phase field and held in place with a tensile force representing the intermediate filaments.

Combining these proposed directions leads us to the field of early developmental biology. Embryogenesis is a challenging scenario to model at single-cell resolution. The position and number of cells in the system change rapidly and respond to mechanical and chemical cues. In early embryonic development, the embryo exists as a single sheet of cells. Then, the embryo undergoes three-dimensional folding, exerting large-scale forces that initiate differentiation and establish the foundational body axes. This behavior is challenging to simulate at the single-cell level because not only are there multiple scales of physical forces, but there are also chemical signals that span the entire embryo. Phase-field modeling has been adapted to study embryogenesis in *C. elegans* [368]; however, gastrulation in this organism has relatively mild forces and minor reorganization [371]. The phase-field approach offers a powerful mechanism for modeling embryogenesis because of the dense 3D mesh, which gives necessary chemical and physical information. Additionally, cells are free to move with respect to one another, allowing the freedom required for large-scale spatial rearrangements that happen in embryogenesis. Experiments provide accurate measurements of forces experienced by embryos during gastrulation and epithelial folding [372]. These forces could be integrated into a phase-field model as a boundary condition to study large-scale reorganization.

6.2.2 Closing the loop between phase field models and experiments

The phase-field results I demonstrated in Chapters 3&5 were both able to reproduce dynamics on biologically relevant time scales without fitting to any real-life systems. I believe the phase field model offers tremendous ability to fit biological data quantitatively. One often-overlooked biological phenomenon is the heterogeneity of physical parameters among cells. For instance, it is well known that cell size varies throughout tissues [373], but many multicellular models assume uniform size. Likewise, many physical models of cell motility assume constant parameters across all cells. One potential future direction is allowing a distribution of parameter ranges and fitting the model to experimental data to learn how heterogeneous system parameters are.

Learning cell dynamics is a tricky task due to the origin of heterogeneity in biological systems. There are multiple sources of noise that could interrupt the ability to fit the range of internal cell parameters. For example, cell dynamics are non-stationary, meaning that the fit could be disrupted by changing cell parameters. Likewise, the changes in behavior could come from unintended variability in the environment or other experimental protocols. These challenges require large datasets of long-time cell behavior to ensure that the dynamical system remains stationary for part of the simulation. One possible fitting method is to generate an experimental distribution of a specific observable behavior, such as cell protrusion rate, and then perform Monte Carlo simulations to select parameter values that generate comparable simulated distributions [374].

On the experimental side, I would like to specifically fit the excitable cell phase-field model to the motion of fibroblasts in confinement. Mechanical waves have been seen in mostly fibroblast populations [332, 333]. But, most confinement studies are done on epithelial cells [341, 342]. My model predicts that linear mechanical waves should be present in jammed fibroblasts in square confinement. However, this motion may be challenging to observe without also imaging the actin dynamics of the cell. To my knowledge, no existing large-scale confinement assays image actin dynamics. This provides a promising future direction for studies of mechanical waves in tissues.

The multicellular model discussed in Section 1.2 gives exciting new ways to test drug based hypotheses. The model allows us to link physical concentrations of proteins inside the cell to model parameters. For example, as shown in Table 5.1, the activation threshold is 1 μM of coronin. The size of this activation threshold can be decreased by drugs such as Jasplakinolide [55], which would cause the cells to become more active. We could use the drug treatment to test the model prediction of higher cell activity leading to synchronization and global rotations. Drugs such as latrunculin and cytochalacin can be used to inhibit polymerization [66], which should lead to collective desynchronization of cells. Finally, we may be able to quantitatively link fluorescent intensity in experimental data to real chemical concentrations inside the cell by fitting the model to experimental data.

6.2.3 Enabling quantitative linking between models and experiments in 3D

In Chapter 2, I analyzed the morphology and actin dynamics of 12Z cells in 2D. This data was originally collected on a 3D lattice light sheet microscope, and analysis in 3D proved to be a formidable task. Because we did not stain all of the cells with a membrane marker, we instead used the actin stain to locate the boundary. As long as the cells are not blebbing, the actin cortex should be colocalized with the cell membrane. To effectively use this data in 3D, we must first threshold the actin channel and then extract a 3D mesh of the membrane of the cell. Next, we would need to determine how the actin was flowing on that mesh. This has been done previously through spherical harmonic analysis [375].

The primary challenge with 3D datasets stems from their higher dimensionality. Larger datasets require larger computational efforts and more sophisticated analysis approaches. We did not attempt 3D optical flow due to time constraints; however, it could provide insight into the vertical motion of ruffles observed in the 12Z data. Finally, traditional morphological parameters such as circularity and solidity do not extend easily to 3D environments when cells take non-elliptical shapes. Instead, we could use principal component analysis to obtain the variation from a standard shape. This would require significantly more data in order to produce a valid principal mode. Although the challenges are great, extending the analysis to 3D could elucidate more differences between endometriotic cells treated with estrogen. Ultimately, 3D cell modeling allows us to make predictions about cell behavior and validate them experimentally, which could improve experimental efforts by reducing the search space of biological experiments. I believe this is a necessity in biophysics research due to the sheer complexity of 3D cell dynamics. The future of biophysics is bright, but to analyze the new massive sets of data we are generating, we will need to devote careful and dedicated effort.

Appendix A: Visualizations for excitable multicellular phase-field mode

This appendix serves as a visualization companion to Chapter 5 because movies cannot be included in a dissertation. The figures in this chapter are all alike, they contain snapshots of simulations from the excitable phase-field approach.

Each of the following figures contains 9 evenly spaced snapshots of dynamics. Figures A.1 & A.3 span a time of 100 s, Figure A.3 spans a time of 400 s, while Figures A.4 & A.5 span a time of 1 hour. The gray outlines represent the $\phi = 0.5$ isosurface that denotes the edge of the cell. The color field has brightness representing the strength of the activator A and color representing the angle of A with respect to the center-of-mass. If confinement is present, it is represented as a bold white geometric outline.

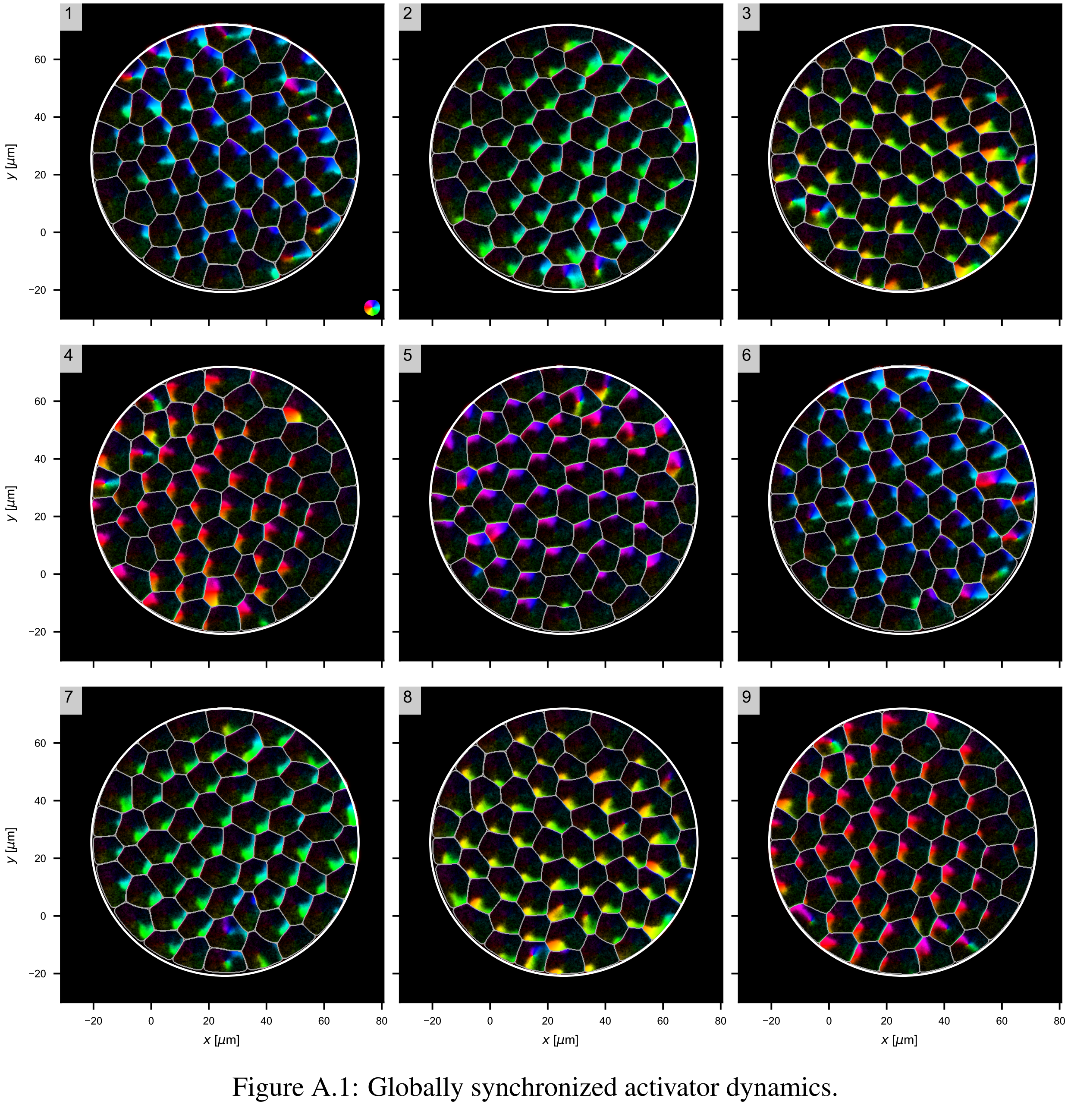

Figure A.1: Globally synchronized activator dynamics.

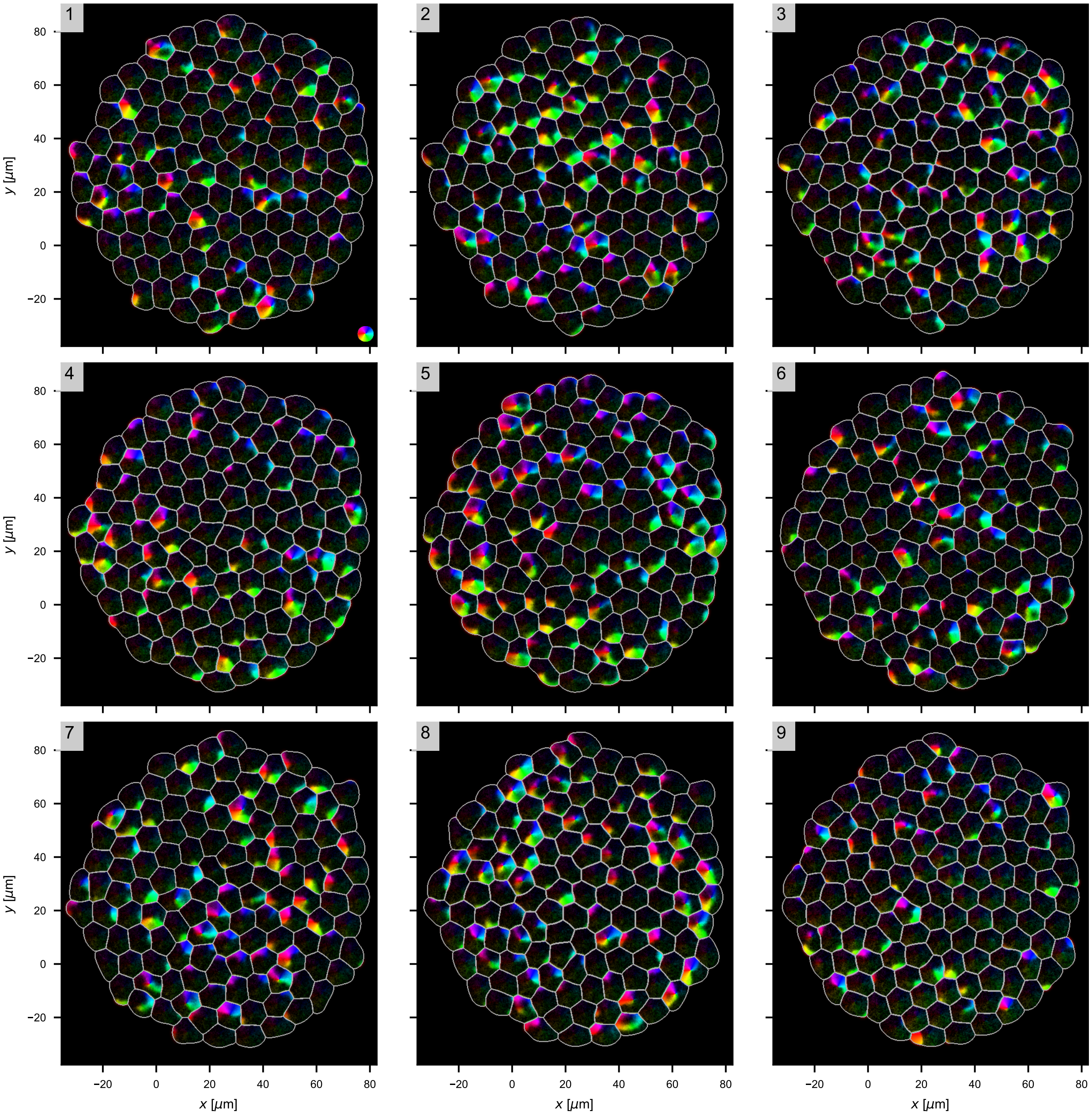

Figure A.2: Pulsating waves in free adhesive cluster. Note that panel 2 has the activator moving inwared, followed by panel 5 with the activator moving outward. This pattern is repeated again in panels 7 and 8.

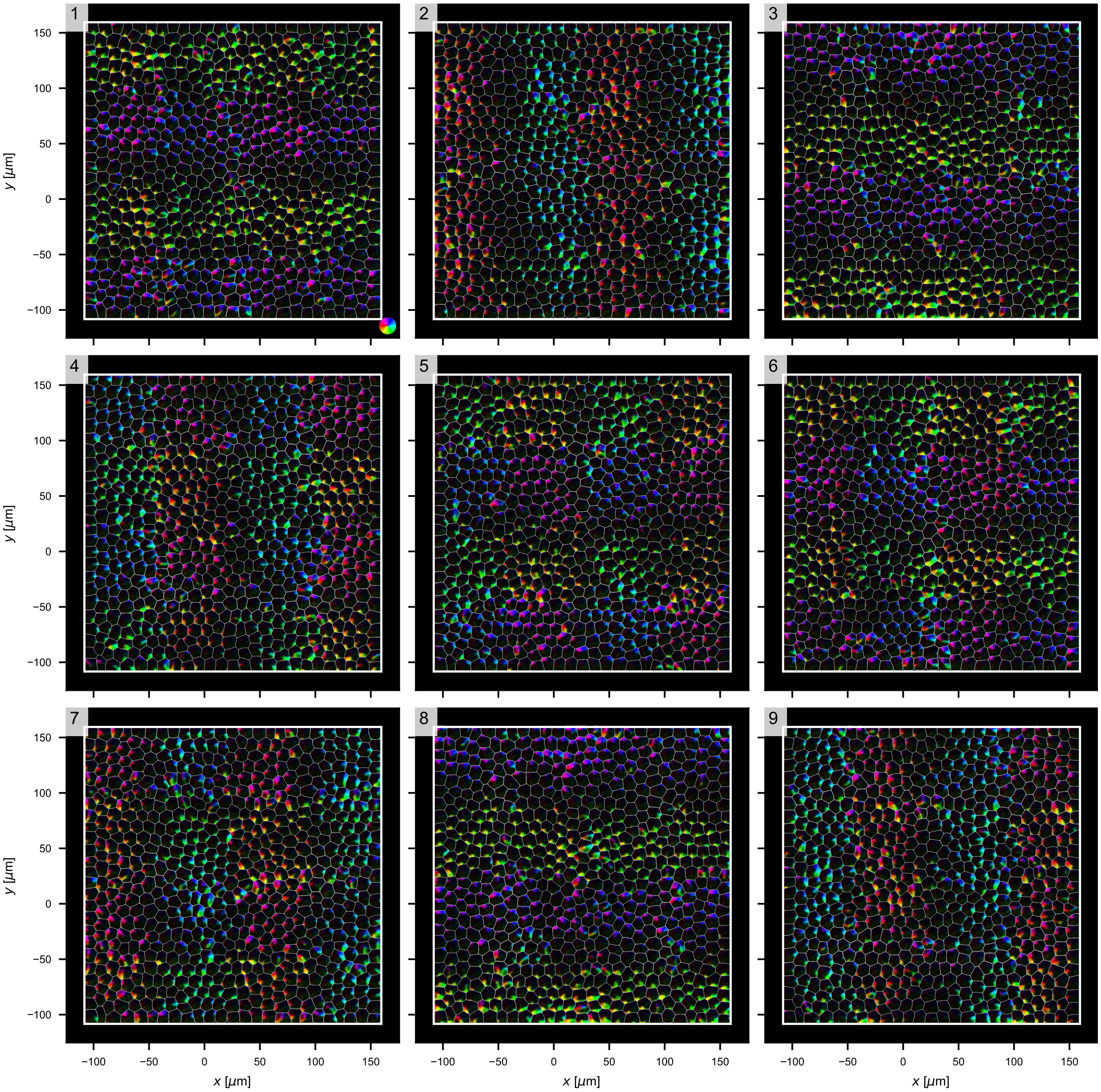

Figure A.3: Activator dynamics in square confinement.

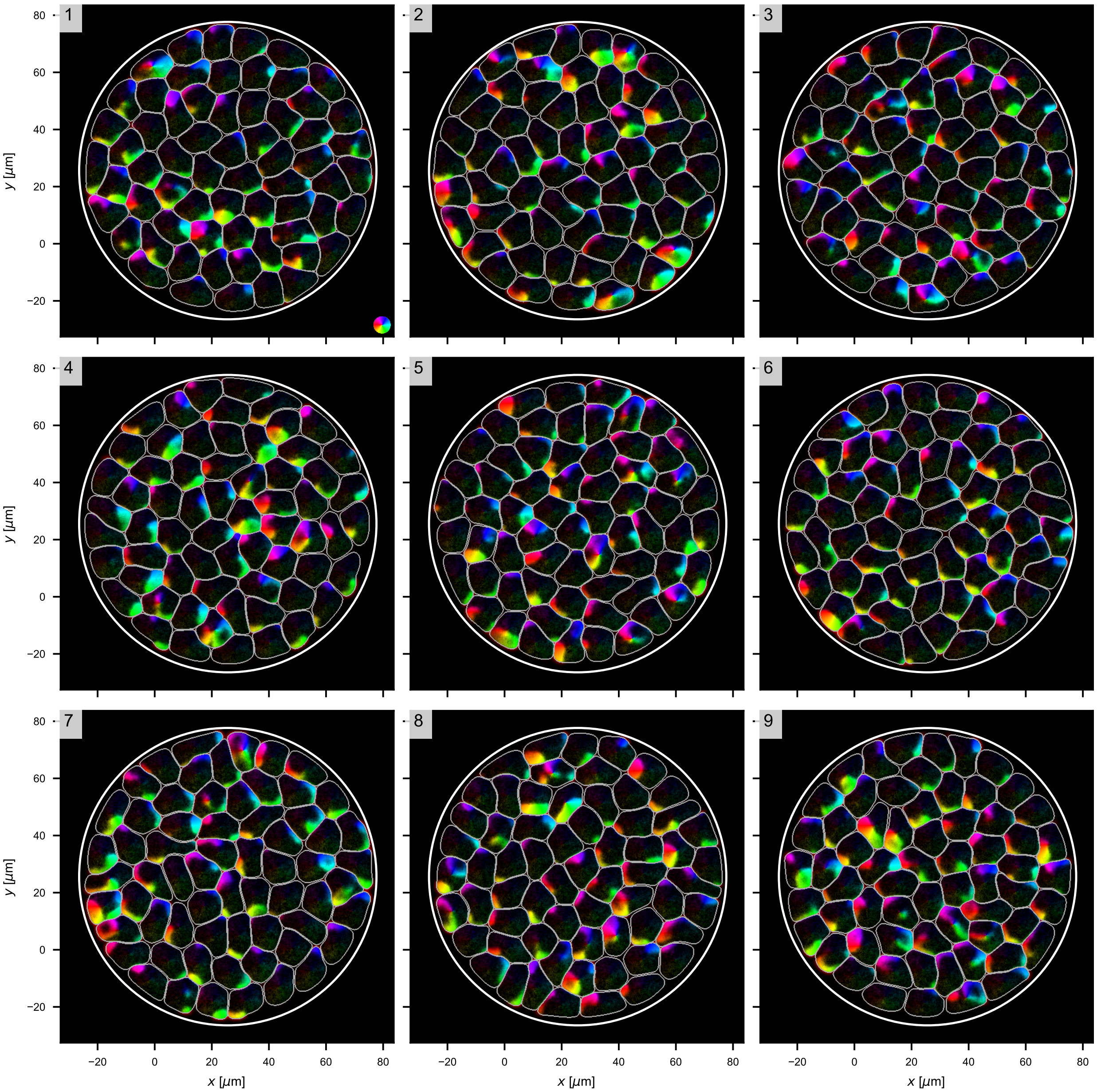

Figure A.4: Chaotic motile state in circular confinement.

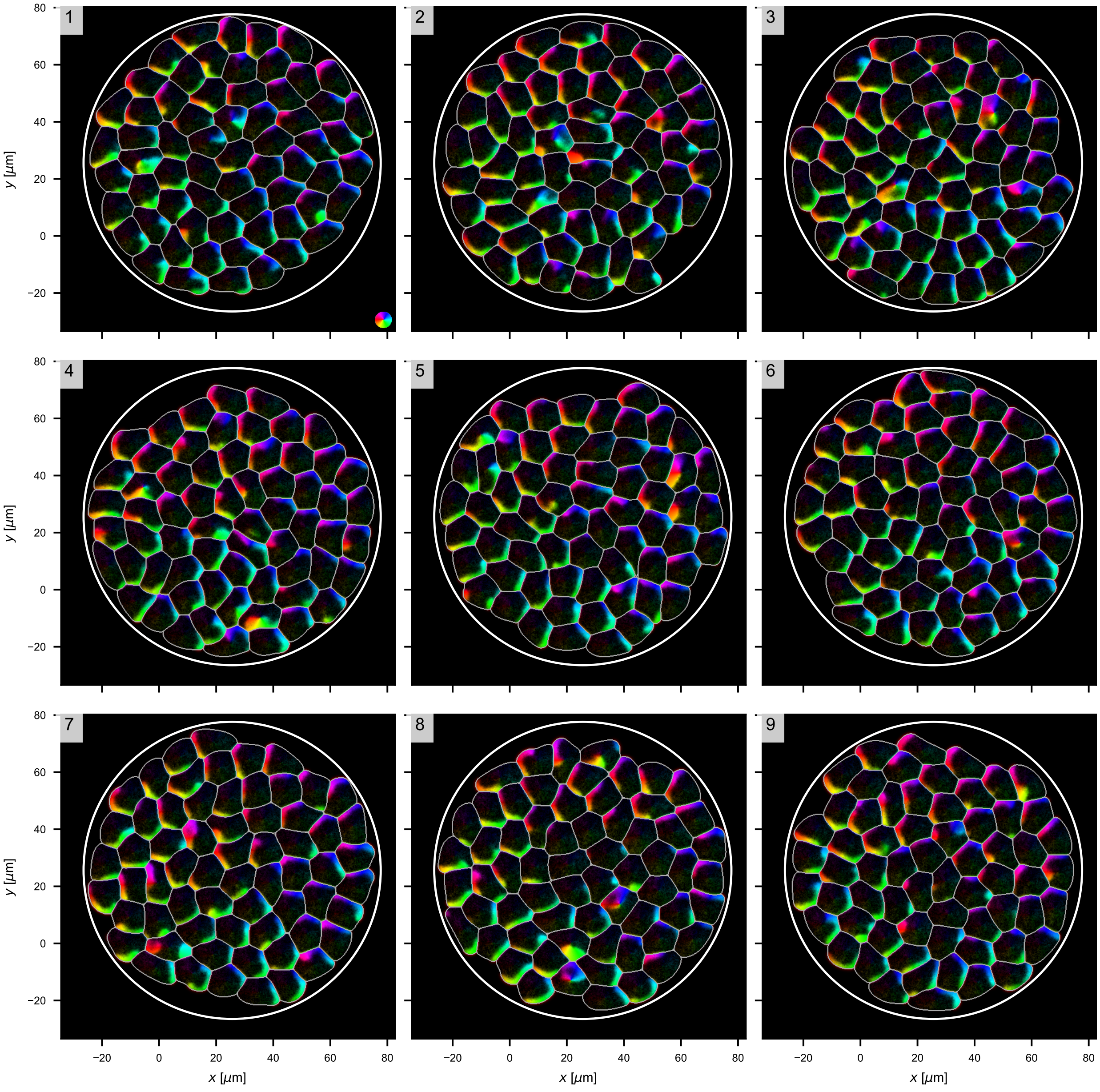

Figure A.5: Globally rotating state in circular confinement.

Bibliography

[1] Kimberly M. Stroka and Konstantinos Konstantopoulos. “Physical Biology in Cancer. 4. Physical Cues Guide Tumor Cell Adhesion and Migration”. *American Journal of Physiology-Cell Physiology* 306.2 (Jan. 15, 2014), pp. C98–C109.

[2] Hadi T. Nia, Hao Liu, Giorgio Seano, Meenal Datta, Dennis Jones, Nuh Rahbari, Joao Incio, Vikash P. Chauhan, Keehoon Jung, John D. Martin, Vasileios Askoxylakis, Timothy P. Padera, Dai Fukumura, Yves Boucher, Francis J. Hornicek, Alan J. Grodzinsky, James W. Baish, Lance L. Munn, and Rakesh K. Jain. “Solid Stress and Elastic Energy as Measures of Tumour Mechanopathology”. *Nature Biomedical Engineering* 1.1 (Nov. 28, 2016), pp. 1–11.

[3] *Frontiers | Defining the Role of Solid Stress and Matrix Stiffness in Cancer Cell Proliferation and Metastasis*.

[4] Juliane Winkler, Abisola Abisoye-Ogunniyan, Kevin J. Metcalf, and Zena Werb. “Concepts of Extracellular Matrix Remodelling in Tumour Progression and Metastasis”. *Nature Communications* 11.1 (Oct. 9, 2020), p. 5120.

[5] Zichen Xu, Keming Li, Ying Xin, Kai Tang, Mo Yang, Guixue Wang, and Youhua Tan. “Fluid Shear Stress Regulates the Survival of Circulating Tumor Cells via Nuclear Expansion”. *Journal of Cell Science* 135.10 (May 26, 2022), jcs259586.

[6] V. T. Turitto. “Blood Viscosity, Mass Transport, and Thrombogenesis”. *Progress in Hemostasis and Thrombosis* 6 (1982), pp. 139–177.

[7] Sagar Regmi, Afu Fu, and Kathy Qian Luo. “High Shear Stresses under Exercise Condition Destroy Circulating Tumor Cells in a Microfluidic System”. *Scientific Reports* 7.1 (Jan. 5, 2017), p. 39975.

[8] Christopher L. Yankaskas, Kaustav Bera, Konstantin Stoletov, Selma A. Serra, Julia Carrillo-Garcia, Soontorn Tuntithavornwat, Panagiotis Mistriotis, John D. Lewis, Miguel A. Valverde, and Konstantinos Konstantopoulos. “The Fluid Shear Stress Sensor TRPM7 Regulates Tumor Cell Intravasation”. *Science Advances* 7.28 (July 9, 2021), eabh3457.

[9] Ayushi Agrawal, Yousef Javanmardi, Sara A. Watson, Bianca Serwinski, Boris Djordjevic, Wenbin Li, Amir R. Aref, Russell W. Jenkins, and Emad Moeendarbary. “Mechanical Signatures in Cancer Metastasis”. *npj Biological Physics and Mechanics* 2.1 (Feb. 4, 2025), pp. 1–20.

[10] J. C. Coates and A. J. Harwood. “Cell-Cell Adhesion and Signal Transduction during Dictyostelium Development”. *Journal of Cell Science* 114 (Pt 24 Dec. 2001), pp. 4349–4358.

[11] Shuyao Gu, Abby Bull, Jeneh K. Perry, Amilee Huang, Matt J. Hourwitz, Mona Abostate, John T. Fourkas, Andrey A. Korchevskiy, Ann G. Wylie, and Wolfgang Losert. “Excitable Systems: A New Perspective on the Cellular Impact of Elongate Mineral Particles”. *Environmental Research*. The Monticello II Conference on Elongate Mineral Particles 230 (Aug. 1, 2023), p. 115353.

[12] Balázs Enyedi and Philipp Niethammer. “Mechanisms of Epithelial Wound Detection”. *Trends in cell biology* 25.7 (July 2015), pp. 398–407.

[13] Hasan Ucar, Satoshi Watanabe, Jun Noguchi, Yuichi Morimoto, Yusuke Iino, Sho Yagishita, Noriko Takahashi, and Haruo Kasai. “Mechanical Actions of Dendritic-Spine Enlargement on Presynaptic Exocytosis”. *Nature* 600.7890 (Dec. 2021), pp. 686–689.

[14] Viola Vogel and Michael Sheetz. “Local Force and Geometry Sensing Regulate Cell Functions”. *Nature Reviews Molecular Cell Biology* 7.4 (Apr. 2006), pp. 265–275.

[15] T.B. Stanishneva-Konovalova, N.I. Derkacheva, S.V. Polevova, and O.S. Sokolova. “The Role of BAR Domain Proteins in the Regulation of Membrane Dynamics”. *Acta Naturae* 8.4 (2016), pp. 60–69.

[16] “Membrane Curvature Drives the Formation of Integrin Adhesions on Soft ECM Fibres”. *Nature Cell Biology* 25.11 (Nov. 2023), pp. 1573–1574.

[17] Ewa Sitarska, Silvia Dias Almeida, Marianne Sandvold Beckwith, Julian Stopp, Jakub Czuchnowski, Marc Siggel, Rita Roessner, Aline Tschanz, Christer Ejsing, Yannick Schwab, Jan Kosinski, Michael Sixt, Anna Kreshuk, Anna Erzberger, and Alba Diz-Muñoz. “Sensing Their Plasma Membrane Curvature Allows Migrating Cells to Circumvent Obstacles”. *Nature Communications* 14.1 (Sept. 13, 2023), p. 5644.

[18] Carsten Mim and Vinzenz M Unger. “Membrane Curvature and Its Generation by BAR Proteins”. *Trends in biochemical sciences* 37.12 (Dec. 2012), pp. 526–533.

[19] Jennifer L. Gallop and Harvey T. McMahon. “BAR Domains and Membrane Curvature: Bringing Your Curves to the BAR”. *Biochemical Society Symposium* 72 (2005), pp. 223–231.

[20] Marta Kapałczyńska, Tomasz Kolenda, Weronika Przybyła, Maria Zajączkowska, Anna Teresiak, Violetta Filas, Matthew Ibbs, Renata Bliźniak, Łukasz Łuczewski, and Katarzyna Lamperska. “2D and 3D Cell Cultures – a Comparison of Different Types of Cancer Cell Cultures”. *Archives of Medical Science : AMS* 14.4 (June 2018), pp. 910–919.

[21] Carolina Pontes Soares, Victor Midlej, Maria Eduarda Weschollek de Oliveira, Marlene Benchimol, Manoel Luis Costa, and Cláudia Mermelstein. “2D and 3D-organized Car-

diac Cells Shows Differences in Cellular Morphology, Adhesion Junctions, Presence of Myofibrils and Protein Expression". *PloS One* 7.5 (2012), e38147.

[22] Caleb Jensen and Yong Teng. "Is It Time to Start Transitioning From 2D to 3D Cell Culture?" *Frontiers in Molecular Biosciences* 7 (Mar. 6, 2020), p. 33.

[23] Xiaoyu Sun, Matt J. Hourwitz, Eleni M. Baker, B. U. Sebastian Schmidt, Wolfgang Losert, and John T. Fourkas. "Replication of Biocompatible, Nanotopographic Surfaces". *Scientific Reports* 8.1 (1 Jan. 12, 2018), p. 564.

[24] Xiaoyu Sun, Meghan K. Driscoll, Can Guven, Satarupa Das, Carole A. Parent, John T. Fourkas, and Wolfgang Losert. "Asymmetric Nanotopography Biases Cytoskeletal Dynamics and Promotes Unidirectional Cell Guidance". *Proceedings of the National Academy of Sciences* 112.41 (Oct. 13, 2015), p. 12557.

[25] Meghan K. Driscoll, Xiaoyu Sun, Can Guven, John T. Fourkas, and Wolfgang Losert. "Cellular Contact Guidance through Dynamic Sensing of Nanotopography". *ACS Nano* 8.4 (Apr. 22, 2014), pp. 3546–3555.

[26] Song Chen, Matt J. Hourwitz, Leonard Campanello, John T. Fourkas, Wolfgang Losert, and Carole A. Parent. "Actin Cytoskeleton and Focal Adhesions Regulate the Biased Migration of Breast Cancer Cells on Nanoscale Asymmetric Sawteeth". *ACS Nano* (Feb. 6, 2019), acsnano.8b07140.

[27] Arja Ray, Oscar Lee, Zaw Win, Rachel M. Edwards, Patrick W. Alford, Deok-Ho Kim, and Paolo P. Provenzano. "Anisotropic Forces from Spatially Constrained Focal Adhesions Mediate Contact Guidance Directed Cell Migration". *Nature Communications* 8.1 (Apr. 12, 2017), p. 14923.

[28] Diane Hoffman-Kim, Jennifer A. Mitchel, and Ravi V. Bellamkonda. "Topography, Cell Response, and Nerve Regeneration". *Annual Review of Biomedical Engineering* 12 (Aug. 15, 2010), pp. 203–231.

[29] Rajeswari Ravichandran, Susan Liao, Clarisse CH Ng, Casey K Chan, Michael Raghunath, and Seeram Ramakrishna. "Effects of Nanotopography on Stem Cell Phenotypes". *World Journal of Stem Cells* 1.1 (Dec. 31, 2009), pp. 55–66.

[30] Tatyana Svitkina. "The Actin Cytoskeleton and Actin-Based Motility". *Cold Spring Harbor Perspectives in Biology* 10.1 (Jan. 2018), a018267.

[31] Wen-Lu Chung, Matthias Eibauer, Wenhong Li, Rajaa Boujemaa-Paterski, Benjamin Geiger, and Ohad Medalia. "A Network of Mixed Actin Polarity in the Leading Edge of Spreading Cells". *Communications Biology* 5.1 (Dec. 7, 2022), pp. 1–11.

[32] Parinaz Ahangar, Xanthe L. Strudwick, and Allison J. Cowin. "Wound Healing from an Actin Cytoskeletal Perspective". *Cold Spring Harbor Perspectives in Biology* 14.8 (Aug. 2022), a041235.

[33] Orion D. Weiner, Guy Servant, Matthew D. Welch, Timothy J. Mitchison, John W. Sedat, and Henry R. Bourne. “Spatial Control of Actin Polymerization during Neutrophil Chemotaxis”. *Nature cell biology* 1.2 (June 1999), pp. 75–81.

[34] Laurent Blanchoin, Rajaa Boujemaa-Paterski, Cécile Sykes, and Julie Plastino. “Actin Dynamics, Architecture, and Mechanics in Cell Motility”. *Physiological Reviews* 94.1 (Jan. 2014), pp. 235–263.

[35] Thomas D. Pollard, Laurent Blanchoin, and R. Dyche Mullins. “Molecular Mechanisms Controlling Actin Filament Dynamics in Nonmuscle Cells”. *Annual Review of Biophysics* 29 (Volume 29, 2000 June 1, 2000), pp. 545–576.

[36] Dominique Pantaloni, Christophe Le Clainche, and Marie-France Carlier. “Mechanism of Actin-Based Motility”. *Science* 292.5521 (May 25, 2001), pp. 1502–1506.

[37] Priyamvada Chugh and Ewa K. Paluch. “The Actin Cortex at a Glance”. *Journal of Cell Science* 131.14 (July 19, 2018), jcs186254.

[38] Sari Tojkander, Gergana Gateva, and Pekka Lappalainen. “Actin Stress Fibers–Assembly, Dynamics and Biological Roles”. *Journal of Cell Science* 125 (Pt 8 Apr. 15, 2012), pp. 1855–1864.

[39] Alex Mogilner. “On the Edge: Modeling Protrusion”. *Current Opinion in Cell Biology*. Cell Structure and Dynamics 18.1 (Feb. 1, 2006), pp. 32–39.

[40] Hiroki Katsuta, Masahiro Sokabe, and Hiroaki Hirata. “From Stress Fiber to Focal Adhesion: A Role of Actin Crosslinkers in Force Transmission”. *Frontiers in Cell and Developmental Biology* 12 (Aug. 13, 2024).

[41] H. R. Karfunkel and F. F. Seelig. “Excitable Chemical Reaction Systems I. Definition of Excitability and Simulation of Model Systems”. *Journal of Mathematical Biology* 2.2 (June 1, 1975), pp. 123–132.

[42] A. L. Hodgkin and A. F. Huxley. “A Quantitative Description of Membrane Current and Its Application to Conduction and Excitation in Nerve”. *The Journal of Physiology* 117.4 (1952), pp. 500–544.

[43] Richard FitzHugh. “Impulses and Physiological States in Theoretical Models of Nerve Membrane”. *Biophysical Journal* 1.6 (July 1961), pp. 445–466.

[44] Rodolphe Sepulchre, Guillaume Drion, and Alessio Franci. “Excitable Behaviors”. *Emerging Applications of Control and Systems Theory: A Festschrift in Honor of Mathukumalli Vidyasagar*. Ed. by Roberto Tempo, Stephen Yurkovich, and Pradeep Misra. Cham: Springer International Publishing, 2018, pp. 269–280.

[45] M. Girardi-Schappo, M. H. R. Tragtenberg, and O. Kinouchi. “A Brief History of Excitable Map-Based Neurons and Neural Networks”. *Journal of Neuroscience Methods*.

Latin American School on Computational Neuroscience (LASCON) 2012 220.2 (Nov. 15, 2013), pp. 116–130.

[46] Gwendal Le Masson, Sylvie Le Masson, and Maurice Moulins. “From Conductances to Neural Network Properties: Analysis of Simple Circuits Using the Hybrid Network Method”. *Progress in Biophysics and Molecular Biology* 64.2 (Jan. 1, 1995), pp. 201–220.

[47] Rupamanjari Majumder. “In Silico Thermal Control of Spiral Wave Dynamics in Excitable Cardiac Tissue”. *Biophysical Reports* 4.3 (Sept. 11, 2024), p. 100170.

[48] J M Davidenko, P F Kent, D R Chialvo, D C Michaels, and J Jalife. “Sustained Vortex-like Waves in Normal Isolated Ventricular Muscle.” *Proceedings of the National Academy of Sciences* 87.22 (Nov. 1990), pp. 8785–8789.

[49] Jorge M. Davidenko, Arcady V. Pertsov, Remy Salomonsz, William Baxter, and José Jalife. “Stationary and Drifting Spiral Waves of Excitation in Isolated Cardiac Muscle”. *Nature* 355.6358 (Jan. 1992), pp. 349–351.

[50] Orion D. Weiner, William A. Marganski, Lani F. Wu, Steven J. Altschuler, and Marc W. Kirschner. “An Actin-Based Wave Generator Organizes Cell Motility”. *PLOS Biology* 5.9 (Aug. 14, 2007), e221.

[51] Tatsuo Shibata, Masatoshi Nishikawa, Satomi Matsuoka, and Masahiro Ueda. “Intracellular Encoding of Spatiotemporal Guidance Cues in a Self-Organizing Signaling System for Chemotaxis in Dictyostelium Cells”. *Biophysical Journal* 105.9 (Nov. 5, 2013), pp. 2199–2209.

[52] Daniel Cebrián-Lacasa, Pedro Parra-Rivas, Daniel Ruiz-Reynés, and Lendert Gelens. “Six Decades of the FitzHugh–Nagumo Model: A Guide through Its Spatio-Temporal Dynamics and Influence across Disciplines”. *Physics Reports*. Six Decades of the FitzHugh-Nagumo Model: A Guide through Its Spatio-Temporal Dynamics and Influence across Disciplines 1096 (Dec. 12, 2024), pp. 1–39.

[53] V. S. Zykov. “Spiral Wave Initiation in Excitable Media”. *Philosophical Transactions of the Royal Society A: Mathematical, Physical and Engineering Sciences* 376.2135 (Nov. 12, 2018), p. 20170379.

[54] Peter N. Devreotes, Sayak Bhattacharya, Marc Edwards, Pablo A. Iglesias, Thomas Lampert, and Yuchuan Miao. “Excitable Signal Transduction Networks in Directed Cell Migration”. *Annual review of cell and developmental biology* 33 (Oct. 6, 2017), pp. 103–125.

[55] Yuchuan Miao, Sayak Bhattacharya, Tatsat Banerjee, Bedri Abubaker-Sharif, Yu Long, Takanari Inoue, Pablo A Iglesias, and Peter N Devreotes. “Wave Patterns Organize Cellular Protrusions and Control Cortical Dynamics”. *Molecular Systems Biology* 15.3 (Mar. 12, 2019), e8585.

[56] Yuchuan Miao, Sayak Bhattacharya, Marc Edwards, Huaqing Cai, Takanari Inoue, Pablo A. Iglesias, and Peter N. Devreotes. "Altering the Threshold of an Excitable Signal Transduction Network Changes Cell Migratory Modes". *Nature Cell Biology* 19.4 (4 Apr. 2017), pp. 329–340.

[57] Jonathan B. Michaux, François B. Robin, William M. McFadden, and Edwin M. Munro. "Excitable RhoA Dynamics Drive Pulsed Contractions in the Early C. Elegans Embryo". *The Journal of Cell Biology* 217.12 (Dec. 3, 2018), pp. 4230–4252.

[58] Ani Michaud, Marcin Leda, Zachary T. Swider, Songeun Kim, Jiaye He, Jennifer Landino, Jenna R. Valley, Jan Huisken, Andrew B. Goryachev, George von Dassow, and William M. Bement. "A Versatile Cortical Pattern-Forming Circuit Based on Rho, F-actin, Ect2, and RGA-3/4". *The Journal of Cell Biology* 221.8 (June 16, 2022), e202203017.

[59] Erik Bernitt, Hans-Günther Döbereiner, Nir S. Gov, and Arik Yochelis. "Fronts and Waves of Actin Polymerization in a Bistability-Based Mechanism of Circular Dorsal Ruffles". *Nature Communications* 8.1 (June 19, 2017), p. 15863.

[60] Carsten Beta, Leah Edelstein-Keshet, Nir Gov, and Arik Yochelis. "From Actin Waves to Mechanism and Back: How Theory Aids Biological Understanding". *eLife* 12 (July 10, 2023). Ed. by Alphee Michelot and Anna Akhmanova, e87181.

[61] Sayak Bhattacharya, Tatsat Banerjee, Yuchuan Miao, Huiwang Zhan, Peter N. Devreotes, and Pablo A. Iglesias. "Traveling and Standing Waves Mediate Pattern Formation in Cellular Protrusions". *Science Advances* 6.32 (Aug. 2020), eaay7682.

[62] Debojyoti Biswas, Parijat Banerjee, and Pablo A. Iglesias. "Balancing at the Edge of Excitability: Implications for Cell Movement". *Mathematics of Control, Signals, and Systems* 36.1 (Mar. 1, 2024), pp. 121–137.

[63] Yuan Xiong, Chuan-Hsiang Huang, Pablo A. Iglesias, and Peter N. Devreotes. "Cells Navigate with a Local-Excitation, Global-Inhibition-Biased Excitable Network". *Proceedings of the National Academy of Sciences* 107.40 (Oct. 2010), pp. 17079–17086.

[64] Paolo Maiuri, Jean-François Rupprecht, Stefan Wieser, Verena Ruprecht, Olivier Bénichou, Nicolas Carpi, Mathieu Coppey, Simon De Beco, Nir Gov, Carl-Philipp Heisenberg, Carolina Lage Crespo, Franziska Lautenschlaeger, Maël Le Berre, Ana-Maria Lennon-Dumenil, Matthew Raab, Hawa-Racine Thiam, Matthieu Piel, Michael Sixt, and Raphaël Voituriez. "Actin Flows Mediate a Universal Coupling between Cell Speed and Cell Persistence". *Cell* 161.2 (Apr. 9, 2015), pp. 374–386.

[65] Changji Shi and Pablo A. Iglesias. "Excitable Behaviour in Amoeboid Chemotaxis". *Wiley interdisciplinary reviews. Systems biology and medicine* 5.5 (Sept. 2013), pp. 631–642.

[66] Qixin Yang, Yuchuan Miao, Parijat Banerjee, Matt J. Hourwitz, Minxi Hu, Quan Qing, Pablo A. Iglesias, John T. Fourkas, Wolfgang Losert, and Peter N. Devreotes. "Nanoto-

pography Modulates Intracellular Excitable Systems through Cytoskeleton Actuation". *Proceedings of the National Academy of Sciences* 120.19 (May 9, 2023), e2218906120.

[67] Andrea Ravasio, Ibrahim Cheddadi, Tianchi Chen, Telmo Pereira, Hui Ting Ong, Cristina Bertocchi, Agusti Brugues, Antonio Jacinto, Alexandre J. Kabla, Yusuke Toyama, Xavier Trepat, Nir Gov, Luís Neves de Almeida, and Benoit Ladoux. "Gap Geometry Dictates Epithelial Closure Efficiency". *Nature Communications* 6.1 (July 9, 2015), p. 7683.

[68] Jes K. Klarlund. "Dual Modes of Motility at the Leading Edge of Migrating Epithelial Cell Sheets". *Proceedings of the National Academy of Sciences* 109.39 (Sept. 25, 2012), pp. 15799–15804.

[69] Tianchi Chen, Andrew Callan-Jones, Eduard Fedorov, Andrea Ravasio, Agustí Brugués, Hui Ting Ong, Yusuke Toyama, Boon Chuan Low, Xavier Trepat, Tom Shemesh, Raphaël Voituriez, and Benoît Ladoux. "Large-Scale Curvature Sensing by Directional Actin Flow Drives Cellular Migration Mode Switching". *Nature Physics* 15.4 (Apr. 2019), pp. 393–402.

[70] Zhanghan Wu, Maohan Su, Cheesan Tong, Min Wu, and Jian Liu. "Membrane Shape-Mediated Wave Propagation of Cortical Protein Dynamics". *Nature Communications* 9.1 (Jan. 10, 2018), p. 136.

[71] Rachel M. Lee, Leonard Campanello, Matt J. Hourwitz, Phillip Alvarez, Ava Omidvar, John T. Fourkas, and Wolfgang Losert. "Quantifying Topography-Guided Actin Dynamics across Scales Using Optical Flow". *Molecular Biology of the Cell* 31.16 (July 21, 2020), pp. 1753–1764.

[72] Mukund Gupta, Bryant L. Doss, Leyla Kocgozlu, Meng Pan, René-Marc Mège, Andrew Callan-Jones, Raphaël Voituriez, and Benoît Ladoux. "Cell Shape and Substrate Stiffness Drive Actin-Based Cell Polarity". *Physical Review E* 99.1 (Jan. 10, 2019), p. 012412.

[73] Berthold K. P. Horn and Brian G. Schunck. "Determining Optical Flow". *Artificial Intelligence* 17.1 (Aug. 1, 1981), pp. 185–203.

[74] Dhruv K. Vig, Alex E. Hamby, and Charles W. Wolgemuth. "On the Quantification of Cellular Velocity Fields". *Biophysical Journal* 110.7 (Apr. 2016), pp. 1469–1475.

[75] B. D. Lucas and T. Kanade. "An Iterative Image Registration Technique with an Application to Stereo Vision". *IJCAI'81: 7th International Joint Conference on Artificial Intelligence*. Vol. 2. Vancouver, Canada, 1981, pp. 674–679.

[76] Adam Shellard and Roberto Mayor. "Collective Durotaxis along a Self-Generated Stiffness Gradient in Vivo". *Nature* 600.7890 (Dec. 2021), pp. 690–694.

[77] R. R. Kretschmer and M. L. Collado. "Chemotaxis". *Infection* 8 Suppl 3 (1980), S 299–302.

[78] Lei Qin, Dazhi Yang, Weihong Yi, Huiling Cao, and Guozhi Xiao. “Roles of Leader and Follower Cells in Collective Cell Migration”. *Molecular Biology of the Cell* 32.14 (July 1, 2021), pp. 1267–1272.

[79] Daniel O Velez, Sural K Ranamukhaarachchi, Aditya Kumar, Rishi N Modi, Esther W Lim, Adam J Engler, Christian M Metallo, and Stephanie I Fraley. “3D Collagen Architecture Regulates Cell Adhesion through Degradability, Thereby Controlling Metabolic and Oxidative Stress”. *Integrative Biology* 11.5 (May 2019), pp. 221–234.

[80] Ryan J. Leiphart, Dongning Chen, Ana P. Peredo, Abigail E. Loneker, and Paul A. Janmey. “Mechanosensing at Cellular Interfaces”. *Langmuir: the ACS journal of surfaces and colloids* 35.23 (June 11, 2019), pp. 7509–7519.

[81] Peter Friedl and Roberto Mayor. “Tuning Collective Cell Migration by Cell–Cell Junction Regulation”. *Cold Spring Harbor Perspectives in Biology* 9.4 (Apr. 2017), a029199.

[82] Adam Shellard and Roberto Mayor. “Rules of Collective Migration: From the Wildebeest to the Neural Crest”. *Philosophical Transactions of the Royal Society B: Biological Sciences* 375.1807 (Sept. 14, 2020), p. 20190387.

[83] Aviad Ben-Shmuel, Batel Sabag, Guy Biber, and Mira Barda-Saad. “The Role of the Cytoskeleton in Regulating the Natural Killer Cell Immune Response in Health and Disease: From Signaling Dynamics to Function”. *Frontiers in Cell and Developmental Biology* 9 (Feb. 1, 2021).

[84] Andrea Herrero-Cervera, Oliver Soehnlein, and Ellinor Kenne. “Neutrophils in Chronic Inflammatory Diseases”. *Cellular & Molecular Immunology* 19.2 (Feb. 2022), pp. 177–191.

[85] Jifei Miao, Haixia Ma, Yang Yang, Yuanpin Liao, Cui Lin, Juanxia Zheng, Muli Yu, and Jiao Lan. “Microglia in Alzheimer’s Disease: Pathogenesis, Mechanisms, and Therapeutic Potentials”. *Frontiers in Aging Neuroscience* 15 (June 15, 2023).

[86] *Endometriosis*.

[87] Konstantin A. Toniyan, Elena Yu. Gorbacheva, Valery V. Boyarintsev, and Irina V. Ogneva. “Endometriosis of the Cervix: A Rare Clinical Case with the Possibility of Comparing the Eutopic and Ectopic Endometrium at the Cellular Level”. *International Journal of Molecular Sciences* 24.3 (Jan. 22, 2023), p. 2184.

[88] Mikkel Herholdt Jensen, Eliza J. Morris, Cynthia M. Gallant, Kathleen G. Morgan, David A. Weitz, and Jeffrey R. Moore. “Mechanism of Calponin Stabilization of Cross-Linked Actin Networks”. *Biophysical Journal* 106.4 (Feb. 18, 2014), pp. 793–800.

[89] Kirsten Morris, Ivanna Ihnatovych, Emily Ionetz, Jennifer Reed, Andrea Braundmeier, and Zuzana Strakova. “Cofilin and Slingshot Localization in the Epithelium of Uterine Endometrium Changes during the Menstrual Cycle and in Endometriosis”. *Reproductive Sciences (Thousand Oaks, Calif.)* 18.10 (Oct. 2011), pp. 1014–1024.

[90] Wioletta Arendt, Konrad Kleszczyński, Maciej Gagat, and Magdalena Izdebska. “Endometriosis and Cytoskeletal Remodeling: The Functional Role of Actin-Binding Proteins”. *Cells* 14.5 (Feb. 28, 2025), p. 360.

[91] Juliet Lee, Akira Ishihara, Julie A. Theriot, and Ken Jacobson. “Principles of Locomotion for Simple-Shaped Cells”. *Nature* 362.6416 (Mar. 1993), pp. 167–171.

[92] Kinneret Keren, Zachary Pincus, Greg M. Allen, Erin L. Barnhart, Gerard Marriott, Alex Mogilner, and Julie A. Theriot. “Mechanism of Shape Determination in Motile Cells”. *Nature* 453.7194 (May 2008), pp. 475–480.

[93] H. P. Grimm, A. B. Verkhovsky, A. Mogilner, and J.-J. Meister. “Analysis of Actin Dynamics at the Leading Edge of Crawling Cells: Implications for the Shape of Keratocyte Lamellipodia”. *European Biophysics Journal* 32.6 (Oct. 1, 2003), pp. 563–577.

[94] Michael M. Kozlov and Alex Mogilner. “Model of Polarization and Bistability of Cell Fragments”. *Biophysical Journal* 93.11 (Dec. 1, 2007), pp. 3811–3819.

[95] Falko Ziebert and Igor S. Aranson. “Computational Approaches to Substrate-Based Cell Motility”. *npj Computational Materials* 2.1 (July 15, 2016), pp. 1–16.

[96] Changji Shi, Chuan-Hsiang Huang, Peter N. Devreotes, and Pablo A. Iglesias. “Interaction of Motility, Directional Sensing, and Polarity Modules Recreates the Behaviors of Chemotaxing Cells”. *PLOS Computational Biology* 9.7 (July 4, 2013), e1003122.

[97] M. Machacek and G. Danuser. “Morphodynamic Profiling of Protrusion Phenotypes”. *Biophysical Journal* 90.4 (Feb. 15, 2006), pp. 1439–1452.

[98] Liu Yang, Janet C. Effler, Brett L. Kutscher, Sarah E. Sullivan, Douglas N. Robinson, and Pablo A. Iglesias. “Modeling Cellular Deformations Using the Level Set Formalism”. *BMC Systems Biology* 2.1 (July 24, 2008), p. 68.

[99] Esa Kuusela and Wolfgang Alt. “Continuum Model of Cell Adhesion and Migration”. *Journal of Mathematical Biology* 58.1 (Jan. 1, 2009), pp. 135–161.

[100] Charles W. Wolgemuth and Mark Zajac. “The Moving Boundary Node Method: A Level Set-Based, Finite Volume Algorithm with Applications to Cell Motility”. *Journal of Computational Physics* 229.19 (Sept. 20, 2010), pp. 7287–7308.

[101] Jonathan R. Karr, Jayodita C. Sanghvi, Derek N. Macklin, Miriam V. Gutschow, Jared M. Jacobs, Benjamin Bolival, Nacyra Assad-Garcia, John I. Glass, and Markus W. Covert. “A Whole-Cell Computational Model Predicts Phenotype from Genotype”. *Cell* 150.2 (July 20, 2012), pp. 389–401.

[102] Derek N. Macklin, Travis A. Ahn-Horst, Heejo Choi, Nicholas A. Ruggero, Javier Carrera, John C. Mason, Gwanggyu Sun, Eran Agmon, Mialy M. DeFelice, Inbal Maayan, Keara Lane, Ryan K. Spangler, Taryn E. Gillies, Morgan L. Paull, Sajia Akhter, Samuel R. Bray, Daniel S. Weaver, Ingrid M. Keseler, Peter D. Karp, Jerry H. Morrison, and

Markus W. Covert. “Simultaneous Cross-Evaluation of Heterogeneous E. Coli Datasets via Mechanistic Simulation”. *Science (New York, N.Y.)* 369.6502 (July 24, 2020), eaav3751.

[103] Travis A. Ahn-Horst, Luis Santiago Mille, Gwanggyu Sun, Jerry H. Morrison, and Markus W. Covert. “An Expanded Whole-Cell Model of E. Coli Links Cellular Physiology with Mechanisms of Growth Rate Control”. *npj Systems Biology and Applications* 8.1 (Aug. 19, 2022), pp. 1–21.

[104] Chao Ye, Nan Xu, Cong Gao, Gaoqiang Liu, Jianzhong Xu, Weiguo Zhang, Xiulai Chen, Jens Nielsen, and Liming Liu. “Comprehensive Understanding of Saccharomyces Cerevisiae Phenotypes with Whole-Cell Model WM_S288C”. *Biotechnology and Bioengineering* 117.5 (May 2020), pp. 1562–1574.

[105] Zane R. Thornburg, David M. Bianchi, Troy A. Brier, Benjamin R. Gilbert, Tyler M. Earnest, Marcelo C. R. Melo, Nataliya Safronova, James P. Sáenz, András T. Cook, Kim S. Wise, Clyde A. Hutchison, Hamilton O. Smith, John I. Glass, and Zaida Luthey-Schulten. “Fundamental Behaviors Emerge from Simulations of a Living Minimal Cell”. *Cell* 185.2 (Jan. 20, 2022), 345–360.e28.

[106] Adrian Moure and Hector Gomez. “Phase-Field Modeling of Individual and Collective Cell Migration”. *Archives of Computational Methods in Engineering* 28.2 (Mar. 1, 2021), pp. 311–344.

[107] B A Camley and W-J Rappel. “Physical Models of Collective Cell Motility: From Cell to Tissue”. *Journal of Physics D: Applied Physics* 50.11 (Feb. 2017), p. 113002.

[108] Dapeng Bi, Xingbo Yang, M. Cristina Marchetti, and M. Lisa Manning. “Motility-Driven Glass and Jamming Transitions in Biological Tissues”. *Physical Review X* 6.2 (Apr. 21, 2016), p. 021011.

[109] Jin-Ah Park, Jae Hun Kim, Dapeng Bi, Jennifer A. Mitchel, Nader Taheri Qazvini, Kelan Tantisira, Chan Young Park, Maureen McGill, Sae-Hoon Kim, Bomi Gweon, Jacob Notbohm, Robert Steward Jr, Stephanie Burger, Scott H. Randell, Alvin T. Kho, Dhananjay T. Tambe, Corey Hardin, Stephanie A. Shore, Elliot Israel, David A. Weitz, Daniel J. Tschumperlin, Elizabeth P. Henske, Scott T. Weiss, M. Lisa Manning, James P. Butler, Jeffrey M. Drazen, and Jeffrey J. Fredberg. “Unjamming and Cell Shape in the Asthmatic Airway Epithelium”. *Nature Materials* 14.10 (Oct. 2015), pp. 1040–1048.

[110] Stefan Hoehme and Dirk Drasdo. “A Cell-Based Simulation Software for Multi-Cellular Systems”. *Bioinformatics* 26.20 (Oct. 15, 2010), pp. 2641–2642.

[111] Markus Basan, Jens Elgeti, Edouard Hannezo, Wouter-Jan Rappel, and Herbert Levine. “Alignment of Cellular Motility Forces with Tissue Flow as a Mechanism for Efficient Wound Healing”. *Proceedings of the National Academy of Sciences* 110.7 (Feb. 12, 2013), pp. 2452–2459.

[112] E. Palsson. “A Three-Dimensional Model of Cell Movement in Multicellular Systems”. *Future Generation Computer Systems*. Particle Based Modelling Methods Applied in Biology 17.7 (May 1, 2001), pp. 835–852.

[113] Ahmadreza Ghaffarizadeh, Randy Heiland, Samuel H. Friedman, Shannon M. Mumenthaler, and Paul Macklin. “PhysiCell: An Open Source Physics-Based Cell Simulator for 3-D Multicellular Systems”. *PLOS Computational Biology* 14.2 (Feb. 23, 2018), e1005991.

[114] Silvanus Alt, Poulami Ganguly, and Guillaume Salbreux. “Vertex Models: From Cell Mechanics to Tissue Morphogenesis”. *Philosophical Transactions of the Royal Society B: Biological Sciences* 372.1720 (Mar. 27, 2017), p. 20150520.

[115] O. Wartlick, P. Mumcu, A. Kicheva, T. Bittig, C. Seum, F. Jülicher, and M. González-Gaitán. “Dynamics of Dpp Signaling and Proliferation Control”. *Science* 331.6021 (Mar. 4, 2011), pp. 1154–1159.

[116] Tinri Aegerter-Wilmsen, Maria B. Heimlicher, Alister C. Smith, Pierre Barbier de Reuille, Richard S. Smith, Christof M. Aegerter, and Konrad Basler. “Integrating Force-Sensing and Signaling Pathways in a Model for the Regulation of Wing Imaginal Disc Size”. *Development* 139.17 (Sept. 1, 2012), pp. 3221–3231.

[117] Guillaume Salbreux, Linda K. Barthel, Pamela A. Raymond, and David K. Lubensky. “Coupling Mechanical Deformations and Planar Cell Polarity to Create Regular Patterns in the Zebrafish Retina”. *PLOS Computational Biology* 8.8 (Aug. 23, 2012), e1002618.

[118] Katharina P. Landsberg, Reza Farhadifar, Jonas Ranft, Daiki Umetsu, Thomas J. Widmann, Thomas Bittig, Amani Said, Frank Jülicher, and Christian Dahmann. “Increased Cell Bond Tension Governs Cell Sorting at the *Drosophila* Anteroposterior Compartment Boundary”. *Current Biology* 19.22 (Dec. 1, 2009), pp. 1950–1955.

[119] François Graner and James A. Glazier. “Simulation of Biological Cell Sorting Using a Two-Dimensional Extended Potts Model”. *Physical Review Letters* 69.13 (Sept. 28, 1992), pp. 2013–2016.

[120] James A. Glazier and François Graner. “Simulation of the Differential Adhesion Driven Rearrangement of Biological Cells”. *Physical Review E* 47.3 (Mar. 1, 1993), pp. 2128–2154.

[121] M. P Anderson, D. J Srolovitz, G. S Grest, and P. S Sahni. “Computer Simulation of Grain Growth—I. Kinetics”. *Acta Metallurgica* 32.5 (May 1, 1984), pp. 783–791.

[122] Jos Käfer, Paulien Hogeweg, and Athanasius F. M Marée. “Moving Forward Moving Backward: Directional Sorting of Chemotactic Cells Due to Size and Adhesion Differences”. *PLoS Computational Biology* 2.6 (June 2006), e56.

[123] Andrea Sottoriva, Louis Vermeulen, and Simon Tavaré. “Modeling Evolutionary Dynamics of Epigenetic Mutations in Hierarchically Organized Tumors”. *PLoS Computational Biology* 7.5 (May 5, 2011), e1001132.

[124] Alvaro Köhn-Luque, Walter de Back, Jörn Starruß, Andrea Mattiotti, Andreas Deutsch, José María Pérez-Pomares, and Miguel A. Herrero. “Early Embryonic Vascular Patterning by Matrix-Mediated Paracrine Signalling: A Mathematical Model Study”. *PLoS ONE* 6.9 (Sept. 19, 2011), e24175.

[125] Anja Voss-Böhme. “Multi-Scale Modeling in Morphogenesis: A Critical Analysis of the Cellular Potts Model”. *PLoS ONE* 7.9 (Sept. 11, 2012), e42852.

[126] I. S. Aranson, V. A. Kalatsky, and V. M. Vinokur. “Continuum Field Description of Crack Propagation”. *Physical Review Letters* 85.1 (July 3, 2000), pp. 118–121.

[127] Lukas Schöller, Daniel Schneider, Christoph Herrmann, Andreas Prahs, and Britta Nestler. “Phase-Field Modeling of Crack Propagation in Heterogeneous Materials with Multiple Crack Order Parameters”. *Computer Methods in Applied Mechanics and Engineering* 395 (May 15, 2022), p. 114965.

[128] Alain Karma and Wouter-Jan Rappel. “Quantitative Phase-Field Modeling of Dendritic Growth in Two and Three Dimensions”. *Physical Review E* 57.4 (Apr. 1, 1998), pp. 4323–4349.

[129] W. J. Boettinger, J. A. Warren, C. Beckermann, and A. Karma. “Phase-Field Simulation of Solidification”. *Annual Review of Materials Research* 32 (Volume 32, 2002 Aug. 1, 2002), pp. 163–194.

[130] Seong Gyoon Kim, Won Tae Kim, and Toshio Suzuki. “Phase-Field Model for Binary Alloys”. *Physical Review E* 60.6 (Dec. 1, 1999), pp. 7186–7197.

[131] Julien Kockelkoren, Herbert Levine, and Wouter-Jan Rappel. “Computational Approach for Modeling Intra- and Extracellular Dynamics”. *Physical Review E* 68.3 (Sept. 26, 2003), p. 037702.

[132] Flavio H. Fenton, Elizabeth M. Cherry, Alain Karma, and Wouter-Jan Rappel. “Modeling Wave Propagation in Realistic Heart Geometries Using the Phase-Field Method”. *Chaos: An Interdisciplinary Journal of Nonlinear Science* 15.1 (Feb. 4, 2005), p. 013502.

[133] Amir Abdollahi and Irene Arias. “Phase-Field Modeling of Fracture in Ferroelectric Materials”. *Archives of Computational Methods in Engineering* 22.2 (Apr. 1, 2015), pp. 153–181.

[134] Jin Zhang, Alexander F. Chadwick, David L. Chopp, and Peter W. Voorhees. “Phase Field Modeling with Large Driving Forces”. *npj Computational Materials* 9.1 (Sept. 8, 2023), p. 166.

[135] Robert F. Sekerka. “Morphology: From Sharp Interface to Phase Field Models”. *Journal of Crystal Growth*. Proceedings of the Symposium - Progress in Crystal Growth 264.4 (Mar. 31, 2004), pp. 530–540.

[136] John W. Cahn and John E. Hilliard. “Free Energy of a Nonuniform System. I. Interfacial Free Energy”. *The Journal of Chemical Physics* 28.2 (Feb. 1, 1958), pp. 258–267.

[137] John W Cahn. “On Spinodal Decomposition”. *Acta Metallurgica* 9.9 (Sept. 1, 1961), pp. 795–801.

[138] Hao Wu. “A Review on the Cahn–Hilliard Equation: Classical Results and Recent Advances in Dynamic Boundary Conditions”. *Electronic Research Archive* 30.era-30-08-143 (8 2022), pp. 2788–2832.

[139] Hector Gomez and Kristoffer G. van der Zee. “Computational Phase-Field Modeling”. *Encyclopedia of Computational Mechanics Second Edition*. John Wiley & Sons, Ltd, 2017, pp. 1–35.

[140] Falko Ziebert, Sumanth Swaminathan, and Igor S. Aranson. “Model for Self-Polarization and Motility of Keratocyte Fragments”. *Journal of The Royal Society Interface* 9.70 (Oct. 2011), pp. 1084–1092.

[141] A. Dreher, I. S. Aranson, and K. Kruse. “Spiral Actin-Polymerization Waves Can Generate Amoeboidal Cell Crawling”. *New Journal of Physics* 16.5 (May 2014), p. 055007.

[142] W. Marth, S. Praetorius, and A. Voigt. “A Mechanism for Cell Motility by Active Polar Gels”. *Journal of The Royal Society Interface* 12.107 (June 6, 2015), p. 20150161.

[143] Matthew S. Mizuhara, Leonid Berlyand, and Igor S. Aranson. “Minimal Model of Directed Cell Motility on Patterned Substrates”. *Physical Review E* 96.5 (Nov. 15, 2017), p. 052408.

[144] John J. Molina and Ryoichi Yamamoto. “Modeling the Mechanosensitivity of Fast-Crawling Cells on Cyclically Stretched Substrates”. *Soft Matter* 15.4 (2019), pp. 683–698.

[145] Elsen Tjhung, Davide Marenduzzo, and Michael E. Cates. “Spontaneous Symmetry Breaking in Active Droplets Provides a Generic Route to Motility”. *Proceedings of the National Academy of Sciences* 109.31 (July 31, 2012), pp. 12381–12386.

[146] Jakob Löber, Falko Ziebert, and Igor S Aranson. “Modeling Crawling Cell Movement on Soft Engineered Substrates”. *Soft matter* 10.9 (2014), pp. 1365–1373.

[147] Benjamin Winkler, Igor S Aranson, and Falko Ziebert. “Membrane Tension Feedback on Shape and Motility of Eukaryotic Cells”. *Physica D: Nonlinear Phenomena* 318 (2016), pp. 26–33.

[148] Danying Shao, Wouter-Jan Rappel, and Herbert Levine. “A Computational Model for Cell Morphodynamics”. *Physical review letters* 105.10 (Sept. 3, 2010), p. 108104.

[149] Brian A Camley, Yunsong Zhang, Yanxiang Zhao, Bo Li, Eshel Ben-Jacob, Herbert Levine, and Wouter-Jan Rappel. “Polarity Mechanisms Such as Contact Inhibition of Locomotion Regulate Persistent Rotational Motion of Mammalian Cells on Micropatterns”. *Proceedings of the National Academy of Sciences* 111.41 (2014), pp. 14770–14775.

[150] Yuansheng Cao, Elisabeth Ghabache, and Wouter-Jan Rappel. “Plasticity of Cell Migration Resulting from Mechanochemical Coupling”. *eLife* 8 (), e48478.

[151] Jakob Löber, Falko Ziebert, and Igor S. Aranson. “Collisions of Deformable Cells Lead to Collective Migration”. *Scientific Reports* 5.1 (Mar. 17, 2015), p. 9172.

[152] D. Wenzel and A. Voigt. “Multiphase Field Models for Collective Cell Migration”. *Physical Review E* 104.5 (Nov. 24, 2021), p. 054410.

[153] Michael Chiang, Austin Hopkins, Benjamin Loewe, Davide Marenduzzo, and M. Cristina Marchetti. “Multiphase Field Model of Cells on a Substrate: From Three Dimensional to Two Dimensional”. *Physical Review E* 110.4 (Oct. 17, 2024), p. 044403.

[154] Makiko Nonomura. “Study on Multicellular Systems Using a Phase Field Model”. *PLOS ONE* 7.4 (Apr. 23, 2012), e33501.

[155] Aditya Shankar Paspunurwar, Adrian Moure, and Hector Gomez. “Dynamic Cluster Field Modeling of Collective Chemotaxis”. *Scientific Reports* 14.1 (Oct. 24, 2024), p. 25162.

[156] Yunsong Zhang, Herbert Levine, and Yanxiang Zhao. *Phase Field Modeling of Dictyostelium Discoideum Chemotaxis*. arXiv, Feb. 2023.

[157] Shohini Banerjee, Corey Herr, Wolfgang Losert, and Kimberly M. Stroka. *Estradiol Alters Actin and Protrusion Dynamics in Endometriotic Epithelial Cells*. May 18, 2025. URL: https://www.biorxiv.org/content/10.1101/2025.05.14.654086v1 (visited on 05/24/2025). Pre-published.

[158] Davide Gentilini, Paola Vigano, Edgardo Somigliana, Lucia Maria Vicentini, Michele Vignali, Mauro Busacca, and Anna Maria Di Blasio. “Endometrial Stromal Cells from Women with Endometriosis Reveal Peculiar Migratory Behavior in Response to Ovarian Steroids”. *Fertility and Sterility* 93.3 (Feb. 2010), pp. 706–715.

[159] Mosami Galvankar, Neha Singh, and Deepak Modi. “Estrogen Is Essential but Not Sufficient to Induce Endometriosis”. *Journal of Biosciences* 42.2 (June 2017), pp. 251–263.

[160] Yu Du, Zhibing Zhang, Wenqian Xiong, Na Li, Hengwei Liu, Haitang He, Qi Li, Yi Liu, and Ling Zhang. “Estradiol Promotes EMT in Endometriosis via MALAT1/miR200s Sponge Function”. *Reproduction (Cambridge, England)* 157.2 (Feb. 2019), pp. 179–188.

[161] Wenqian Xiong, Ling Zhang, Hengwei Liu, Na Li, Yu Du, Haitang He, Zhibing Zhang, and Yi Liu. “E $_2$ -mediated EMT by Activation of β-catenin/Snail Signalling during the Development of Ovarian Endometriosis”. *Journal of Cellular and Molecular Medicine* 23.12 (Dec. 2019), pp. 8035–8045.

[162] Marie Maynadier, Philippe Nirdé, Jean-Marie Ramirez, Anne Marie Cathiard, Nadine Platet, Monique Chambon, and Marcel Garcia. "Role of Estrogens and Their Receptors in Adhesion and Invasiveness of Breast Cancer Cells". *Hormonal Carcinogenesis V*. Ed. by Jonathan J. Li, Sara A. Li, Suresh Mohla, Henri Rochefort, and Thierry Maudelonde. Vol. 617. New York, NY: Springer New York, 2008, pp. 485–491.

[163] Rui Han, Shanzhi Gu, Yujiao Zhang, Anqi Luo, Xin Jing, Lin Zhao, Xinhan Zhao, and Lingxiao Zhang. "Estrogen Promotes Progression of Hormone-Dependent Breast Cancer through CCL2-CCR2 Axis by Upregulation of Twist via PI3K/AKT/NF-κB Signaling". *Scientific Reports* 8.1 (June 2018), p. 9575.

[164] Shuhui Zheng, Jinghe Huang, Kewen Zhou, Chengxi Zhang, Qiuling Xiang, Zhi Tan, Tinghuai Wang, and Xiaodong Fu. "17β-Estradiol Enhances Breast Cancer Cell Motility and Invasion via Extra-Nuclear Activation of Actin-Binding Protein Ezrin". *PLoS ONE* 6.7 (July 2011). Ed. by Jean-Marc Vanacker, e22439.

[165] Maria Silvia Giretti, Xiao-Dong Fu, Giovanni De Rosa, Ivana Sarotto, Chiara Baldacci, Silvia Garibaldi, Paolo Mannella, Nicoletta Biglia, Piero Sismondi, Andrea Riccardo Genazzani, and Tommaso Simoncini. "Extra-Nuclear Signalling of Estrogen Receptor to Breast Cancer Cytoskeletal Remodelling, Migration and Invasion". *PLoS ONE* 3.5 (May 2008). Ed. by Neil Hotchin, e2238.

[166] Qi Che, Xirong Xiao, Jun Xu, Miao Liu, Yongning Lu, Suying Liu, and Xi Dong. "17β-Estradiol Promotes Endometrial Cancer Proliferation and Invasion through IL-6 Pathway". *Endocrine Connections* 8.7 (July 2019), pp. 961–968.

[167] Jingxin Ding, Youji Feng, Lianhua Yin, Hongyan Jin, Xiaoxia Liu, Liangqing Yao, and Yunyan Sun. "The Effect of 17β- Estradiol on Invasion by the Ovarian Clear Cell Adenocarcinoma Cell Line ES - 2 and the Molecular Mechanism Involved". *Chinese Journal of Clinical Oncology* 2.4 (Aug. 2005), pp. 717–725.

[168] Shengnan Li, Kuo Jiang, Jia Li, Xiaohua Hao, Wenguang Chu, Ceng Luo, Yuanyuan Zhu, Rougang Xie, and Biliang Chen. "Estrogen Enhances the Proliferation and Migration of Ovarian Cancer Cells by Activating Transient Receptor Potential Channel C3". *Journal of Ovarian Research* 13.1 (Dec. 2020), p. 20.

[169] Zhenbo Zhang, Dongmei Zhou, Yunli Lai, Yongjuan Liu, Xiang Tao, Qianqian Wang, Guixu Zhao, Hongqin Gu, Hong Liao, Yaping Zhu, Xiaowei Xi, and Youji Feng. "Estrogen Induces Endometrial Cancer Cell Proliferation and Invasion by Regulating the Fat Mass and Obesity-Associated Gene via PI3K/AKT and MAPK Signaling Pathways". *Cancer Letters* 319.1 (June 2012), pp. 89–97.

[170] M.I. Flamini, A.M. Sanchez, L. Goglia, V. Tosi, A.R. Genazzani, and T. Simoncini. "Differential Actions of Estrogen and SERMs in Regulation of the Actin Cytoskeleton of Endometrial Cells". *Molecular Human Reproduction* 15.10 (Oct. 2009), pp. 675–685.

[171] Marina Ines Flamini, Angel Matias Sanchez, Andrea Riccardo Genazzani, and Tommaso Simoncini. “Estrogen Regulates Endometrial Cell Cytoskeletal Remodeling and Motility via Focal Adhesion Kinase”. *Fertility and Sterility* 95.2 (Feb. 2011), pp. 722–726.

[172] Victor Briz and Michel Baudry. “Estrogen Regulates Protein Synthesis and Actin Polymerization in Hippocampal Neurons through Different Molecular Mechanisms”. *Frontiers in Endocrinology* 5 (2014).

[173] Matthias Schaks, Grégory Giannone, and Klemens Rottner. “Actin Dynamics in Cell Migration”. *Essays in Biochemistry* 63.5 (Oct. 2019), pp. 483–495.

[174] Dale D. Tang and Brennan D. Gerlach. “The Roles and Regulation of the Actin Cytoskeleton, Intermediate Filaments and Microtubules in Smooth Muscle Cell Migration”. *Respiratory Research* 18.1 (Dec. 2017), p. 54.

[175] Julieann I. Puleo, Sara S. Parker, Mackenzie R. Roman, Adam W. Watson, Kiarash Rahmani Eliato, Leilei Peng, Kathylynn Saboda, Denise J. Roe, Robert Ros, Frank B. Gertler, and Ghassan Mouneimne. “Mechanosensing during Directed Cell Migration Requires Dynamic Actin Polymerization at Focal Adhesions”. *Journal of Cell Biology* 218.12 (Dec. 2019), pp. 4215–4235.

[176] Erdinç Atilgan, Denis Wirtz, and Sean X. Sun. “Mechanics and Dynamics of Actin-Driven Thin Membrane Protrusions”. *Biophysical Journal* 90.1 (Jan. 2006), pp. 65–76.

[177] Christoph Ballestrem, Bernhard Wehrle-Haller, Boris Hinz, and Beat A. Imhof. “Actin-Dependent Lamellipodia Formation and Microtubule-dependent Tail Retraction Control-directed Cell Migration”. *Molecular Biology of the Cell* 11.9 (Sept. 2000). Ed. by Ted Salmon, pp. 2999–3012.

[178] Marie Schoumacher, Robert D. Goldman, Daniel Louvard, and Danijela M. Vignjevic. “Actin, Microtubules, and Vimentin Intermediate Filaments Cooperate for Elongation of Invadopodia”. *Journal of Cell Biology* 189.3 (May 2010), pp. 541–556.

[179] Katarzyna Augoff, Anita Hryniewicz-Jankowska, and Renata Tabola. “Invadopodia: Clearing the Way for Cancer Cell Invasion”. *Annals of Translational Medicine* 8.14 (July 2020), pp. 902–902.

[180] Erik S. Welf, Christopher E. Miles, Jaewon Huh, Etai Sapoznik, Joseph Chi, Meghan K. Driscoll, Tadamoto Isogai, Jungsik Noh, Andrew D. Weems, Theresa Pohlkamp, Kevin Dean, Reto Fiolka, Alex Mogilner, and Gaudenz Danuser. “Actin-Membrane Release Initiates Cell Protrusions”. *Developmental Cell* 55.6 (Dec. 2020), 723–736.e8.

[181] Christoph Ballestrem, Bernhard Wehrle-Haller, and Beat A. Imhof. “Actin Dynamics in Living Mammalian Cells”. *Journal of Cell Science* 111.12 (June 1998), pp. 1649–1658.

[182] Chi-Li Chiu, Michelle A. Digman, and Enrico Gratton. “Measuring Actin Flow in 3D Cell Protrusions”. *Biophysical Journal* 105.8 (Oct. 2013), pp. 1746–1755.

[183] A. Zeitvogel, R. Baumann, and A. Starzinski-Powitz. “Identification of an Invasive, N-cadherin-expressing Epithelial Cell Type in Endometriosis Using a New Cell Culture Model”. *The American Journal of Pathology* 159.5 (Nov. 2001), pp. 1839–1852.

[184] Guillaume T. Charras, Chi-Kuo Hu, Margaret Coughlin, and Timothy J. Mitchison. “Reassembly of Contractile Actin Cortex in Cell Blebs”. *The Journal of Cell Biology* 175.3 (Nov. 6, 2006), pp. 477–490.

[185] Tatyana M. Svitkina and Gary G. Borisy. “Arp2/3 Complex and Actin Depolymerizing Factor/Cofilin in Dendritic Organization and Treadmilling of Actin Filament Array in Lamellipodia”. *The Journal of Cell Biology* 145.5 (May 1999), pp. 1009–1026.

[186] Nathalie Fuentes and Patricia Silveyra. “Estrogen Receptor Signaling Mechanisms”. *Advances in Protein Chemistry and Structural Biology*. Vol. 116. Elsevier, 2019, pp. 135–170.

[187] Tommy Heck, Diego A. Vargas, Bart Smeets, Herman Ramon, Paul Van Liedekerke, and Hans Van Oosterwyck. “The Role of Actin Protrusion Dynamics in Cell Migration through a Degradable Viscoelastic Extracellular Matrix: Insights from a Computational Model”. *PLOS Computational Biology* 16.1 (Jan. 2020). Ed. by Roeland M.H. Merks, e1007250.

[188] Richard L Klemke. “Trespassing Cancer Cells: ‘Fingerprinting’ Invasive Protrusions Reveals Metastatic Culprits”. *Current Opinion in Cell Biology* 24.5 (Oct. 2012), pp. 662–669.

[189] Chetan K Rane and Audrey Minden. “P21 Activated Kinases: Structure, Regulation, and Functions”. *Small GTPases* 5.1 (Jan. 2014), e28003.

[190] Désirée Spiering and Louis Hodgson. “Dynamics of the Rho-family Small GTPases in Actin Regulation and Motility”. *Cell Adhesion & Migration* 5.2 (Mar. 2011), pp. 170–180.

[191] Naomi Courtemanche, Thomas D. Pollard, and Qian Chen. “Avoiding Artefacts When Counting Polymerized Actin in Live Cells with LifeAct Fused to Fluorescent Proteins”. *Nature Cell Biology* 18.6 (June 2016), pp. 676–683.

[192] Andrew J. Spracklen, Tiffany N. Fagan, Kaylee E. Lovander, and Tina L. Tootle. “The Pros and Cons of Common Actin Labeling Tools for Visualizing Actin Dynamics during Drosophila Oogenesis”. *Developmental Biology* 393.2 (Sept. 2014), pp. 209–226.

[193] Rui Xu and Shaojun Du. “Overexpression of Lifeact-GFP Disrupts F-Actin Organization in Cardiomyocytes and Impairs Cardiac Function”. *Frontiers in Cell and Developmental Biology* 9 (Oct. 2021), p. 746818.

[194] Timothy A. Sanders, Esther Llagostera, and Maria Barna. “Specialized Filopodia Direct Long-Range Transport of SHH during Vertebrate Tissue Patterning”. *Nature* 497.7451 (May 2013), pp. 628–632.

[195] Julia Riedl, Alvaro H Crevenna, Kai Kessenbrock, Jerry Haochen Yu, Dorothee Neukirchen, Michal Bista, Frank Bradke, Dieter Jenne, Tad A Holak, Zena Werb, Michael Sixt, and Roland Wedlich-Soldner. “Lifeact: A Versatile Marker to Visualize F-actin”. *Nature Methods* 5.7 (July 2008), pp. 605–607.

[196] D. Gentilini, M. Busacca, S. Di Francesco, M. Vignali, P. Viganò, and A.M. Di Blasio. “PI3K/Akt And ERK1/2 Signalling Pathways Are Involved in Endometrial Cell Migration Induced by 17β-Estradiol and Growth Factors”. *MHR: Basic science of reproductive medicine* 13.5 (May 2007), pp. 317–322.

[197] Manuel Guizar-Sicairos, Samuel T. Thurman, and James R. Fienup. “Efficient Subpixel Image Registration Algorithms”. *Optics Letters* 33.2 (Jan. 2008), p. 156.

[198] C.D. Kuglin. “The Phase Correlation Image Alignment Method”. IEEE, 1975, pp. 163–165.

[199] G. Le Besnerais and F. Champagnat. “Dense Optical Flow by Iterative Local Window Registration”. *IEEE International Conference on Image Processing 2005*. Genova, Italy: IEEE, 2005, pp. I–137.

[200] S. Uras, F. Girosi, A. Verri, and V. Torre. “A Computational Approach to Motion Perception”. *Biological Cybernetics* 60.2 (Dec. 1988), pp. 79–87.

[201] Kate M. O’Neill, Emanuela Saracino, Barbara Barile, Nicholas J. Mennona, Maria Grazia Mola, Spandan Pathak, Tamara Posati, Roberto Zamboni, Grazia P. Nicchia, Valentina Benfenati, and Wolfgang Losert. “Decoding Natural Astrocyte Rhythms: Dynamic Actin Waves Result from Environmental Sensing by Primary Rodent Astrocytes”. *Advanced Biology* 7.6 (June 2023), p. 2200269.

[202] Corey Herr, Benjamin Winkler, Falko Ziebert, Igor S. Aranson, John T. Fourkas, and Wolfgang Losert. “Spontaneous Polarization and Cell Guidance on Asymmetric Nanotopography”. *Communications Physics* 5.1 (May 2022), pp. 1–8.

[203] Erik Sahai. “Illuminating the Metastatic Process”. *Nature Reviews Cancer* 7.10 (10 Oct. 2007), pp. 737–749.

[204] Chun-Min Lo, Hong-Bei Wang, Micah Dembo, and Yu-li Wang. “Cell Movement Is Guided by the Rigidity of the Substrate”. *Biophysical Journal* 79.1 (July 1, 2000), pp. 144–152.

[205] Carole A. Parent and Peter N. Devreotes. “A Cell’s Sense of Direction”. *Science* 284.5415 (Apr. 30, 1999), pp. 765–770.

[206] Nathan D. Bade, Tina Xu, Randall D. Kamien, Richard K. Assoian, and Kathleen J. Stebe. “Gaussian Curvature Directs Stress Fiber Orientation and Cell Migration”. *Biophysical Journal* 114.6 (Mar. 27, 2018), pp. 1467–1476.

[207] P. Clark, P. Connolly, A. S. Curtis, J. A. Dow, and C. D. Wilkinson. “Topographical Control of Cell Behaviour: II. Multiple Grooved Substrata”. *Development (Cambridge, England)* 108.4 (Apr. 1990), pp. 635–644.

[208] Matthew John Dalby, Mathis O. Riehle, Duncan S. Sutherland, Hossein Agheli, and Adam S. G. Curtis. “Changes in Fibroblast Morphology in Response to Nano-Columns Produced by Colloidal Lithography”. *Biomaterials* 25.23 (Oct. 1, 2004), pp. 5415–5422.

[209] Christopher J Bettinger, Robert Langer, and Jeffrey T Borenstein. ““Engineering Substrate Micro- and Nanotopography to Control Cell Function””. *Angewandte Chemie (International ed. in English)* 48.30 (2009), pp. 5406–5415.

[210] Melvin Schindler, Alam Nur-E-Kamal, Ijaz Ahmed, Jabeen Kamal, Hsing-Yin Liu, Nathan Amor, Abdul S. Ponery, David P. Crockett, Timothy H. Grafe, H. Young Chung, Thom Weik, Elizabeth Jones, and Sally Meiners. “Living in Three Dimensions”. *Cell Biochemistry and Biophysics* 45.2 (June 1, 2006), pp. 215–227.

[211] Alison Abbott. “Biology’s New Dimension”. *Nature* 424.6951 (6951 Aug. 1, 2003), pp. 870–872.

[212] Danying Shao, Herbert Levine, and Wouter-Jan Rappel. “Coupling Actin Flow, Adhesion, and Morphology in a Computational Cell Motility Model”. *Proceedings of the National Academy of Sciences* 109.18 (2012), pp. 6851–6856.

[213] E. Tjhung, A. Tiribocchi, D. Marenduzzo, and M. E. Cates. “A Minimal Physical Model Captures the Shapes of Crawling Cells”. *Nature Communications* 6.1 (Jan. 2015), p. 5420.

[214] Benoit Palmieri, Yony Bresler, Denis Wirtz, and Martin Grant. “Multiple Scale Model for Cell Migration in Monolayers: Elastic Mismatch between Cells Enhances Motility”. *Scientific Reports* 5.1 (1 July 2, 2015), p. 11745.

[215] Thuan Beng Saw, Amin Doostmohammadi, Vincent Nier, Leyla Kocgozlu, Sumesh Thampi, Yusuke Toyama, Philippe Marcq, Chwee Teck Lim, Julia M. Yeomans, and Benoit Ladoux. “Topological Defects in Epithelia Govern Cell Death and Extrusion”. *Nature* 544.7649 (7649 Apr. 2017), pp. 212–216.

[216] Romain Mueller, Julia M. Yeomans, and Amin Doostmohammadi. “Emergence of Active Nematic Behavior in Monolayers of Isotropic Cells”. *Physical Review Letters* 122.4 (Feb. 1, 2019), p. 048004.

[217] Wieland Marth and Axel Voigt. “Signaling Networks and Cell Motility: A Computational Approach Using a Phase Field Description”. *Journal of Mathematical Biology* 69.1 (July 1, 2014), pp. 91–112.

[218] Benjamin Loewe, Michael Chiang, Davide Marenduzzo, and M. Cristina Marchetti. “Solid-Liquid Transition of Deformable and Overlapping Active Particles”. *Physical Review Letters* 125.3 (July 15, 2020), p. 038003.

[219] Benjamin Winkler, Igor S. Aranson, and Falko Ziebert. "Confinement and Substrate Topography Control Cell Migration in a 3D Computational Model". *Communications Physics* 2.1 (July 2019), pp. 1–11.

[220] Alexander B Verkhovsky, Tatyana M Svitkina, and Gary G Borisy. "Self-Polarization and Directional Motility of Cytoplasm". *Current Biology* 9.1 (1999), 11–S1.

[221] Céline Labouesse, Alexander B. Verkhovsky, Jean-Jacques Meister, Chiara Gabella, and Benoît Vianay. "Cell Shape Dynamics Reveal Balance of Elasticity and Contractility in Peripheral Arcs". *Biophysical Journal* 108.10 (May 19, 2015), pp. 2437–2447.

[222] Claudia Tanja Mierke, Daniel Rösel, Ben Fabry, and Jan Brábek. "Contractile Forces in Tumor Cell Migration". *European journal of cell biology* 87.8–9 (Sept. 2008), pp. 669–676.

[223] Kun-Chun Lee and Andrea J. Liu. "New Proposed Mechanism of Actin-Polymerization-Driven Motility". *Biophysical Journal* 95.10 (Nov. 15, 2008), pp. 4529–4539.

[224] Stefan Linder. "The Matrix Corroded: Podosomes and Invadopodia in Extracellular Matrix Degradation". *Trends in cell biology* 17.3 (2007), pp. 107–117.

[225] Yuliya Klymenko, Oleg Kim, Elizabeth Loughran, Jing Yang, Rachel Lombard, Mark Alber, and M Sharon Stack. "Cadherin Composition and Multicellular Aggregate Invasion in Organotypic Models of Epithelial Ovarian Cancer Intraperitoneal Metastasis". *Oncogene* 36.42 (2017), pp. 5840–5851.

[226] Alex Mogilner. "Mathematics of Cell Motility: Have We Got Its Number?" *Journal of Mathematical Biology* 58.1 (May 7, 2008), p. 105.

[227] Nobuyuki Otsu. "A Threshold Selection Method from Gray-Level Histograms". *IEEE transactions on systems, man, and cybernetics* 9.1 (1979), pp. 62–66.

[228] A. D. Luster, R. Alon, and U. H. von Andrian. "Immune Cell Migration in Inflammation: Present and Future Therapeutic Targets". *Nature immunology* 6.12 (2005), pp. 1182–1190.

[229] S. Seetharaman and S. Etienne-Manneville. "Cytoskeletal Crosstalk in Cell Migration". *Trends in cell biology* 30.9 (2020), pp. 720–735.

[230] H. Yamaguchi and J. Condeelis. "Regulation of the Actin Cytoskeleton in Cancer Cell Migration and Invasion". *Biochimica et biophysica acta* 1773.5 (2007), pp. 642–652.

[231] H. Chen, G. Zhu, Y. Li, R. N. Padia, Z. Dong, Z. K. Pan, K. Liu, and S. Huang. "Extracellular Signal-Regulated Kinase Signaling Pathway Regulates Breast Cancer Cell Migration by Maintaining Slug Expression". *Cancer research* 69.24 (2009), pp. 9228–9235.

[232] V. M. Zohrabian, B. Forzani, Z. Chau, R. Murali, and M. Jhanwar-Uniyal. "Rho/ROCK and MAPK Signaling Pathways Are Involved in Glioblastoma Cell Migration and Proliferation". *Anticancer research* 29 (2009), pp. 119–124.

[233] Z. Mostafavi-Pour, J. A. Askari, S. J. Parkinson, P. J. Parker, T. T. Ng, and M. J. Humphries. “Integrin-Specific Signaling Pathways Controlling Focal Adhesion Formation and Cell Migration”. *The Journal of cell biology* 161.1 (2003), pp. 155–167.

[234] Y. Li, J. P. Wang, R. J. Santen, T. H. Kim, H. Park, P. Fan, and W. Yue. “Estrogen Stimulation of Cell Migration Involves Multiple Signaling Pathway Interactions”. *Endocrinology* 151.11 (2010), pp. 5146–5156.

[235] J. Yamauchi, J. R. Chan, and E. M. Shooter. “Neurotrophins Regulate Schwann Cell Migration by Activating Divergent Signaling Pathways Dependent on Rho GTPases”. *Proceedings of the National Academy of Sciences of the United States of America* 101.23 (2004), pp. 8774–8779.

[236] K. Dumstrei, R. Mennecke, and E. Raz. “Signaling Pathways Controlling Primordial Germ Cell Migration in Zebrafish”. *Journal of cell science* 117 (Pt 20 2004), pp. 4787–4795.

[237] X. Zhao and J. L. Guan. “Focal Adhesion Kinase and Its Signaling Pathways in Cell Migration and Angiogenesis”. *Advanced drug delivery reviews* 63.8 (2011), pp. 610–615.

[238] J. Harris, L. Honigberg, N. Robinson, and C. Kenyon. “Neuronal Cell Migration in C. Elegans: Regulation of Hox Gene Expression and Cell Position”. *Development (Cambridge, England)* 122 (1996), pp. 3117–3131.

[239] I. Mannaerts, B. Schroyen, S. Verhulst, L. Van Lommel, F. Schuit, M. Nyssen, and L. A. van Grunsven. “Gene Expression Profiling of Early Hepatic Stellate Cell Activation Reveals a Role for Igfbp3 in Cell Migration”. *PLoS One* 8.12 (2013), e84071.

[240] J. M. Rhoads, X. Niu, J. Odle, and L. M. Graves. “Role of mTOR Signaling in Intestinal Cell Migration”. *American journal of physiology. Gastrointestinal and liver physiology* 291.3 (2006), G510–G517.

[241] C. Burrows, N. Abd Latip, S. J. Lam, L. Carpenter, K. Sawicka, G. Tzolovsky, H. Gabra, M. Bushell, D. M. Glover, A. E. Willis, and S. P. Blagden. “The RNA Binding Protein Larp1 Regulates Cell Division, Apoptosis and Cell Migration”. *Nucleic acids research* 38.16 (2010), pp. 5542–5553.

[242] Z. Guo, F. Pan, L. Peng, S. Tian, J. Jiao, L. Liao, C. Lu, G. Zhai, Z. Wu, H. Dong, X. Xu, J. Wu, P. Chen, X. Bai, D. Lin, L. Xu, E. Li, and K. Zhang. “Systematic Proteome and Lysine Succinylome Analysis Reveals the Enhanced Cell Migration by Hyposuccinylation in Esophageal Squamous Cell Cancer”. *Molecular & cellular proteomics : MCP* (2021), p. 100053.

[243] S. Yan, V. Golumba-Nagy, K. Kotschenreuther, J. Thiele, N. Refaian, D. Shuya, L. Gloyer, M. Dittrich-Salamon, A. Meyer, L. M. Heindl, and D. M. Kofler. “Membrane-Bound IL-6R Is Upregulated on Th17 Cells and Inhibits Treg Cell Migration by Regulating Post-

Translational Modification of VASP in Autoimmune Arthritis". *Cellular and molecular life sciences : CMLS* 79.1 (2022), p. 3.

[244] N. T. Snider and M. B. Omary. "Post-Translational Modifications of Intermediate Filament Proteins: Mechanisms and Functions". *Nature reviews. Molecular cell biology* 15.3 (2014), pp. 163–177.

[245] N. K. Verma, E. Dempsey, J. Conroy, P. Olwell, A. M. McElligott, A. M. Davies, D. Kelleher, S. Butini, G. Campiani, D. C. Williams, D. M. Zisterer, M. Lawler, and Y. Volkov. "A New Microtubule-Targeting Compound PBOX-15 Inhibits T-cell Migration via Post-Translational Modifications of Tubulin". *Journal of molecular medicine* 86.4 (2008), pp. 457–469.

[246] A. R. Horwitz and J. T. Parsons. "Cell Migration–Movin' On". *Science* 286.5442 (1999), pp. 1102–1103.

[247] S. SenGupta, C. A. Parent, and J. E. Bear. "The Principles of Directed Cell Migration". *Nature reviews. Molecular cell biology* 22.8 (2021), pp. 529–547.

[248] E. Theveneau and R. Mayor. "Neural Crest Delamination and Migration: From Epithelium-to-Mesenchyme Transition to Collective Cell Migration". *Developmental biology* 366.1 (2012), pp. 34–54.

[249] Cassandra L. Buchheit, Kelsey J. Weigel, and Zachary T. Schafer. "Cancer Cell Survival during Detachment from the ECM: Multiple Barriers to Tumour Progression". *Nature Reviews Cancer* 14.9 (9 Sept. 2014), pp. 632–641.

[250] M. P. Stemmler, R. L. Eccles, S. Brabletz, and T. Brabletz. "Non-Redundant Functions of EMT Transcription Factors". *Nature cell biology* 21.1 (2019), pp. 102–112.

[251] E. Sanchez-Tillo, Y. Liu, O. de Barrios, L. Siles, L. Fanlo, M. Cuatrecasas, D. S. Darling, D. C. Dean, A. Castells, and A. Postigo. "EMT-activating Transcription Factors in Cancer: Beyond EMT and Tumor Invasiveness". *Cellular and molecular life sciences : CMLS* 69.20 (2012), pp. 3429–3456.

[252] S. Di Cio and J. E. Gautrot. "Cell Sensing of Physical Properties at the Nanoscale: Mechanisms and Control of Cell Adhesion and Phenotype". *Acta biomaterialia* 30 (2016), pp. 26–48.

[253] B. K. K. Teo, S. T. Wong, C. K. Lim, T. Y. S. Kung, C. H. Yap, Y. Ramagopal, L. H. Romer, and E. K. F. Yim. "Nanotopography Modulates Mechanotransduction of Stem Cells and Induces Differentiation through Focal Adhesion Kinase". *ACS Nano* 7.6 (2013), pp. 4785–4798.

[254] A. A. Moe, M. Suryana, G. Marcy, S. K. Lim, S. Ankam, J. Z. Goh, J. Jin, B. K. Teo, J. B. Law, H. Y. Low, E. L. Goh, M. P. Sheetz, and E. K. Yim. "Microarray with Micro- and Nano-Topographies Enables Identification of the Optimal Topography for Directing the

Differentiation of Primary Murine Neural Progenitor Cells". *Small* 8.19 (2012), pp. 3050–3061.

[255] S. H. Lim, X. Y. Liu, H. Song, K. J. Yarema, and H. Q. Mao. "The Effect of Nanofiber-Guided Cell Alignment on the Preferential Differentiation of Neural Stem Cells". *Biomaterials* 31.34 (2010), pp. 9031–9039.

[256] Z. Yin, X. Chen, J. L. Chen, W. L. Shen, T. M. Hieu Nguyen, L. Gao, and H. W. Ouyang. "The Regulation of Tendon Stem Cell Differentiation by the Alignment of Nanofibers". *Biomaterials* 31.8 (2010), pp. 2163–2175.

[257] K. Chatterjee, S. Lin-Gibson, W. E. Wallace, S. H. Parekh, Y. J. Lee, M. T. Cicerone, M. F. Young, and Jr. Simon C. G. "The Effect of 3D Hydrogel Scaffold Modulus on Osteoblast Differentiation and Mineralization Revealed by Combinatorial Screening". *Biomaterials* 31.19 (2010), pp. 5051–5062.

[258] D. E. Discher, P. Janmey, and Y. Wang. "Tissue Cells Feel and Respond to the Stiffness of Their Substrate". *Science* 310 (2005), pp. 1139–1143.

[259] L. Trichet, J. Le Digabel, R. J. Hawkins, S. R. Vedula, M. Gupta, C. Ribrault, P. Hersen, R. Voituriez, and B. Ladoux. "Evidence of a Large-Scale Mechanosensing Mechanism for Cellular Adaptation to Substrate Stiffness". *Proceedings of the National Academy of Sciences of the United States of America* 109.18 (2012), pp. 6933–6938.

[260] K. Kulangara and K. W. Leong. "Substrate Topography Shapes Cell Function". *Soft Matter* 5.21 (2009), pp. 4072–4076.

[261] J. S. Chua, C. P. Chng, A. A. Moe, J. Y. Tann, E. L. Goh, K. H. Chiam, and E. K. Yim. "Extending Neurites Sense the Depth of the Underlying Topography during Neuronal Differentiation and Contact Guidance". *Biomaterials* 35.27 (2014), pp. 7750–7761.

[262] S. Heydarkhan-Hagvall, C. H. Choi, J. Dunn, S. Heydarkhan, K. Schenke-Layland, W. R. MacLellan, and R. E. Beygui. "Influence of Systematically Varied Nano-Scale Topography on Cell Morphology and Adhesion". *Cell communication & adhesion* 14.5 (2007), pp. 181–194.

[263] A. Curtis and C. Wilkinson. "Topographical Control of Cells". *Biomaterials* 18.24 (1997), pp. 1573–1583.

[264] Y. Hou, W. Xie, L. Yu, L. C. Camacho, C. Nie, M. Zhang, R. Haag, and Q. Wei. "Surface Roughness Gradients Reveal Topography-Specific Mechanosensitive Responses in Human Mesenchymal Stem Cells". *Small* 16.10 (2020), e1905422.

[265] J. Huang, Y. Chen, C. Tang, Y. Fei, H. Wu, D. Ruan, M. E. Paul, X. Chen, Z. Yin, B. C. Heng, W. Chen, and W. Shen. "The Relationship between Substrate Topography and Stem Cell Differentiation in the Musculoskeletal System". *Cellular and molecular life sciences : CMLS* 76.3 (2019), pp. 505–521.

[266] X. Liu, J. Y. Lim, H. J. Donahue, R. Dhurjati, A. M. Mastro, and E. A. Vogler. “Influence of Substratum Surface Chemistry/Energy and Topography on the Human Fetal Osteoblastic Cell Line hFOB 1.19: Phenotypic and Genotypic Responses Observed in Vitro”. *Biomaterials* 28.31 (2007), pp. 4535–4550.

[267] L. Lara Rodriguez and I. C. Schneider. “Directed Cell Migration in Multi-Cue Environments”. *Integrative biology : quantitative biosciences from nano to macro* 5.11 (2013), pp. 1306–1323.

[268] C. C. DuFort, M. J. Paszek, and V. M. Weaver. “Balancing Forces: Architectural Control of Mechanotransduction”. *Nature reviews. Molecular cell biology* 12.5 (2011), pp. 308–319.

[269] N. Gjorevski and C. M. Nelson. “Bidirectional Extracellular Matrix Signaling during Tissue Morphogenesis”. *Cytokine & growth factor reviews* 20.5–6 (2009), pp. 459–465.

[270] J. Albuschies and V. Vogel. “The Role of Filopodia in the Recognition of Nanotopographies”. *Scientific reports* 3 (2013), p. 1658.

[271] D. Guadarrama Bello, A. Fouillen, A. Badia, and A. Nanci. “A Nanoporous Titanium Surface Promotes the Maturation of Focal Adhesions and Formation of Filopodia with Distinctive Nanoscale Protrusions by Osteogenic Cells”. *Acta biomaterialia* 60 (2017), pp. 339–349.

[272] V. Bhingardive, A. Kossover, M. Iraqi, B. Khand, G. Le Saux, A. Porgador, and M. Schvartzman. “Antibody-Functionalized Nanowires: A Tuner for the Activation of T Cells”. *Nano letters* 21.10 (2021), pp. 4241–4248.

[273] W. Zhang, Y. Yang, and B. Cui. “New Perspectives on the Roles of Nanoscale Surface Topography in Modulating Intracellular Signaling”. *Current opinion in solid state & materials science* 25.1 (2021), p. 100873.

[274] Y. Chen, J. Wang, X. Li, N. Hu, N. H. Voelcker, X. Xie, and R. Elnathan. “Emerging Roles of 1D Vertical Nanostructures in Orchestrating Immune Cell Functions”. *Advanced Materials* 32.40 (2020), e2001668.

[275] S. Lehoux, Y. Castier, and A. Tedgui. “Molecular Mechanisms of the Vascular Responses to Haemodynamic Forces”. *Journal of internal medicine* 259.4 (2006), pp. 381–392.

[276] R. G. LeBaron and K. A. Athanasiou. “Extracellular Matrix Cell Adhesion Peptides: Functional Applications in Orthopedic Materials”. *Tissue engineering* 6.2 (2000), pp. 85–103.

[277] B. J. Peter, H. M. Kent, I. G. Mills, Y. Vallis, P. J. G. Butler, P. R. Evans, and H. T. McMahon. “BAR Domains as Sensors of Membrane Curvature: The Amphiphysin BAR Structure”. *Science* 303 (2004), pp. 495–499.

[278] V. K. Bhatia, K. L. Madsen, P. Y. Bolinger, A. Kunding, P. Hedegard, U. Gether, and D. Stamou. “Amphipathic Motifs in BAR Domains Are Essential for Membrane Curvature Sensing”. *The EMBO journal* 28.21 (2009), pp. 3303–3314.

[279] V. K. Bhatia, N. S. Hatzakis, and D. Stamou. “A Unifying Mechanism Accounts for Sensing of Membrane Curvature by BAR Domains, Amphipathic Helices and Membrane-Anchored Proteins”. *Seminars in cell & developmental biology* 21.4 (2010), pp. 381–390.

[280] T. Ozdemir, L. C. Xu, C. Siedlecki, and J. L. Brown. “Substrate Curvature Sensing through Myosin IIa Upregulates Early Osteogenesis”. *Integrative biology : quantitative biosciences from nano to macro* 5.11 (2013), pp. 1407–1416.

[281] C. G. Galbraith and M. P. Sheetz. “Forces on Adhesive Contacts Affect Cell Function”. *Current opinion in cell biology* 10 (1998), pp. 566–571.

[282] X. Sun and G. M. Alushin. “Cellular Force-Sensing through Actin Filaments”. *The FEBS journal* 290.10 (2023), pp. 2576–2589.

[283] Q. Yang, Y. Miao, L. J. Campanello, M. J. Hourwitz, B. Abubaker-Sharif, A. L. Bull, P. N. Devreotes, J. T. Fourkas, and W. Losert. “Cortical Waves Mediate the Cellular Response to Electric Fields”. *Elife* 11 (2022), e73198.

[284] A. L. Bull, L. Campanello, M. J. Hourwitz, Q. Yang, M. Zhao, J. T. Fourkas, and W. Losert. “Actin Dynamics as a Multiscale Integrator of Cellular Guidance Cues”. *Frontiers in cell and developmental biology* 10 (2022), p. 873567.

[285] C. M. Ketchum, X. Sun, A. Suberi, J. T. Fourkas, W. Song, and A. Upadhyaya. “Subcellular Topography Modulates Actin Dynamics and Signaling in B-cells”. *Molecular biology of the cell* 29.13 (2018), pp. 1732–1742.

[286] M. Azatov, X. Sun, A. Suberi, J. T. Fourkas, and A. Upadhyaya. “Topography on a Subcellular Scale Modulates Cellular Adhesions and Actin Stress Fiber Dynamics in Tumor Associated Fibroblasts”. *Physical biology* 14.6 (2017), p. 065003.

[287] C. Herr, B. Winkler, F. Ziebert, I. S. Aranson, J. T. Fourkas, and W. Losert. “Spontaneous Polarization and Cell Guidance on Asymmetric Nanotopography”. *Communications On Physics* 5.1 (2022), p. 114.

[288] B. A. Wheatley, I. Rey-Suarez, M. J. Hourwitz, S. Kerr, H. Shroff, J. T. Fourkas, and A. Upadhyaya. “Nanotopography Modulates Cytoskeletal Organization and Dynamics during T Cell Activation”. *Molecular biology of the cell* 33.10 (2022), ar88.

[289] Y. W. Heng and C. G. Koh. “Actin Cytoskeleton Dynamics and the Cell Division Cycle”. *The international journal of biochemistry & cell biology* 42.10 (2010), pp. 1622–1633.

[290] F. Rizzelli, M. G. Malabarba, S. Sigismund, and M. Mapelli. “The Crosstalk between Microtubules, Actin and Membranes Shapes Cell Division”. *Open biology* 10.3 (2020), p. 190314.

[291] T. G. Chew, C. Lorthongpanich, W. X. Ang, B. B. Knowles, and D. Solter. “Symmetric Cell Division of the Mouse Zygote Requires an Actin Network”. *Cytoskeleton (Hoboken, N.J.)* 69.12 (2012), pp. 1040–1046.

[292] N. Parisis, L. Krasinska, B. Harker, S. Urbach, M. Rossignol, A. Camasses, J. Dewar, N. Morin, and D. Fisher. “Initiation of DNA Replication Requires Actin Dynamics and Formin Activity”. *The EMBO journal* 36.21 (2017), pp. 3212–3231.

[293] V. Hurst, K. Shimada, and S. M. Gasser. “Nuclear Actin and Actin-Binding Proteins in DNA Repair”. *Trends in cell biology* 29.6 (2019), pp. 462–476.

[294] M. Schuh. “An Actin-Dependent Mechanism for Long-Range Vesicle Transport”. *Nature cell biology* 13.12 (2011), pp. 1431–1436.

[295] S. van Helvert, C. Storm, and P. Friedl. “Mechanoreciprocity in Cell Migration”. *Nature cell biology* 20.1 (2018), pp. 8–20.

[296] T. Luo, K. Mohan, P. A. Iglesias, and D. N. Robinson. “Molecular Mechanisms of Cellular Mechanosensing”. *Nature materials* 12.11 (2013), pp. 1064–1071.

[297] A. J. Ridley, M. A. Schwartz, K. Burridge, R. A. Firtel, M. H. Ginsberg, G. Borisy, J. T. Parsons, and A. R. Horwtiz. “Cell Migration: Integrating Signals from Front to Back”. *Science* 302 (2003), pp. 1704–1709.

[298] V. O. Paavilainen, E. Bertling, S. Falck, and P. Lappalainen. “Regulation of Cytoskeletal Dynamics by Actin-Monomer-Binding Proteins”. *Trends in cell biology* 14.7 (2004), pp. 386–394.

[299] A. G. Ammer and S. A. Weed. “Cortactin Branches out: Roles in Regulating Protrusive Actin Dynamics”. *Cell motility and the cytoskeleton* 65.9 (2008), pp. 687–707.

[300] C. L. Tu, W. Chang, and D. D. Bikle. “The Calcium-Sensing Receptor-Dependent Regulation of Cell-Cell Adhesion and Keratinocyte Differentiation Requires Rho and Filamin A”. *The Journal of investigative dermatology* 131.5 (2011), pp. 1119–1128.

[301] Y. Yang, K. Wang, X. Gu, and K. W. Leong. “Biophysical Regulation of Cell Behavior-Cross Talk between Substrate Stiffness and Nanotopography”. *Engineering (Beijing, China)* 3.1 (2017), pp. 36–54.

[302] T. L. Jenkins and D. Little. “Synthetic Scaffolds for Musculoskeletal Tissue Engineering: Cellular Responses to Fiber Parameters”. *NPJ Regenerative medicine* 4 (2019), p. 15.

[303] P. Ringer, G. Colo, R. Fassler, and C. Grashoff. “Sensing the Mechano-Chemical Properties of the Extracellular Matrix”. *Matrix biology : journal of the International Society for Matrix Biology* 64 (2017), pp. 6–16.

[304] T. R. Cox and J. T. Erler. “Remodeling and Homeostasis of the Extracellular Matrix: Implications for Fibrotic Diseases and Cancer”. *Disease models & mechanisms* 4.2 (2011), pp. 165–178.

[305] L. Bozec, G. van der Heijden, and M. Horton. “Collagen Fibrils: Nanoscale Ropes”. *Biophysical journal* 92.1 (2007), pp. 70–75.

[306] R. S. Fischer, X. Sun, M. A. Baird, M. J. Hourwitz, B. R. Seo, A. M. Pasapera, S. B. Mehta, W. Losert, C. Fischbach, J. T. Fourkas, and C. M. Waterman. “Contractility, Focal Adhesion Orientation, and Stress Fiber Orientation Drive Cancer Cell Polarity and Migration along Wavy ECM Substrates”. *Proceedings of the National Academy of Sciences of the United States of America* 118.22 (2021), e2021135118.

[307] P. K. Sengupta, E. M. Smith, K. Kim, M. J. Murnane, and B. D. Smith. “DNA Hypermethylation near the Transcription Start Site of Collagen Alpha2(I) Gene Occurs in Both Cancer Cell Lines and Primary Colorectal Cancers”. *Cancer research* 63 (2003), pp. 1789–1797.

[308] C. K. Miranti and J. S. Brugge. “Sensing the Environment: A Historical Perspective on Integrin Signal Transduction”. *Nature cell biology* 4 (2002), E83–E90.

[309] T. Walzer, L. Galibert, M. R. Comeau, and T. De Smedt. “Plexin C1 Engagement on Mouse Dendritic Cells by Viral Semaphorin A39R Induces Actin Cytoskeleton Rearrangement and Inhibits Integrin-Mediated Adhesion and Chemokine-Induced Migration”. *Journal of immunology (Baltimore, Md. : 1950)* 174.1 (2005), pp. 51–59.

[310] D. C. Edwards, L. C. Sanders, G. M. Bokoch, and G. N. Gill. “Activation of LIM Kinase by Pak1 Couples Rac/Cdc42 GTPase Signalling to Actin Cytoskeletal Dynamics”. *Nature cell biology* 1 (1999), pp. 253–259.

[311] K. W. Kwon, H. Park, K. H. Song, J. C. Choi, H. Ahn, M. J. Park, K. Y. Suh, and J. Doh. “Nanotopography-Guided Migration of T Cells”. *Journal of immunology (Baltimore, Md. : 1950)* 189.5 (2012), pp. 2266–2273.

[312] K. H. Song, S. J. Park, D. S. Kim, and J. Doh. “Sinusoidal Wavy Surfaces for Curvature-Guided Migration of T Lymphocytes”. *Biomaterials* 51 (2015), pp. 151–160.

[313] H. Wolfenson, T. Iskratsch, and M. P. Sheetz. “Early Events in Cell Spreading as a Model for Quantitative Analysis of Biomechanical Events”. *Biophysical journal* 107.11 (2014), pp. 2508–2514.

[314] A. C. Hielscher, C. Qiu, and S. Gerecht. “Breast Cancer Cell-Derived Matrix Supports Vascular Morphogenesis”. *American journal of physiology. Cell physiology* 302.8 (2012), pp. C1243–C1256.

[315] P. A. DiMilla, J. A. Stone, J. A. Quinn, S. M. Albelda, and D. A. Lauffenburger. “Maximal Migration of Human Smooth Muscle Cells on Fibronectin and Type IV Collagen Oc-

curs at an Intermediate Attachment Strength". *The Journal of cell biology* 122.3 (1993), pp. 729–737.

[316] K. M. Riching, B. L. Cox, M. R. Salick, C. Pehlke, A. S. Riching, S. M. Ponik, B. R. Bass, W. C. Crone, Y. Jiang, A. M. Weaver, K. W. Eliceiri, and P. J. Keely. "3D Collagen Alignment Limits Protrusions to Enhance Breast Cancer Cell Persistence". *Biophysical journal* 107.11 (2014), pp. 2546–2558.

[317] W. Y. Wang, A. T. Pearson, M. L. Kutys, C. K. Choi, M. A. Wozniak, B. M. Baker, and C. S. Chen. "Extracellular Matrix Alignment Dictates the Organization of Focal Adhesions and Directs Uniaxial Cell Migration". *APL bioengineering* 2.4 (2018), p. 046107.

[318] A. L. Le Roux, X. Quiroga, N. Walani, M. Arroyo, and P. Roca-Cusachs. "The Plasma Membrane as a Mechanochemical Transducer". *Philos Trans R Soc B* 374.1779 (2019), p. 20180221.

[319] H. T. McMahon and E. Boucrot. "Membrane Curvature at a Glance". *Journal of cell science* 128.6 (2015), pp. 1065–1070.

[320] L. Li and J. T. Fourkas. "Multiphoton Polymerization". *Materials Today* 10.6 (2007), pp. 30–37.

[321] Robert Lanza, Robert Langer, Joseph P. Vacanti, and Anthony Atala. *Principles of Tissue Engineering*. Academic Press, Mar. 26, 2020. 1679 pp.

[322] T. J. Mitchison and L. P. Cramer. "Actin-Based Cell Motility and Cell Locomotion". *Cell* 84.3 (Feb. 9, 1996), pp. 371–379.

[323] G. F. Oster and A. S. Perelson. "The Physics of Cell Motility". *Journal of Cell Science. Supplement* 8 (Supplement_8 1987), pp. 35–54.

[324] Igor S. Aranson, ed. *Physical Models of Cell Motility*. Biological and Medical Physics, Biomedical Engineering. Cham: Springer International Publishing, 2016.

[325] Pablo A Iglesias and Peter N Devreotes. "Biased Excitable Networks: How Cells Direct Motion in Response to Gradients". *Current Opinion in Cell Biology*. Cell Regulation 24.2 (Apr. 1, 2012), pp. 245–253.

[326] Alexander Ziepke, Ivan Maryshev, Igor S. Aranson, and Erwin Frey. "Multi-Scale Organization in Communicating Active Matter". *Nature Communications* 13.1 (Nov. 7, 2022), p. 6727.

[327] Steven H Strogatz. *Nonlinear Dynamics and Chaos: With Applications to Physics, Biology, Chemistry, and Engineering*. Chapman and Hall/CRC, 2024.

[328] Jun Allard and Alex Mogilner. "Traveling Waves in Actin Dynamics and Cell Motility". *Current opinion in cell biology* 25.1 (Feb. 2013), pp. 107–115.

[329] Adam C. Martin, Matthias Kaschube, and Eric F. Wieschaus. “Pulsed Contractions of an Actin–Myosin Network Drive Apical Constriction”. *Nature* 457.7228 (Jan. 2009), pp. 495–499.

[330] Ann Sutherland and Alyssa Lesko. “Pulsed Actomyosin Contractions in Morphogenesis”. *F1000Research* 9 (Feb. 25, 2020), F1000 Faculty Rev–142.

[331] Fernanda Pérez-Verdugo, Samuel Banks, and Shiladitya Banerjee. “Excitable Dynamics Driven by Mechanical Feedback in Biological Tissues”. *Communications Physics* 7.1 (May 24, 2024), pp. 1–8.

[332] Xavier Serra-Picamal, Vito Conte, Romaric Vincent, Ester Anon, Dhananjay T. Tambe, Elsa Bazellieres, James P. Butler, Jeffrey J. Fredberg, and Xavier Trepat. “Mechanical Waves during Tissue Expansion”. *Nature Physics* 8.8 (Aug. 2012), pp. 628–634.

[333] Marco P. De Leon, Fu-Lai Wen, Giovanni J. Paylaga, Ying-Ting Wang, Hsiao-Yuh Roan, Chung-Han Wang, Chung-Der Hsiao, Keng-Hui Lin, and Chen-Hui Chen. “Mechanical Waves Identify the Amputation Position during Wound Healing in the Amputated Zebrafish Tailfin”. *Nature Physics* 19.9 (Sept. 2023), pp. 1362–1370.

[334] Ivana Pajic-Lijakovic and Milan Milivojevic. “Mechanical Oscillations in 2D Collective Cell Migration: The Elastic Turbulence”. *Frontiers in Physics* 8 (Nov. 6, 2020).

[335] Dhananjay T. Tambe, Ugo Croutelle, Xavier Trepat, Chan Young Park, Jae Hun Kim, Emil Millet, James P. Butler, and Jeffrey J. Fredberg. “Monolayer Stress Microscopy: Limitations, Artifacts, and Accuracy of Recovered Intercellular Stresses”. *PloS One* 8.2 (2013), e55172.

[336] John Metzcar, Yafei Wang, Randy Heiland, and Paul Macklin. “A Review of Cell-Based Computational Modeling in Cancer Biology”. *JCO Clinical Cancer Informatics* 3 (Feb. 4, 2019), pp. 1–13.

[337] Jonas Pleyer and Christian Fleck. “Agent-Based Models in Cellular Systems”. *Frontiers in Physics* 10 (Jan. 4, 2023).

[338] Alexander G. Fletcher, Miriam Osterfield, Ruth E. Baker, and Stanislav Y. Shvartsman. “Vertex Models of Epithelial Morphogenesis”. *Biophysical Journal* 106.11 (June 3, 2014), pp. 2291–2304.

[339] Eduardo Moreno, Robert Großmann, Carsten Beta, and Sergio Alonso. “From Single to Collective Motion of Social Amoebae: A Computational Study of Interacting Cells”. *Frontiers in Physics* 9 (Feb. 2, 2022).

[340] Eric J. Campbell and Prosenjit Bagchi. “A Computational Model of Amoeboid Cell Motility in the Presence of Obstacles”. *Soft Matter* 14.28 (2018), pp. 5741–5763.

[341] Grégoire Peyret, Romain Mueller, Joseph d’Alessandro, Simon Begnaud, Philippe Marcq, René-Marc Mège, Julia M. Yeomans, Amin Doostmohammadi, and Benoît Ladoux. “Sus-

tained Oscillations of Epithelial Cell Sheets". *Biophysical Journal* 117.3 (Aug. 6, 2019), pp. 464–478.

[342] Wei Wang, Robert A. Law, Emiliano Perez Ipiña, Konstantinos Konstantopoulos, and Brian A. Camley. "Confinement, Jamming, and Adhesion in Cancer Cells Dissociating from a Collectively Invading Strand". *PRX Life* 3.1 (Feb. 25, 2025), p. 013012.

[343] Michael Riedl, Isabelle Mayer, Jack Merrin, Michael Sixt, and Björn Hof. "Synchronization in Collectively Moving Inanimate and Living Active Matter". *Nature Communications* 14.1 (Sept. 13, 2023), p. 5633.

[344] David F. Holmes, Ching-Yan Chloé Yeung, Richa Garva, Egor Zindy, Susan H. Taylor, Yinhui Lu, Simon Watson, Nicholas S. Kalson, and Karl E. Kadler. "Synchronized Mechanical Oscillations at the Cell–Matrix Interface in the Formation of Tensile Tissue". *Proceedings of the National Academy of Sciences* 115.40 (Oct. 2, 2018), E9288–E9297.

[345] Alexander Ziepke, Ivan Maryshev, Igor S Aranson, and Erwin Frey. "Acoustic Signaling Enables Collective Perception and Control in Active Matter Systems". *Physical Review X* (2025).

[346] Kevin P O'Keeffe, Hyunsuk Hong, and Steven H Strogatz. "Oscillators That Sync and Swarm". *Nature communications* 8.1 (2017), p. 1504.

[347] Steven Strogatz. "Sync: The Emerging Science of Spontaneous Order" (2004).

[348] Daniel Boocock, Tsuyoshi Hirashima, and Edouard Hannezo. "Interplay between Mechanochemical Patterning and Glassy Dynamics in Cellular Monolayers". *PRX Life* 1.1 (July 20, 2023), p. 013001.

[349] Alexandros Glentis, Carles Blanch-Mercader, Lakshmi Balasubramaniam, Thuan Beng Saw, Joseph d'Alessandro, Sebastien Janel, Audrey Douanier, Benedicte Delaval, Frank Lafont, Chwee Teck Lim, Delphine Delacour, Jacques Prost, Wang Xi, and Benoit Ladoux. "The Emergence of Spontaneous Coordinated Epithelial Rotation on Cylindrical Curved Surfaces". *Science Advances* 8.37 (Sept. 14, 2022), eabn5406.

[350] Kevin Doxzen, Sri Ram Krishna Vedula, Man Chun Leong, Hiroaki Hirata, Nir S Gov, Alexandre J Kabla, Benoit Ladoux, and Chwee Teck Lim. "Guidance of Collective Cell Migration by Substrate Geometry". *Integrative biology* 5.8 (2013), pp. 1026–1035.

[351] Maureen Cetera, Guillermina R Ramirez-San Juan, Patrick W Oakes, Lindsay Lewellyn, Michael J Fairchild, Guy Tanentzapf, Margaret L Gardel, and Sally Horne-Badovinac. "Epithelial Rotation Promotes the Global Alignment of Contractile Actin Bundles during Drosophila Egg Chamber Elongation". *Nature communications* 5.1 (2014), p. 5511.

[352] Chiara Malinverno, Salvatore Corallino, Fabio Giavazzi, Martin Bergert, Qingsen Li, Marco Leoni, Andrea Disanza, Emanuela Frittoli, Amanda Oldani, Emanuele Martini, et al. "Endocytic Reawakening of Motility in Jammed Epithelia". *Nature materials* 16.5 (2017), pp. 587–596.

[353] Brian A. Camley, Yanxiang Zhao, Bo Li, Herbert Levine, and Wouter-Jan Rappel. "Periodic Migration in a Physical Model of Cells on Micropatterns". *Physical Review Letters* 111.15 (Oct. 10, 2013), p. 158102.

[354] Camila Londono, M. Jimena Loureiro, Benjamin Slater, Petra B. Lücker, John Soleas, Suthamathy Sathananthan, J. Stewart Aitchison, Alexandre J. Kabla, and Alison P. McGuigan. "Nonautonomous Contact Guidance Signaling during Collective Cell Migration". *Proceedings of the National Academy of Sciences of the United States of America* 111.5 (Feb. 4, 2014), pp. 1807–1812.

[355] Abby L. Bull, Molly Mosher, Paula Rodriguez, Shannon Fox, Matt J. Hourwitz, John T. Fourkas, and Wolfgang Losert. "Suppressing Collective Cell Motion with Bidirectional Guidance Cues". *Physical Review E* 111.2 (Feb. 25, 2025), p. 024409.

[356] Charles D. Cox, Yixiao Zhang, Zijing Zhou, Thomas Walz, and Boris Martinac. "Cyclodextrins Increase Membrane Tension and Are Universal Activators of Mechanosensitive Channels". *Proceedings of the National Academy of Sciences* 118.36 (Sept. 7, 2021), e2104820118.

[357] Ido Nitsan, Stavit Drori, Yair E. Lewis, Shlomi Cohen, and Shelly Tzlil. "Mechanical Communication in Cardiac Cell Synchronized Beating". *Nature Physics* 12.5 (May 2016), pp. 472–477.

[358] Amos Zamir, Guanyu Li, Katelyn Chase, Robert Moskovitch, Bo Sun, and Assaf Zaritsky. "Emergence of Synchronized Multicellular Mechanosensing from Spatiotemporal Integration of Heterogeneous Single-Cell Information Transfer". *Cell systems* 13.9 (Sept. 21, 2022), 711–723.e7.

[359] Prachi Richa, Matthias Häring, Qiyan Wang, Ankit Roy Choudhury, Martin C. Göpfert, Fred Wolf, Jörg Großhans, and Deqing Kong. "Synchronization in Epithelial Tissue Morphogenesis". *Current Biology* (Apr. 15, 2025).

[360] Yang Yang, Hongmei Zheng, Yuting Zhan, and Songqing Fan. "An Emerging Tumor Invasion Mechanism about the Collective Cell Migration". *American Journal of Translational Research* 11.9 (Sept. 15, 2019), pp. 5301–5312.

[361] Guanming Zhang, Romain Mueller, Amin Doostmohammadi, and Julia M. Yeomans. "Active Inter-Cellular Forces in Collective Cell Motility". *Journal of The Royal Society Interface* 17.169 (Aug. 12, 2020), p. 20200312.

[362] Çağla Özsoy, Ali Özbek, Michael Reiss, Xosé Luís Deán-Ben, and Daniel Razansky. "Ultrafast Four-Dimensional Imaging of Cardiac Mechanical Wave Propagation with Sparse Optoacoustic Sensing". *Proceedings of the National Academy of Sciences* 118.45 (Nov. 9, 2021), e2103979118.

[363] Stephanie E. Lindsey, Jonathan T. Butcher, and Huseyin C. Yalcin. "Mechanical Regulation of Cardiac Development". *Frontiers in Physiology* 5 (Aug. 21, 2014), p. 318.

[364] Rebecca M. Crossley, Samuel Johnson, Erika Tsingos, Zoe Bell, Massimiliano Berardi, Margherita Botticelli, Quirine J. S. Braat, John Metzcar, Marco Ruscone, Yuan Yin, and Robyn Shuttleworth. “Modeling the Extracellular Matrix in Cell Migration and Morphogenesis: A Guide for the Curious Biologist”. *Frontiers in Cell and Developmental Biology* 12 (Mar. 1, 2024), p. 1354132.

[365] Karen Alim, Olivier Hamant, and Arezki Boudaoud. “Regulatory Role of Cell Division Rules on Tissue Growth Heterogeneity”. *Frontiers in Plant Science* 3 (Aug. 9, 2012), p. 174.

[366] Youyuan Deng, Herbert Levine, Xiaoming Mao, and Leonard M. Sander. “Collective Motility and Mechanical Waves in Cell Clusters”. *The European Physical Journal. E, Soft Matter* 44.11 (Nov. 15, 2021), p. 137.

[367] M Akiyama, M Nonomura, A Tero, and R Kobayashi. “Numerical Study on Spindle Positioning Using Phase Field Method”. *Physical Biology* 16.1 (Nov. 2018), p. 016005.

[368] Xiangyu Kuang, Guoye Guan, Chao Tang, and Lei Zhang. “MorphoSim: An Efficient and Scalable Phase-Field Framework for Accurately Simulating Multicellular Morphologies”. *npj Systems Biology and Applications* 9.1 (Feb. 17, 2023), pp. 1–11.

[369] Paulius Gibieža and Vilma Petrikaitė. “The Regulation of Actin Dynamics during Cell Division and Malignancy”. *American Journal of Cancer Research* 11.9 (Sept. 15, 2021), pp. 4050–4069.

[370] K. Tao, J. Wang, X. Kuang, W. Wang, F. Liu, and L. Zhang. *Tuning Cell Motility via Cell Tension with a Mechanochemical Cell Migration Model*. bioRxiv, Nov. 2019.

[371] Jeremy Nance, Jen-Yi Lee, and Bob Goldstein. “Gastrulation in C. Elegans”. *WormBook: The Online Review of C. Elegans Biology [Internet]*. WormBook, Sept. 26, 2005.

[372] Khaled Khairy, William Lemon, Fernando Amat, and Philipp J. Keller. “A Preferred Curvature-Based Continuum Mechanics Framework for Modeling Embryogenesis”. *Biophysical Journal* 114.2 (Jan. 23, 2018), pp. 267–277.

[373] Rachel Lockridge Mueller. “Genome Biology and the Evolution of Cell-Size Diversity”. *Cold Spring Harbor Perspectives in Biology* 7.11 (Nov. 2015), a019125.

[374] Luis U. Aguilera, Christoph Zimmer, and Ursula Kummer. “A New Efficient Approach to Fit Stochastic Models on the Basis of High-Throughput Experimental Data Using a Model of IRF7 Gene Expression as Case Study”. *BMC Systems Biology* 11.1 (Feb. 20, 2017), p. 26.

[375] Hanieh Mazloom-Farsibaf, Qiongjing Zou, Rebecca Hsieh, Gaudenz Danuser, and Meghan K. Driscoll. “Cellular Harmonics for the Morphology-Invariant Analysis of Molecular Organization at the Cell Surface”. *Nature Computational Science* 3.9 (Sept. 2023), pp. 777–788.